Ornl 1156

ORNL-5265

Creep Deformation and Rupture Behavior of Type 304/308 Stainless Steel Structural Weldments

W. J. McAfee
M. Richardson
W. K. Sartory

Form AEC 426
(6-74)
AECM 3201

U.S. ATOMIC ENERGY COMMISSION

MAJOR CONTRACTOR'S RECOMMENDATION FOR DISPOSITION OF SCIENTIFIC AND TECHNICAL DOCUMENT

*See Instructions on Reverse

1. AEC Report No. ORNL-5265

2. Subject Category No. UC-79e, -h, -k

3. Title Creep Deformation and Rupture Behavior of Type 304/308 Stainless Steel Structural Weldments. Authors: W.J. McAfee, M. Richardson & W.K. Sartory

4. Type of Document ("X" one)

- [X] a. Scientific and Technical Report
- [ ] b. Conference paper:
  - Title of conference _____
  - Date of conference _____
  - Exact location of conference _____
- [ ] c. Other (Specify, Thesis, Translation, etc.)* _____

5. Copies Transmitted ("X" one or more)

- [X] a. Copies being transmitted for standard distribution by AEC-TIC.
- [ ] b. Copies being transmitted for special distribution per attached complete address list.*
- [ ] c. Two completely legible, reproducible copies being transmitted to AEC-TIC.

6. Recommended Distribution ("X" one)

- [X] a. Normal handling (after Patent clearance): no restraints on distribution except as may be required by the security classification.
- [ ] b. Make available only to U.S. Government agencies and their contractors.
- [ ] c. Make available only within AEC and to AEC contractors.
- [ ] d. Make available only within AEC.
- [ ] e. Make available only to those listed in Item 12 below.
- [X] f. Other (Specify)* LMFBR - Base Technology

7. Recommended Announcement ("X" one)

- [ ] a. Normal procedure may be followed.*
- [X] b. Recommend following announcement limitations: LMFBR - Base Technology

8. Reason for Restrictions Recommended in 6 or 7 above.

- [ ] a. Preliminary information.
- [ ] b. Prepared primarily for internal use.
- [ ] c. Other (Explain) _____

9. Patent Clearance ("X" one)

- [X] a. AEC patent clearance has been granted by responsible AEC patent group.
- [ ] b. Document has been sent to responsible AEC patent group for clearance.

10. National Security Information (For classified document only; "X" one)

- [ ] a. Document does contain national security information other than restricted data.
- [ ] b. Document does not contain national security information other than restricted data.

11. Copy Reproduction and Distribution

a. Total number of copies reproduced 381

b. Number of copies distributed outside originating organization 288

12. Additional Information or Remarks (Continue on separate sheet, if necessary)

LMFBR - Base Technology

13. Submitted by (Name and Position) (Please print or type)*

P. S. Baker, Classification Officer

14. Organization

ORNL-5265
Dist. Category UC-79,
-79e, -79h, -79k

Contract No. W-7405-eng-26

Engineering Technology Division

CREEP DEFORMATION AND RUPTURE BEHAVIOR OF TYPE 304/308 STAINLESS STEEL STRUCTURAL WELDMENTS

W. J. McAfee M. Richardson
W. K. Sartory

Manuscript Completed — 5-12-77
Date Published — June 1977

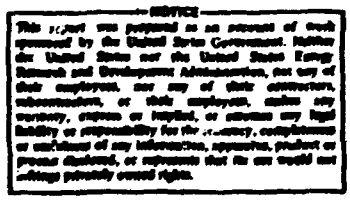

Prepared by the
OAK RIDGE NATIONAL LABORATORY
Oak Ridge, Tennessee 37830
operated by
UNION CARBIDE CORPORATION
for the
ENERGY RESEARCH AND DEVELOPMENT ADMINISTRATION

CONTENTS

CREEP DEFORMATION AND RUPTURE BEHAVIOR OF TYPE 304/308 STAINLESS STEEL STRUCTURAL WELDMENTS

W. J. McAfee M. Richardson
W. K. Sartory

ABSTRACT

The creep deformation and rupture of type 304/308 stainless steel structural weldments at 593°C (1100°F) was experimentally investigated to study the comparative behavior of the base metal and weld metal constituents. The tests were conducted in support of ORNL's program to develop high-temperature structural design methods applicable to liquid-metal fast breeder reactor (LMFBR) system components that operate in the creep range. The specimens used were thin-walled, right circular cylinders capped with either flat or hemispherical heads and tested under internal gas pressure. Circumferential welds were located in different regions of the cylinder or head and, with one exception, were geometrically duplicated by all base metal regions in companion specimens. Results are presented on the comparative deformation and rupture behavior of selected points in the base metal and weldment regions of the different specimens and on the overall surface strains for selected specimens.

Key words: Weldments, creep-rupture, high-temperature design, pressurized cylinders, stainless steel, LMFBR, structural tests.

---

1. INTRODUCTION

The extensive use of welded stainless steel pressure vessels and piping at temperatures within the creep range requires an increased understanding of the time-dependent deformation and failure behavior of weldments. A weldment in this context is considered to be the deposited weld and a region of base metal around the weld whose behavior is influenced by the presence of the weld. The properties of weldments vary widely[1] due to differences in weld procedures, weld metals, and weld geometries. The design rules[2] for nuclear components fabricated from austenitic stainless steels to operate at temperatures above 427°C (800°F) permit the use of

base metal properties in weld design but require that permanent deformation be limited to one-half that allowed for base metal. Such rules do not account for metallurgical discontinuities nor for geometric discontinuities that may be introduced through differences in inelastic deformation behavior of the base and weld metal.

This report presents the results of a series of creep-rupture tests of type 304/308 stainless steel weldments. The primary objective of these tests was to study the comparative deformation and failure behavior of the weld and base metal constituents of structural weldments. In addition, the basic specimen configuration, a capped right circular-cylindrical shell, is one simple structure geometry being used in development and verification of inelastic structural analysis methods.[3]

The specimens tested were fabricated using material from the highly characterized Oak Ridge National Laboratory (ORNL) reference heat (heat 9T2796) of type 304 stainless steel. The welds were deposited in multiple passes using bare type 308 stainless steel wire and the tungsten arc (TIG) welding process.

The tests were conducted in air at 593°C (1100°F). Two series of tests were run: series 1 was intended to be short-term tests and had rupture times from 35 to 408 hr; series 2 was designed and tested to achieve longer lifetimes and had rupture times from 475 to 9712 hr.

A pattern of scribe lines on the cylinder and cap of each specimen established a reference grid from which comparative sets of dimensional measurements were made. At specified times throughout the test lifetimes, each specimen was depressurized, cooled, and removed from the furnace for dimensional inspection. The dimensional measurements were made at the radial and axial locations of the nodes of the reference grid. The nodal locations were used to describe, through least-squares fitting, mathematical surfaces that depicted the deformed geometry of the specimen. Inside and outside surface strains were calculated by utilizing the strain-displacement relationships of continuum mechanics and the equations of thin-shell analysis applied to the mathematical descriptions of the deformed surfaces.

Section 2 of this report describes the design and fabrication of the test specimens. Section 3 discusses the test facility, test procedures,

and test histories. Section 4 presents the deformation data and the techniques used to convert these data to total inelastic strain. Section 5 is a summary of results and the subsequent conclusions. An appendix is included that contains experimental surface strain distributions for selected times in the lives of different specimens.

2. TEST SPECIMENS

2.1 Test Specimen Design and Fabrication

Two series of specimens were prepared for testing. These were designated as the weldment creep-rupture 1 (WCR-1) series and the weldment creep-rupture[2] (WCR-2) series. The WCR-1 series was intended to investigate weldment deformation and failure for times of 1000 hr or less. In addition, the information and experience gained from testing this series of specimens were to provide guidance in the design of WCR-2 series specimens. The WCR-2 series specimens were to be essentially of the same configuration as WCR-1 specimens but were to be tested under conditions yielding failure times of approximately 8000 hr. For the WCR-1 specimens, the von Mises effective stress was used as the failure criterion. This was based on the results of Anderson et al.,[4] which indicated that at 593°C (1100°F) pressurized tube failure data on annealed type 304 stainless steel correlated better with the von Mises rather than the maximum principal stress failure criterion. However, the failure results from WCR-1 specimens correlated best with the maximum principal stress failure criterion. Thus, this criterion was used in the design of the WCR-2 specimens.

In each series of specimens, the intent was to investigate the comparative behavior of base metal and deposited weld metal subjected to different stress or strain fields. The specimens were thus to have welds located in different areas where each weldment was duplicated by an unwelded "control," generally as part of another specimen.

2.1.1 WCR-1 specimens

The basic specimen configuration to be tested was a thin-walled right circular cylinder with a flat head. The nominal diameter was chosen to utilize product forms from the ORNL reference heat (heat 9T2796) of type 304 stainless steel. These product forms were 114-mm-diam (4.500-in.) bar and 102-mm (4-in.) sched-160 pipe. The chemical compositions[5,6] of these two product forms, as determined by ladle, check, and ORNL analyses, are given in Table 1.

Table 1. Chemical composition (wt %) of product forms of type 304 stainless steel (heat 9T2796) used for WCR-1 specimens

Element	Ladle analysis	114-mm-diam bar		102-mm sched-160 pipe	
		Vendor analysis[a]	ORNL analysis	Vendor analysis	ORNL analysis
C	0.048	NA	0.039	0.046	0.039
Mn	1.22	NA	1.31	1.23	1.31
P	0.028	NA	0.028	0.026	0.028
S	0.015	NA	0.014	0.020	0.014
Si	0.48	NA		0.50	0.42
Ni	9.70	NA	9.64	9.58	9.64
Cr	18.60	NA	18.54	18.57	18.54
Mo	0.32	NA	0.32	NA	0.32
N	NA	NA	0.027	NA	0.027
Cu	0.24	NA		NA	0.30
Sn	0.015	NA		NA	NA
Ti	0.010	NA		NA	>0.01
Co	0.18	NA		NA	0.20

[a]NA = not available.

The basic specimen wall thickness was set as 5.08 mm (0.200 in.). This dimension was established as a compromise between several factors. A thin wall was desirable for the tubular structure to behave as a thin shell and required less internal pressure to achieve the high stress levels required. However, a wall of significant thickness was desirable so that a composite weld structure, that is, a weld composed of several welding passes, would be tested. The possibility of premature failure through undetected microscopic flaws in the weld would thus be minimized.

With the nominal wall thickness fixed, elastic analyses were performed using different head-to-thickness ratios to investigate the general stress magnitudes and distributions in the cylinder, head, and cylinder-to-head junction region. The model used for these calculations was a right circular

cylinder with a circumferential weld at the cylinder midpoint. The cylinder was closed at one end with a flat head and was built in at the other end. The results of these calculations were used as a basis for selecting the head-to-cylinder thickness ratio such that the calculated maximum effective elastic stress in the center region of the head was comparable to the effective elastic stress in the membrane region of the cylinder. No exact comparison could be made since the stresses in the head varied with radial position. The calculated stress distribution in the cylinder was used as a basis for adjusting the specimen length to provide a region of membrane stress between the circumferential weld and each end of the cylinder. These regions of membrane stress were intended to isolate each discontinuity region from the influence of other regions. The above analyses indicated that a head-to-cylinder thickness ratio of 2:1 would yield comparable maximum elastic stresses in the head and cylinder and that a length of 2 to 3 diameters between discontinuities would be sufficient spacing to provide undisturbed membrane regions.

Test welds were to be located in three different test areas of the structures. The first area was circumferentially in the membrane region of the cylinder which would be typical of a pipe butt weld. For the internal pressure loading only, the applied membrane stress field had a 2:1 biaxiality ratio. The second area was the junction region between the head and cylinder. The weld in this region was intended to be in a field of high bending stress. Also, due to the bending and the constraint of the head, the maximum strain would be in the axial direction transverse to the weld. The third test area was in the head of the specimen; the intent was to locate a test weld in a stress field that would approach a 1:1 biaxiality ratio. The weld would be subjected to bending stresses parallel and transverse to the weld direction.

The WCR-1 series consisted of three specimens; these are shown in Fig. 1, along with the locations of each test weld. Specimen 1-M1 had a weld in the cylinder-to-head junction region with no welds in the membrane stress region of the cylinder. The cylinder thus served as the control for the circumferential pipe butt weld. The cylinder was machined from pipe, and the flat head was machined from bar stock. Specimen 2-M1 had a pipe butt weld in the cylinder; the upper half of the specimen was machined

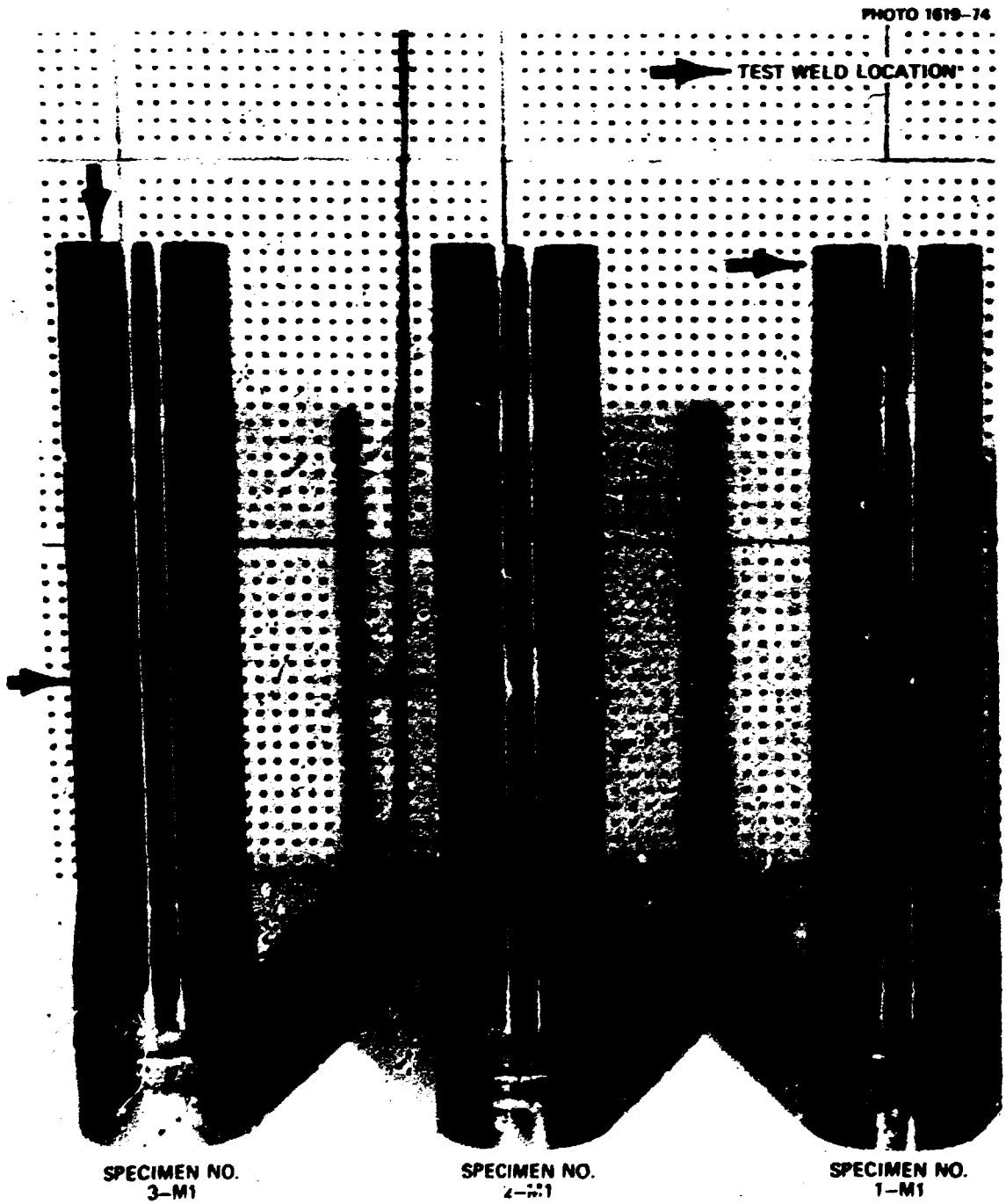

Fig. 1. WCR-1 specimens showing test weld locations.

from solid bar stock, and the lower cylinder region was made of pipe. The upper part of this specimen served as a control for the behavior of the weld in the cylinder-to-head junction region and for the weld in the head. Specimen 3-M1 had a circumferential weld in the head and a pipe

butt weld in the cylinder. The upper part of this specimen was machined from solid bar stock. A 38.1-mm-diam (1 1/2-in.) plug was removed from the center of the head, the edges of plug and head were machined to the correct geometry, and the plug was welded back into the head to yield the desired circumferential weld in the head. The lower part of this specimen was made of pipe material.

To control the geometric variables that affect weld behavior, the specimens were machined smooth after welding to remove the drawdown of the weld region and the surface discontinuity of the weld head. Also, the specimens were annealed prior to welding using the ORNL reference anneal.[7]

To prevent excess distortion during welding and to provide adequate material for machining of the final specimen geometry, sections thicker than those proposed for the final specimens were required. The cylindrical sections of the specimens were machined to a 10.2-mm (0.400-in.) thickness, and the heads were machined to a 11.4-mm (0.450-in.) thickness. The weld surfaces were prepared in this machining step. The specimen parts were annealed in argon using the reference anneal. Figure 2 shows a specimen, 4-M2, from the second series of specimens that typifies this stage of preparation. The weld surfaces were cleaned by steel brushing and the parts were welded together into the required assemblies.

These welded specimens were machined to the final dimensions and configuration. It was found that the amount of drawdown in the head weld of specimen 3-M1 and in the pipe butt weld of specimens 2-M1 and 3-M1 required removing more material than was originally anticipated. While this did not modify the basic specimen geometry, it did cause minor changes in dimensions. The final specimen wall thickness became 4.52 mm (0.178 in.), the head thickness was 7.62 mm (0.300 in.), and the outside diameter was 0.103 m (4.050 in.). After finish machining, the outside surfaces of the specimens were lightly polished, and circumferential scribe lines approximately 0.025 mm (0.001 in.) deep were machined at specified locations on the cylinder and head. These lines, which are visible in Fig. 3, were used as part of a reference grid for making dimensional measurements. The axial spacing of the lines on the cylinder was nominally 25.4 mm

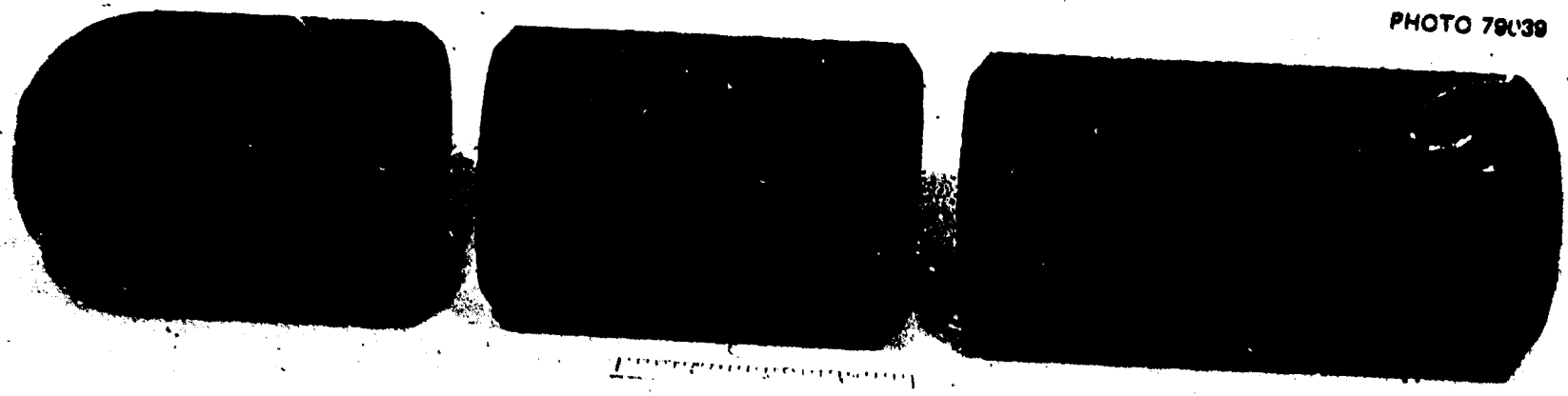

Fig. 2. View of weldment creep-rupture specimen that typifies condition of all specimens after preparatory machining and annealing.

Fig. 3. Typical weldment creep-rupture specimen showing circumferential scribe lines on cylinder and head.

(1 in.) but was reduced to 6.35 mm (1/4 in.) in regions, such as the cylinder-to-head junction region, where variations in the strain distribution were expected. The scribe lines on the head were concentric circles with their center being the geometric center of the head. The diameters of these circles ranged from 12.7 mm (1/2 in.) to 88.9 mm (3 1/2 in.) in 12.7-mm (1/2-in.) increments. These lines were used in data acquisition, as discussed in detail in Section 4.

The radiographic inspection of the pipe butt weld of specimen 2-M1 revealed deposits of high-density material in the root pass of the weld. These deposits were tentatively identified as boron, and the size and number were bases for the weld failing to pass the required inspection. During the subsequent weld removal, weld surface preparation, and rewelding, it was necessary to remove a region of base metal on each side of the weld, along with the weld. Thus, the final overall length of specimen 2-M1 was about 25.4 mm (1 in.) shorter than the other two specimens. This was not considered to be a problem since there was an adequate region of membrane stress between the pipe butt weld and each end of the specimen.

A schematic of an assembled specimen is shown in Fig. 4. A carbon steel core was used for inside filler, and the specimen was closed using

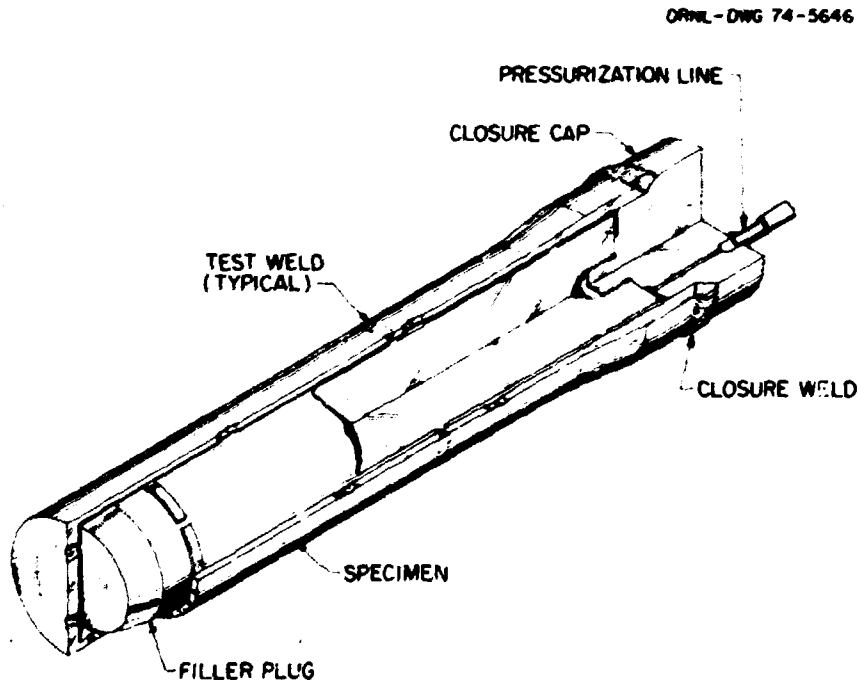

Fig. 4. Schematic of a typical weldment creep-rupture assembly.

a fairly heavy cylindrical cap. The core was machined to a 1.27-mm (0.05-in.) clearance with all inside surfaces of the specimen and displaced approximately 80% of the gas volume. The closure cap was designed to provide a relatively rigid base for the cylindrical section of the test specimen. This cap was made of type 304 stainless steel and was welded to the specimen using the same weld rod and welding procedure that was used for the test welds. The cap also served to support the specimen core through a threaded connection as shown in Fig. 4 and to properly align the core with the specimen such that contact of the two was prevented. Two 2.38-mm-diam (3/32-in.) holes with centers on a 61-mm-diam (2.4-in.) circle were drilled axially through the cap. The outer end of each hole was machined for autoclave fittings. One of these fittings was connected to the pressurization line, while the other was attached to a short length of high-pressure tubing that extended outside the furnace and ended in a valve. This line was used for venting the specimen during gas purging and pressure release. Due to problems encountered in maintaining the integrity of the seals between the pressure tubing and the specimen, the autoclave fittings were later removed and the tubing was welded directly to the specimen. A 12.7-mm-diam (1/2-in.), 22.2-mm (7/8-in.) deep hole was drilled and tapped in the center of the outside end of the cap, and a threaded rod, by which the specimen was suspended in the furnace, was screwed into this hole. These details are shown in Fig. 4.

Axial reference lines approximately 25.4 mm (1 in.) long were scribed at 60° increments around the circumference of the closure cap. The lines were not scribed along the entire length of the specimen since there was a possibility that such axial scribe marks on the test section would serve as stress raisers that might lead to premature specimen failure. These lines were identified as A–F using metal indentation stamps in order to provide permanent markings for reference purposes. These axial scribe lines, in conjunction with the circumferential scribe lines on the specimen, were used as part of the grid for data acquisition which is discussed in detail in Section 4.

2.1.2 WCR-2 specimens

The second series of weldment creep-rupture specimens (WCR-2) were essentially the same geometrically as the first series. By allowing more

material during the intermediate machining steps, the restrictions on specimen diameter and thickness caused by weld drawdown were overcome. The nominal dimensions of the WCR-2 specimens were: diameter, 0.102 m (4 in.); wall thickness, 5.08 mm (0.2 in.); and head thickness, 10.2 mm (0.4 in.). A 4.8-mm (3/16-in.) radius fillet was added to smooth the transition from the cylinder to the head. The same scheme of product form usage and weld location as for the WCR-1 specimens was used. To reflect this continuity, the WCR-2 specimens were given the same numbers as the geometrically similar WCR-1 specimens and subsequently the specimens were referred to as -M1 (model 1) or -M2 (model 2) specimens, respectively.

An additional specimen, a cylinder with a hemispherical cap, was introduced into the second series of tests. This specimen had two circumferential welds in the cylinder and one in the head. The weld in the head region would be subjected to equal biaxial elastic stresses in a comparatively uniform stress field. The thickness of the hemispherical section, which was machined from solid bar stock, was 2.92 mm (0.115 in.) to yield the initial elastic maximum principal stress in the cap the same as that in the 5.08-mm-thick (0.2-in.) cylinder region.

Figure 5 shows the set of WCR-2 specimens prior to testing. The locations of the test welds are indicated by the arrows. Note that, as with WCR-1 specimens, the surfaces were scribed to yield reference points for dimensional measurements.

2.2 Description of Test Welds

The type of weld used for this set of specimens was selected on the basis of current (current at time of test program initiation) thinking for the Fast-Flux Test Facility (FFTF) pipe welds. For type 304 stainless steel pipe, type 308 stainless steel alloy weld rod and TIG welding process was to be used. The pipe would be mill annealed and no postweld heat treatment would be applied. The exact chemistry of the weld rod and rod coating had not been selected.

It was thus decided to use a high-quality weld procedure and bare type 308 stainless steel weld rod. The weld specification used was ORNL Welding Procedure Specification WPS-302, which, for the weld geometries

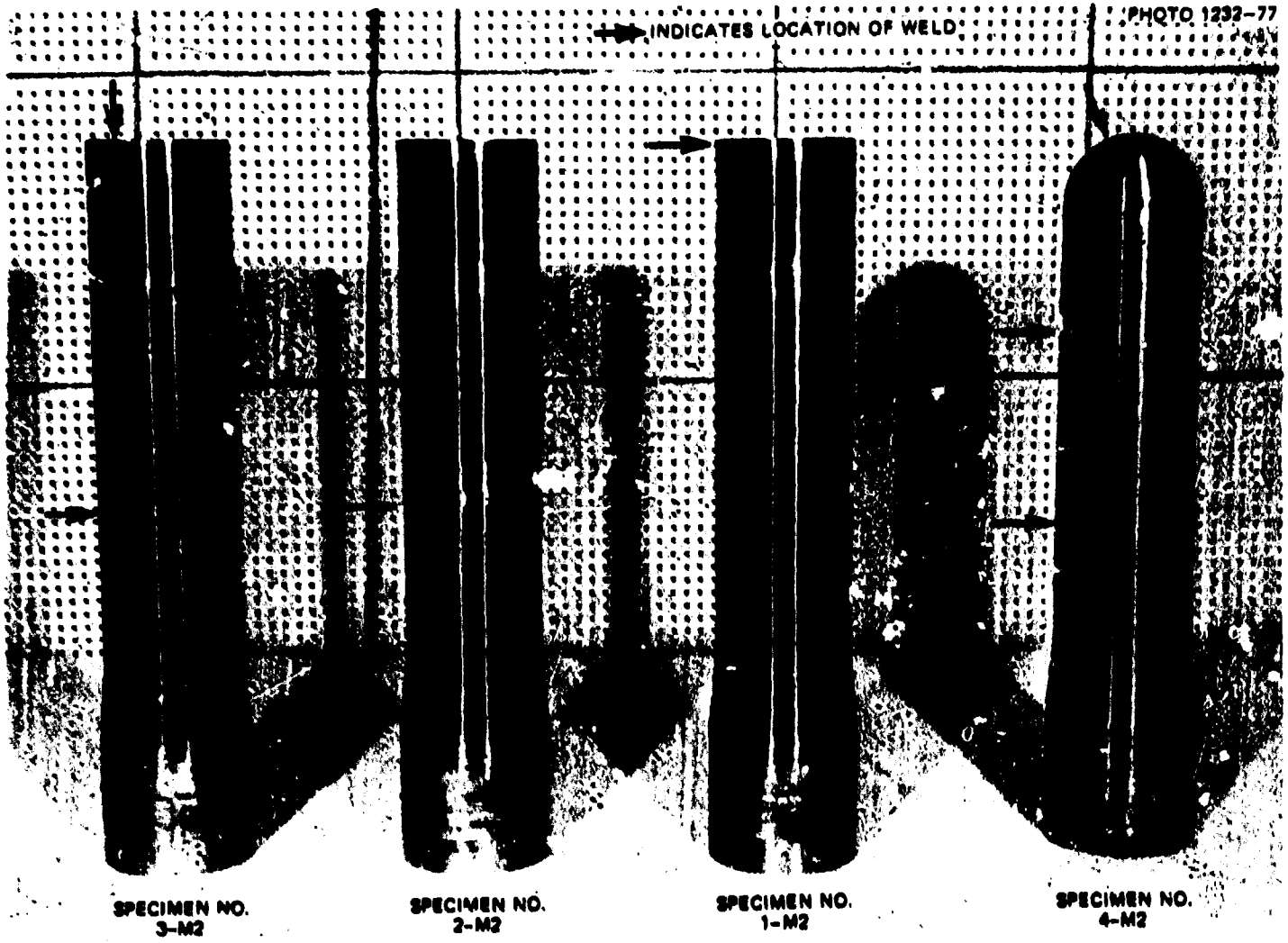

Fig. 5. WCR-2 specimens showing test weld locations.

used, is qualified to RDT F6-5 and is for the TIG process. These specifications require dye-penetrant and 100% radiographic inspection.

The weld geometries were of two types as shown in Fig. 6. The single-U geometry was used for the plug-to-head weld of specimens 3-M1, 3-M2, and 4-M2. The single-V geometry was used for all other welds, including the specimen closure weld. The weld rod used was bare type 308 stainless steel in 1.59-mm (1/16-in.) and 2.38-mm (3/32-in.) diameters. This rod was all from the same heat (Unibraze Corp. heat I3806031-C). The vendor-supplied chemistry and an ORNL analysis is given in Table 2.

ORNL-DWG 72-6428A

GROOVE TYPE	GROOVE DIMENSIONS					THICKNESS
	B (deg)	G (deg)	RF (in)	RO (in.)	R (in)	(in)
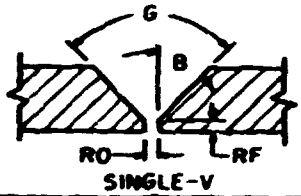 SINGLE-V	45 ± 2.5	90 ± 5	0.010 ±0.005	$\frac{1}{16}{}^{+0}_{-\frac{1}{64}}$		0.100 to 0.500
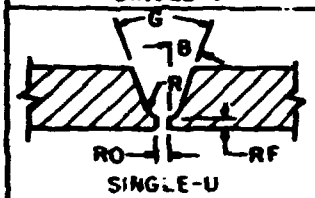 SINGLE-U	20 ± 2.5	40 ± 5	0.062 +0.016 −0	$\frac{1}{16}{}^{+0}_{-\frac{1}{64}}$	0.094 +0.016 −0	0.375 to 1.0

Fig. 6. Weld geometries used for weldment creep-rupture specimens.

Table 2. Chemistry of type 308 stainless steel weld rod (Unibraze Corp. heat I3806031-C) used for test welds of WCR-2 specimens

Element	Analysis (wt %)	
	Vendor[a]	ORNL
C	0.07	0.026
Mn	1.0–2.0	2.10
P	0.03	0.029
S	0.03	0.0078
Si	0.25–0.60	0.3
Ni	9.5–11.0	11.98
Cr	20.0–22.0	19.67
Mo	NA	0.048
N	NA	0.032
Cu	NA	0.06
B	NA	0.0005
Ti	NA	0.005
Nb	NA	0.0003

[a]NA = not available.

3. TEST PROCEDURES AND TEST HISTORIES

3.1 Description of Test Facility

A special test facility was set up to study the creep-rupture behavior of these weldments. Four identical test stands were prepared using a common safety enclosure as shown in Fig. 7. A schematic of a single test stand is shown in Fig. 8. The furnaces were cylindrical, electrically heated muffle furnaces with a 0.3-m-diam (12-in.) by 0.81-m-long (32-in.) cavity. When properly powered these furnaces have a temperature range from room temperature to 1010°C (1850°F). A steel liner composed of a 0.22-m (8 1/2-in.) sched-80 pipe with a pipe cap welded to one end was used to protect the furnace wall and heater elements from the potential damage of rupturing specimens.

Temperature control was provided by Brown Electronik recorder-controllers, which are pneumatic-type controllers with both manual and automatic control features. The instrument output controlled a pneumatically driven variable furnace power supply to maintain the specimen at the required set point. Since the furnace was greatly overpowered, the controller tended to cycle approximately ±2.8°C (5°F) throughout the test period. Twelve thermocouples* were used; two were mounted in parallel near furnace midheight for temperature control, and ten were installed at 50.8-mm (2-in.) increments along the vertical axis of the specimen. In preliminary tests of the furnace system, the readings from these thermocouples indicated that the temperature dropped off rather sharply at each end of the furnace such that the desired uniform distribution was not established. Trimming heaters were thus installed at the top and bottom ends of the furnace cavity. These small manually adjusted heaters were used to balance the heat load to maintain a uniform heat distribution along the vertical axis of the specimen.

The specimens were pressurized through a common manifold system connected to a 17.9-MPa (2600-psig) supply of bottled argon gas. Figure 9

*Chromel-Alumel, type K, 3.2-mm-diam (1/8-in.), 304 stainless steel sheathed, 0.75% accuracy.

Fig. 7. Test stands and safety enclosure used for weldment creep-rupture studies.

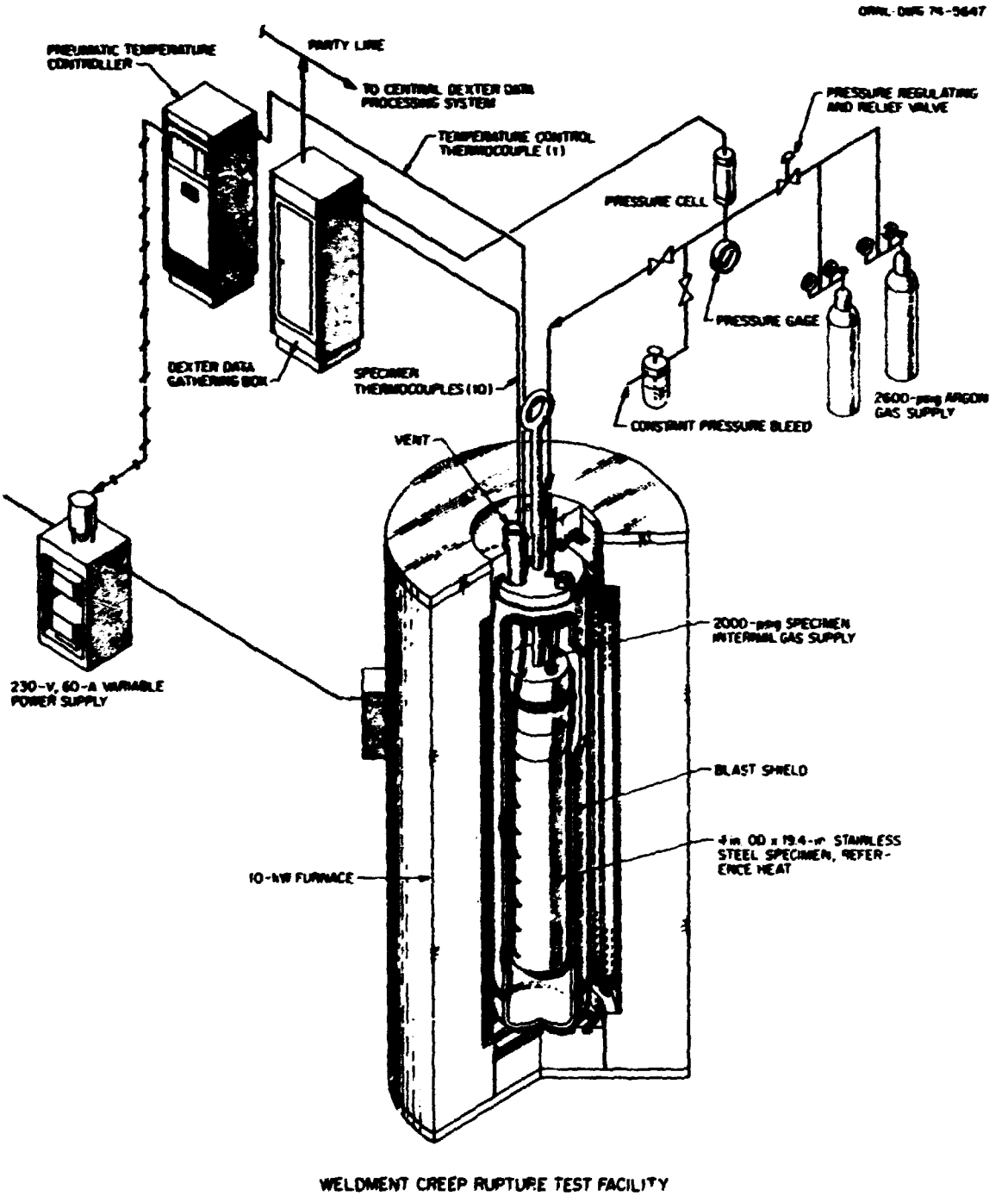

Fig. 8. Schematic of one of the weldment creep-rupture test stands.

Fig. 9. Argon supply system used in pressurizing weldment creep-rupture specimens.

shows the gas supply system, which includes: (a) a gas bottle and regulator; (b) a Grove flow control valve, regulating and relief type; and (c) a Heise gage, which was used to calibrate the pressure transducers. Figure 10 shows the manifold takeoff used to supply each specimen. Autoclave block valves were used to adjust the gas flow rate, a dial pressure indicator provided on-site monitoring of specimen pressure, and a Baldwin SR-4 pressure cell provided remote measurement of specimen pressure.

Figure 11 shows the control panel for the system and the cabinet (door open) housing the on-site data-gathering box. Signals from the pressure transducer and the thermocouples were passed through this system to a central processing complex where printouts of temperature and pressure vs time were prepared.

3.2 Test Procedure and Histories

The initial part of each test run was devoted to checking and stabilization of system parameters. For the initial loading of an undeformed specimen, the specimen was purged slowly with argon (essentially atmospheric pressure) as the heat was applied. When the furnace reached nominal temperature, the manual trimming heaters were adjusted to establish a uniform temperature distribution along the length of the specimen. The time required for this varied but was usually 24 to 36 hr. With the temperature stabilized, the pressure was applied in predetermined stages from zero to full load. The specimen was held briefly at each stage primarily to check for continuing leaktightness of the system. The hold time at each pressure level was minimized in order to bring the specimen to full load as quickly as possible. The total loading time usually was 10 to 30 min. Time zero was measured from the point where full load was reached, after which the pressure was held constant for the remainder of the test. A typical histogram is shown in Fig. 12 for specimen 2B-M1, which ruptured after 181 hr at full pressure. The test duration was determined either by rupture or by achieving a specified time in test where the specimen was unloaded, cooled, and removed from the furnace for dimensional inspection.

The loading procedure was slightly different for a test that was a resumption of one that had been interrupted for dimensional inspection.

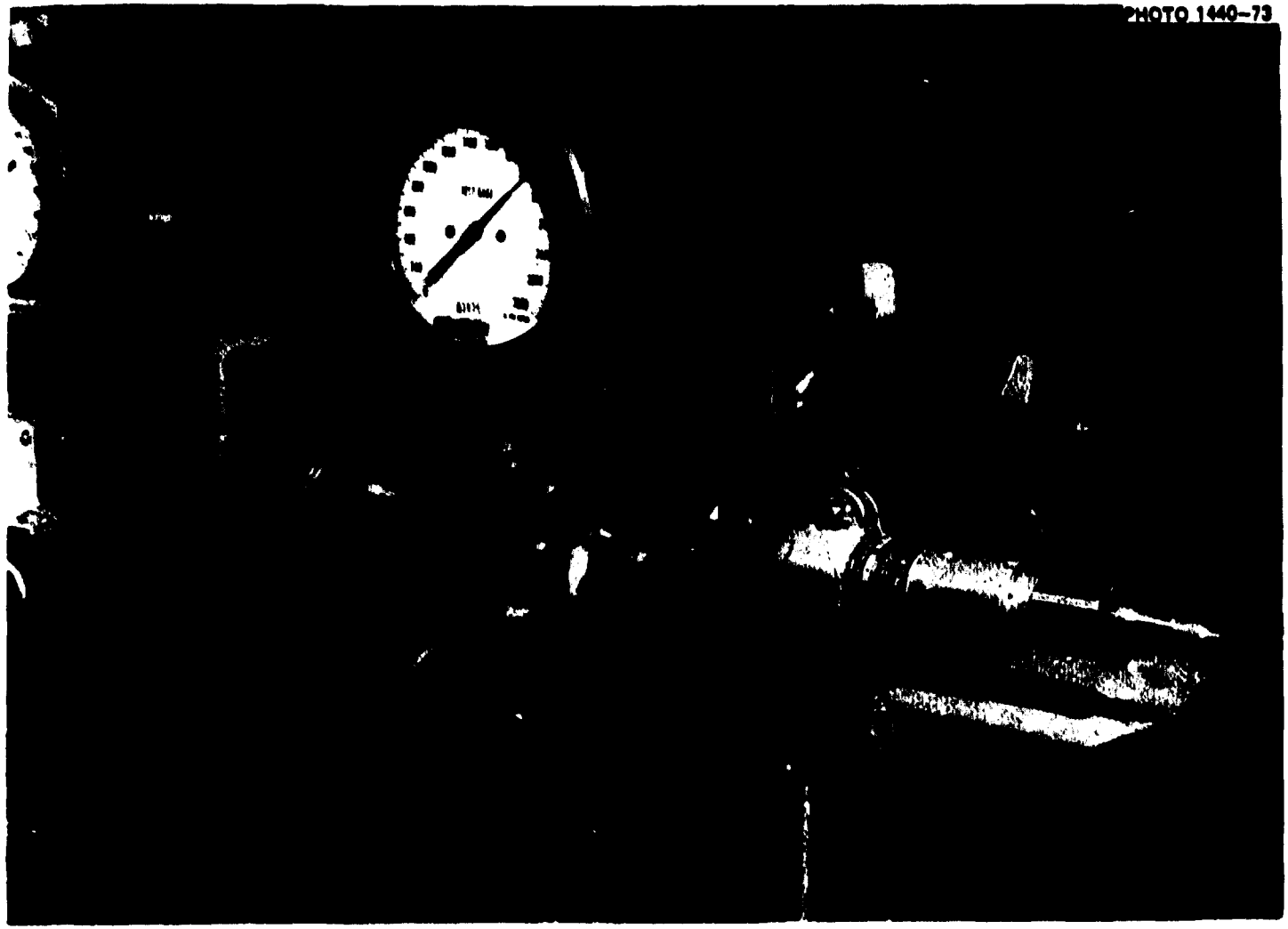

Fig. 10. Individual pressure adjustment and measurement system for each weldment creep-rupture specimen.

Fig. 11. Control panel and data acquisition system for weldment creep-rupture tests.

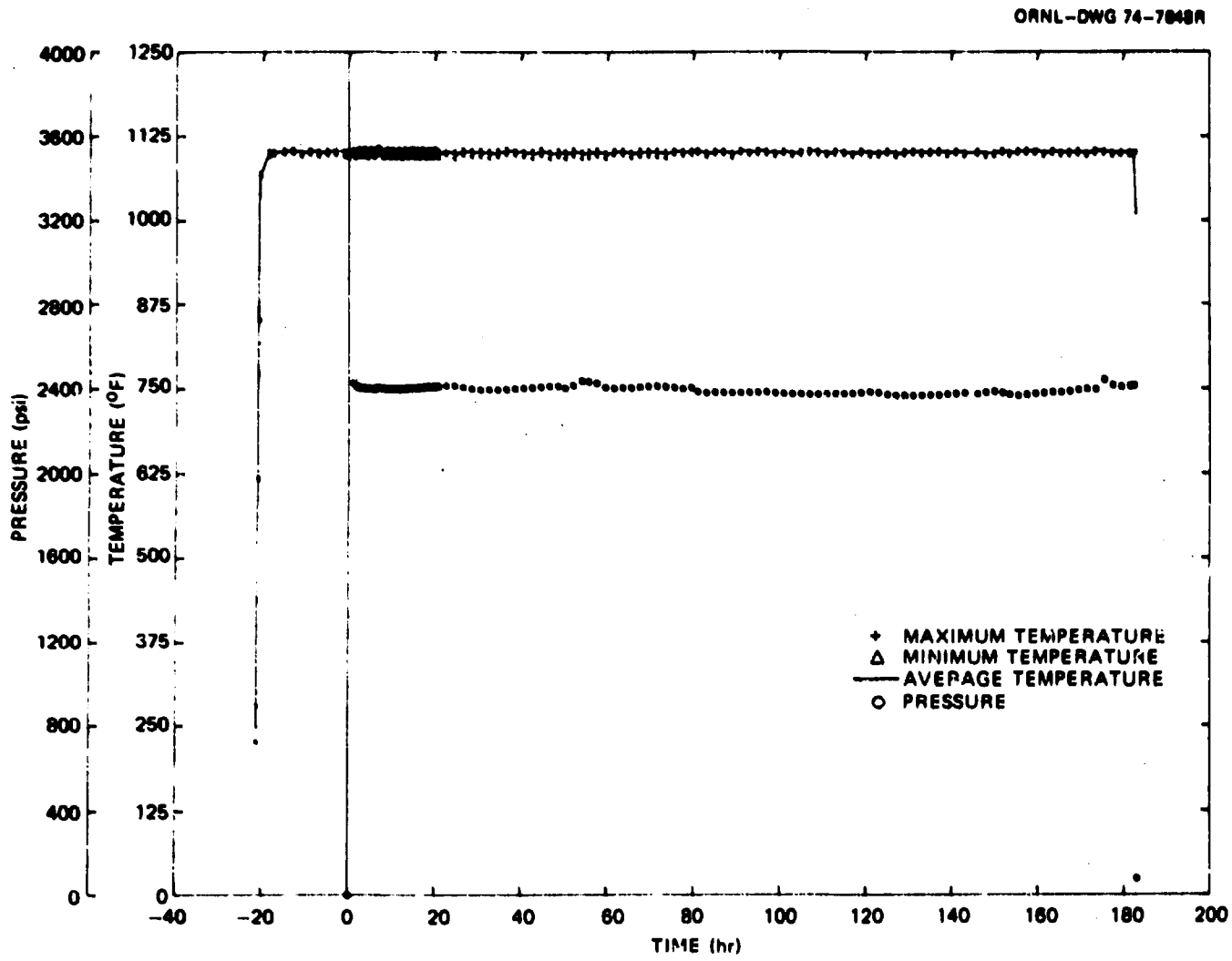

Fig. 12. Typical histogram for a weldment creep-rupture specimen.

The specimen was first pressurized at room temperature to approximately half the test pressure. This pressure was held constant during furnace heatup, system checkout, and stabilization, at which time full pressure was applied and the test was continued. This technique, recommended by Yaggee et al.,[8] was intended to retain the microstructure corresponding to the accrued strain history prior to interruption of the test.

In the following discussion of test histories, it will be helpful to refer to Table 3, which summarizes specimen types, test conditions, and failures.

3.2.1 Specimen 1-M1

The test for this specimen was the most straightforward one of the first series of specimens. The specimen was pressurized to 16.6 MPa (2410 psig) for 408 hr, at which time rupture occurred by a long axial crack in the cylindrical region of the specimen (see Fig. 13).

3.2.2 Specimen 2-M1

This specimen was tested at 16.6 MPa (2410 psig) for 35 hr, when failure occurred by complete separation of the flat head from the cylinder (see Fig. 14). There was evidence that the filler core had contacted the specimen cap and put an axial thrust on the cap. This would have caused the specimen to fail in a shorter time period than if loaded by pressure alone. The specimen was thus rebuilt by (a) removing the ruptured end back to near midcylinder length; (b) reducing the length of the filler core by 13 mm (0.5 in.); (c) machining a new cylinder and head (an integral piece) from bar stock; and (d) welding this to the existing specimen. This specimen, designated specimen 2A-M1, was returned to test. After 88 hr, failure occurred by head-to-cylinder separation as with 2-M1. The ruptured area of specimen 2A-M1 was sealed by welding a flat circular disk to the cylinder. This specimen, designated specimen 2B-M1, was tested for an additional 123 hr before failure occurred by an axial crack in the cylinder portion of the original specimen 2-M1 (i.e., this section failed after a time in test of 304 hr). The type of failure is shown in Fig. 15.

Table 3. Summary of weldment creep-rupture specimen histories

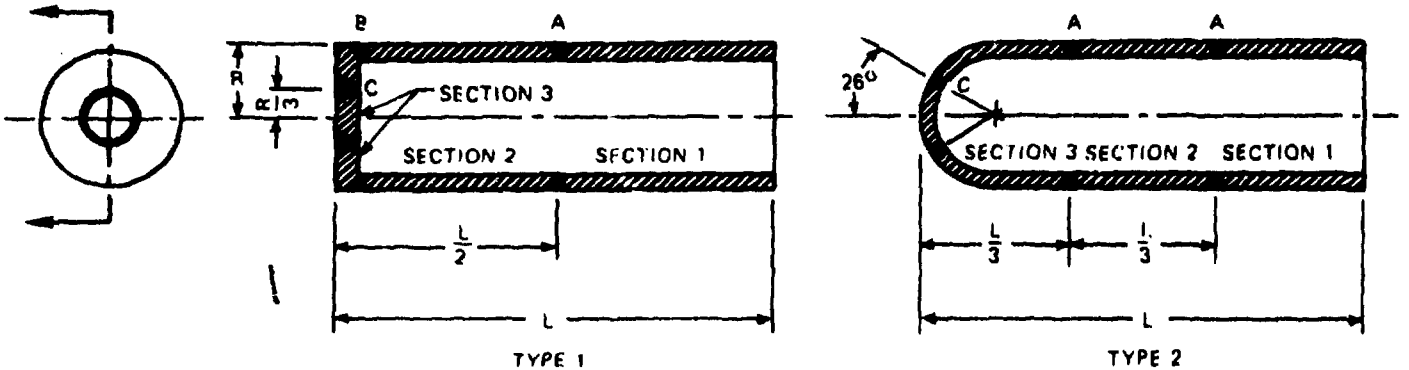

NOMINAL DIMENSIONS: L = 0.51 m (20 in.), R = 51 mm (2.0 in.)
A, B, AND C DENOTE TYPICAL WELD LOCATIONS
PIPE: 102 mm (4 in.) SCHED 160, BAR 114 mm (4 1/2 in.) diam
TEST TEMPERATURE: 593°C (1100°F)

Specimen No.	Type	Material			Weld locations	Test weld locations	Pressure (MPa/psig)	Time (hr)	Failure mode
		Section 1	Section 2	Section 3					
1-M1	1	Pipe	Pipe	Bar	B	B	16.6/2410	408	Axial crack
2-M1	1	Pipe	Bar	Bar	A	A	16.6/2410	35	Circumferential crack
(2A-M1)	1	Pipe	Bar	Bar	A, C	C	16.6/2410	68	Circumferential crack
(2B-M1)	1	Pipe	Bar	a	A, B	None	16.6/2410	181	Axial crack
3-M1	1	Pipe	Bar	Bar	A, C	A, C	16.6/2410	43	Circumferential crack
(3A-M1)	1	Pipe	Bar	a	A, B	A	16.6/2410	153	Axial crack
1-M2	1	Pipe	Pipe	Bar	B	B	14.1/2040	475	Pinhole leak
(1A-M2)	1	Pipe	Pipe	a	B	None	14.1/2040	3576	Axial crack
2-M2	1	Pipe	Pipe	Bar	A	A	14.1/2040	3996	Axial crack
3-M2	1	Pipe	Bar	Bar	A, C	A, C	14.1/2040	9712	Axial crack
4-M2	2	Pipe	Pipe	Bar	A, C	A, C	14.1/2400	1136	Pinhole leak

[a]Plate material used for closure only, not reference heat.

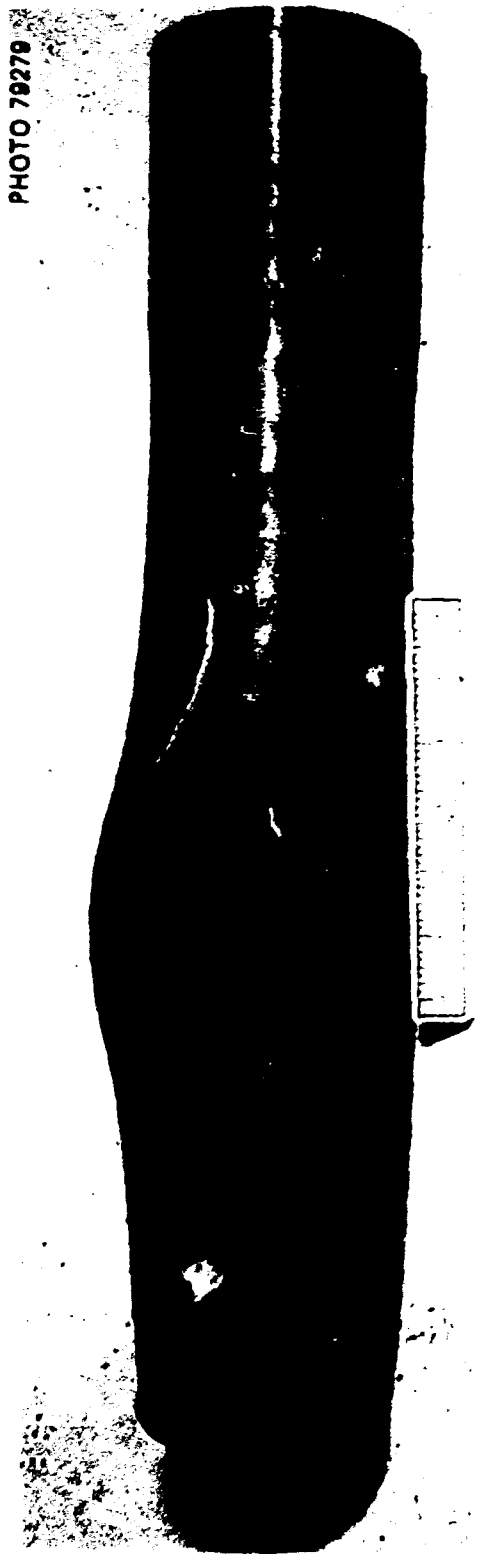

Fig. 13. Failed weldment of creep-rupture specimen 1-M1 (408-hr life).

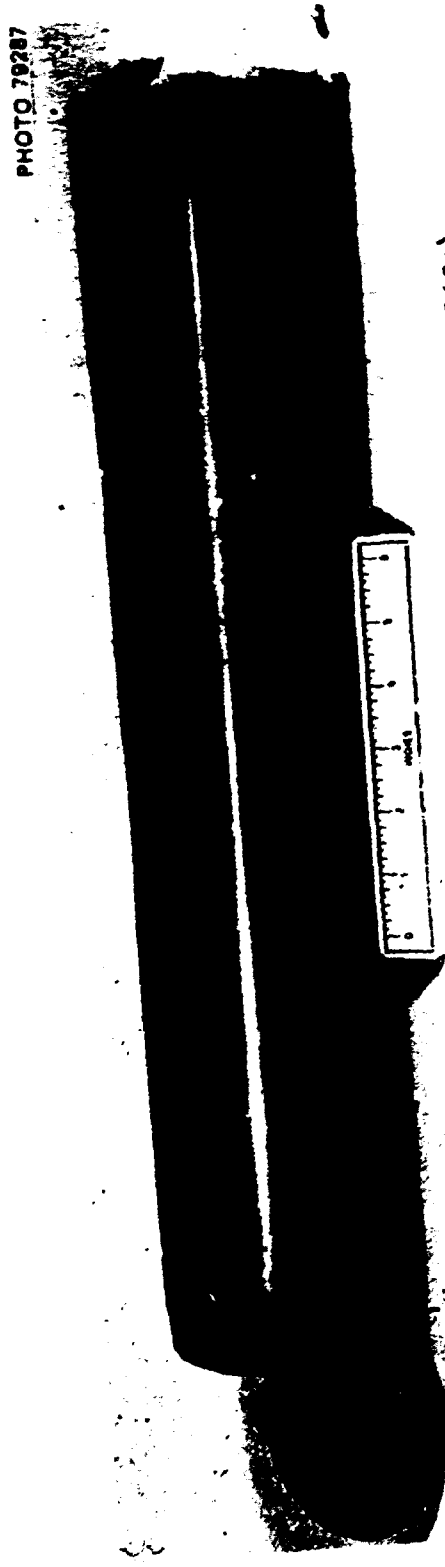

Fig. 14. Failed weldment of creep-rupture specimen 2-ML (35-hr life).

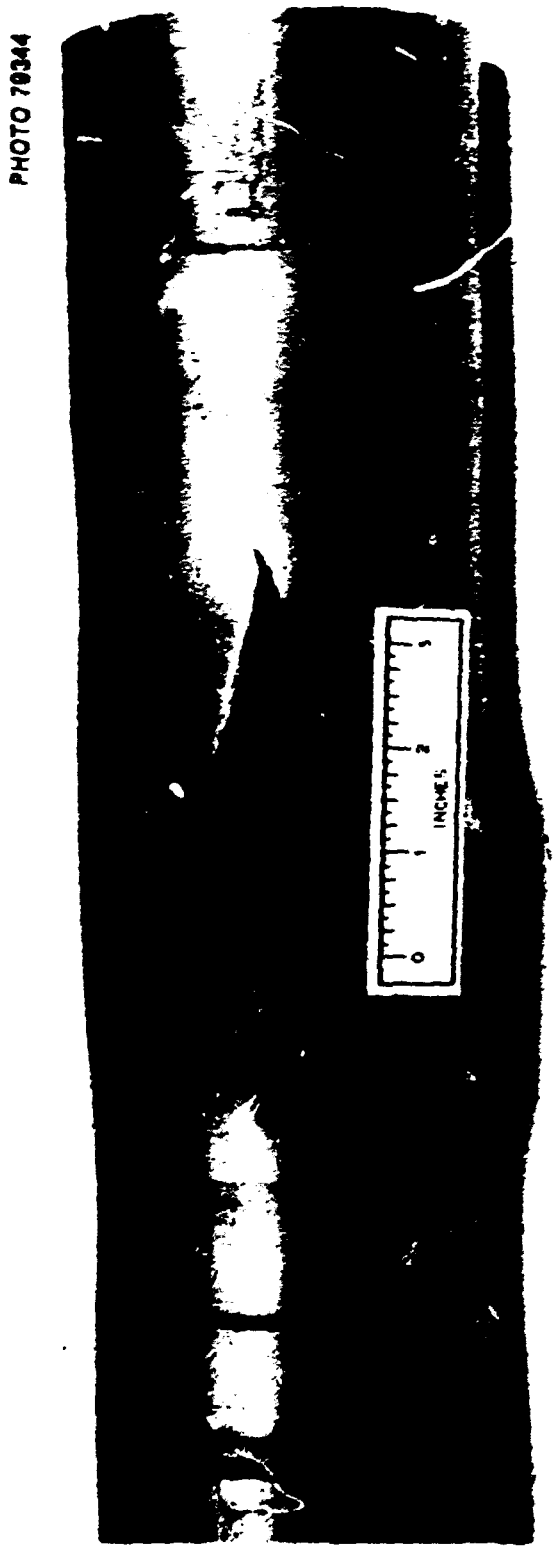

Fig. 15. Type of failure exhibited by specimens 2B-M1 and 3A-M1.

3.2.3 Specimen 3-M1

Specimen 3-M1 was pressurized to 16.6 MPa (2410 psig) and failed after 43 hr by complete separation of the head from the cylinder (as with specimen 2-M1). On this specimen, contact between the filler core and the specimen cap also may have occurred. The 43-hr failure point, as with the 35-hr failure point for specimen 2-M1, was thus not recorded as valid creep-rupture data. Repair was made by welding a flat circular disk to the end of the cylinder, and this specimen, specimen 3A-M1, failed after 153 hr by an axial crack in the cylinder. The total test time at failure was 196 hr.

3.2.4 Specimen 1-M2

This specimen was tested at 14.1 MPa (2040 psig) for 475 hr, at which time pressure was lost due to development of a pinhole leak in the head-to-cylinder weld region. The specimen was repaired by removal of about 25.4 mm (1 in.) of the end of the specimen and welding a flat circular disk to the end of the cylinder. The resulting modified specimen, designated specimen 1A-M2, was returned to test. The test was interrupted for dimensional inspections at total test times of 1000 and 2000 hr. Failure occurred at a total test time of 3576 hr by an axial crack in the cylindrical portion of the specimen (see Fig. 16).

3.2.5 Specimen 2-M2

This specimen, pressurized to 14.1 MPa (2040 psig), was tested as planned with interruptions for dimensional inspections after total test times of 500, 1500, and 2000 hr. Failure occurred at 3996 hr, when a series of small axial cracks developed in the cylinder similar to those shown in Figs. 16 and 17.

3.2.6 Specimen 3-M2

This specimen, tested at a pressure of 14.1 MPa (2040 psig), was interrupted for dimensional inspections at 500, 1000, 2000, 4000, and 8000 hr total test time. The specimen failed at 9712 hr through a very fine pattern of cracks in the cylinder as shown in Fig. 17.

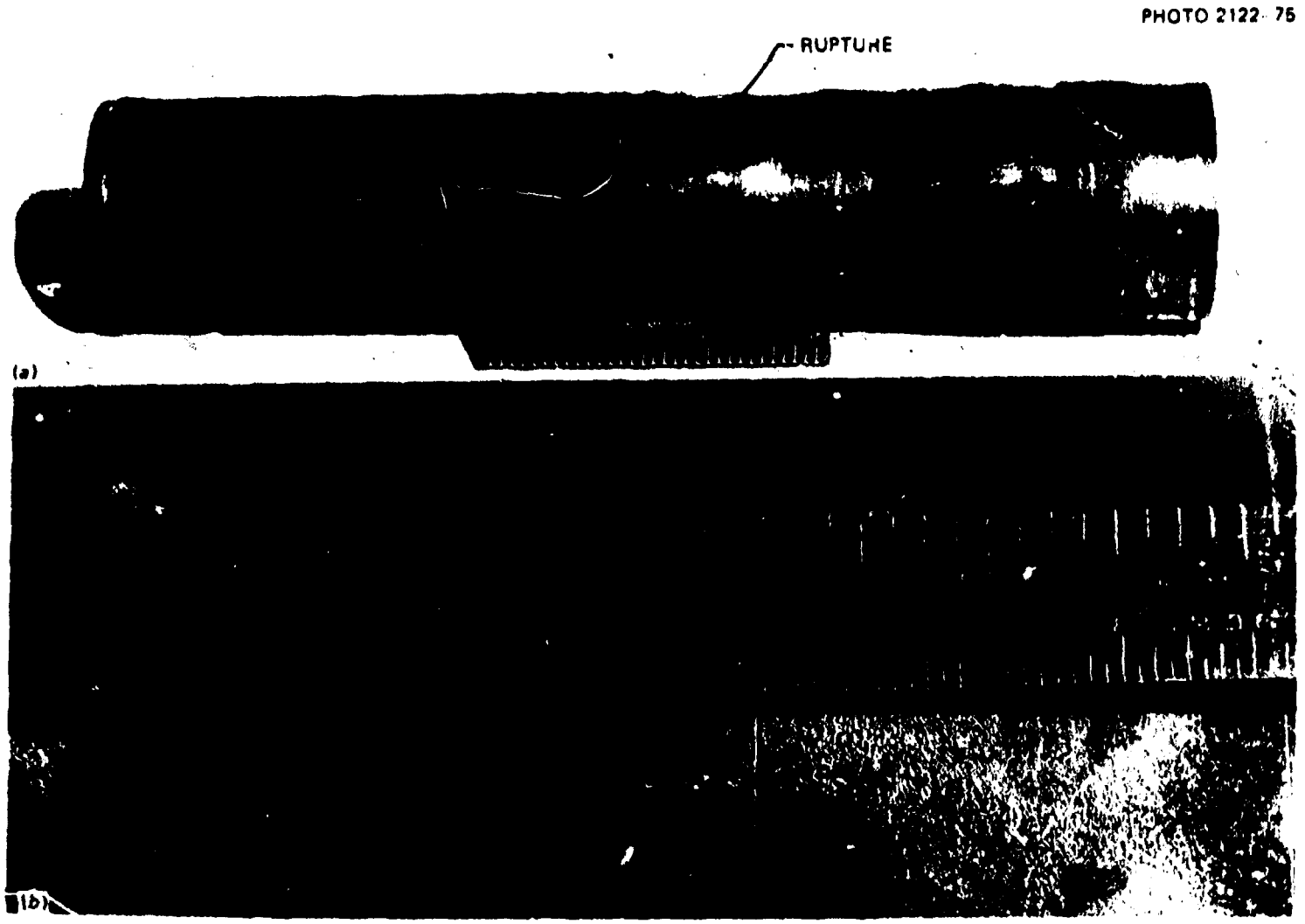

Fig. 16. Failed weldment of creep-rupture specimen 1A-M2. (a) Overall view; (b) closeup.

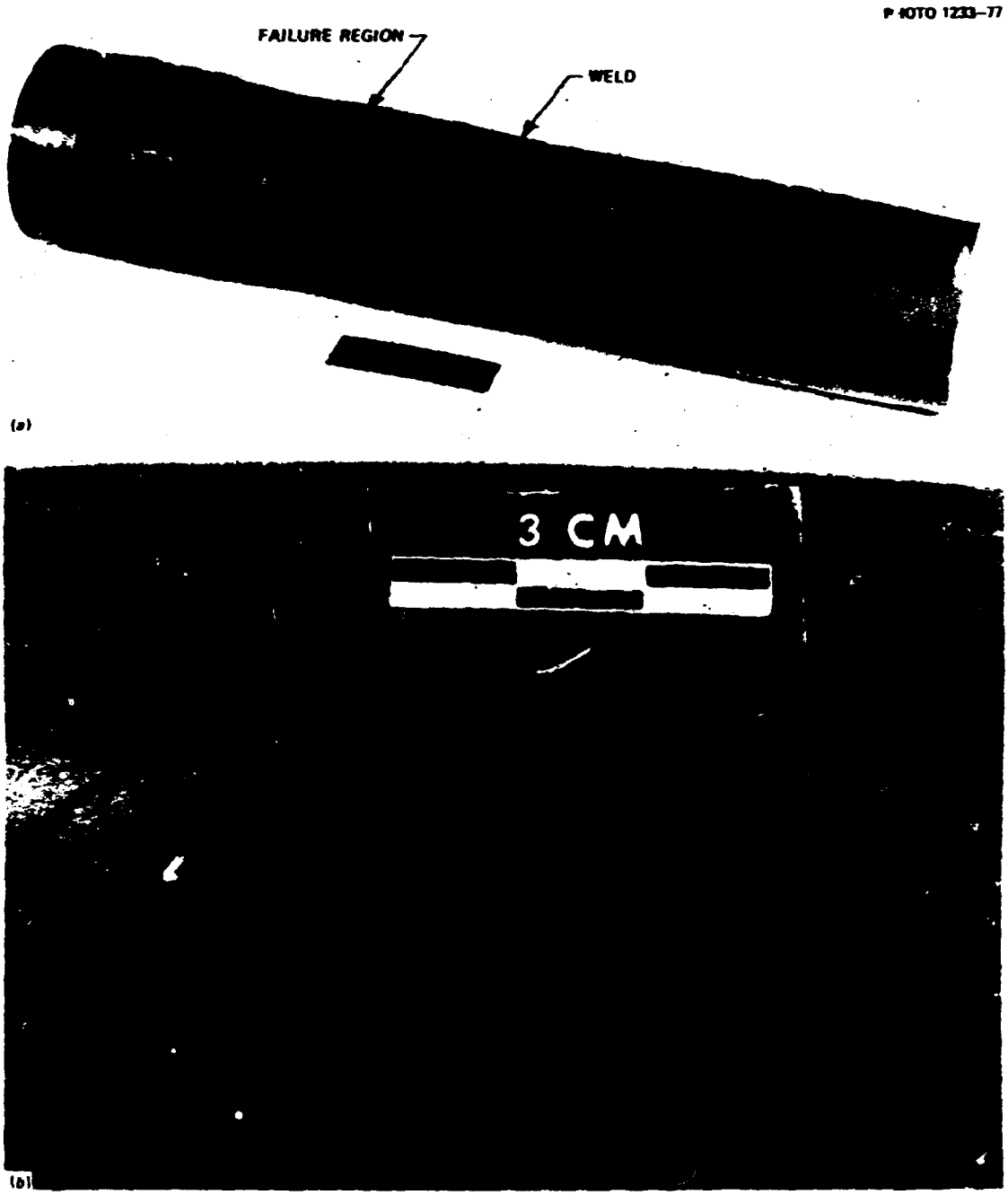

Fig. 17. Failed weldment of creep-rupture specimen 3-M2. (a) Overall view; (b) closeup showing pattern of small cracks in failure region.

3.2.7 Specimen 4-M2

This specimen, like the first series of weldment specimens, was tested at 16.6 MPa (2410 psig). The test was interrupted at 500 and 1000 hr, and failure occurred at 1136 hr. However, this is not considered a valid failure point since it occurred during a temperature excursion caused by a malfunction of the temperature controller.

4. DEFORMATION DATA AND ANALYSIS

4.1 Deformation Data

Measurements of strains and/or deformations at these test temperatures present many difficulties. It was thus decided that acceptable deformation results could be obtained by making comparative sets of dimensional measurements at room temperature for discrete times throughout the life of a specimen. To provide a datum, the specimens were scribed with circumferential lines on the cylinder and cap and with axial lines each 60° around the circumference of the closure cap. The latter lines defined the ends of six radii formed by three planes passing through the longitudinal axis of the cylinder. These scribe lines are visible in Fig. 3.

The dimensional measurements were made using a highly sophisticated machine that normally is used for making dimensional inspections of complex structural parts. This machine has a rotating index table and a sensitive surface probe with precise x-y-z movement.

The specimen was mounted in an upright position (i.e., closure cap down) on the indexing table with the longitudinal axis of the specimen in line with the geometric center of the table. The radial displacement of the probe was measured from the center of the table, and its height was referenced to the top surface of the table. The table was rotated to align the probe with one of the six scribe lines on the closure cap. Then the probe was moved vertically up the surface of the specimen and across the head with a measurement of height and radial displacement being made at each circumferential scribe line. This procedure was repeated for each of the six scribe line positions (i.e., at 60° intervals) around the circumference of the specimen closure cap. The resulting set of measurements of heights and radii were used in comparison to similar dimensional measurements for the original undeformed specimen to compute the displacement of specific points on the specimen surface. These displacements were used to calculate the total inelastic strain, as will be discussed in Subsection 4.2.

One limitation on this procedure was that it was assumed that the deformations would be essentially axisymmetric. This proved to be acceptable, although significant circumferential displacement occurred in cases where the specimen failed through a long axial crack (see Fig. 12). This displacement, however, was concentrated in the rupture region where the specimens were distorted due to the failure. The distortion thus placed limits on the reliability of the computed strains in the rupture region.

4.2 Analysis of Deformation Data

The method used for converting the deformation data into strains was to identify material particles on the surface of the specimen by considering the specimen to be in a hypothetical reference state in which its geometry was a perfect cylinder, flat head, or hemisphere depending on the region or type of the specimen being considered. The surface strains were calculated based on the deviation of the actual surface, obtained from the dimensional measurements, from this hypothetical perfect surface.

For the cylindrical region of the specimen, a cylindrical coordinate system was then set up and each particle was identified by the reference coordinates $(\bar{\theta}, \bar{z})$. The deformed location of a particle was given by its Cartesian coordinates (x, y, z), and the undeformed location was given by the Cartesian coordinates $(\hat{x}, \hat{y}, \hat{z})$. To interpolate between measured points, the following series was used:

$$x(\bar{\theta}, \bar{z}) = P_1(\bar{z}) + P_2(\bar{z}) \cos \bar{\theta} + P_3(\bar{z}) \sin \bar{\theta} + P_4(\bar{z}) \cos 2\bar{\theta} + P_5(\bar{z}) \sin 2\bar{\theta} + P_6(\bar{z}) \cos 3\bar{\theta} ,$$

where $P_1, \ldots, P_6$ are polynomial spline functions. The spline functions are continuous and have two continuous derivatives across the scribe rings. Interpolation equations of the same form were used for y, z, $\hat{x}$, $\hat{y}$, $\hat{z}$.

For a hemispherical cap the reference state was a perfect hemisphere, and the interpolation equation was

$$x(\bar{\theta}, \bar{\phi}) = P_1(\cos \bar{\phi}) + \sin \bar{\phi}\, P_2(\cos \bar{\phi}) \cos \bar{\theta}$$

$$+ \sin \bar{\phi}\, P_3(\cos \bar{\phi}) \sin \bar{\theta} + \sin^2 \bar{\phi}\, P_4(\cos \bar{\phi}) \cos 2\bar{\theta}$$

$$+ \sin^2 \bar{\phi}\, P_5(\cos \bar{\phi}) \sin 2\bar{\theta} + \sin^3 \bar{\phi}\, P_6(\cos \bar{\phi}) \cos 3\bar{\theta} ,$$

where $\bar{\phi}$ is the reference angle measured from the pole.

For a flat head, the reference state was a flat disk, and the interpolation function was

$$x(\bar{r}, \bar{\theta}) = P_1(\bar{r}^2) + \bar{r}P_2(\bar{r}^2) \cos \bar{\theta} + \bar{r}P_3(\bar{r}^2) \sin \bar{\theta}$$

$$+ \bar{r}^2P_4(\bar{r}^2) \cos 2\bar{\theta} + \bar{r}^2P_5(\bar{r}^2) \sin 2\bar{\theta} + \bar{r}^3P_6(\bar{r}^2) \cos 3\bar{\theta} .$$

The form of the head equations was chosen so as to force the deformation to be analytic at the center point.

Using index notation, the strain tensor is defined as

$$e_{mn} = \frac{1}{2}\left(\frac{\partial x_i}{\partial \bar{x}_m}\frac{\partial x_i}{\partial \bar{x}_n} - \frac{\partial \hat{x}_j}{\partial \bar{x}_m}\frac{\partial \hat{x}_j}{\partial \bar{x}_n}\right),$$

where:

$x_1 = x$, $x_2 = y$, $x_3 = z$,
$\hat{x}_1 = \hat{x}$, $\hat{x}_2 = \hat{y}$, $\hat{x}_3 = \hat{z}$,
$\bar{x}_1 = \bar{r}$, $\bar{x}_2 = \bar{\theta}$, $\bar{x}_3 = \bar{z}$ for a cylinder or flat head,
$\bar{x}_1 = \bar{r}$, $\bar{x}_2 = \bar{\theta}$, $\bar{x}_3 = \bar{\phi}$ for a hemisphere.

Because it follows the conventions of tensor analysis which emphasize simplicity of transformation, the strain tensor e_{mn} does not reduce to engineering strain in the infinitesimal limit. The alternative strain measure

$$e_{mn} = \frac{1}{2}\left(\frac{\partial x_i}{\partial \bar{x}_m}\frac{\partial x_i}{\partial \bar{x}_n} - \frac{\partial \hat{x}_j}{\partial \bar{x}_m}\frac{\partial \hat{x}_j}{\partial \bar{x}_n}\right)\Bigg/\sqrt{\frac{\partial \hat{x}_k}{\partial \bar{x}_m}\frac{\partial \hat{x}_k}{\partial \bar{x}_m}\frac{\partial \hat{x}_\ell}{\partial \bar{x}_n}\frac{\partial \hat{x}_\ell}{\partial \bar{x}_n}} ,$$

(no summation on m, n)

sometimes referred to as the "physical components" of the tensor, is not itself a tensor but does reduce to engineering strain (except for a factor of 2 in shear) and is therefore easier to interpret.

The above discussion is descriptive of the displacement field for the external surface of the specimen. Assuming that the thin-shell geometry relations are valid, it is also possible to calculate the strain field on the inner surface of the specimen. To accomplish this, the following shell analysis was incorporated into the computer program used for data reduction.

Let $\hat{x}_i$ (α_1, α_2), $i = 1, 2, 3$, denote the global Cartesian coordinates of the measured location of a point on the outer surface of the specimen before deformation and let x_i (α_1, α_2) be the corresponding coordinates after deformation, where α_1, α_2 are the local reference coordinates on the outer surface:

	α_1	α_2
Cylinder	$\bar{\theta}$	$\bar{Z}$
Flat head	$\bar{r}$	$\bar{\theta}$
Hemispherical head	$\bar{\varphi}$	$\bar{\theta}$

All the barred coordinates refer to an ideal reference state of the specimen.

A vector normal to the outer surface after deformation is given by the Cartesian coordinate components:

$$u_1 = \frac{\partial x_2}{\partial \alpha_1}\frac{\partial x_3}{\partial \alpha_2} - \frac{\partial x_2}{\partial \alpha_2}\frac{\partial x_3}{\partial \alpha_1},$$

$$u_2 = \frac{\partial x_3}{\partial \alpha_1}\frac{\partial x_1}{\partial \alpha_2} - \frac{\partial x_3}{\partial \alpha_2}\frac{\partial x_1}{\partial \alpha_1},$$

$$u_3 = \frac{\partial x_1}{\partial \alpha_1}\frac{\partial x_2}{\partial \alpha_2} - \frac{\partial x_1}{\partial \alpha_2}\frac{\partial x_2}{\partial \alpha_1},$$

and similarly for the normal vector before deformation. The components of a normal vector of unit length are given by

$$v_1 = u_1/\sqrt{u_1^2 + u_2^2 + u_3^2} ,$$

etc. Then, assuming that a line segment initially normal to the outer surface, and embedded in the material, remains straight and normal after deformation and neglecting changes in wall thickness due to deformation, that is, the Kirchhoff-Love hypothesis of thin-shell theory, the inside surface strain tensor is given (using the summation and range conventions) by

$$e_{mn} = \frac{1}{2}\left[\left(\frac{\partial x_i}{\partial \alpha_m} - h\,\frac{\partial v_i}{\partial \alpha_m}\right)\left(\frac{\partial x_i}{\partial \alpha_n} - h\,\frac{\partial v_i}{\partial \alpha_n}\right) - \left(\frac{\partial \hat{x}_i}{\partial \alpha_m} - h\,\frac{\partial \hat{v}_i}{\partial \alpha_m}\right)\left(\frac{\partial \hat{x}_i}{\partial \alpha_n} - h\,\frac{\partial \hat{v}_i}{\partial \alpha_n}\right)\right] ,$$

where h is the constant wall thickness.

The physical components of the inner surface strain can then be calculated in the same way as for the outer surface. The approximations above greatly simplify the numerical calculations. They are consistent with a large-deflection, small-strain, thin-shell approximation for bending. The outside surface strains, however, are valid for large deflection and large strain since they are based on the measured deformation of the specimen. Results from these calculations are discussed in the next section.

5. TEST RESULTS AND CONCLUSIONS

5.1 Deformation Behavior of Specimens

Calculation of strains for the first series of specimens was made more difficult by the amount of distortion the material underwent at failure. In particular, the flat heads of specimens 2-M1 and 3-M1 were badly warped during rupture. In the regions away from the failure area and in the second series of specimens, where failure generally occurred by small cracks, the calculated strains were much more consistent.

In order to make comparisons of the general behavior of weldments and base metal, two approaches were used. First, selected points on the outer surface of the cylindrical part of the specimens were observed with respect to their time-dependent behavior. Points were chosen in all base metal regions, membrane stress only, and at the center of the deposited welds. The strains at these selected points, calculated from the deformation measurements, indicate the general time-dependent behavior of the weld and base metals.

Results for the first series of specimens are summarized in Table 4. The rupture strains, which are outside surface strains, were taken at points away from the actual failure area and should be indicative of the circumferential strain just prior to failure. Comparable results for the second series of specimens are shown in Table 5 and Fig. 18. In both cases, the strains reported are the total inelastic outside surface strain and therefore include the loading strains.

The deformation response of the second series of specimens, Fig. 18, indicates reasonably consistent comparative creep behavior between the specimens tested. No trend curves are included over the time range 0 to 500 hr since both plastic loading strain and creep occurred in an undefined (for these tests) way. As may be seen in Tables 4 and 5 and Fig. 18, the pipe material exhibited greater total inelastic strain than the bar material. This is consistent with product-form characterization results,[8] which show the pipe material to have a lower initial yield point and slightly higher minimum creep rates than the bar material for stress levels comparable to these weldment specimens. This creep rate behavior is shown in Fig. 19.

Table 4. Comparison of weld-base material behavior in the cylinder region of WCR-1 specimens

Temperature	593°C (1100°F)
Internal pressure	1.66 MPa (240 psi)
Axial stress	90.9 MPa (13,180 psi)
Circumferential stress	181.8 MPa (26,370 psi)
Effective stress (von Mises)	157.2 MPa (22,800 psi)

Specimen No.	Test time (hr)	Total inelastic circumferential strain[a] (%)			Comments on failure mode
		Bar stock[b]	Pipe stock	At weld	
1-M1	408		10.0[c]		Axial crack in cylinder
2-M1	35	2.1	2.8	0.6	Circumferential crack between head and cylinder; upper half (head end) of specimen replaced
2A-M1	123	NA	NA	NA	Circumferential crack between head and cylinder; flat head repaired by welding
2B-M1	304	NA[c]	6.4	2.9	Axial crack in cylinder; failed section tested 269 hr
3-M1	43	NA	NA	NA	Circumferential crack between head and cylinder; flat head repaired by welding
3A-M1	200	4.1	6.9[c]	1.5	Axial crack in cylinder

[a] NA = not available.

[b] Specimens without a flat head/cylinder weld had the flat-head end machined from solid bar stock.

[c] Rupture strain.

The deformation of the base metal was much greater than that of the comparably located weldments. During the first 2000 hr of testing of the second series of specimens, no clearly defined deformation behavior of the weldments was established. The fact that decreases in previously measured strain levels or negative strains are shown for the weldments may be at-

Table 5. Comparison of weld-base metal material behavior in cylinder region of WCR-2 specimens

Specimen No.	Material	Stress[a]		Total test time (hr)						
		MPa	ksi	500	1000	1500	2000	4000	8000	9712
				Average circumferential strain (%)						
1-M2	Base metal (pipe)	117.2	17.0	1.69[b]						
1A-M2	Base metal (pipe)	117.2	17.0		1.99		2.47	3.67[c]		
2-M2	Base metal (pipe)	117.2	17.0	1.48		2.01	2.40	7.05[d]		
	Base metal (bar)	117.2	17.0	1.04		1.52	1.67	1.79		
	Weld	117.2	17.0	0.21		0.17	0.30	0.29		
3-M2	Base metal (pipe)	117.2	17.0	1.57	2.20		2.57	3.35	4.32	5.21[e]
	Base metal (bar)	117.2	17.0	0.98	1.74		1.87	2.44	3.01	3.03
	Weld	117.2	17.0	−0.23	0.27		−0.01	0.24	0.37	0.41
4-M2	Base metal (pipe)	136.5	19.8	1.94	2.56	7.98[f]				
	Base metal (bar)	136.5	19.8	1.73	1.91	6.30[f]				
	Weld	136.5	19.8	0.29	0.27	2.30				
	Weld	136.5	19.8	0.32	0.23	2.46				

[a]Elastically calculated von Mises stress.

[b]Taken at 475 hr.

[c]Failure strain at 3576 hr.

[d]Failure strain at 3996 hr.

[e]Failure strain at 9712 hr.

[f]Strain after temperature increase (1136 hr).

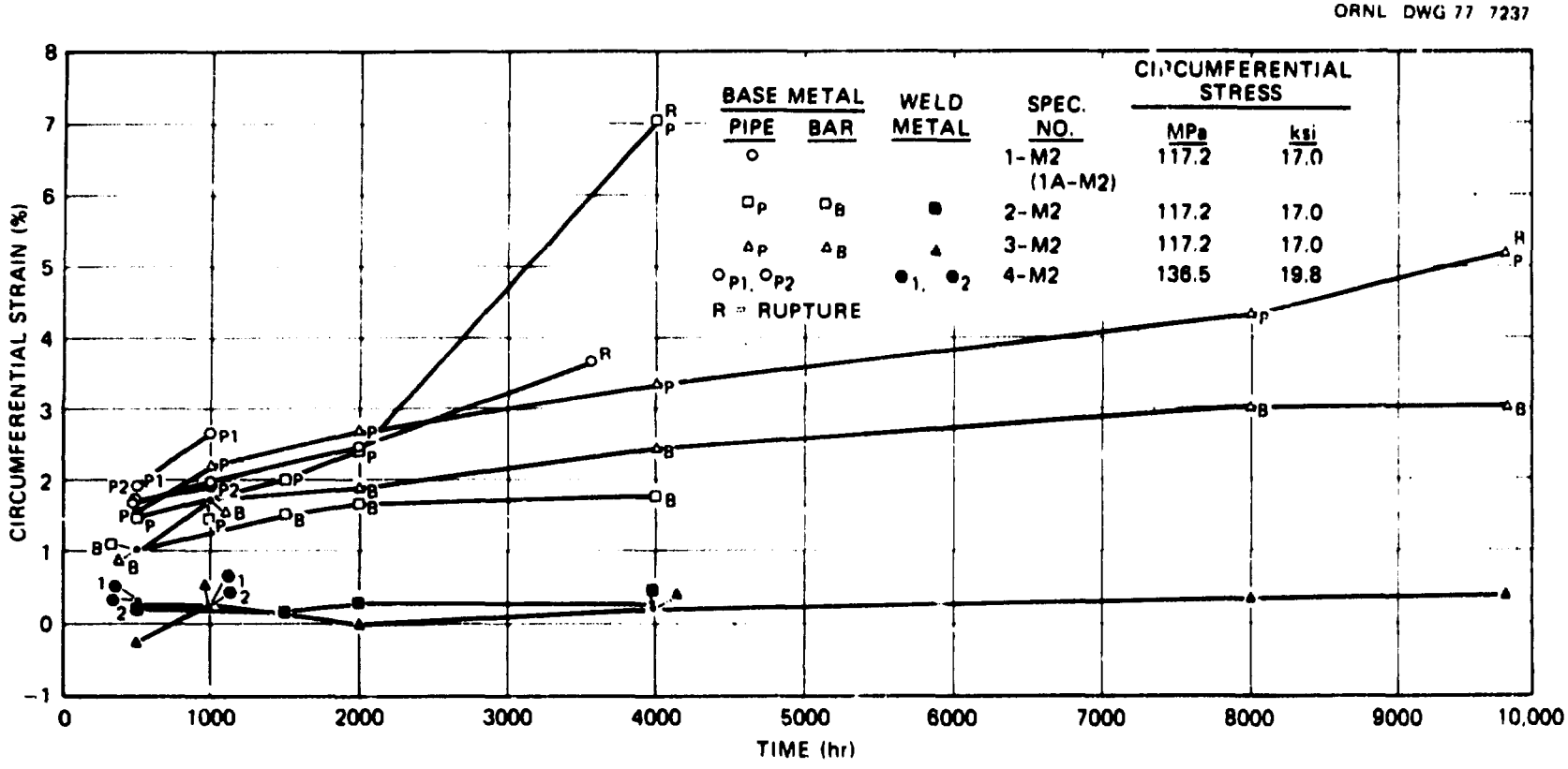

Fig. 18. Comparative deformation behavior of weld and base metals in weldment creep-rupture series 2 specimens.

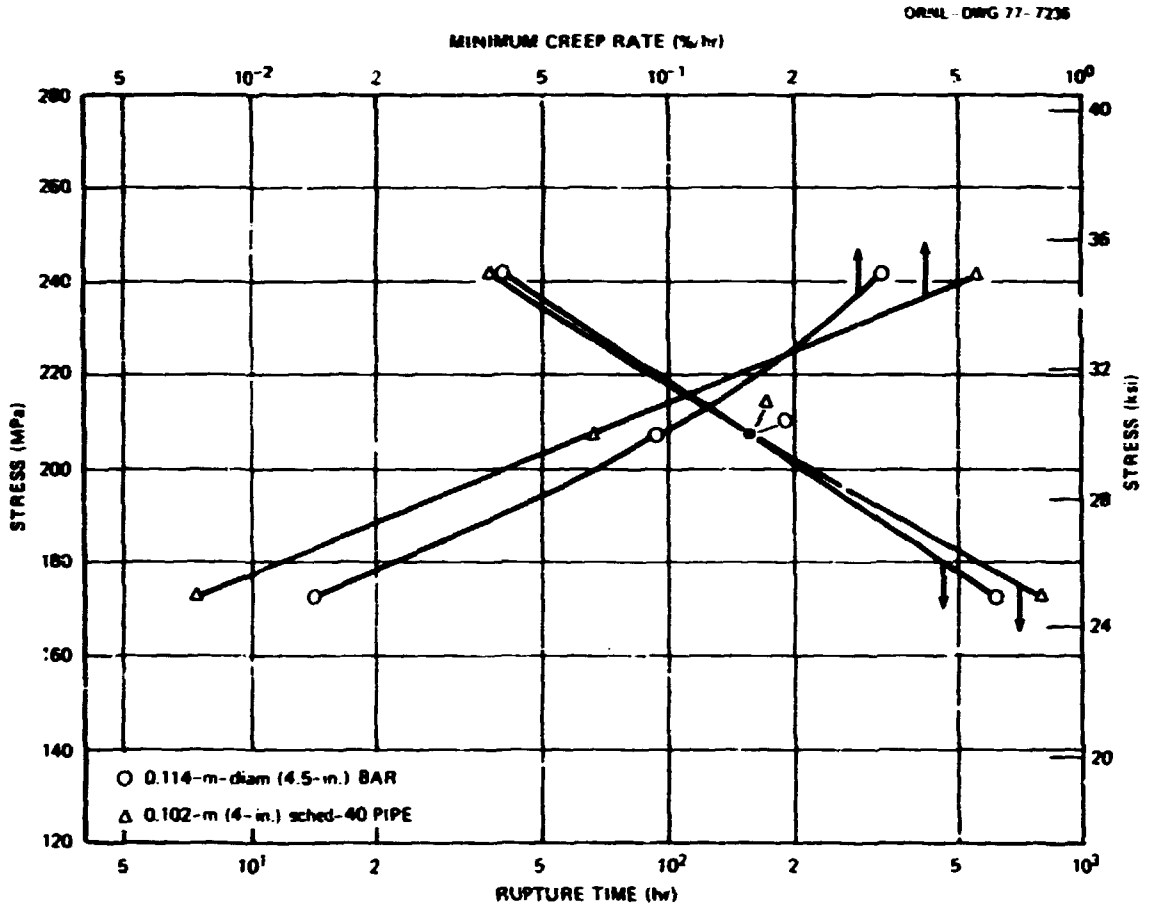

Fig. 19. Minimum creep rate and time to rupture for 0.114-m-diam (4 1/2-in.) bar and 0.102-m (4-in.) sched-40 pipe of type 304 stainless steel (reference heat 9T2796).

tributed to several sources. The accuracy with which the deformation measurements were made would definitely be a contributing factor. For very small deformations, as in the weld area, small absolute errors in measurements could produce scatter in the final calculated strains. The possibility also exists that relaxation of the residual stresses in the weldment could lead to a decrease in specimen diameter at the weld location. Another likely candidate for producing decreases in strain is the precipitation of carbides from the highly stressed weldment at elevated temperature.[10] This precipitation with its associated volume decrease could account in part for the weldment deformation behavior observed.

Although the weldments in the membrane regions of the cylinders did not undergo much strain, these weldments were capable of sustaining large

deformations with no loss of integrity. Welds in the cylinder-to-head junction regions and in the heads of the specimens were subjected to large bending strains as is shown in Fig. 20. Failure of this specimen (failure is discussed in the next subsection) was in the base metal in the cylinder-to-head junction region.

The inside and outside surface strains for a number of different cases were calculated using the approach discussed in Subsection 4.2. These results are contained in the appendix to this report.

5.2 Failure Behavior of Specimens

Failure of these specimens as well as the overall deformation behavior was of interest. The rupture lives of these specimens is shown in Fig. 21. The data are only for failures in the membrane regions of the cylinders for which the biaxial stress ratio was 2:1. Failures that occurred in the head-to-cylinder junction regions of the specimens are not shown due to the complexity of the stress field at these discontinuities. Two sets of symbols are used in Fig. 21, one representing data correlated on the basis of von Mises effective stress and one representing data correlated on the basis of maximum principal stress. The maximum principal stress gave better agreement with the uniaxial trend line over the full range of test conditions.

All the specimen failures originated in the base metal. In the head-to-cylinder junction region, the weldment was much stronger than a geometrically comparable all-base-metal junction region. This is exhibited rather graphically in Fig. 22, which is a cross-sectional micrograph showing the cylinder wall, weldment, and head of specimen 1-M1. This specimen failed by rupture of the cylinder after 408 hr (see Fig. 13). For some period of this time the weld was cracked as shown in Fig. 22, yet continued to function as a pressure boundary. In specimens 2-M1, 2A-M1, and 3-M1, failure occurred in this region, which was all-base metal, within 35 to 88 hr, respectively (see Fig. 14, typical).

Figure 23 shows the head-to-cylinder junction region of specimen 1-M2, which failed after 475 hr. A crack developed in the base metal and propagated into the weld. As can be seen, the weld underwent a significant

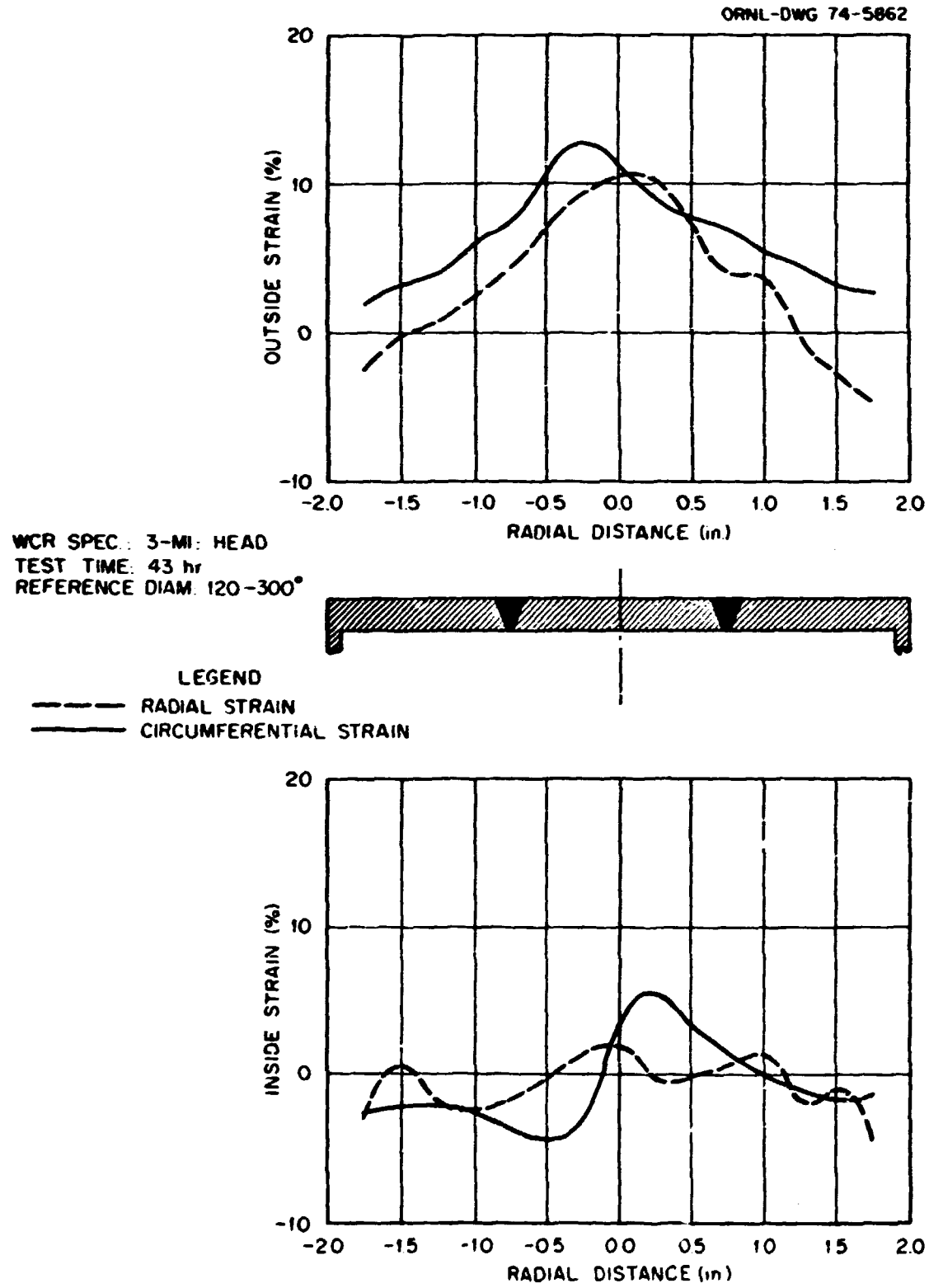

Fig. 20. Strain distribution in head of WCR specimen 3-M1 indicating strain capability of weldment.

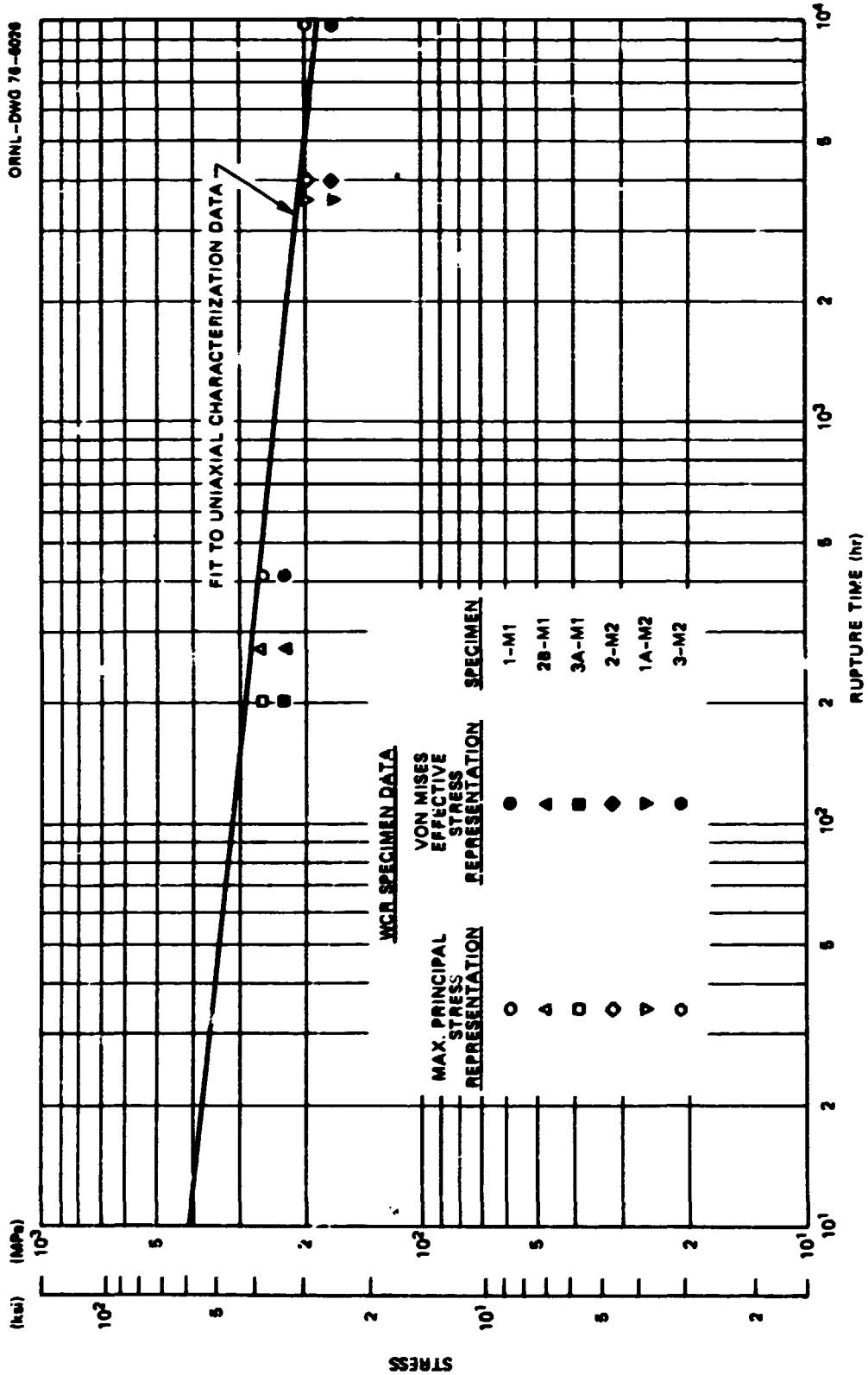

Fig. 21. Biaxial rupture data from weldment specimens tested at 593°C (1100°F).

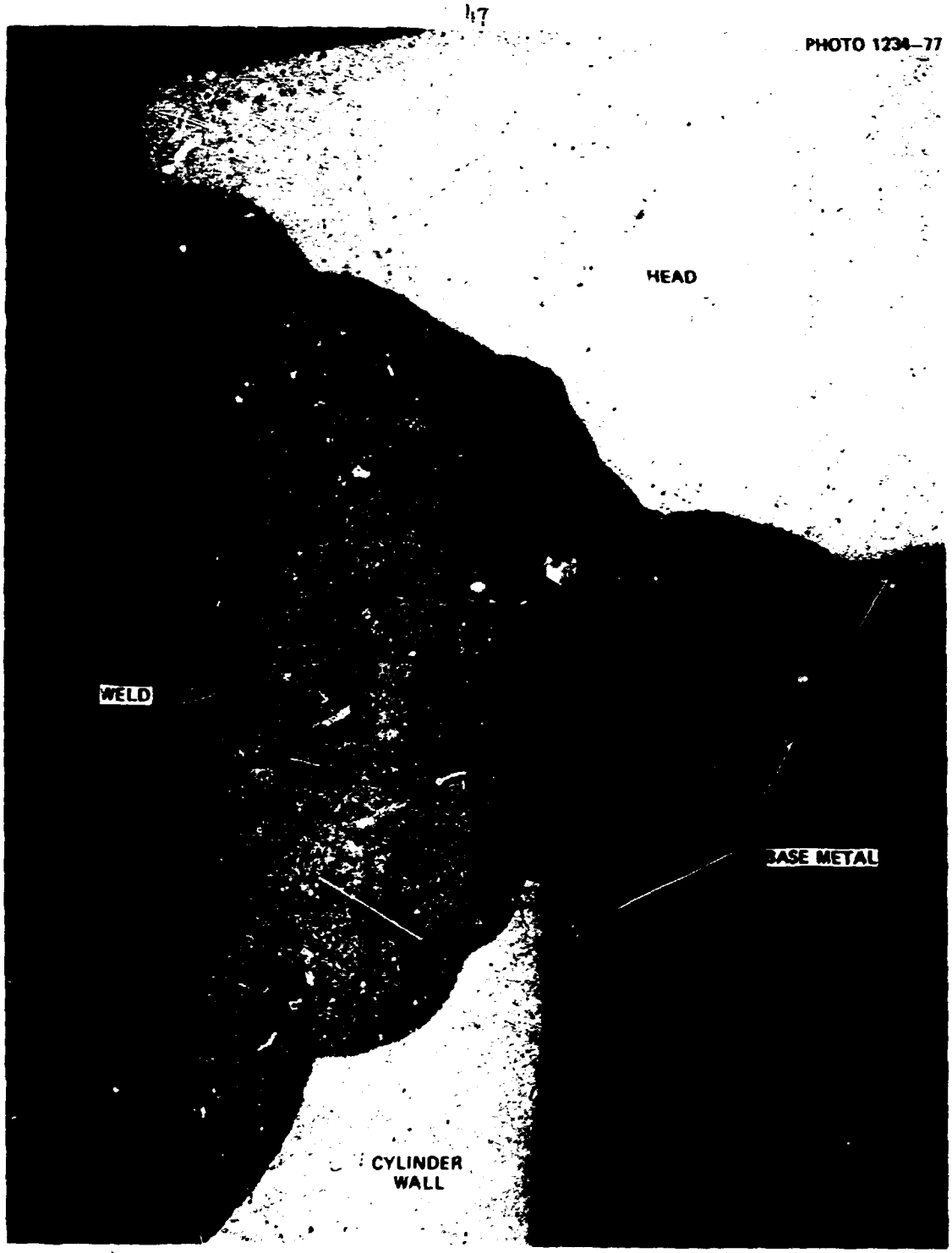

Fig. 22. Cross section of head-to-cylinder junction region in specimen 1-M1 after 408 hr at 593°C (1100°F).

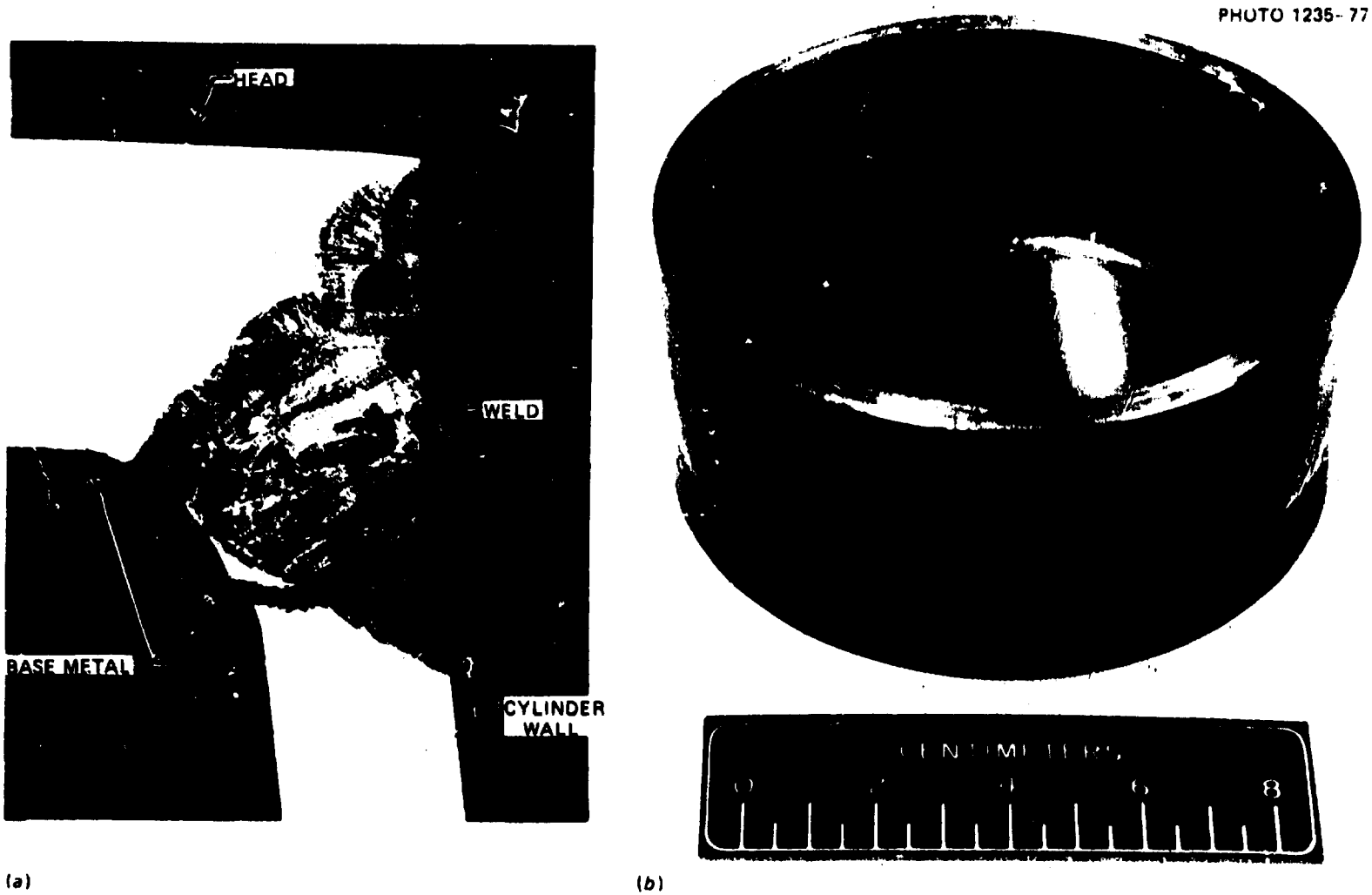

Fig. 23. Head-to-cylinder junction region in specimen 1-M2 after 475 hr at 593°C (1100°F). (a) Cross section of weldment; (b) view showing developed crack in junction region.

amount of deformation before pressure loss through a pinhole leak. In both specimens 1-M1 and 1-M2, the cracks extended a complete 360° around the inside of the junction region.

5.3 Conclusions and Summary

The number of tests conducted was not sufficient to yield what one would consider to be a sound statistical sample so far as rupture behavior is concerned. However, the information obtained is valuable in an assessment of the structural response of weldments subjected to both short- and long-term steady-state creep.

In assessing the results of these tests, several points are important with respect to the comparative behavior of the base metal and weldments.

1. The rupture life of the specimen was determined by the base metal and not by the weldments.

2. The weldments were capable of undergoing large strains without apparent damage through cracking or tearing.

3. The weldments possessed superior resistance to crack growth as compared to the base metal.

4. For the test conditions, the maximum principal stress gave a better correlation between the uniaxial and biaxial failure data.

REFERENCES

1. R. G. Gilliland, The Behavior of Welded Joints in Stainless and Alloy Steels at Elevated Temperatures, ORNL-4781 (August 1972).

2. Interpretations of the ASME Boiler and Pressure Vessel Code, "Case 1592-7, Class 1 Components in Elevated Temperature Service," American Society of Mechanical Engineers, New York, Dec. 22, 1975.

3. J. M. Corum, "Structural Testing," High-Temperature Structural Design Methods for LMFBR Components Quarterly Progress Report for Period Ending September 30, 1972, ORNL-TM-4058, p. 75.

4. W. J. Anderson, D. F. Atkins, and J. H. Shively, Mechanical Properties of Stainless Steels in Sodium, and Application to LMFBR Design, AI-AEC-13000 (Feb. 25, 1972).

5. R. W. Swindeman and R. D. Waddell, "Characterization of the ORNL Reference Heat (No. 9T2796) of Type 304 Stainless Steel," High-Temperature Structural Design Methods for LMFBR Components Quarterly Progress Report for Period Ending September 30, 1972, ORNL-TM-4058, p. 137.

6. H. E. McCoy, "Characterization of Product Form," High-Temperature Structural Design Methods for LMFBR Components Quarterly Progress Report for Period Ending June 30, 1973, ORNL-TM-4356, p. 3.

7. W. L. Greenstreet, J. M. Corum, and C. E. Pugh, Informal Progress Reports on Structural Design Methods for LMFBR Components for October and November 1970, Internal Memorandum, Oak Ridge National Laboratory (Dec. 1, 1970).

8. F. L. Yaggee, J. W. Styles, and S. B. Brak, Semiautomatic Apparatus for Creep and Stress-Rupture Tests of Thin-Wall Fuel-Cladding Tubes Under Internal Gas-Pressure Loading, ANL-7801 (September 1971).

9. H. E. McCoy, "Characterization of Reference Heat Product Forms," High-Temperature Structural Design Methods for LMFBR Components Progress Report for Period Ending December 31, 1973, ORNL-4947, p. 1.

10. G. R. Brophy and D. E. Furman, "The Cyclic Temperature Acceleration of Strain in Heat Resisting Alloys," Trans. ASM 30, 1115-38 (1942).

APPENDIX

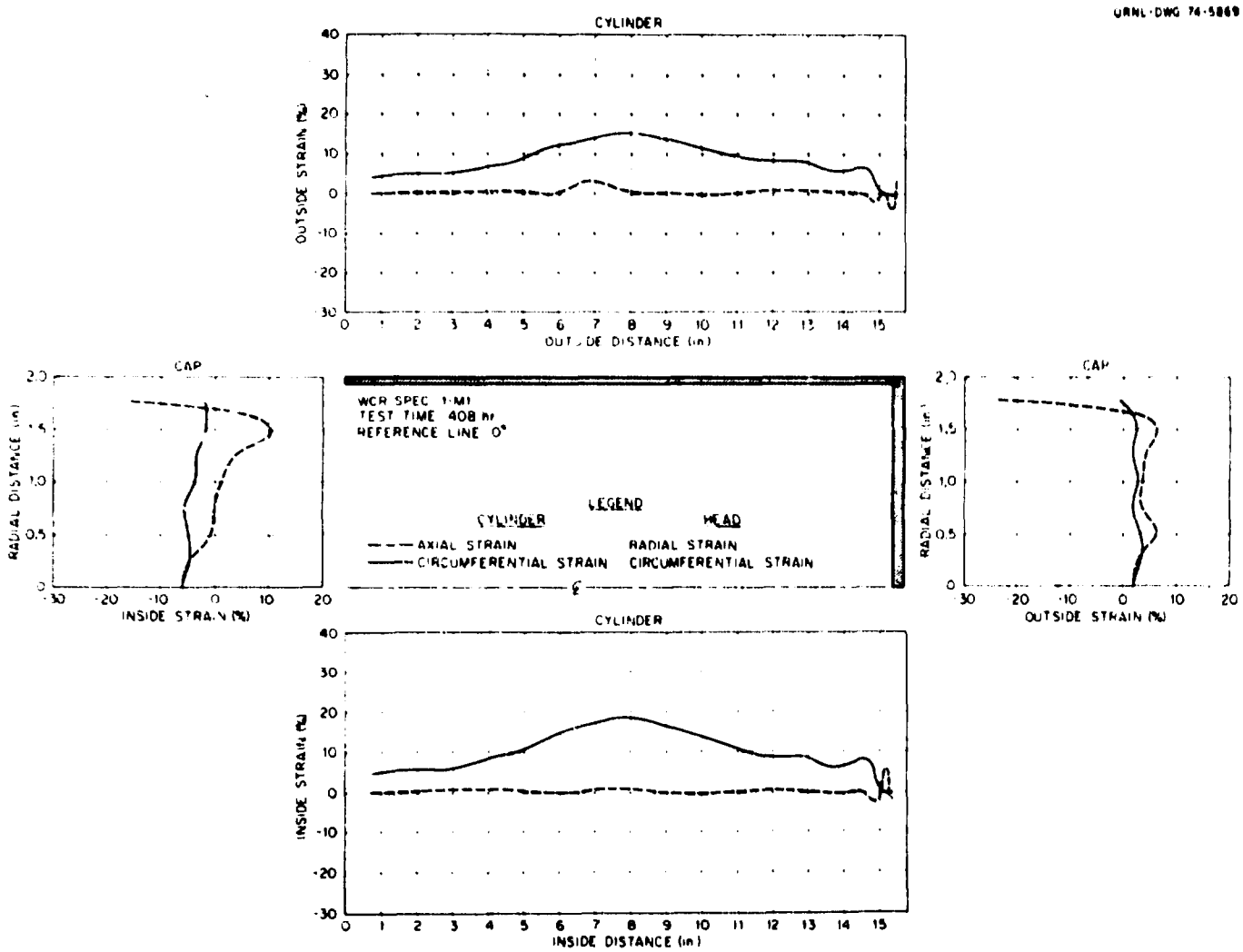

Fig. A1-a. Surface strain distribution for specimen 1-M1 along the axial reference plane, $\theta = 0°$, at 408 hr (1 in. = 2.54 cm).

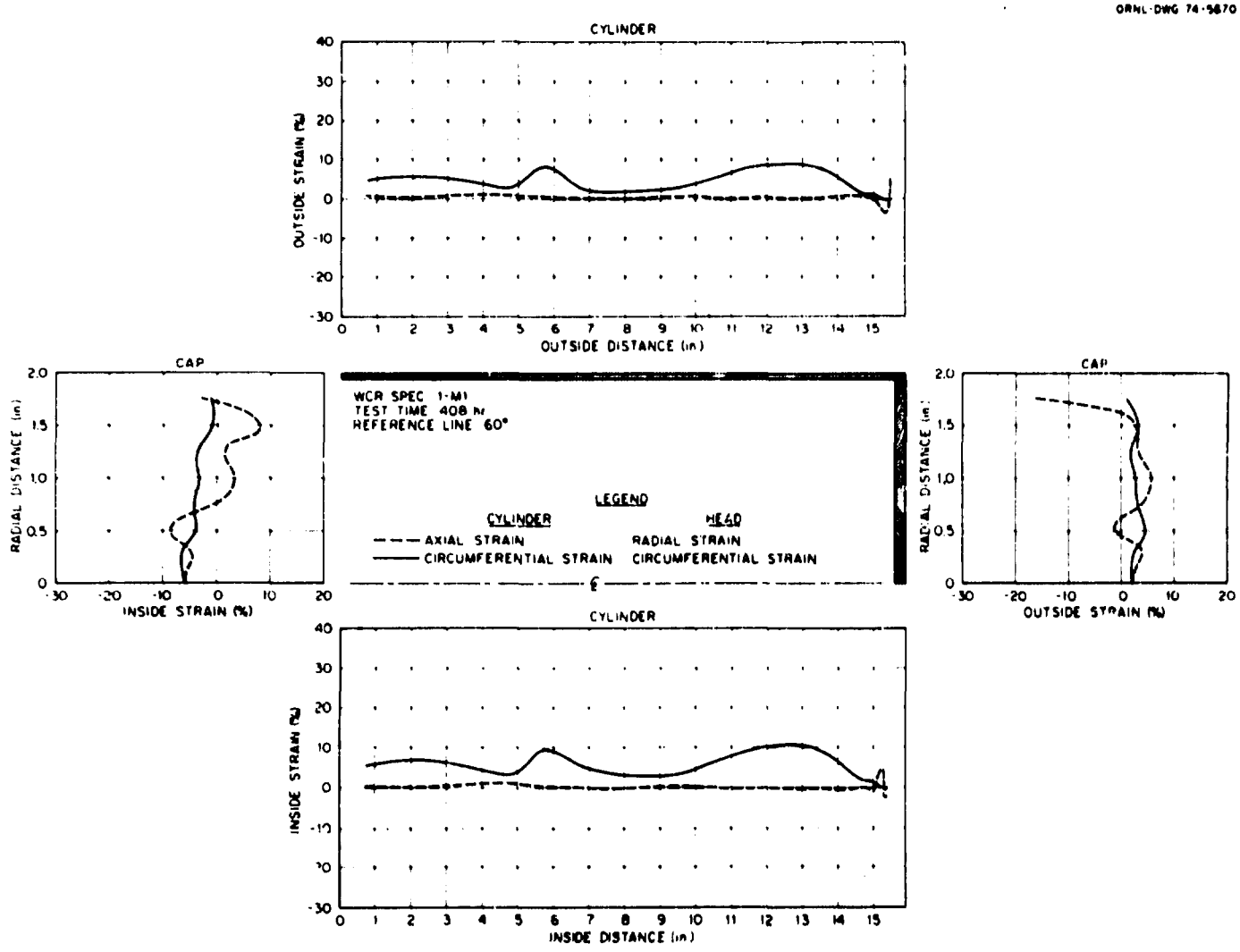

Fig. A1-b. Surface strain distribution for specimen 1-M1 along the axial reference plane, $\theta = 60°$, at 408 hr (1 in. = 2.54 cm).

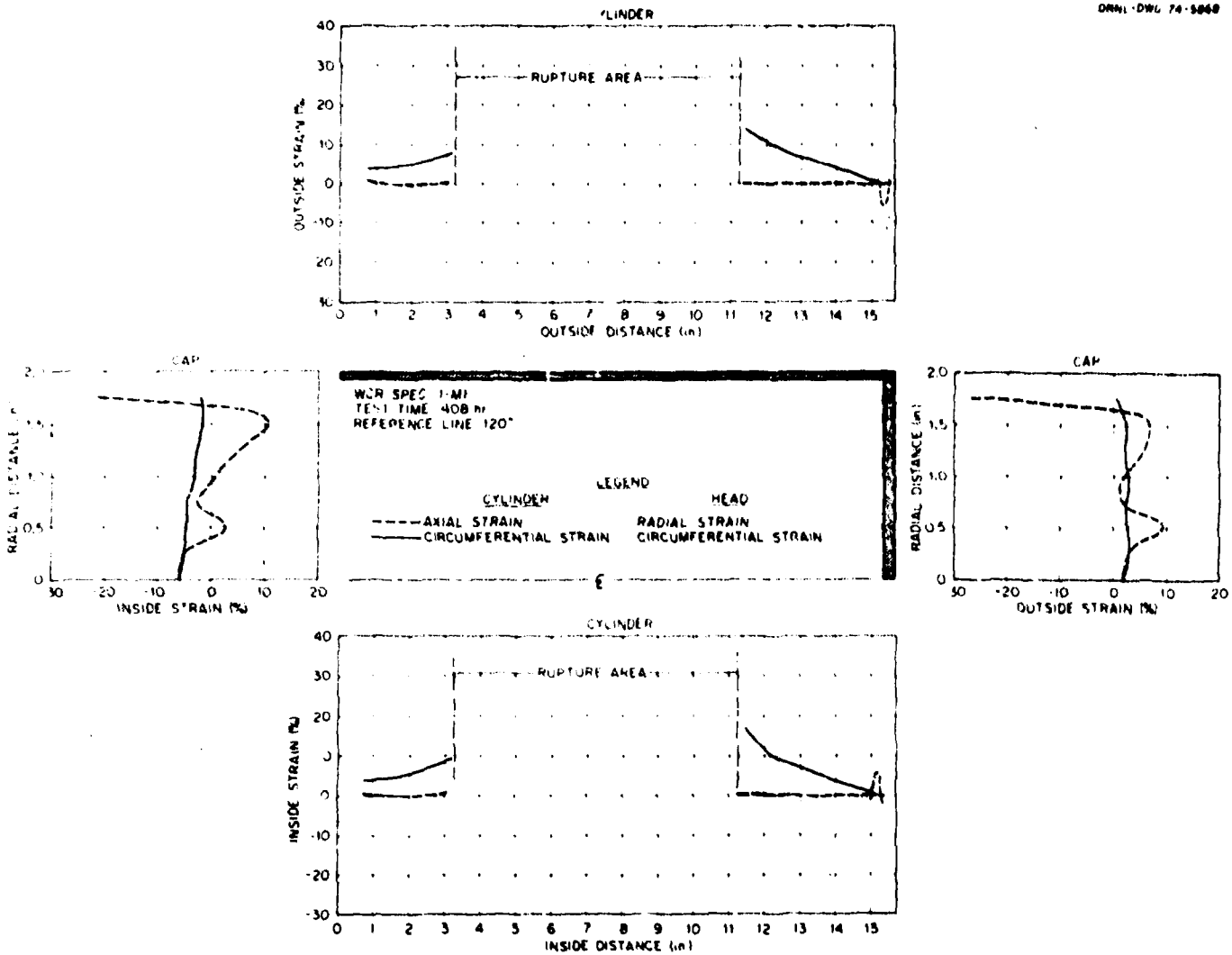

Fig. A1-c. Surface strain distribution for specimen 1-M1 along the axial reference plane, θ = 120°, at 408 hr (1 in. = 2.54 cm).

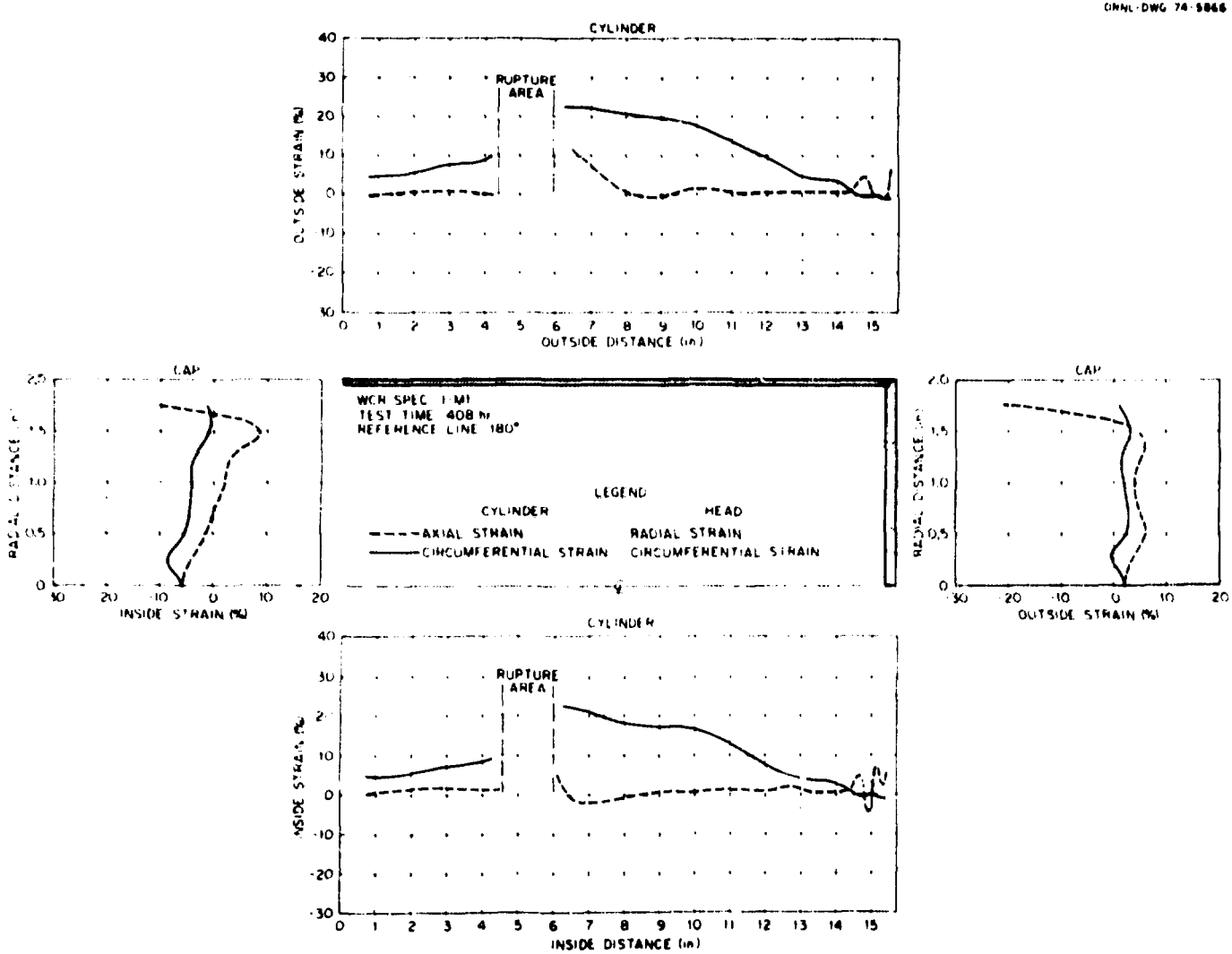

Fig. A1-d. Surface strain distribution for specimen 1-M1 along the axial reference plane, θ = 180°, at 408 hr (1 in. = 2.54 cm).

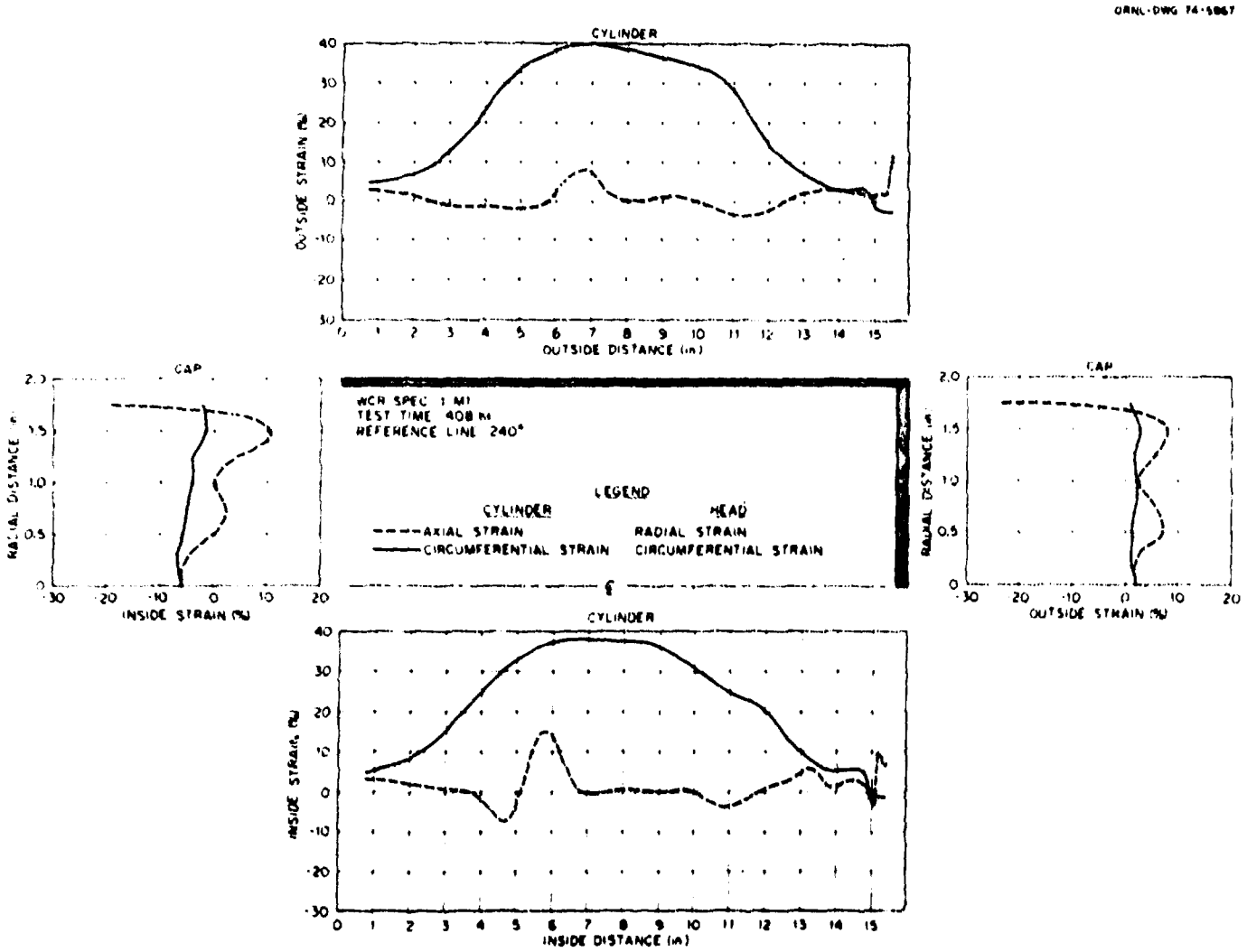

Fig. A1-e. Surface strain distribution for specimen 1-M1 along the axial reference plane, $\theta = 240°$, at 408 hr (1 in. = 2.54 cm).

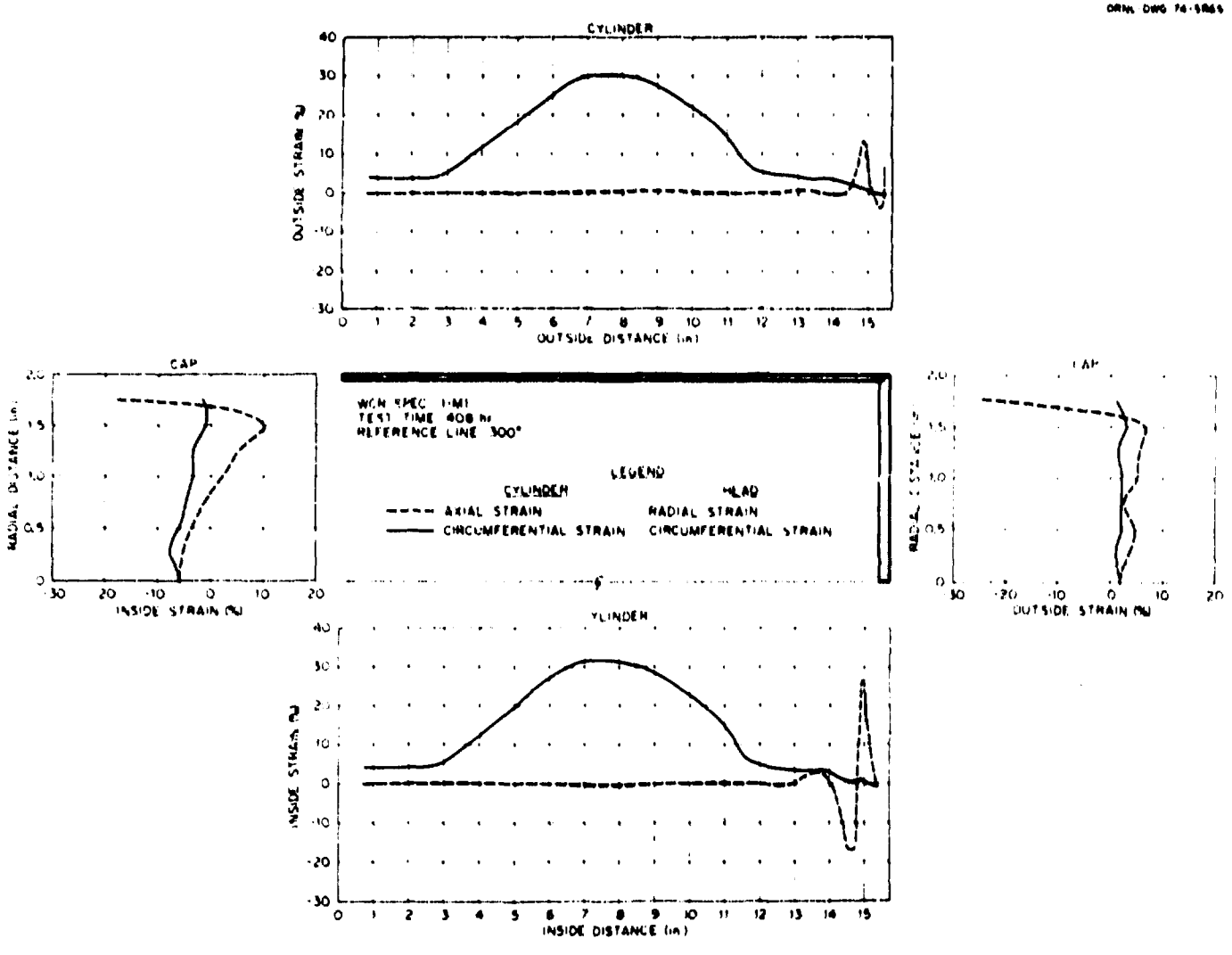

Fig. A1-f. Surface strain distribution for specimen 1-M1 along the axial reference plane, θ = 300°, at 408 hr (1 in. = 2.54 cm).

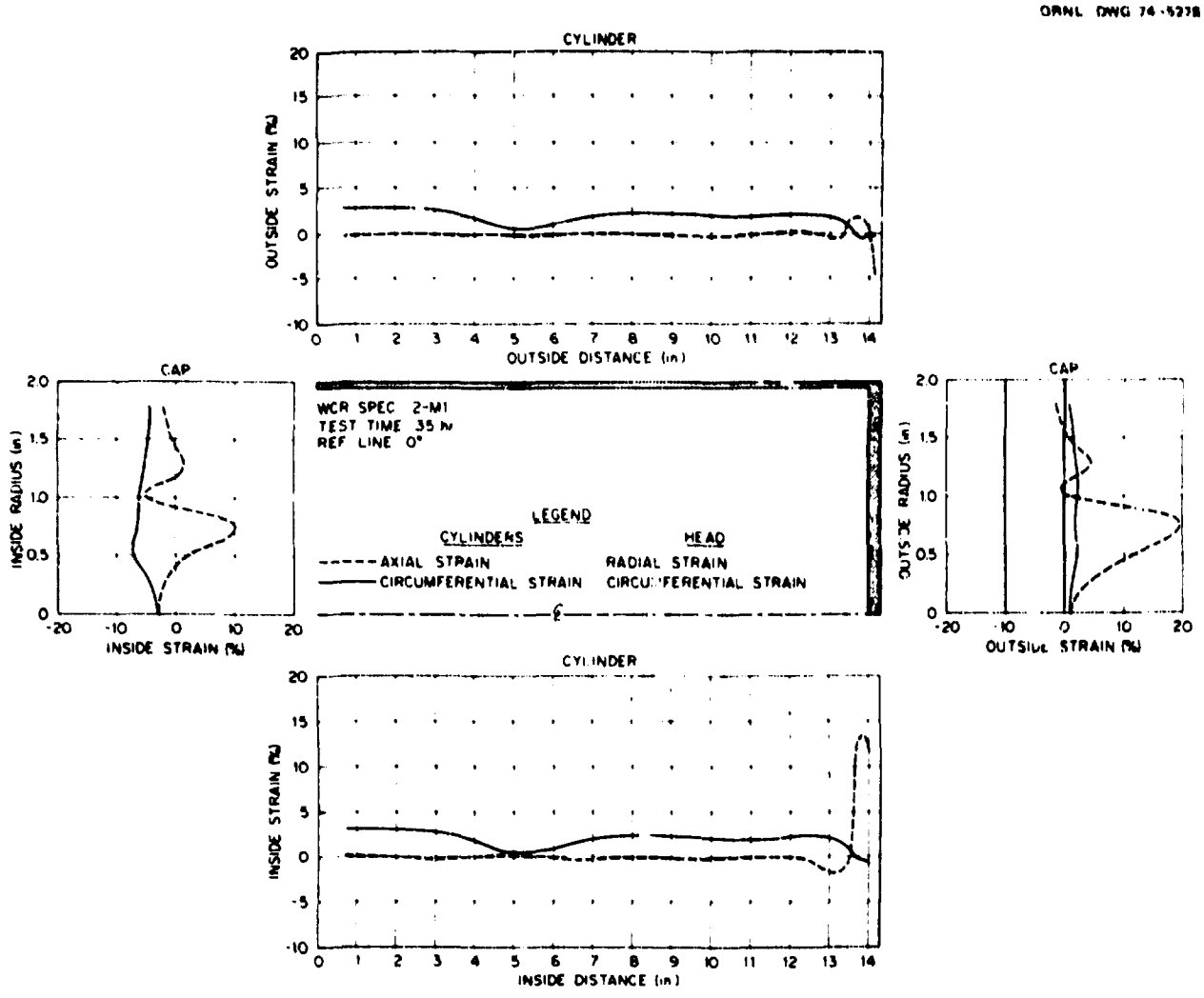

Fig. A2-a. Surface strain distribution for specimen 2-M1 along the axial reference plane, $\theta = 0°$, at 35 hr (1 in. = 2.54 cm).

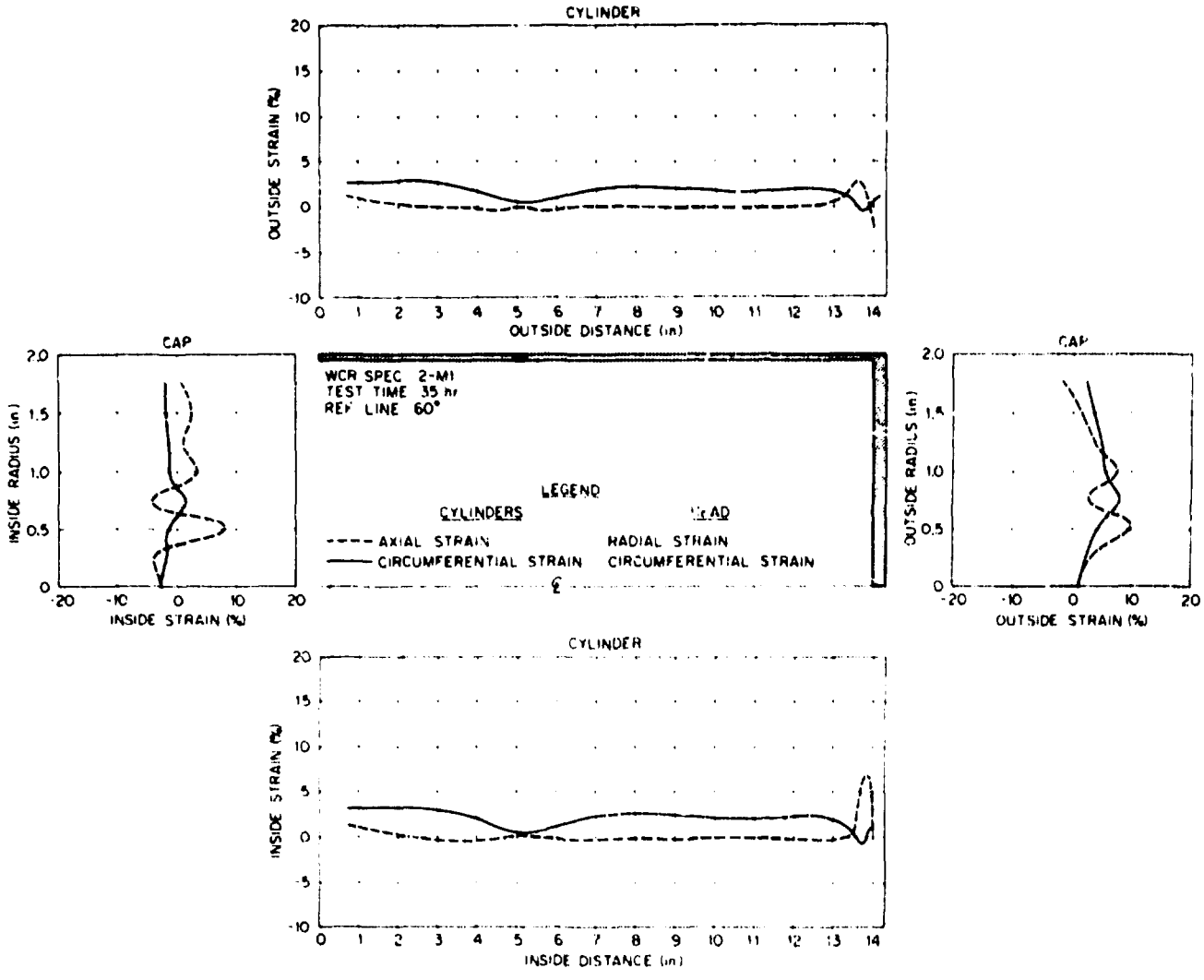

Fig. A2-b. Surface strain distribution for specimen 2-M1 along the axial reference plane, $\theta = 60°$, at 35 hr (1 in. = 2.54 cm).

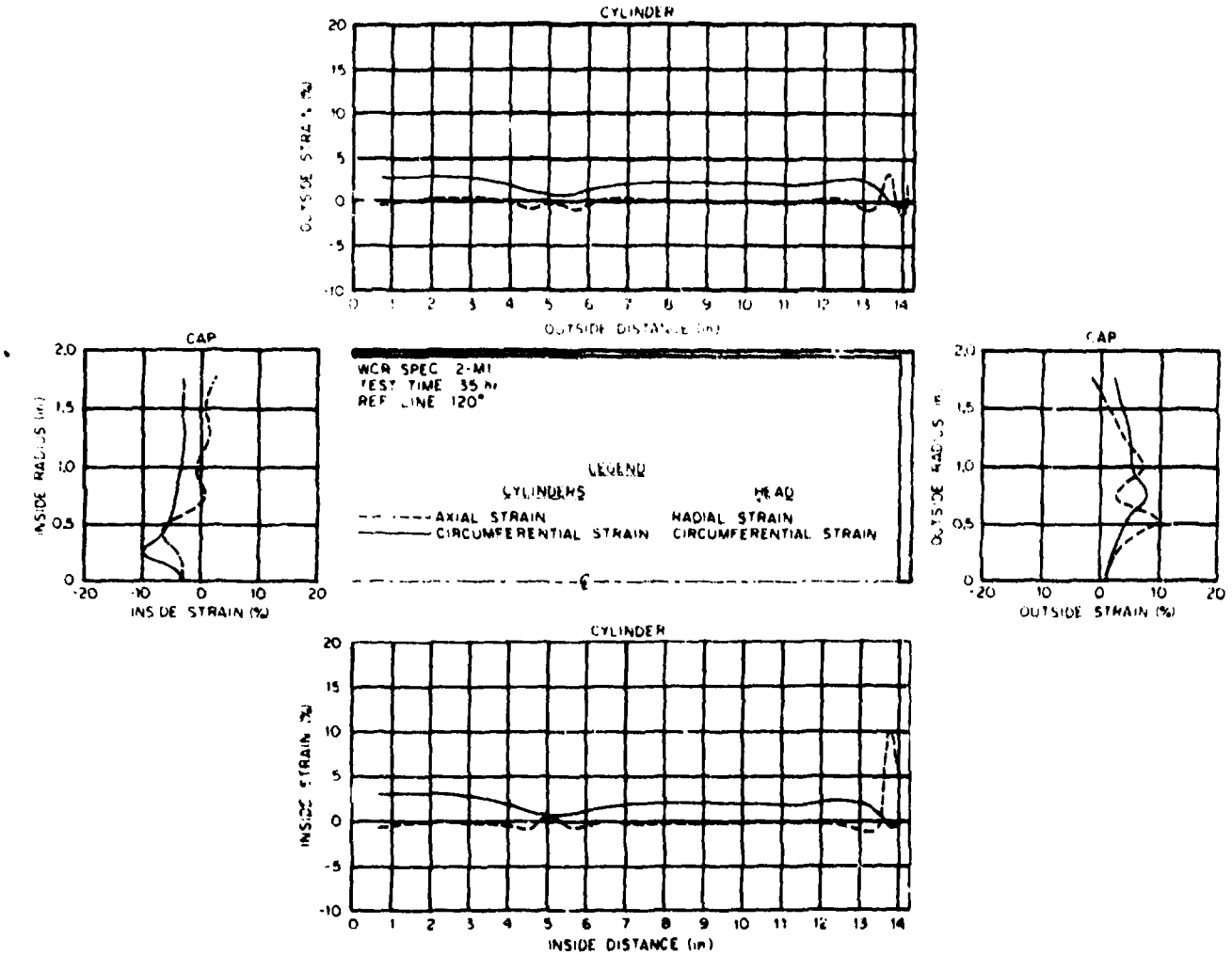

Fig. A2-c. Surface strain distribution for specimen 2-M1 along the axial reference plane, θ = 120°, at 35 hr (1 in. = 2.54 cm).

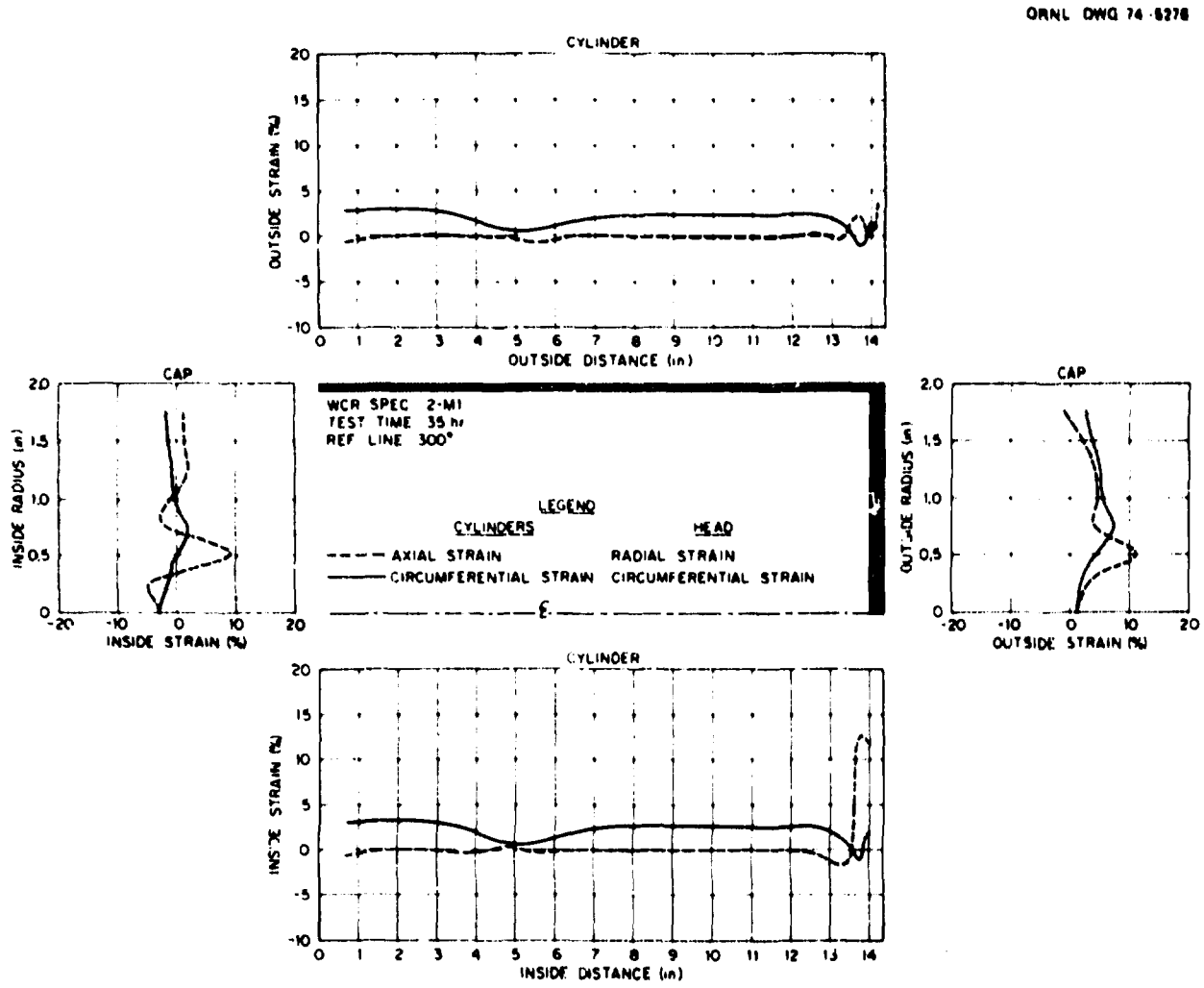

Fig. A2-d. Surface strain distribution for specimen 2-M1 along the axial reference plane, θ = 180°, at 35 hr (1 in. = 2.54 cm).

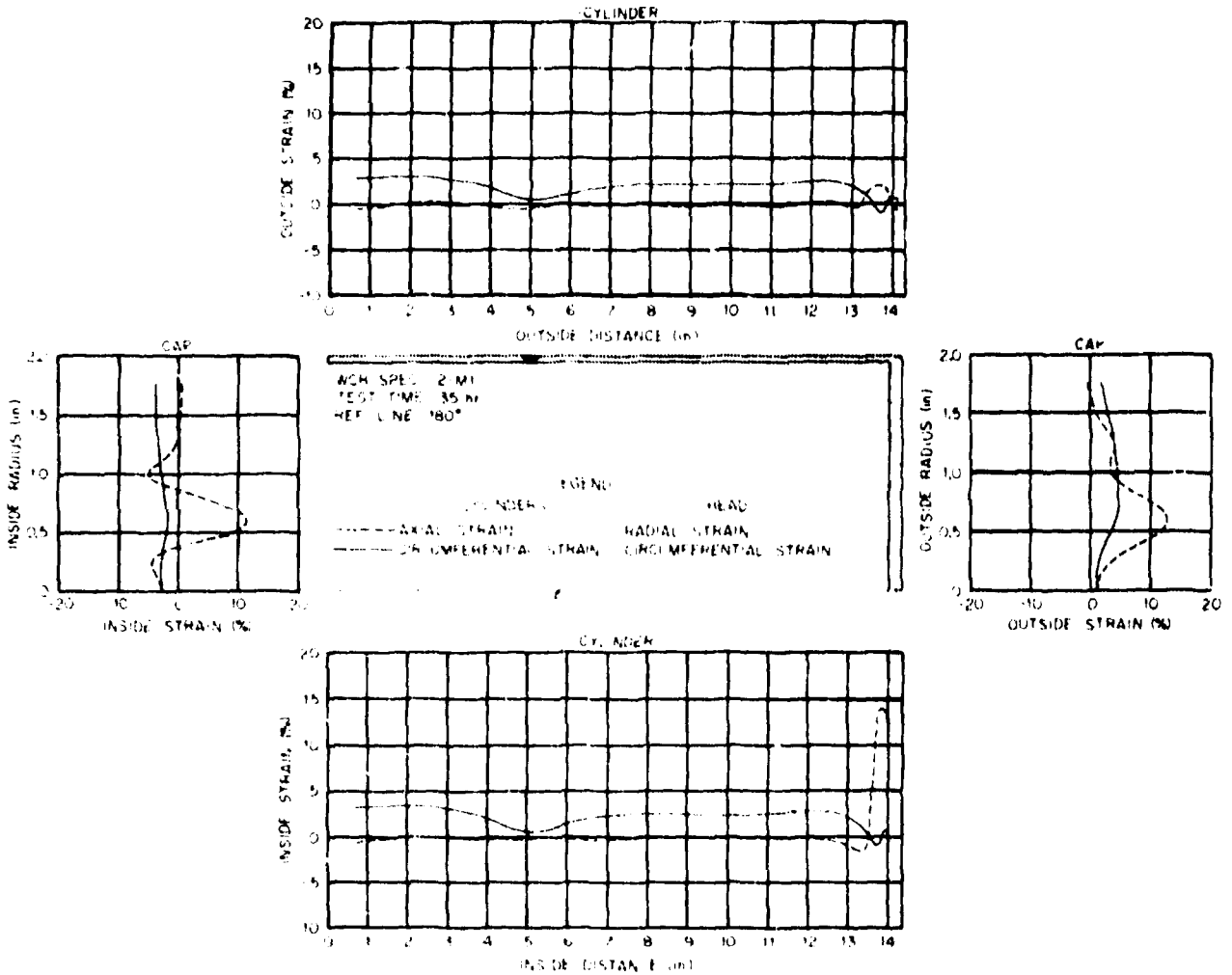

Fig. A2-e. Surface strain distribution for specimen 2-M1 along the axial reference plane, θ = 240°, at 35 hr (1 in. = 2.54 cm).

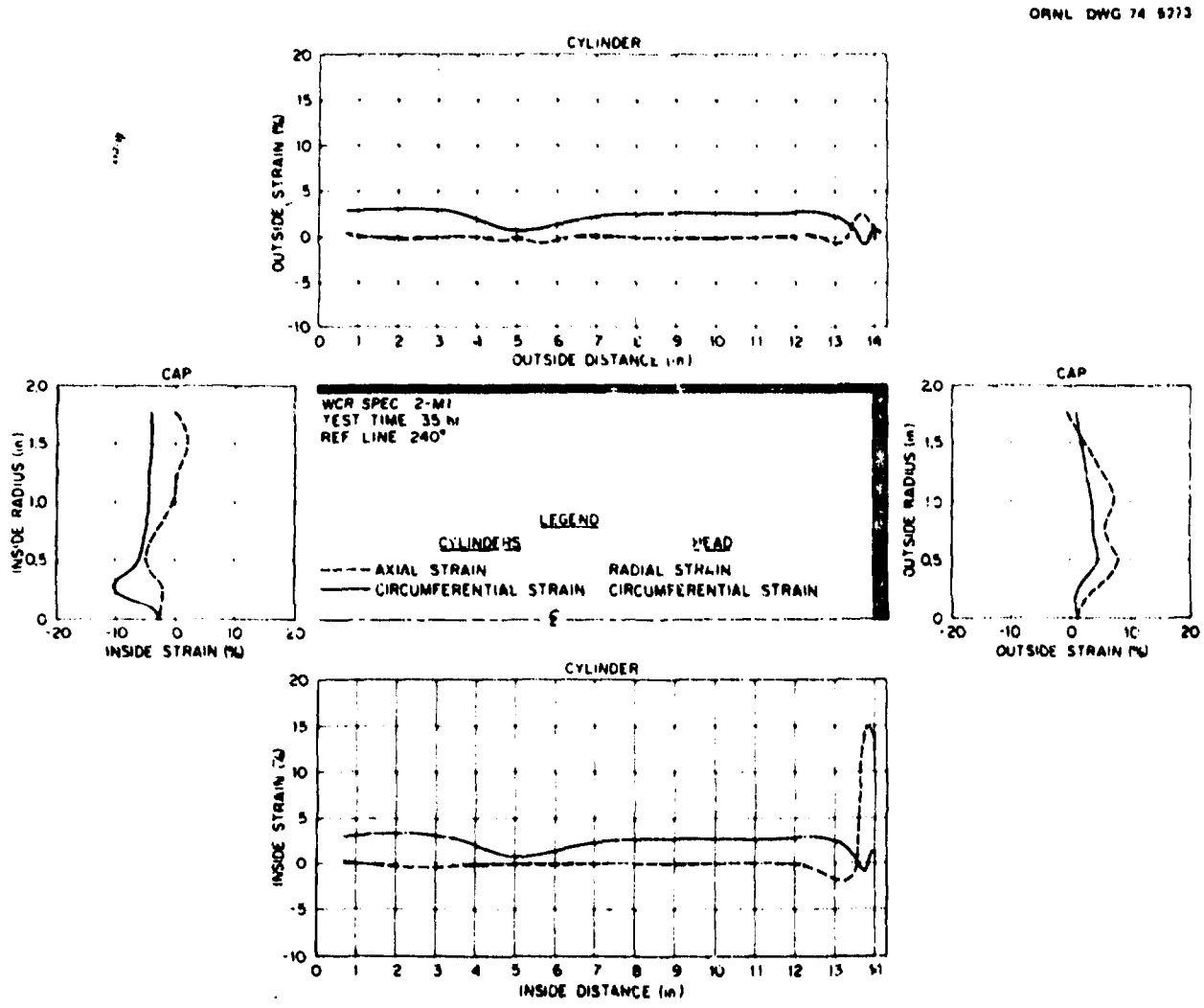

Fig. A2-f. Surface strain distribution for specimen 2-M1 along the axial reference plane, θ = 300°, at 35 hr (1 in. = 2.54 cm).

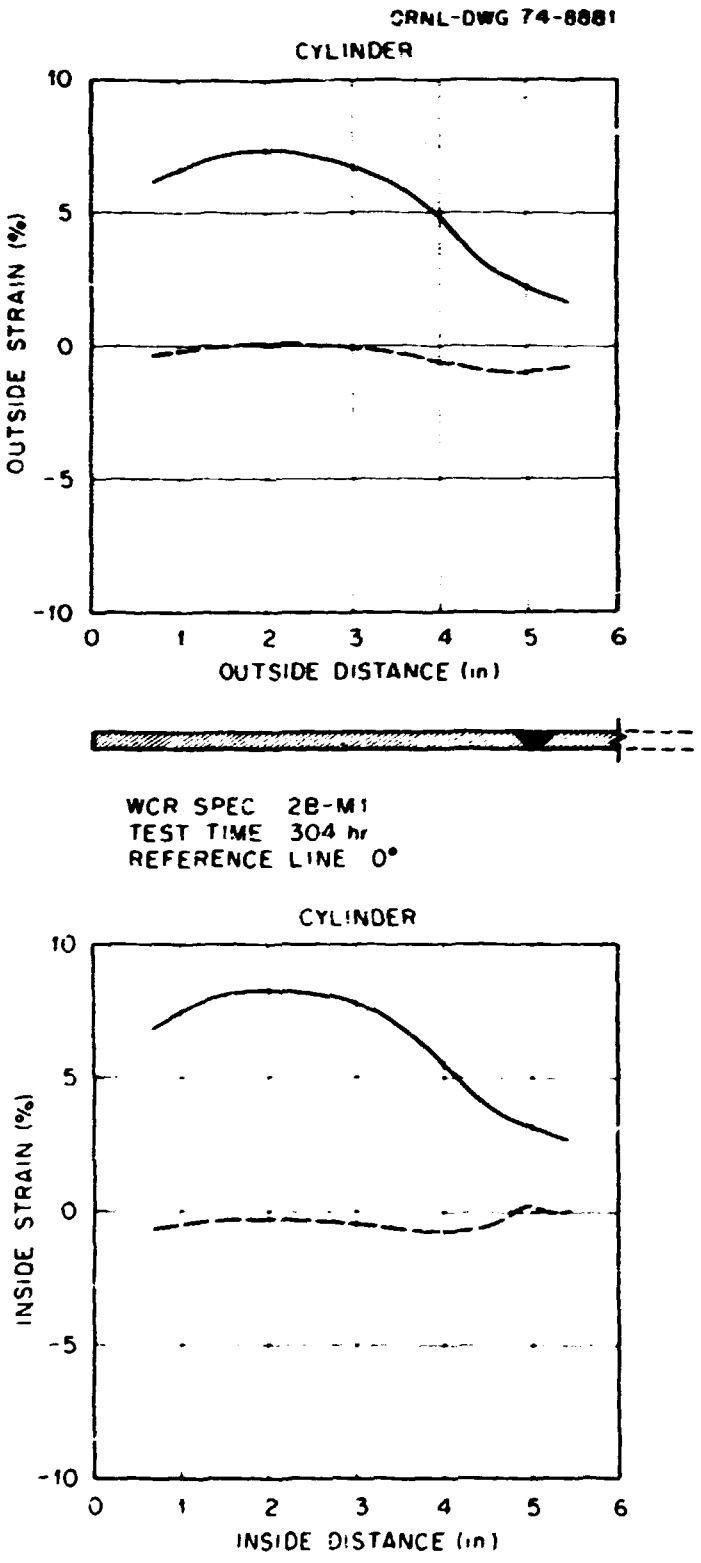

Fig. A3-a. Surface strain distribution for specimen 2B-M1 along the axial reference plane, $\theta = 0°$, at 304 hr (1 in. = 2.54 cm).

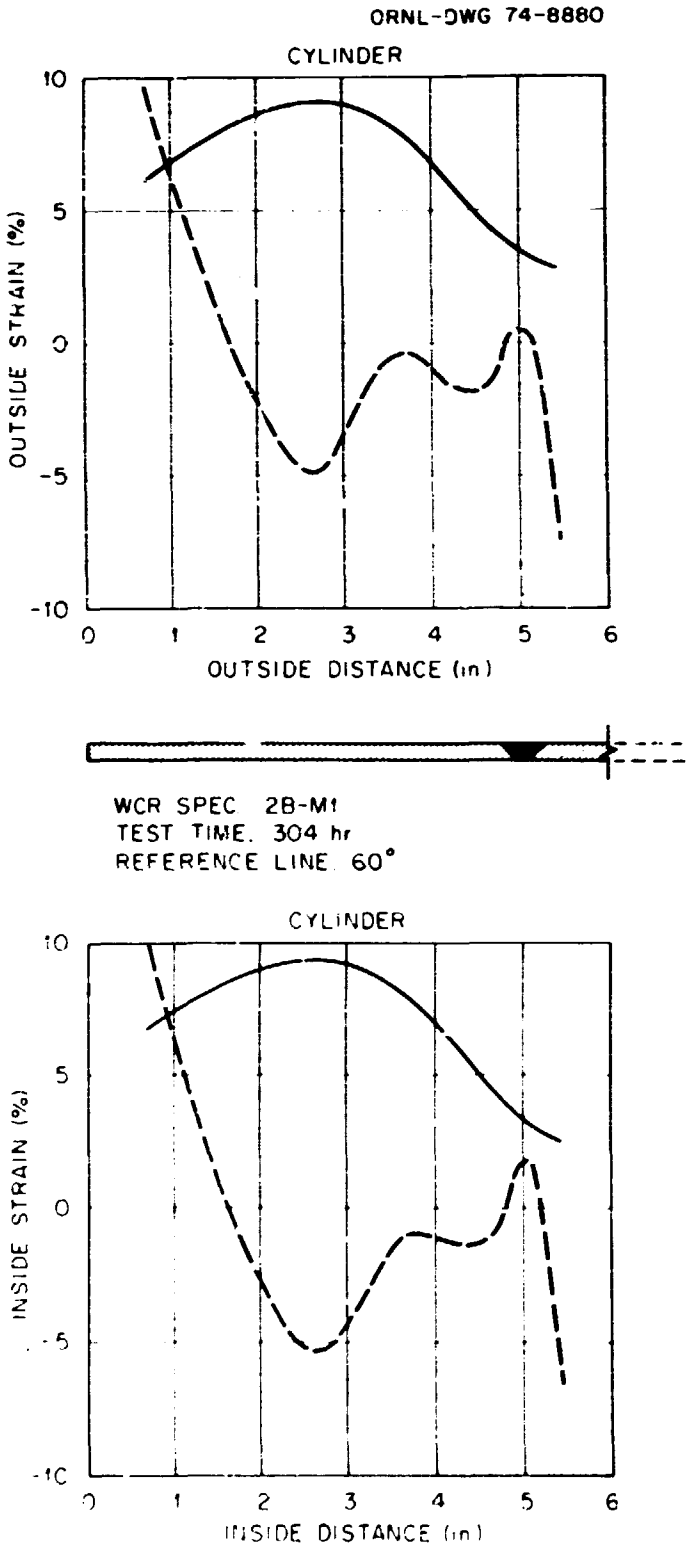

Fig. A3-b. Surface strain distribution for specimen 2B-M1 along the axial reference plane, $\theta = 60^{\circ}$, at 304 hr (1 in. = 2.54 cm).

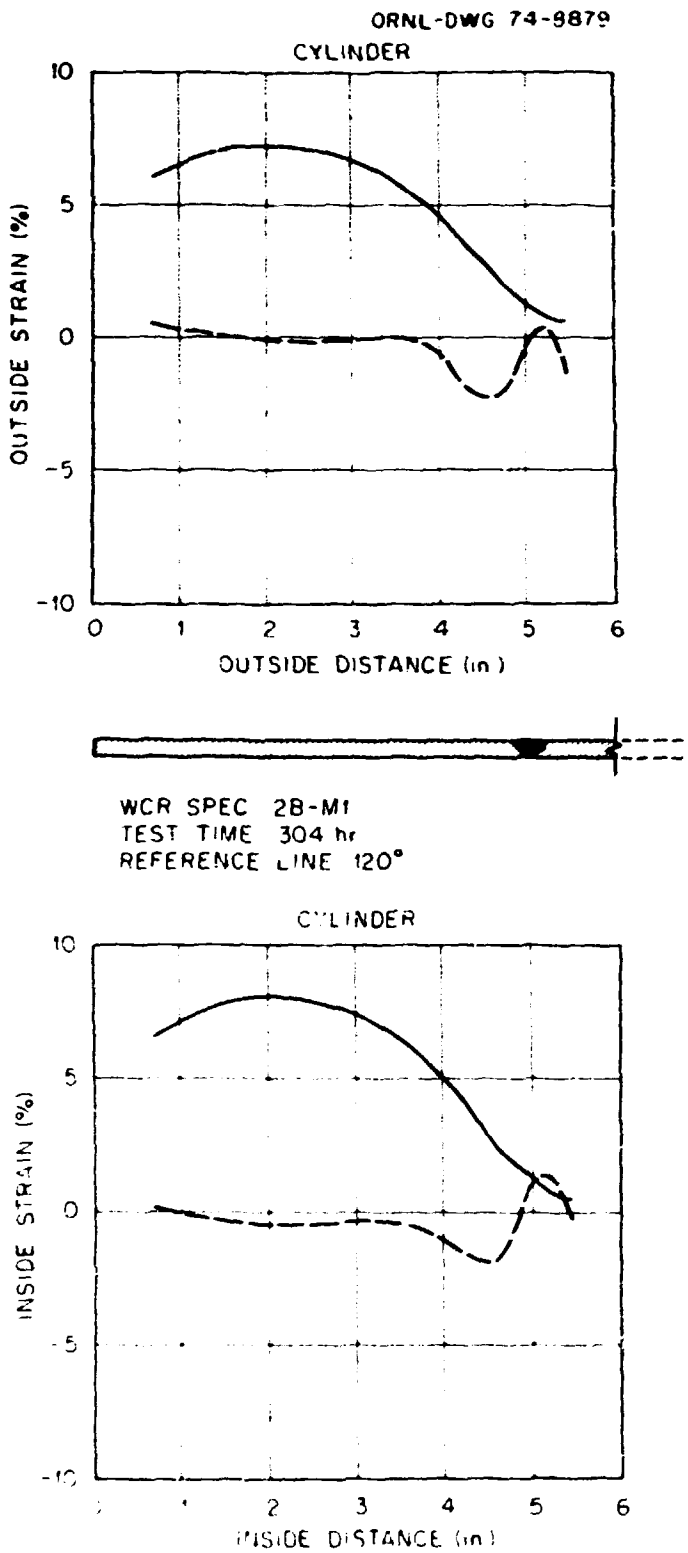

Fig. A3-c. Surface strain distribution for specimen 2B-M1 along the axial reference plane, θ = 120°, at 304 hr (1 in. = 2.54 cm).

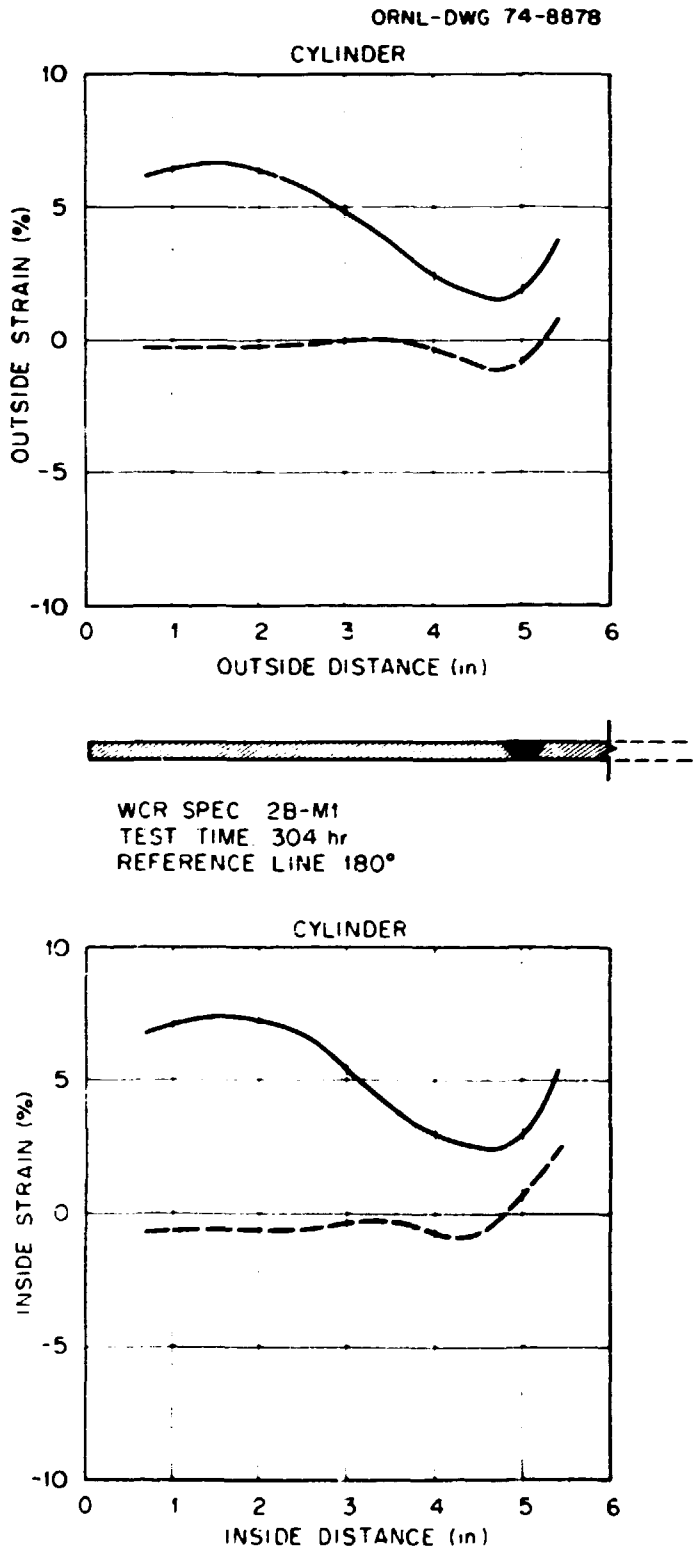

Fig. A3-d. Surface strain distribution for specimen 2B-M1 along the axial reference plane, $\theta = 180°$, at 304 hr (1 in. = 2.54 cm).

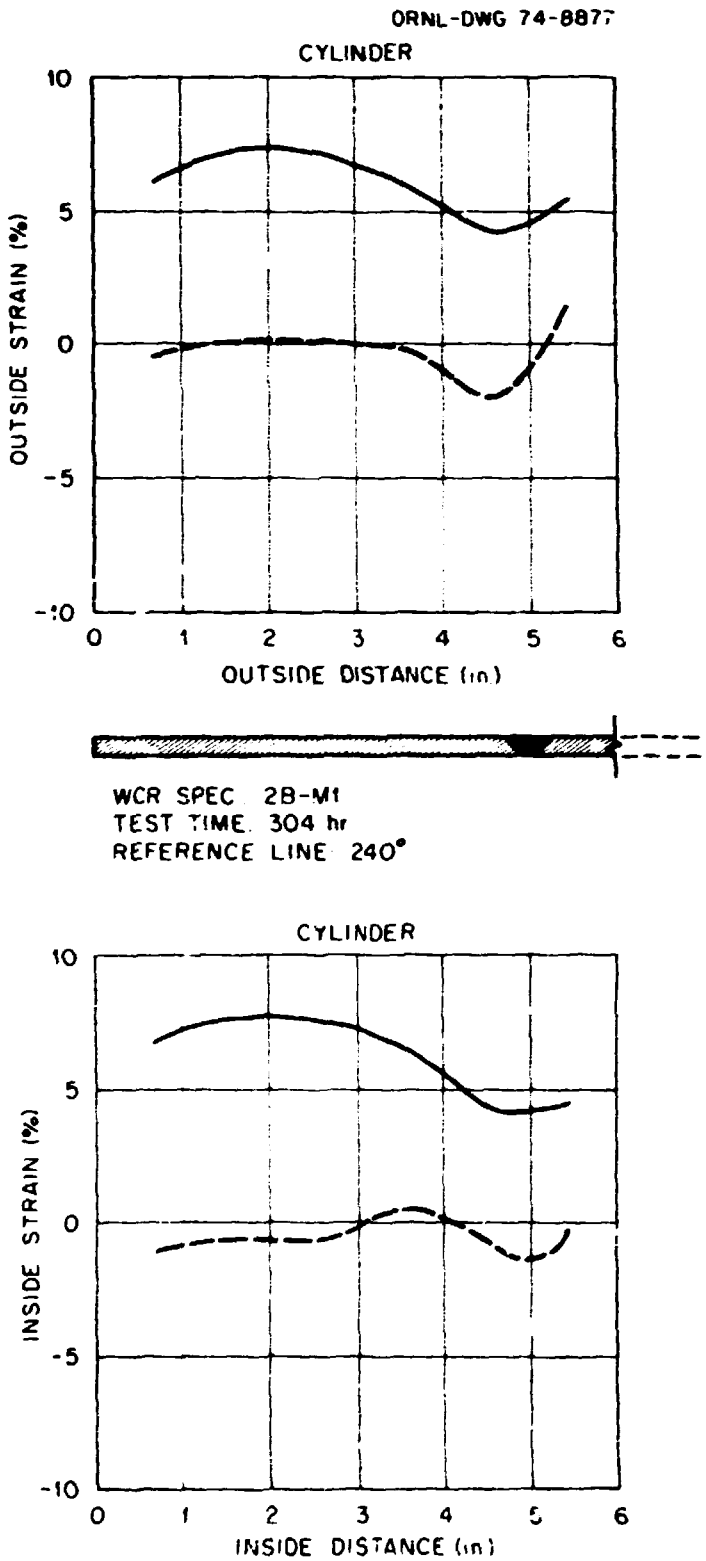

Fig. A3-e. Surface strain distribution for specimen 2B-M1 along the axial reference plane, $\theta = 240°$, at 304 hr (1 in. = 2.54 cm).

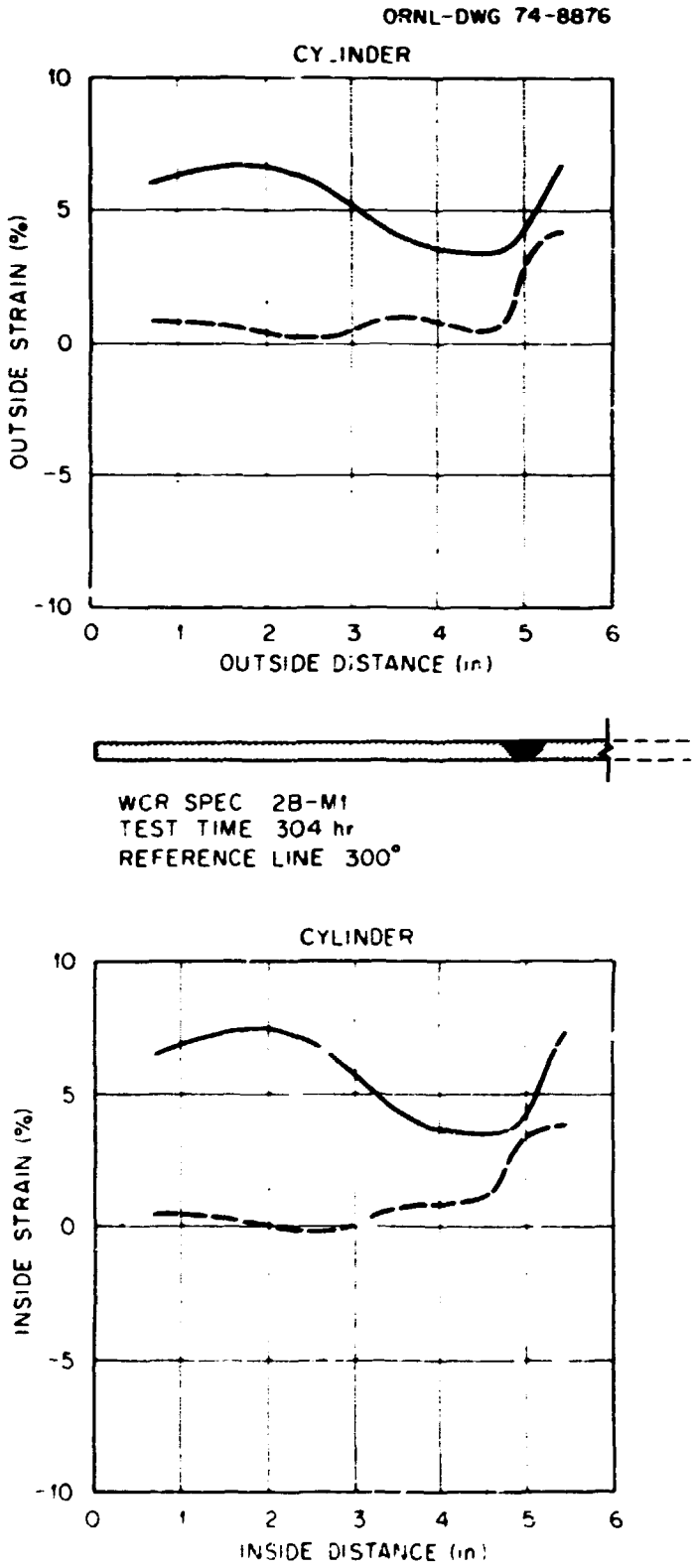

Fig. A3-f. Surface strain distribution for specimen 2B-M1 along the axial reference plane, θ = 300°, at 304 hr (1 in. = 2.54 cm).

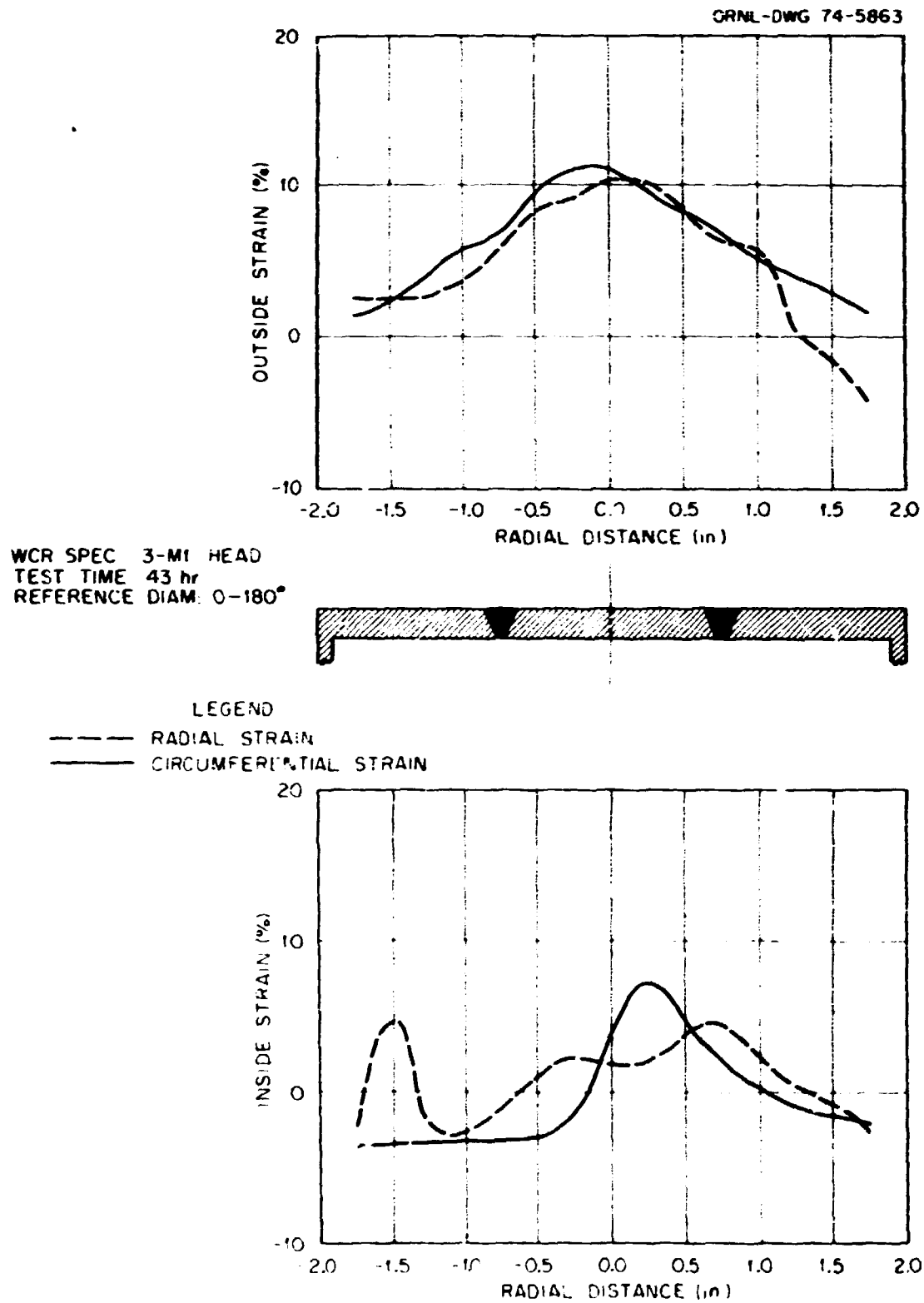

Fig. A4-a. Surface strain distribution on the head of specimen 3-M1 along the diameter, 0–180° (1 in. = 2.54 cm).

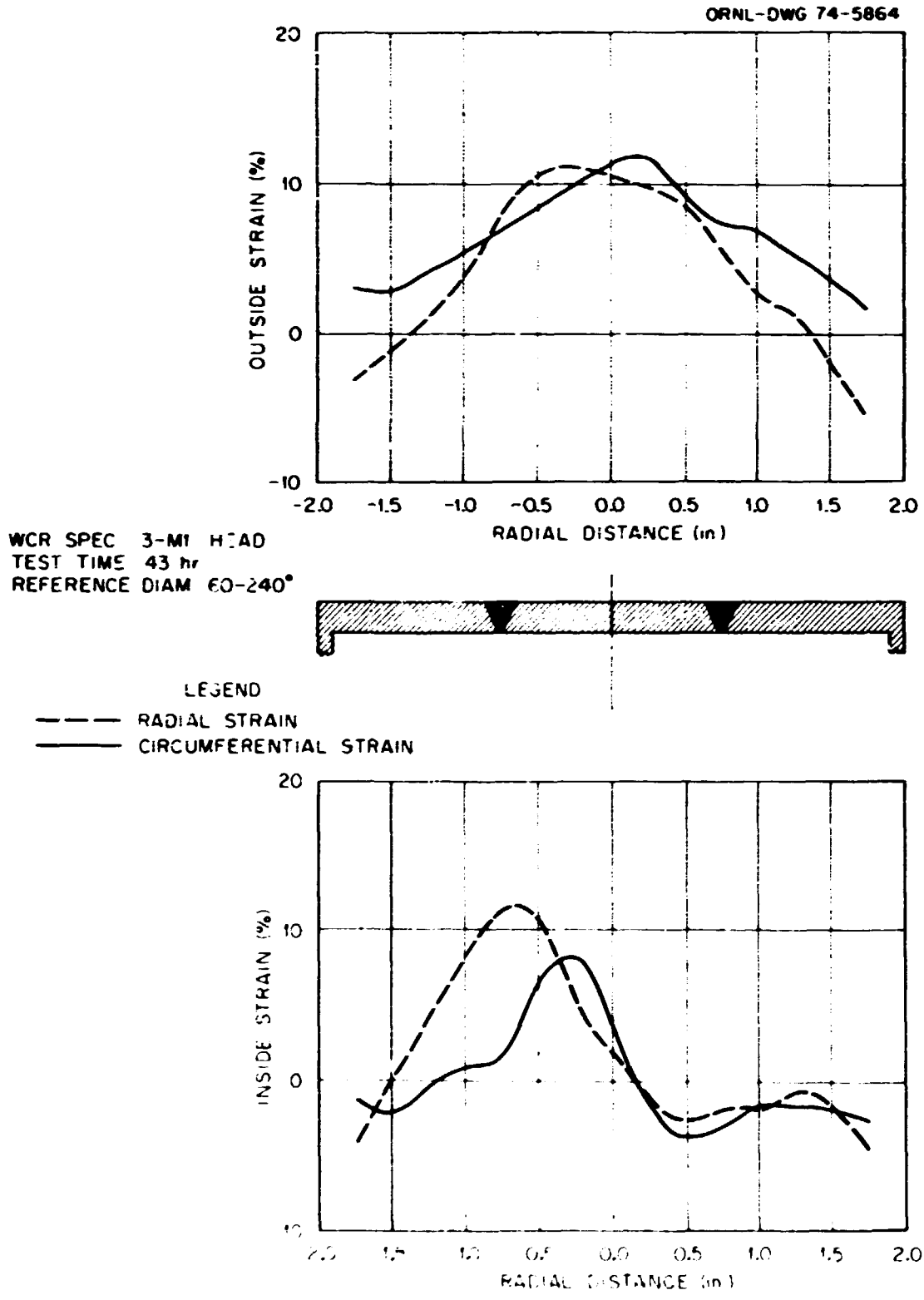

Fig. A4-b. Surface strain distribution on the head of specimen 3-M1 along the diameter, 60-240° (1 in. = 2.54 cm).

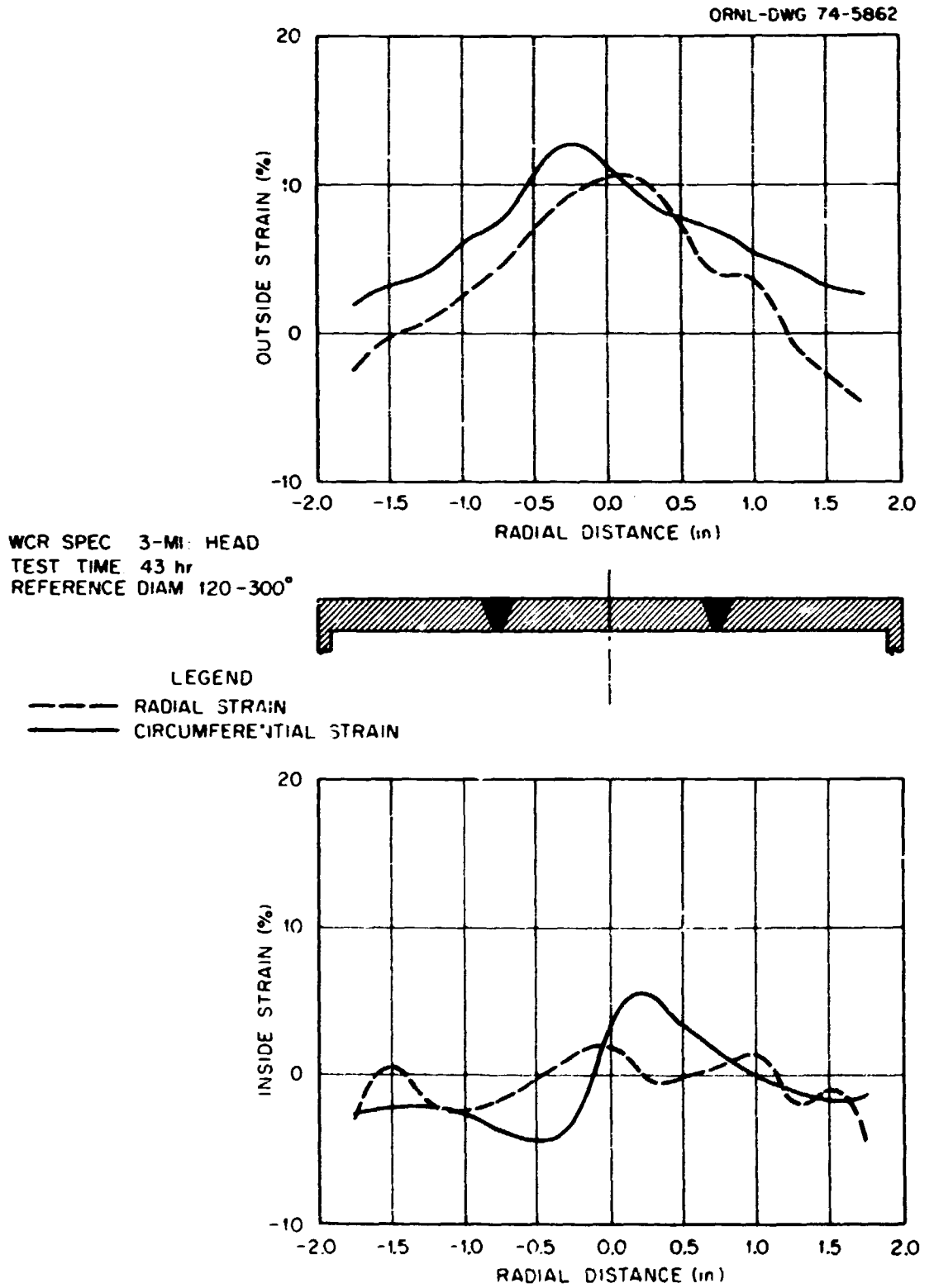

Fig. A4-c. Surface strain distribution on the head of specimen 3-M1 along the diameter, 120–300° (1 in. = 2.54 cm).

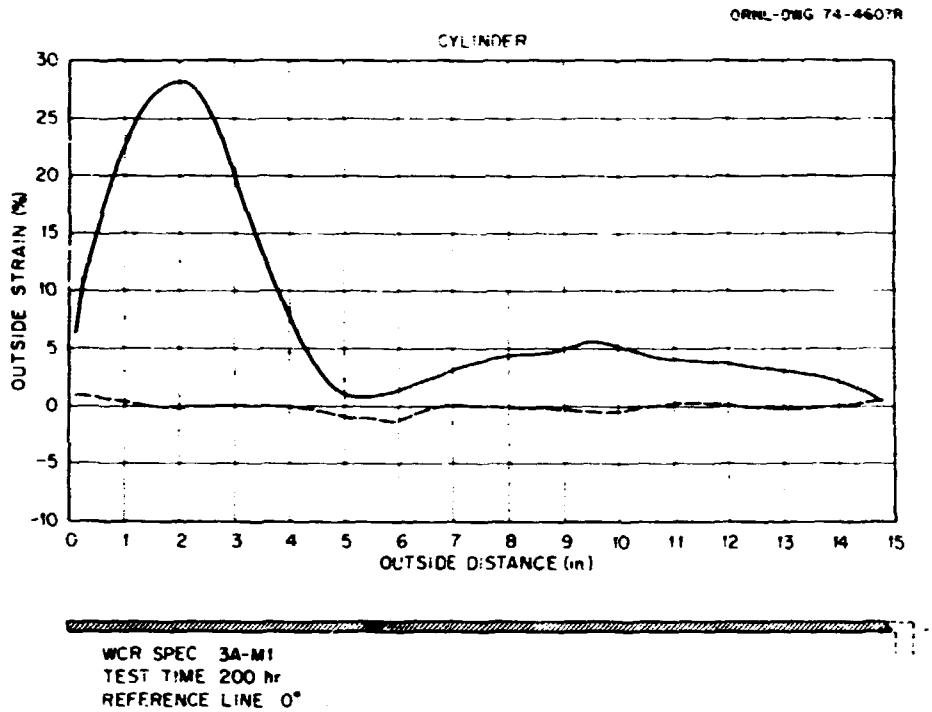

Fig. A5-a. Surface strain distribution for specimen 3A-M1 along the axial reference plane, $\theta = 0^{\circ}$, at 200 hr (1 in. = 2.54 cm).

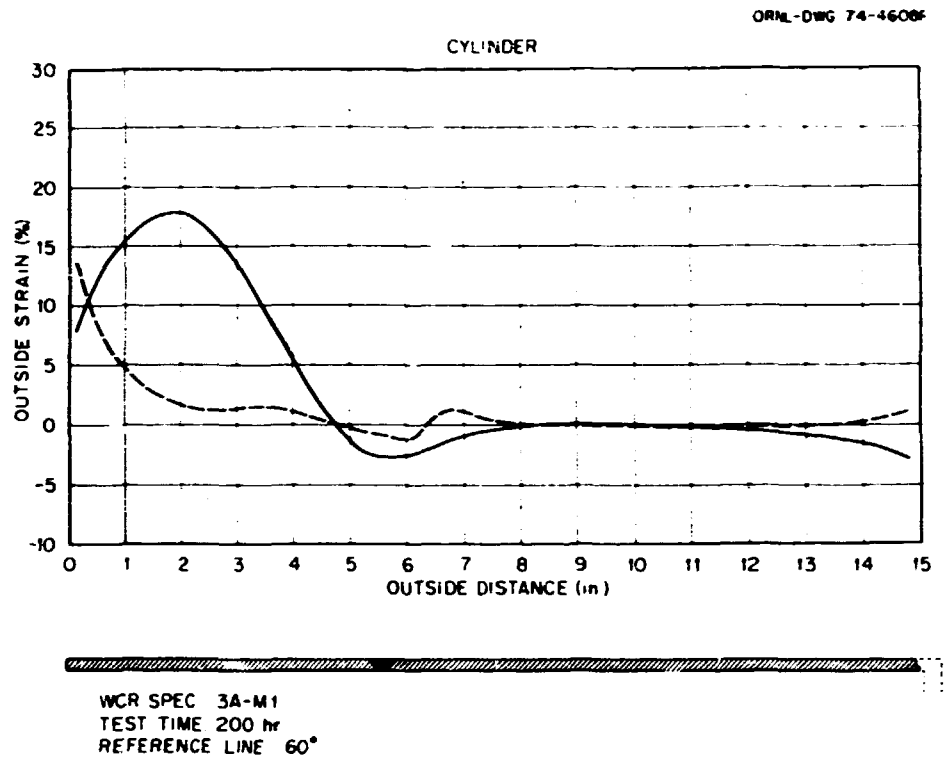

Fig. A5-b. Surface strain distribution for specimen 3A-M1 along the axial reference plane, $\theta = 60^{\circ}$, at 200 hr (1 in. = 2.54 cm).

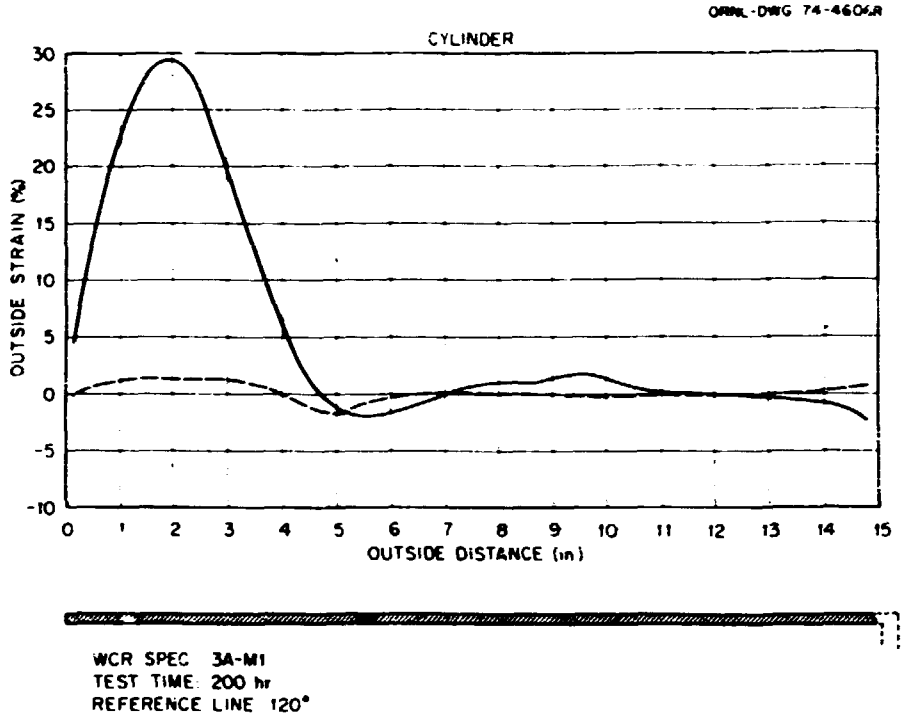

Fig. A5-c. Surface strain distribution for specimen 3A-M1 along the axial reference plane, θ = 120°, at 200 hr (1 in. = 2.54 cm).

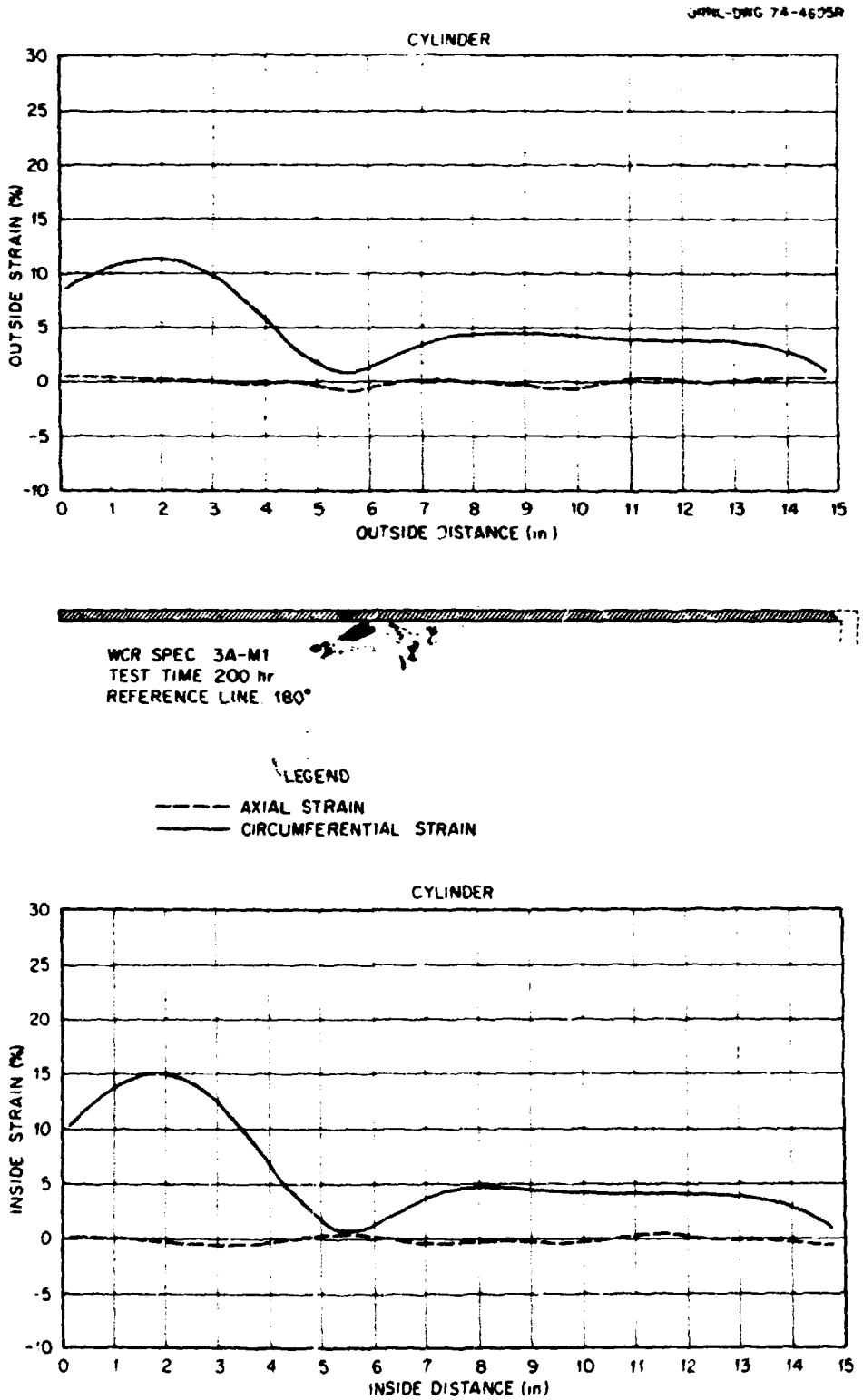

Fig. A5-d. Surface strain distribution for specimen 3A-M1 along the axial reference plane, θ = 180°, at 200 hr (1 in. = 2.54 cm).

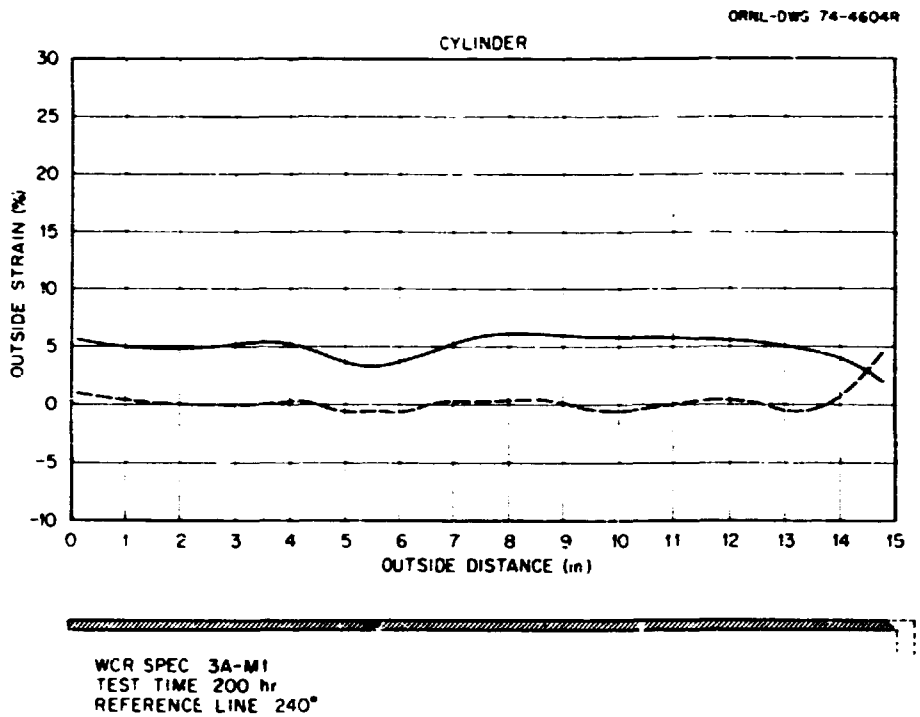

Fig. A5-e. Surface strain distribution for specimen 3A-M1 along the axial reference plane, $\theta = 240°$, at 200 hr (1 in. = 2.54 cm).

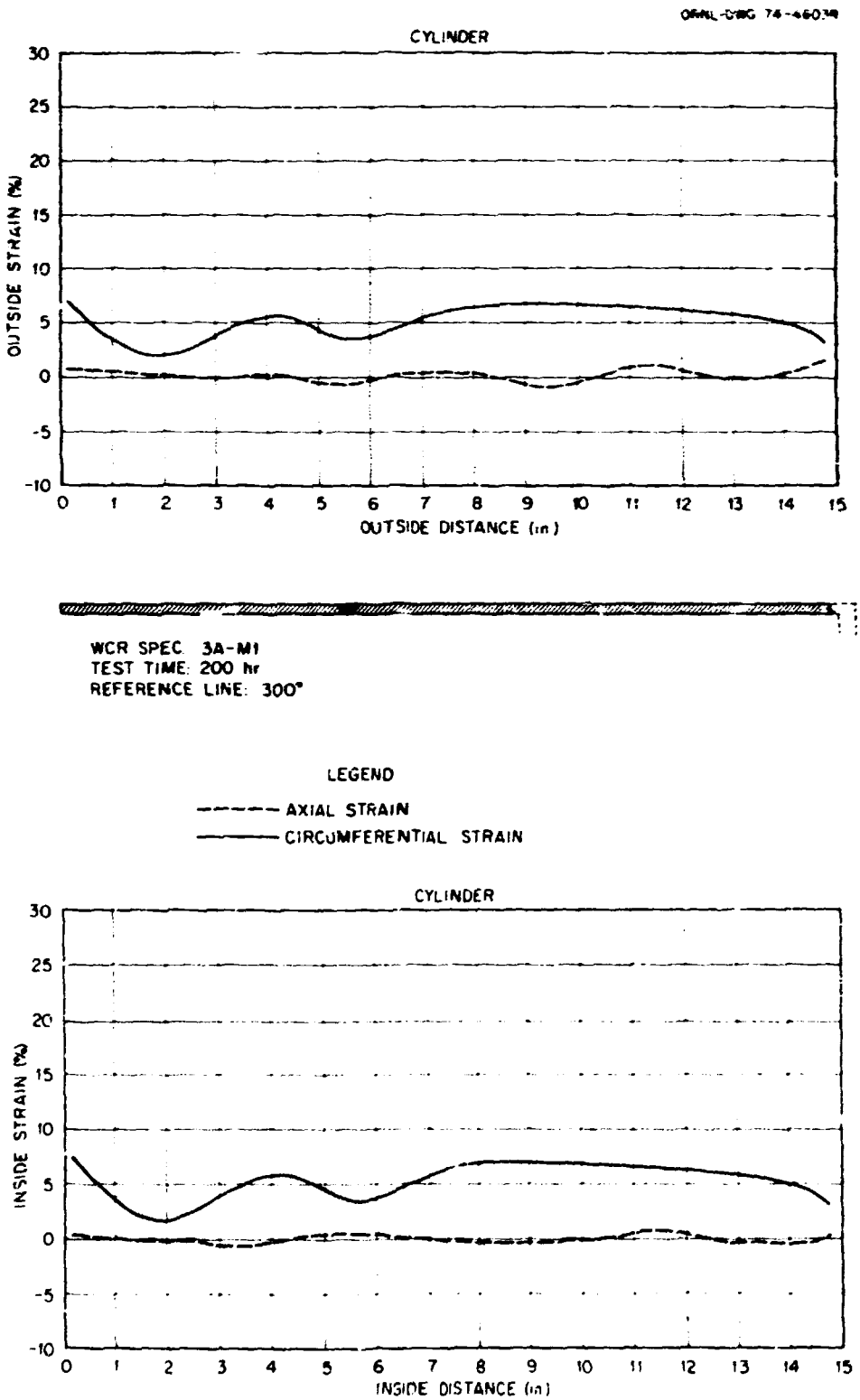

Fig. A5-f. Surface strain distribution for specimen 3A-M1 along the axial reference plane, θ = 300°, at 200 hr (1 in. = 2.54 cm).

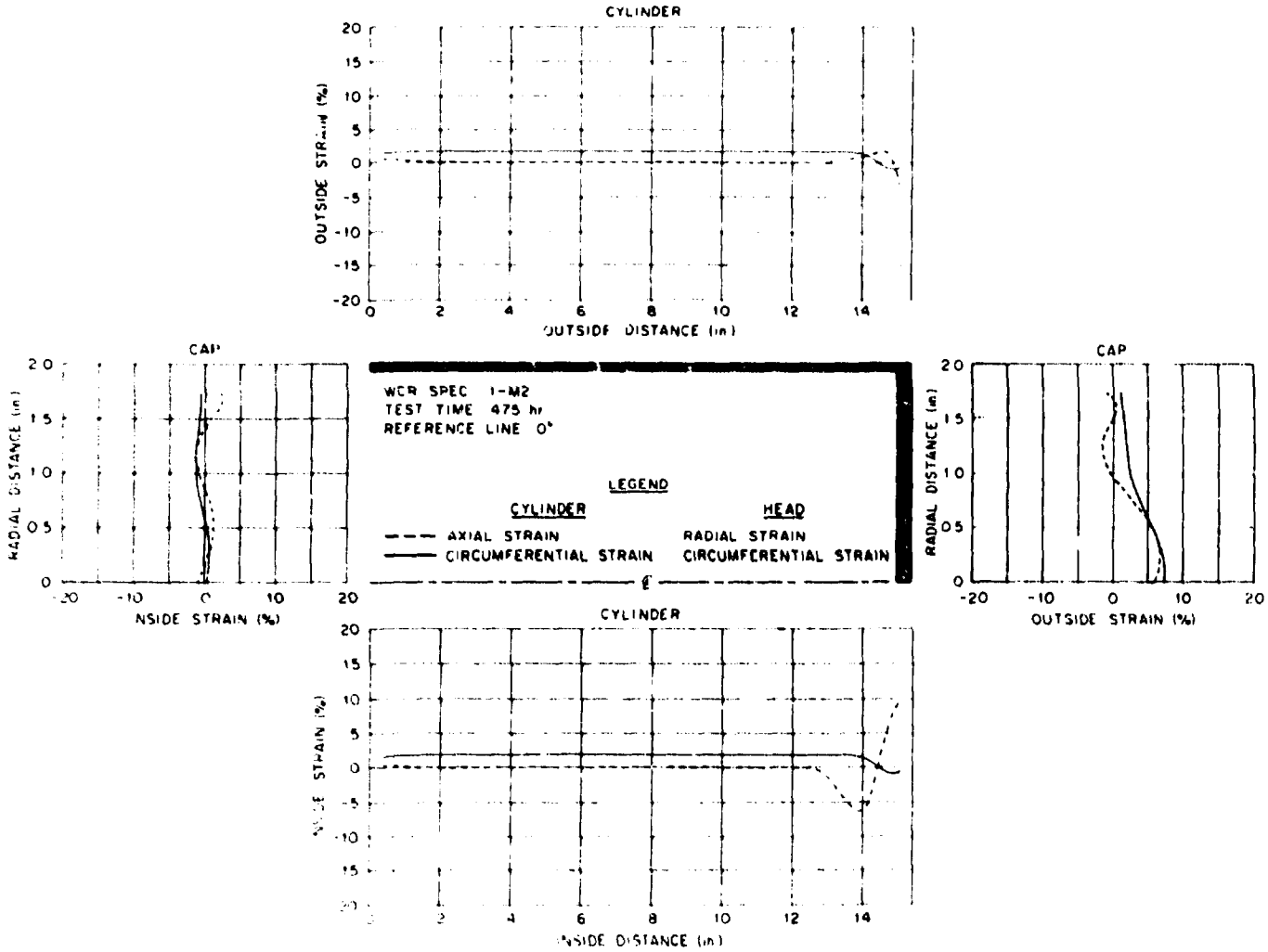

Fig. A6-a. Surface strain distribution for specimen 1-M2 along the axial reference plane, $\theta = 0°$, at 475 hr (1 in. = 2.54 cm).

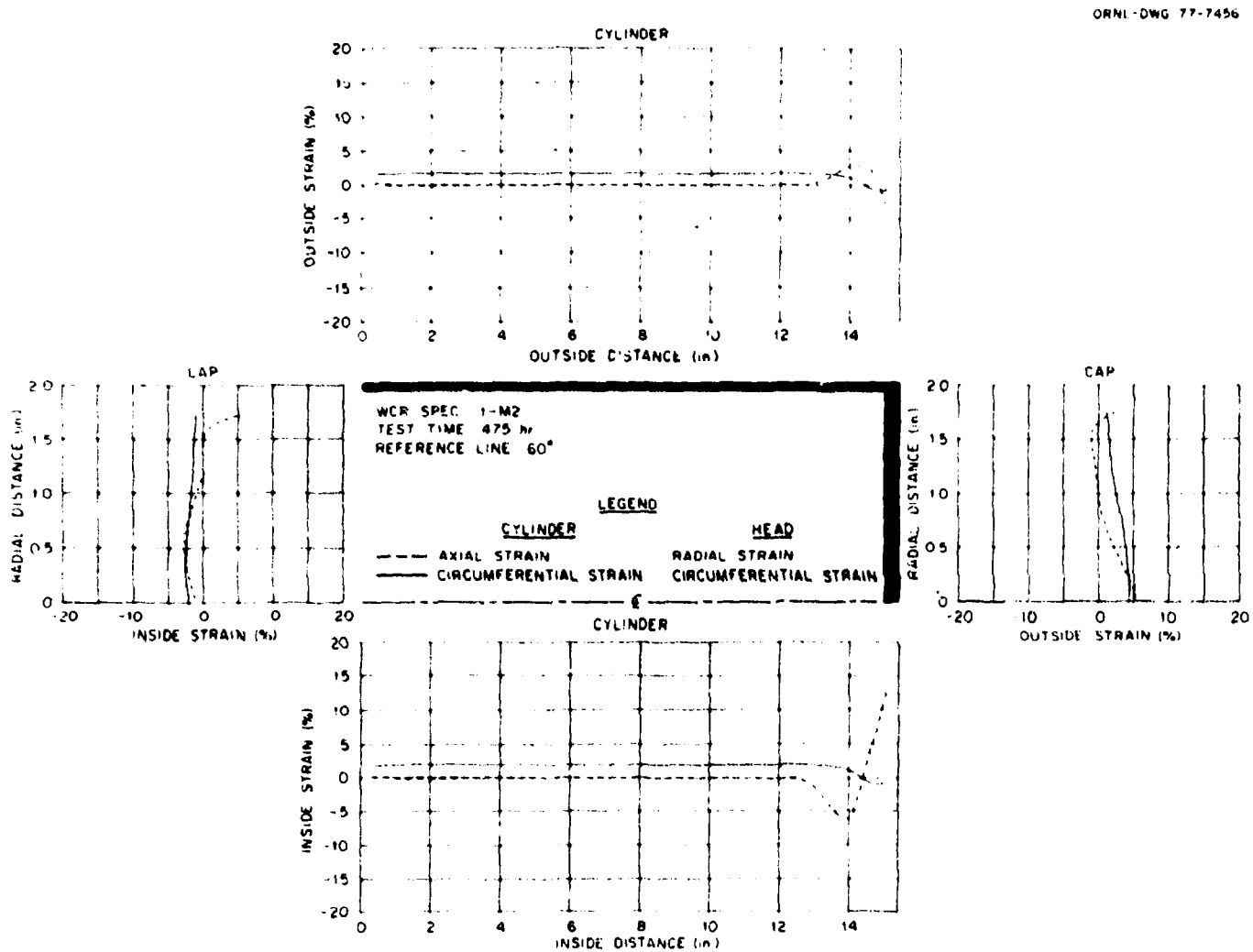

Fig. A6-b. Surface strain distribution for specimen 1-M2 along the axial reference plane, $\theta = 60°$, at 475 hr (1 in. = 2.54 cm).

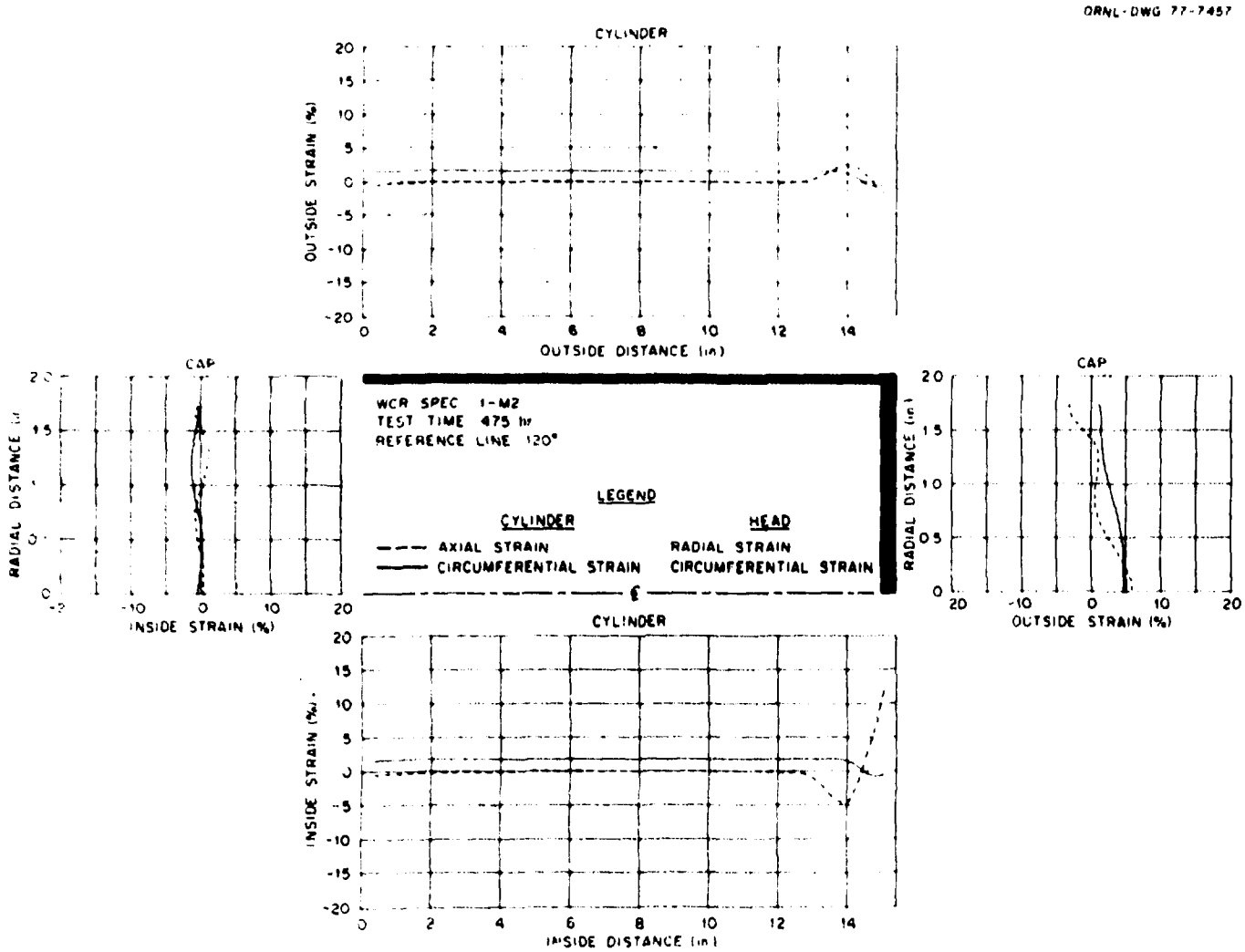

Fig. A6-c. Surface strain distribution for specimen 1-M2 along the axial reference plane, θ = 120°, at 475 hr (1 in. = 2.54 cm).

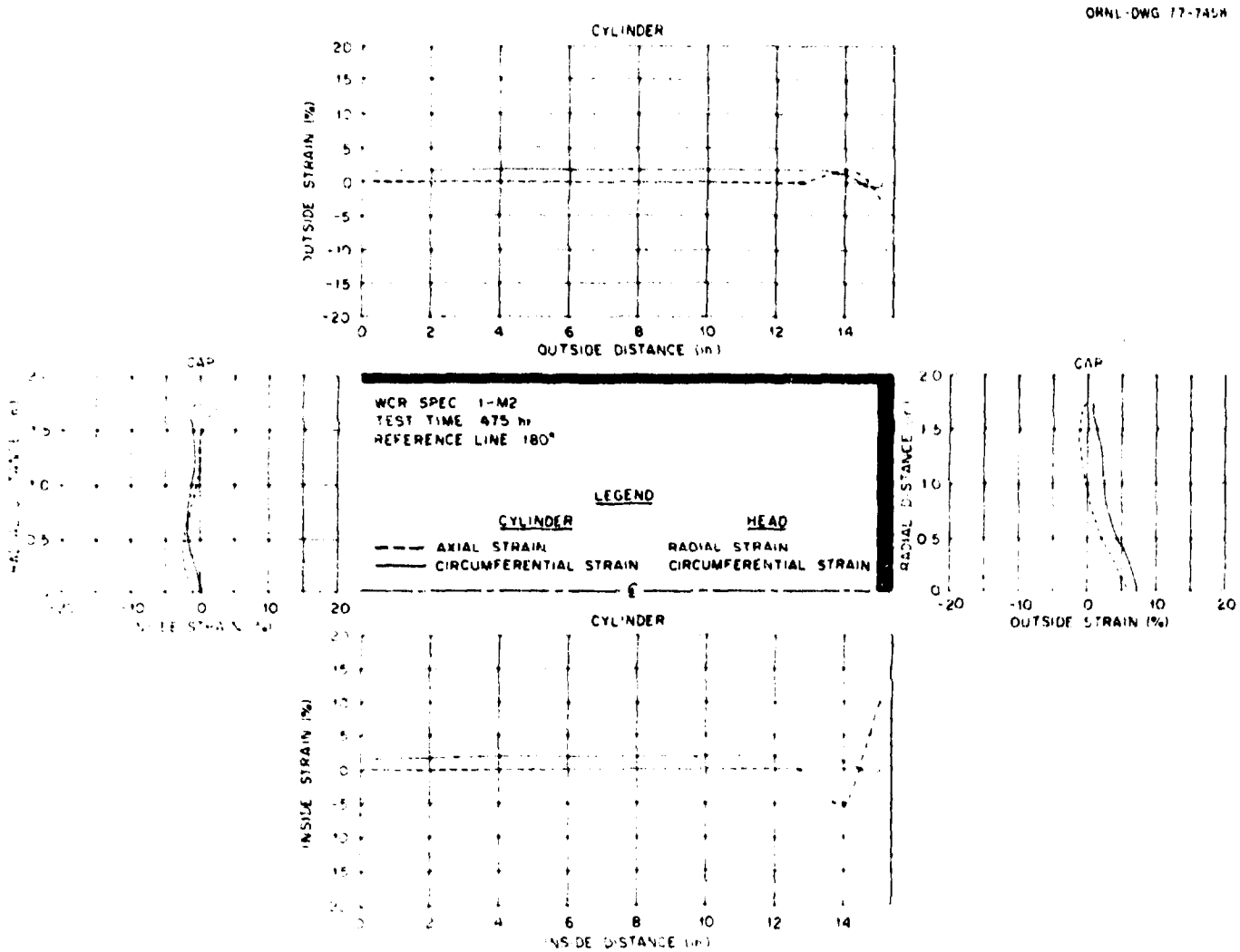

Fig. A6-d. Surface strain distribution for specimen 1-M2 along the axial reference plane, $\theta = 180°$, at 475 hr (1 in. = 2.54 cm).

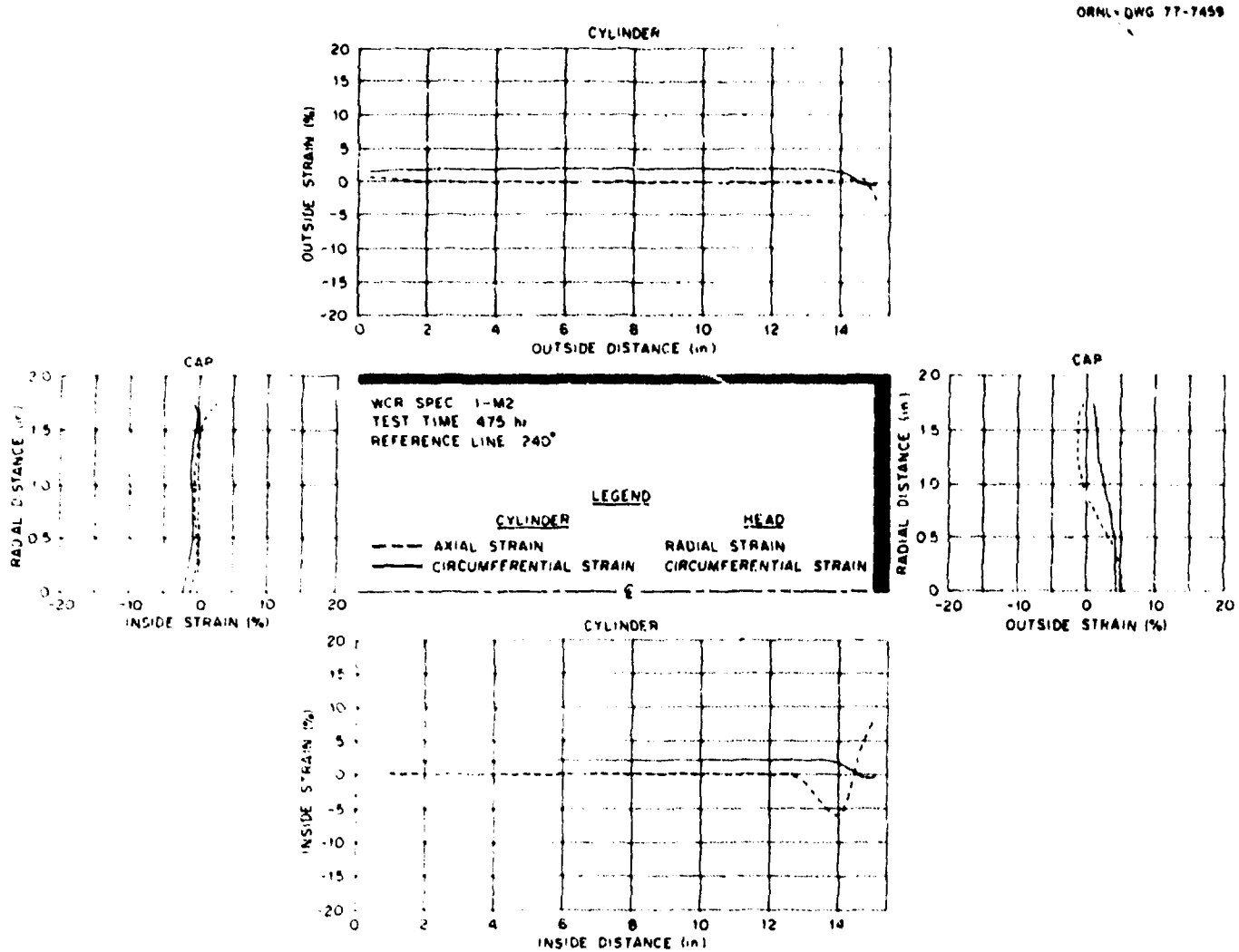

Fig. A6-e. Surface strain distribution for specimen 1-M2 along the axial reference plane, $\theta = 240°$, at 475 hr (1 in. = 2.54 cm).

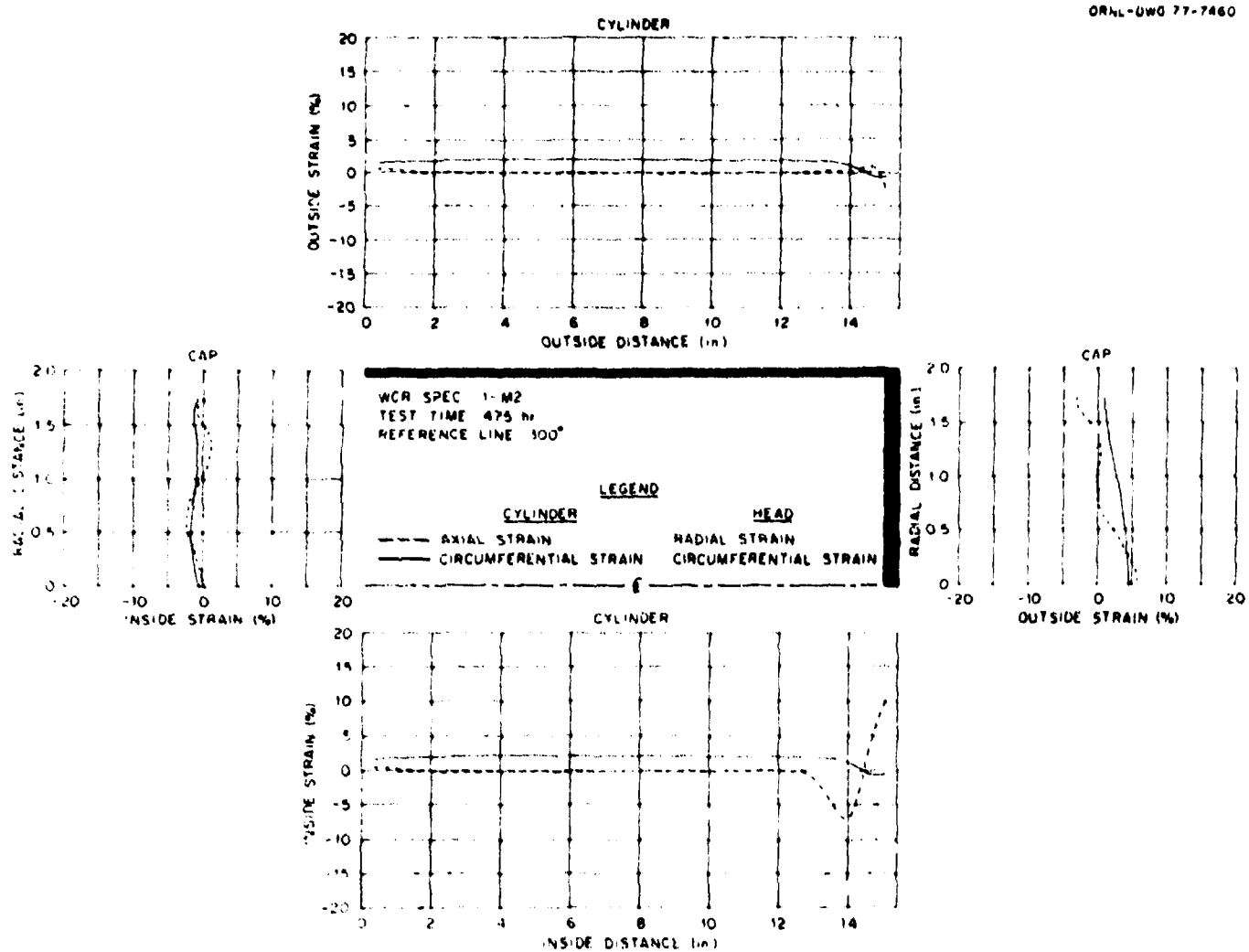

Fig. A6-f. Surface strain distribution for specimen 1-M2 along the axial reference plane, $\theta = 300°$, at 475 hr (1 in. = 2.54 cm).

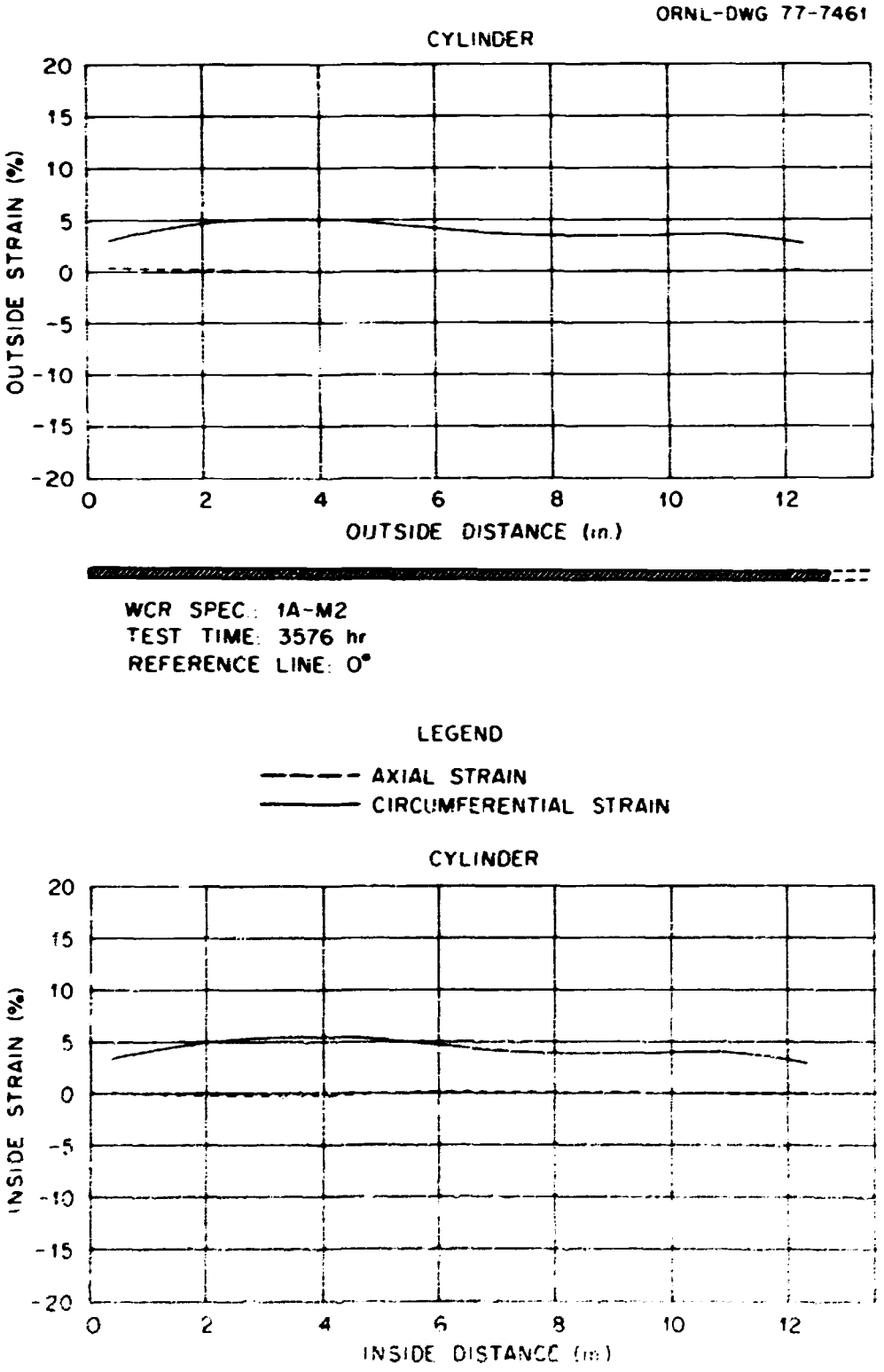

Fig. A7-a. Surface strain distribution for specimen 1A-M2 along the axial reference plane, $\theta = 0°$, at 3576 hr (1 in. = 2.54 cm).

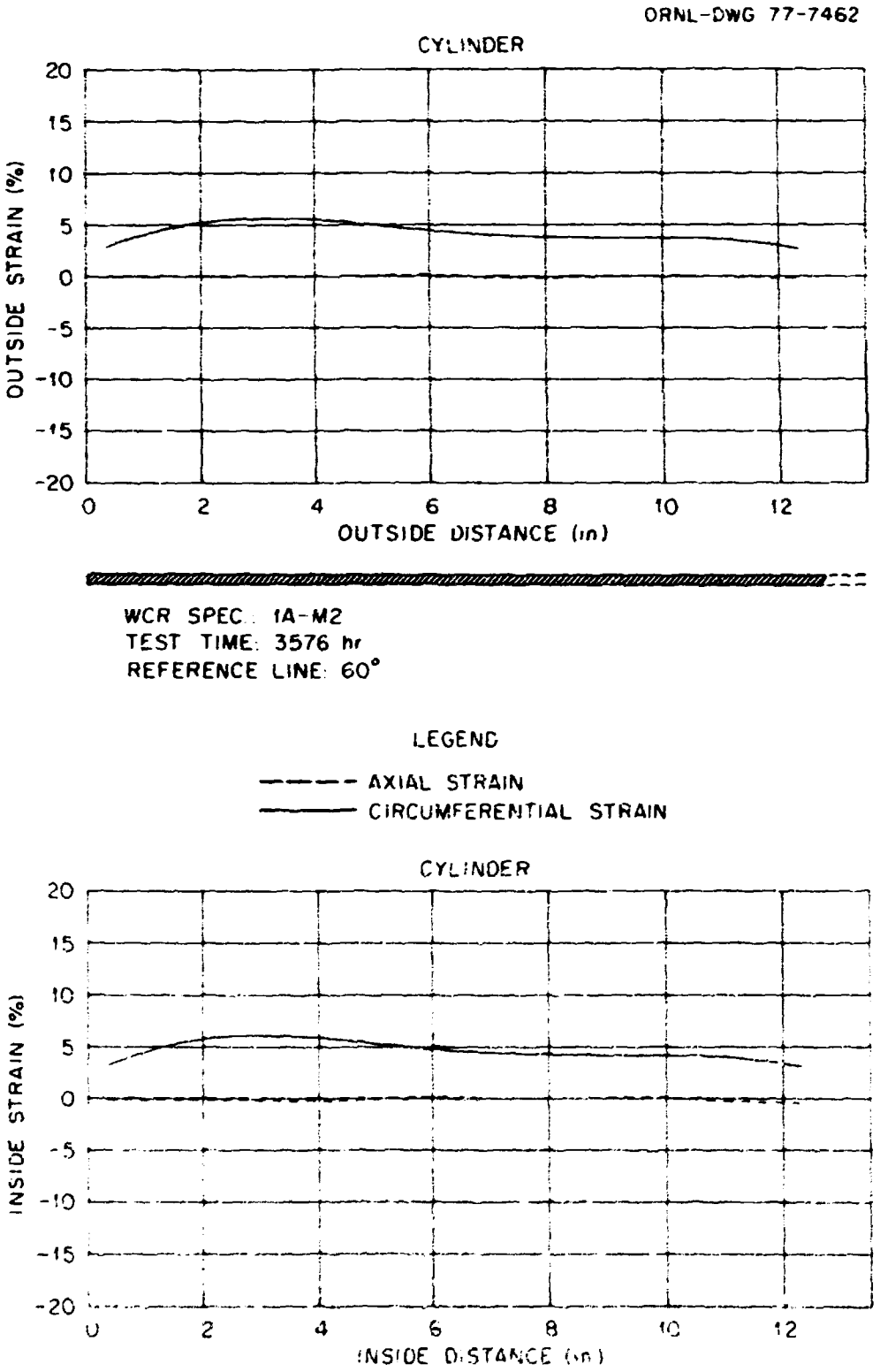

Fig. A7-b. Surface strain distribution for specimen 1A-M2 along the axial reference plane, $\theta = 60°$, at 3576 hr (1 in. = 2.54 cm).

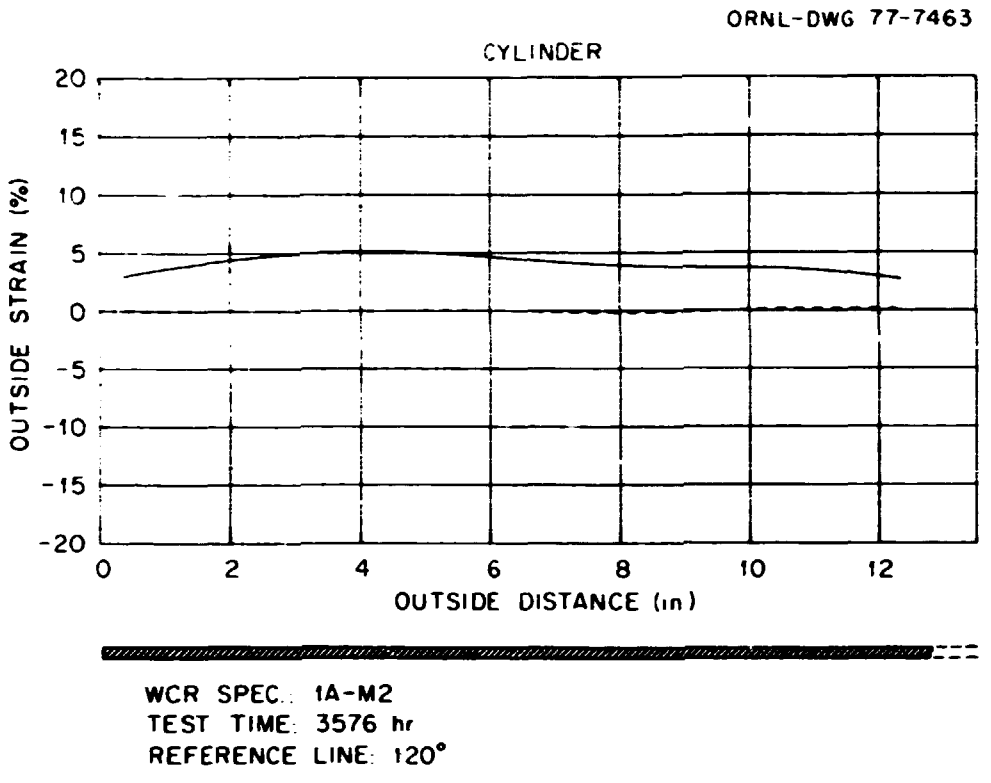

Fig. A7-c. Surface strain distribution for specimen 1A-M2 along the axial reference plane, $\theta = 120^{\circ}$, at 3576 hr (1 in. = 2.54 cm).

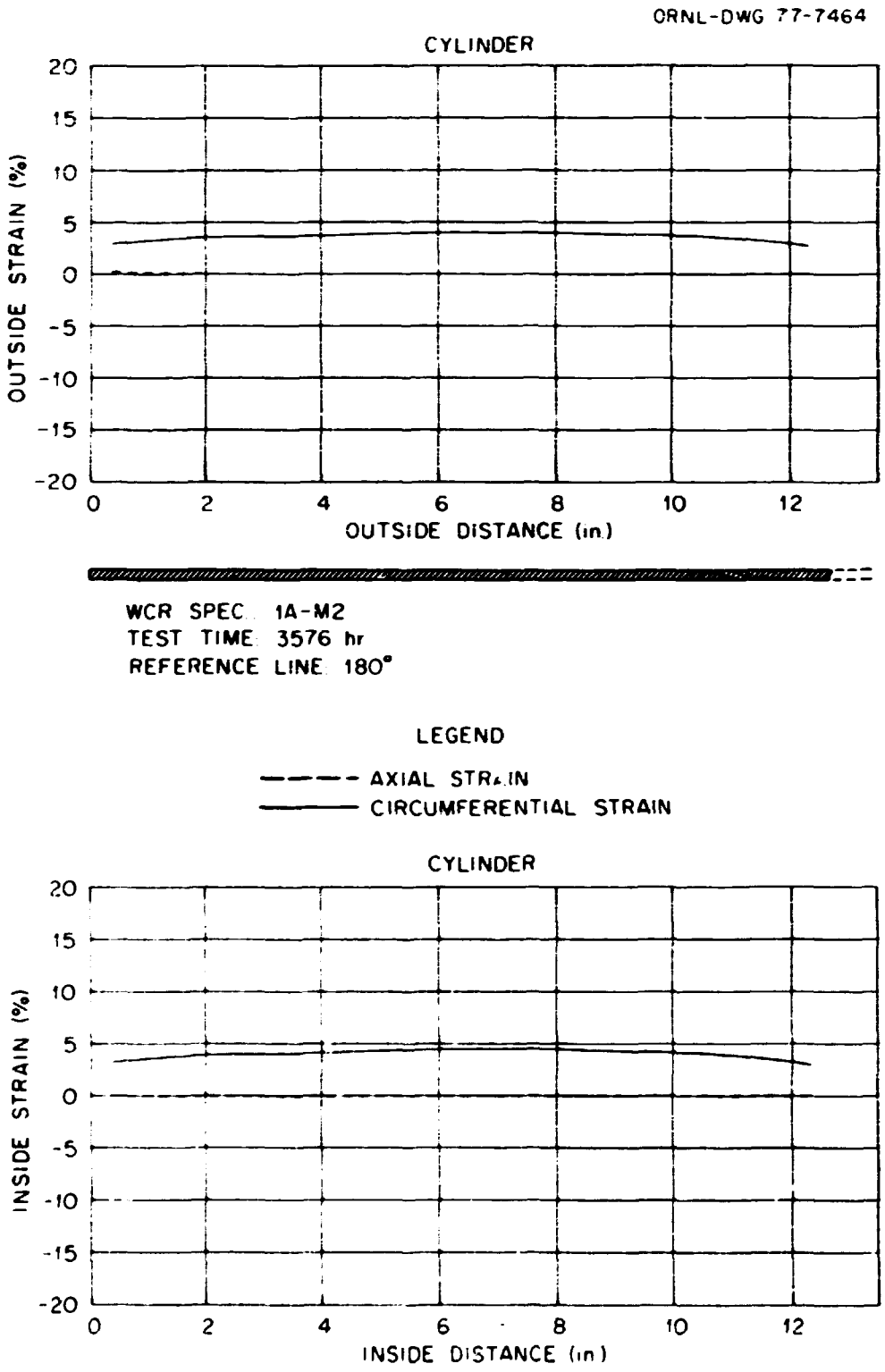

Fig. A7-d. Surface strain distribution for specimen 1A-M2 along the axial reference plane, $\theta = 180°$, at 3576 hr (1 in. = 2.54 cm).

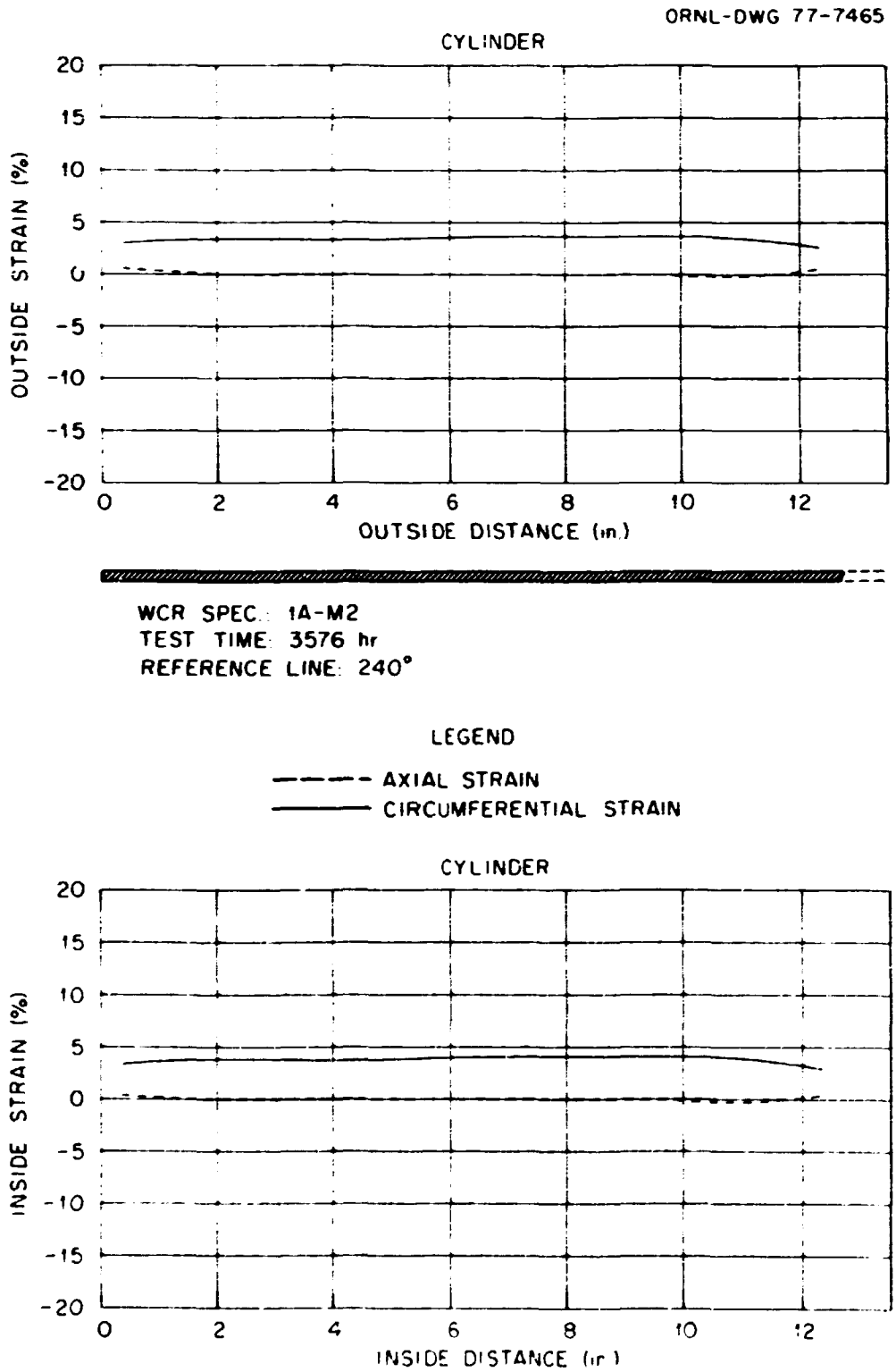

Fig. A7-e. Surface strain distribution for specimen 1A-M2 along the axial reference plane, θ = 240°, at 3576 hr (1 in. = 2.54 cm).

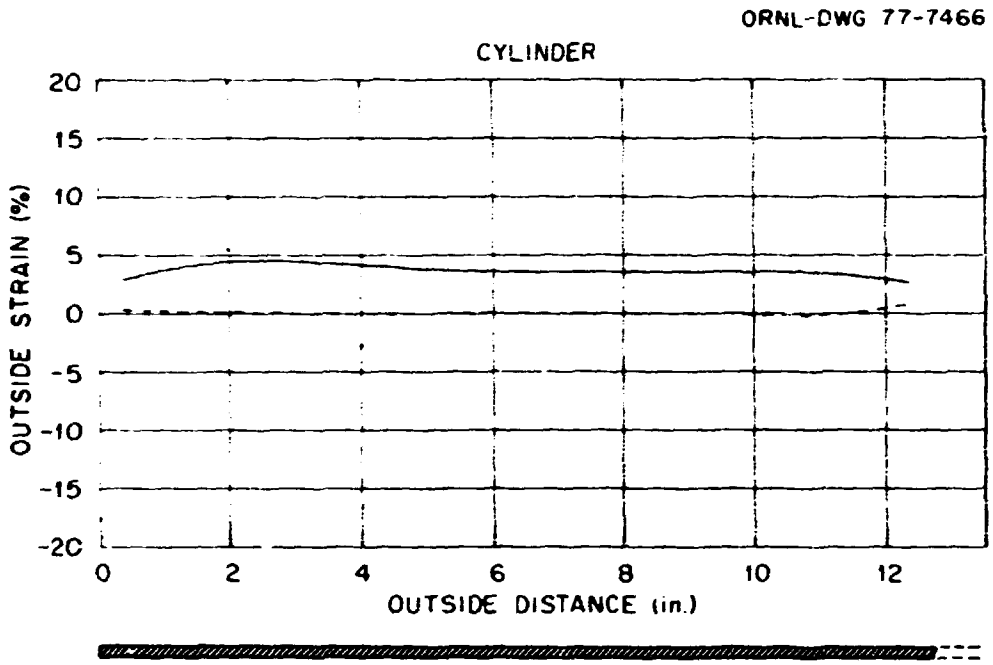

Fig. A7-f. Surface strain distribution for specimen 1A-M2 along the axial reference plane, $\theta = 300°$, at 3576 hr (1 in. = 2.54 cm).

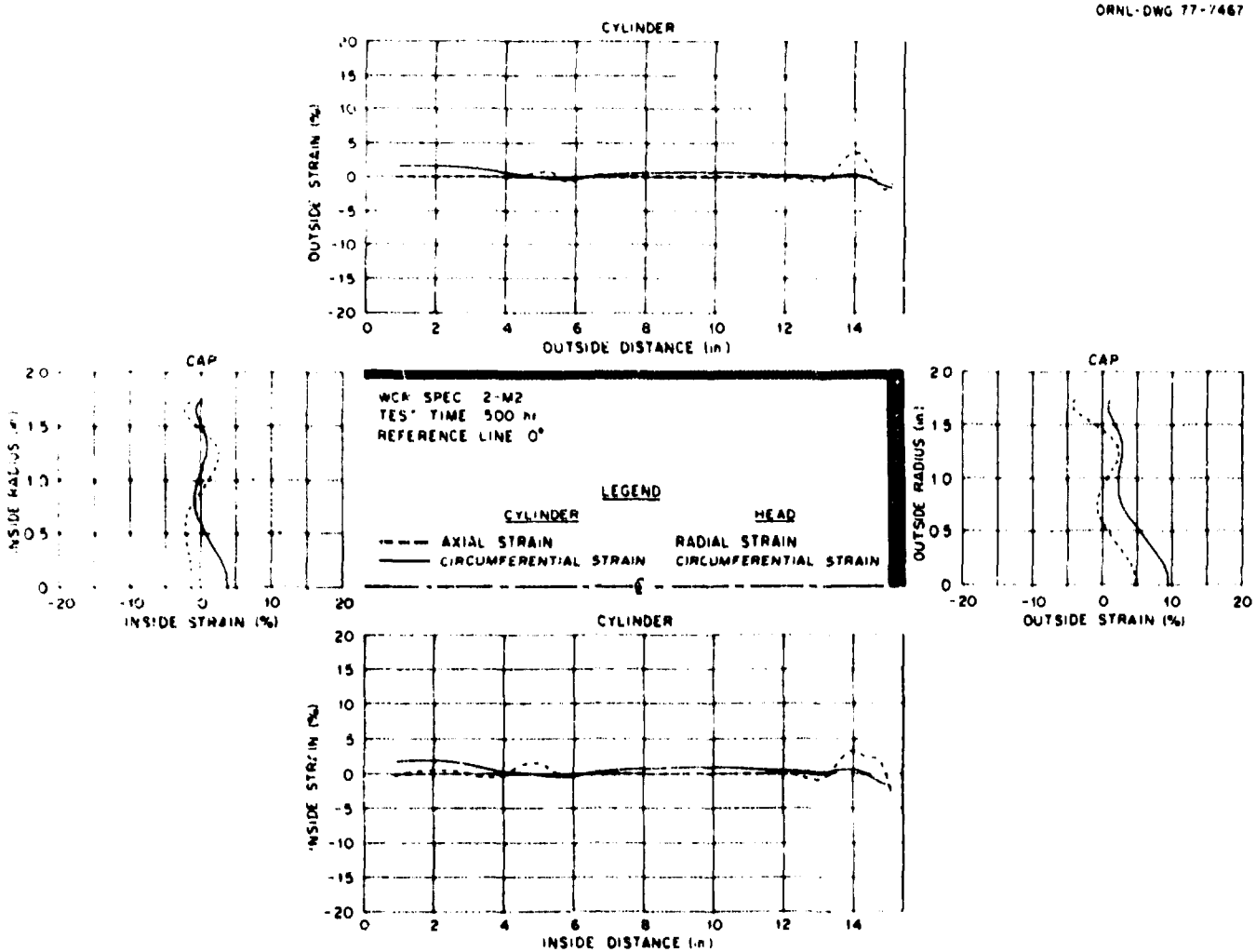

Fig. A8-a. Surface strain distribution for specimen 2-M2 along the axial reference plane, $\theta = 0°$, at 500 hr (1 in. = 2.54 cm).

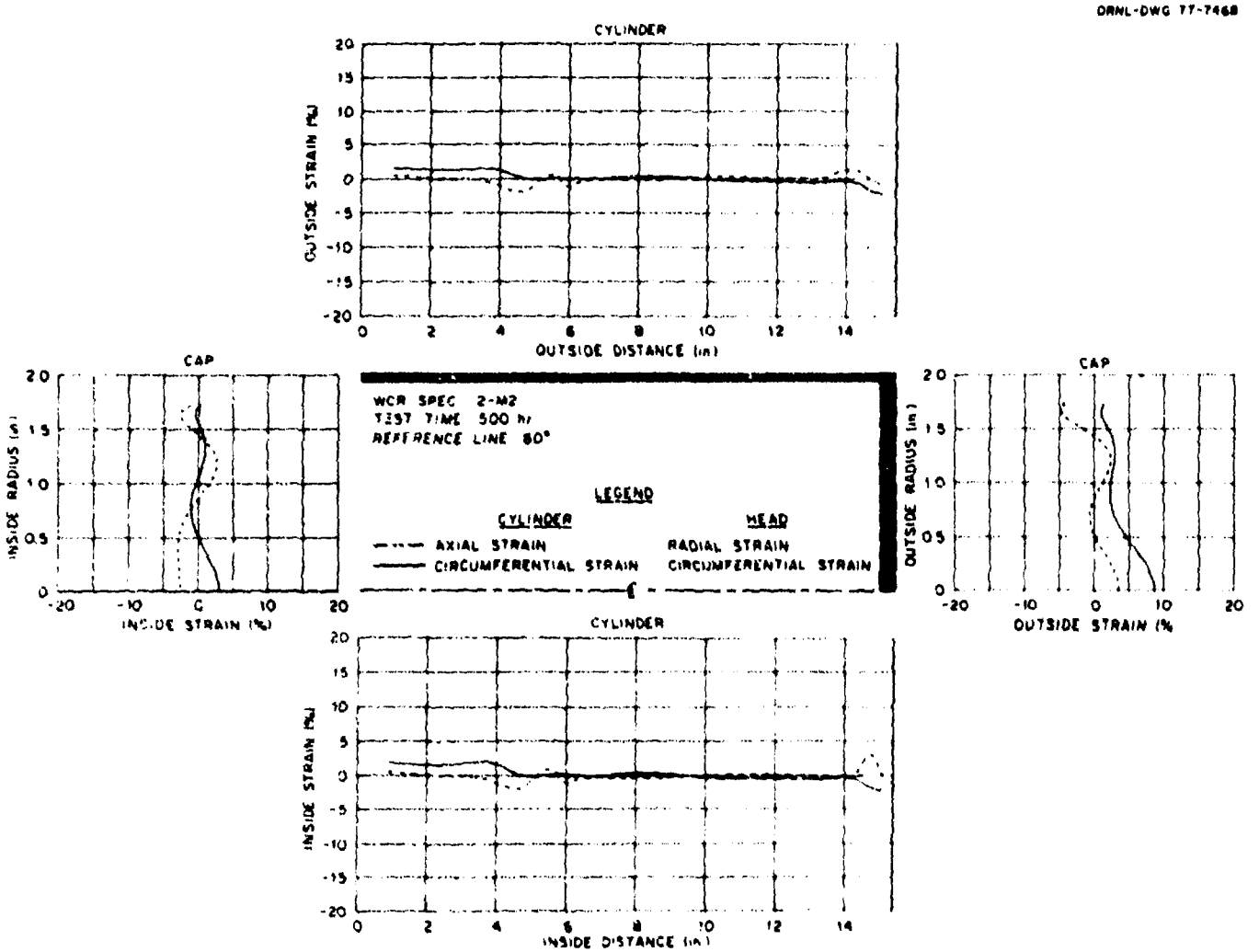

Fig. A8-b. Surface strain distribution for specimen 2-M2 along the axial reference plane, $\theta = 60°$, at 500 hr (1 in. = 2.54 cm).

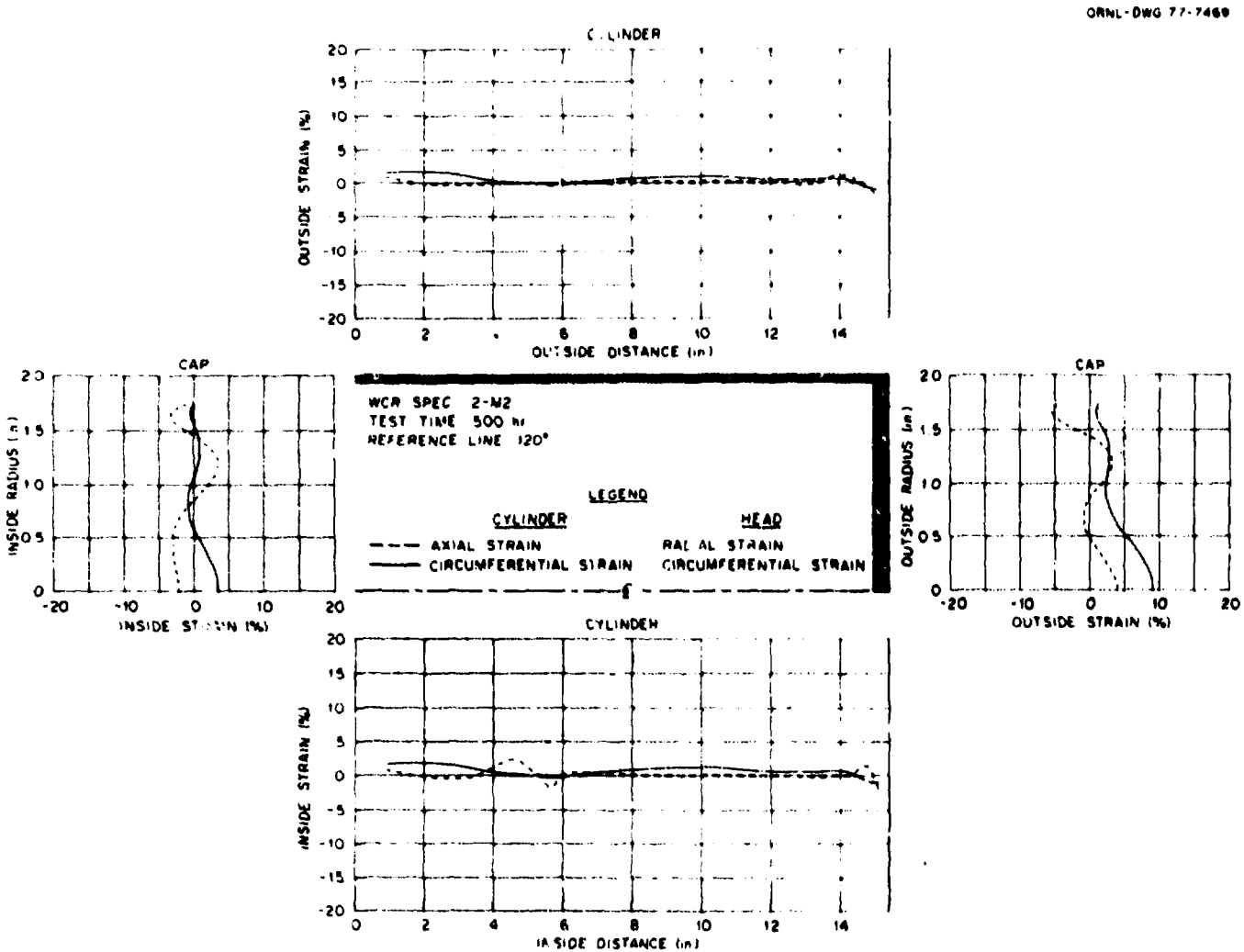

Fig. A8-c. Surface strain distribution for specimen 2-M2 along the axial reference plane, $\theta = 120^{\circ}$, at 500 hr (1 in. = 2.54 cm).

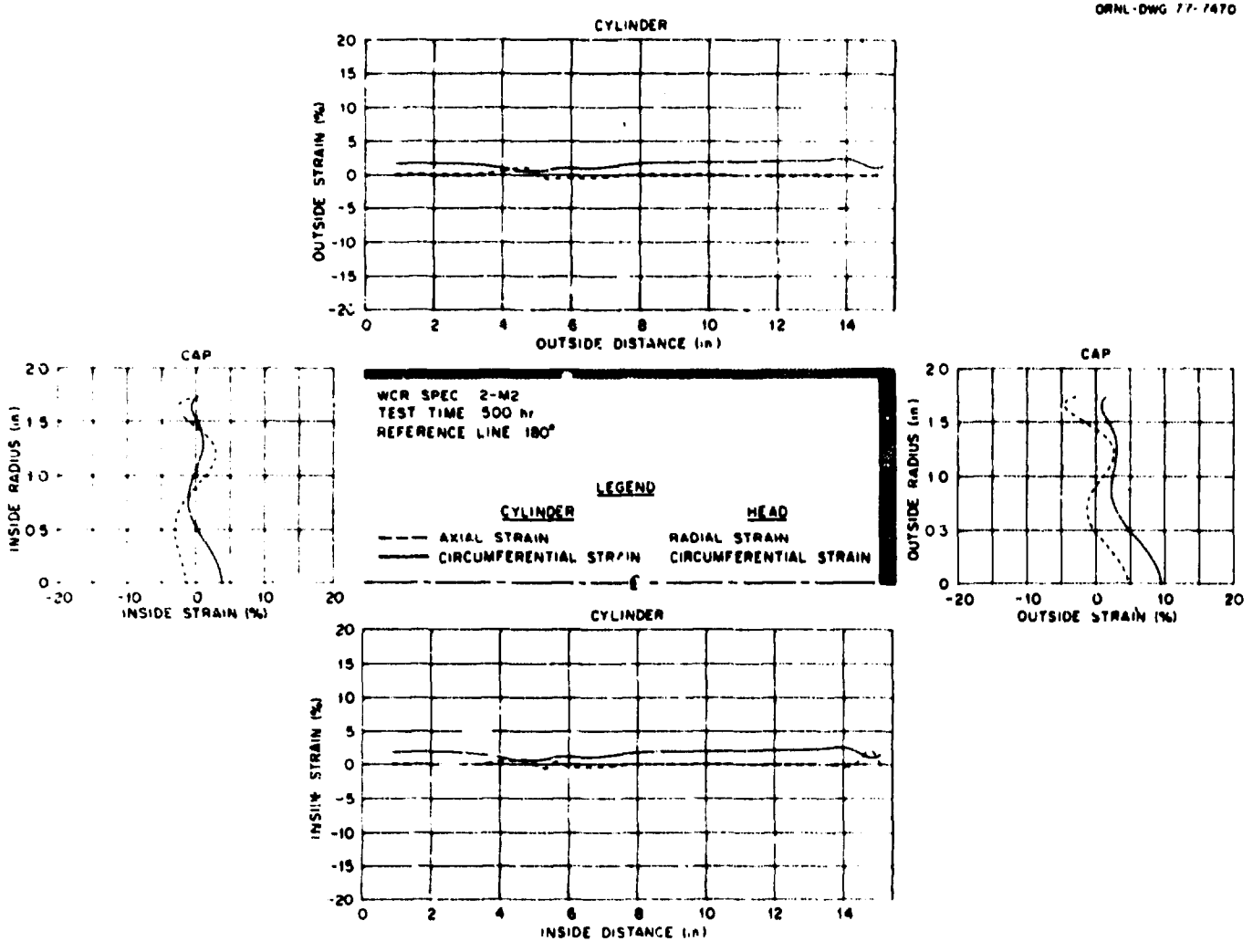

Fig. A8-d. Surface strain distribution for specimen 2-M2 along the axial reference plane, $\theta = 180^{\circ}$, at 500 hr (1 in. = 2.54 cm).

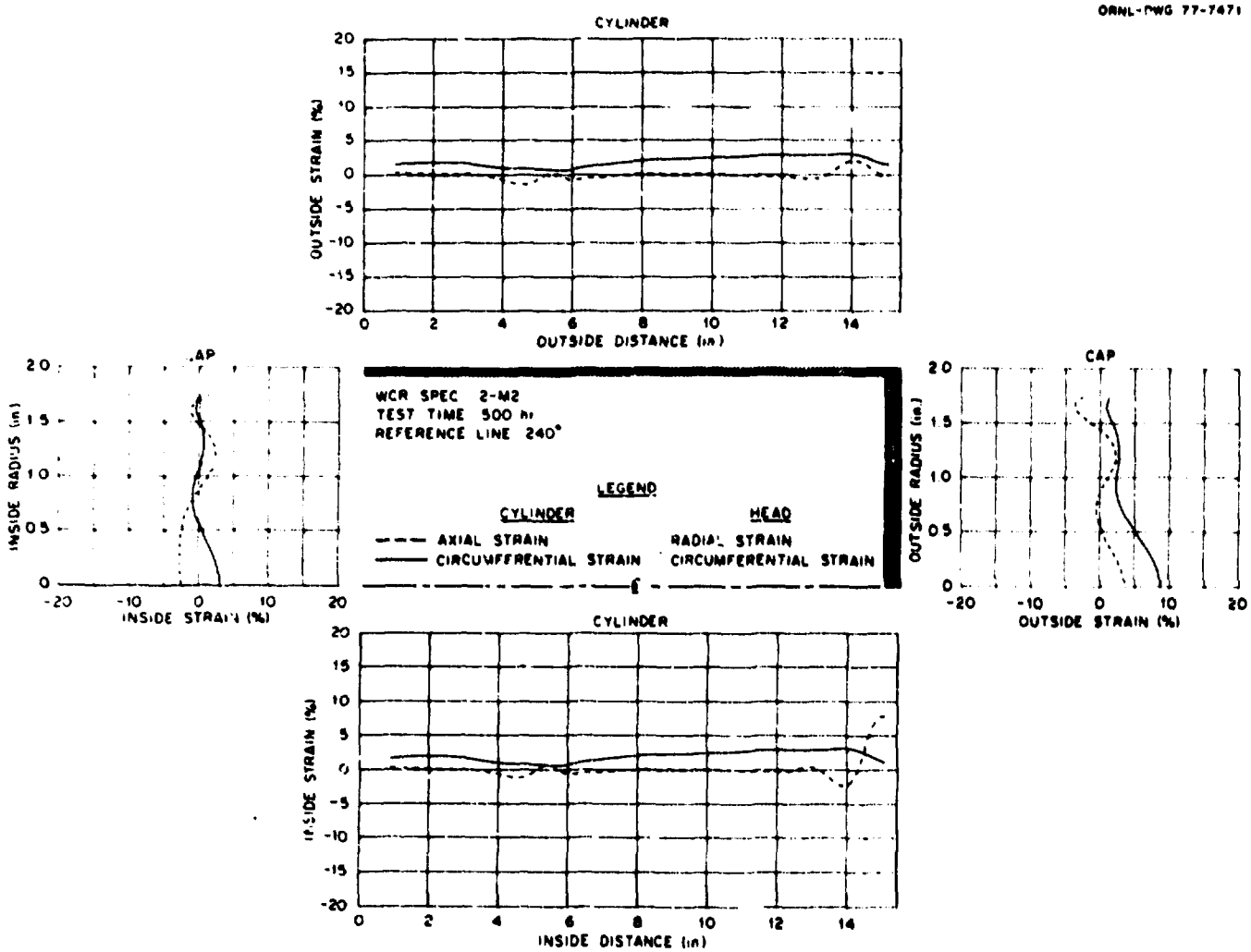

Fig. A8-e. Surface strain distribution for specimen 2-M2 along the axial reference plane, θ = 240°, at 500 hr (1 in. = 2.54 cm).

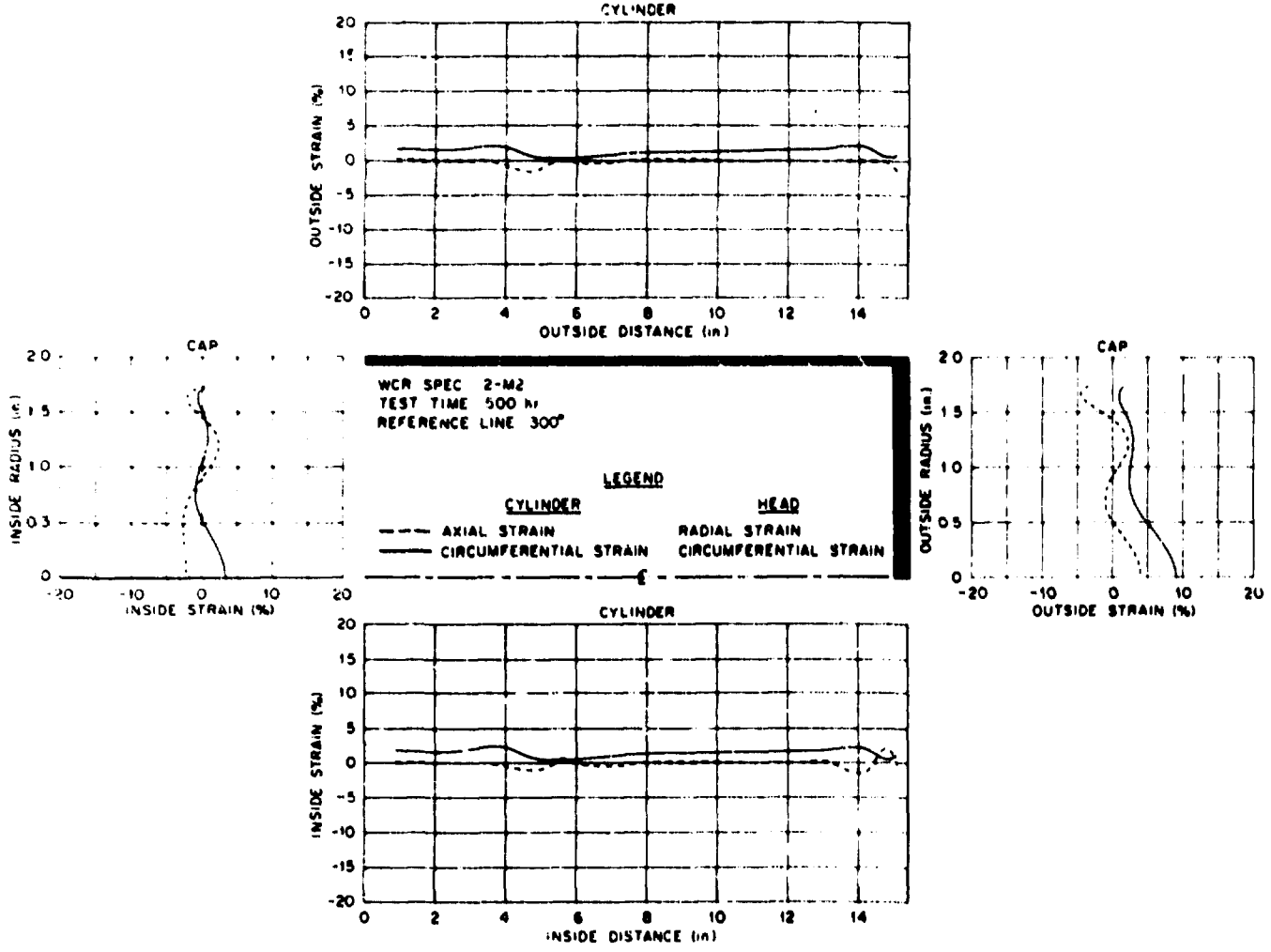

Fig. A8-f. Surface strain distribution for specimen 2-M2 along the axial reference plane, $\theta = 300°$, at 500 hr (1 in. = 2.54 cm).

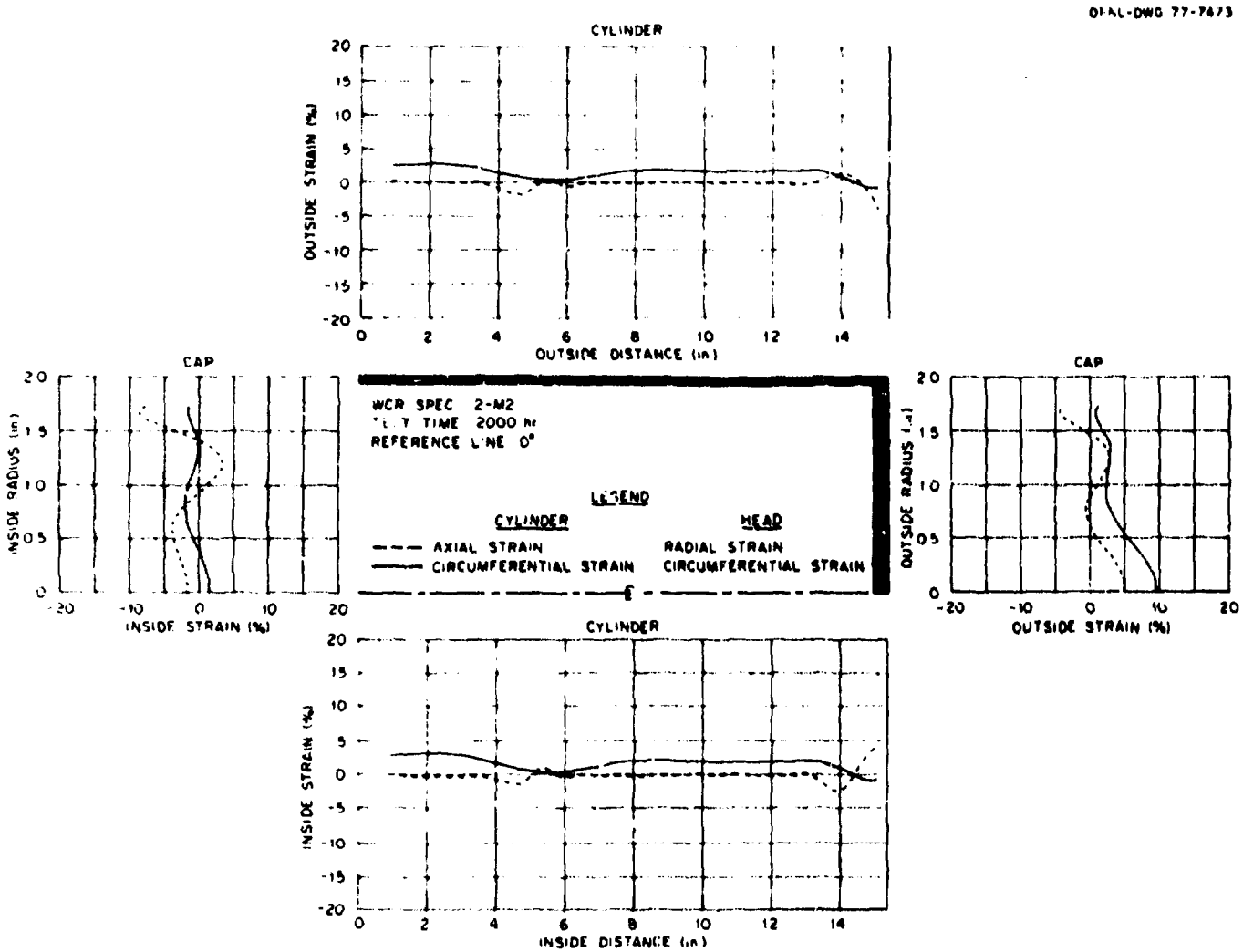

Fig. A9-a. Surface strain distribution for specimen 2-M2 along the axial reference plane, $\theta = 0°$, at 2000 hr (1 in. = 2.54 cm).

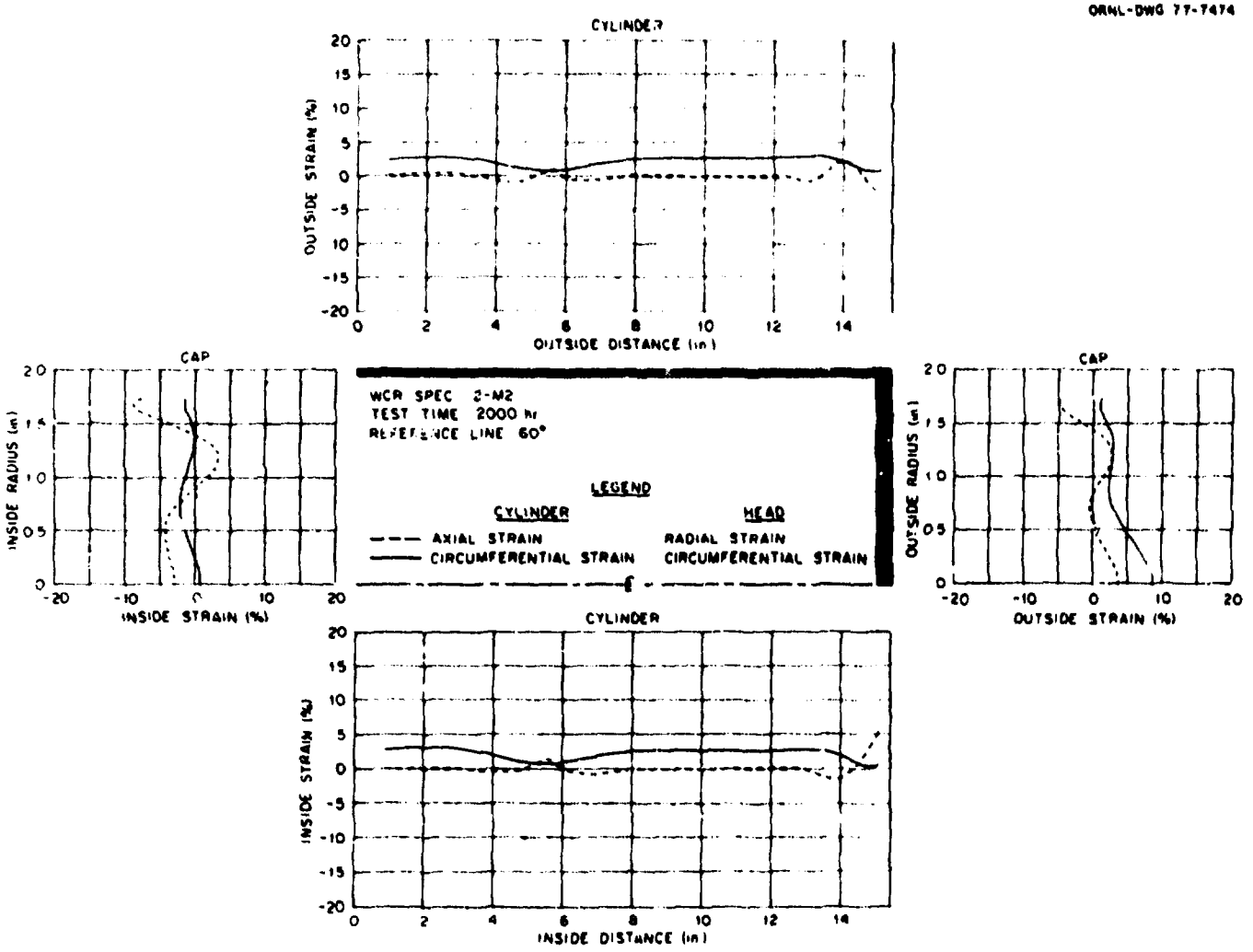

Fig. A9-b. Surface strain distribution for specimen 2-M2 along the axial reference plane, $\theta = 60°$, at 2000 hr (1 in. = 2.54 cm).

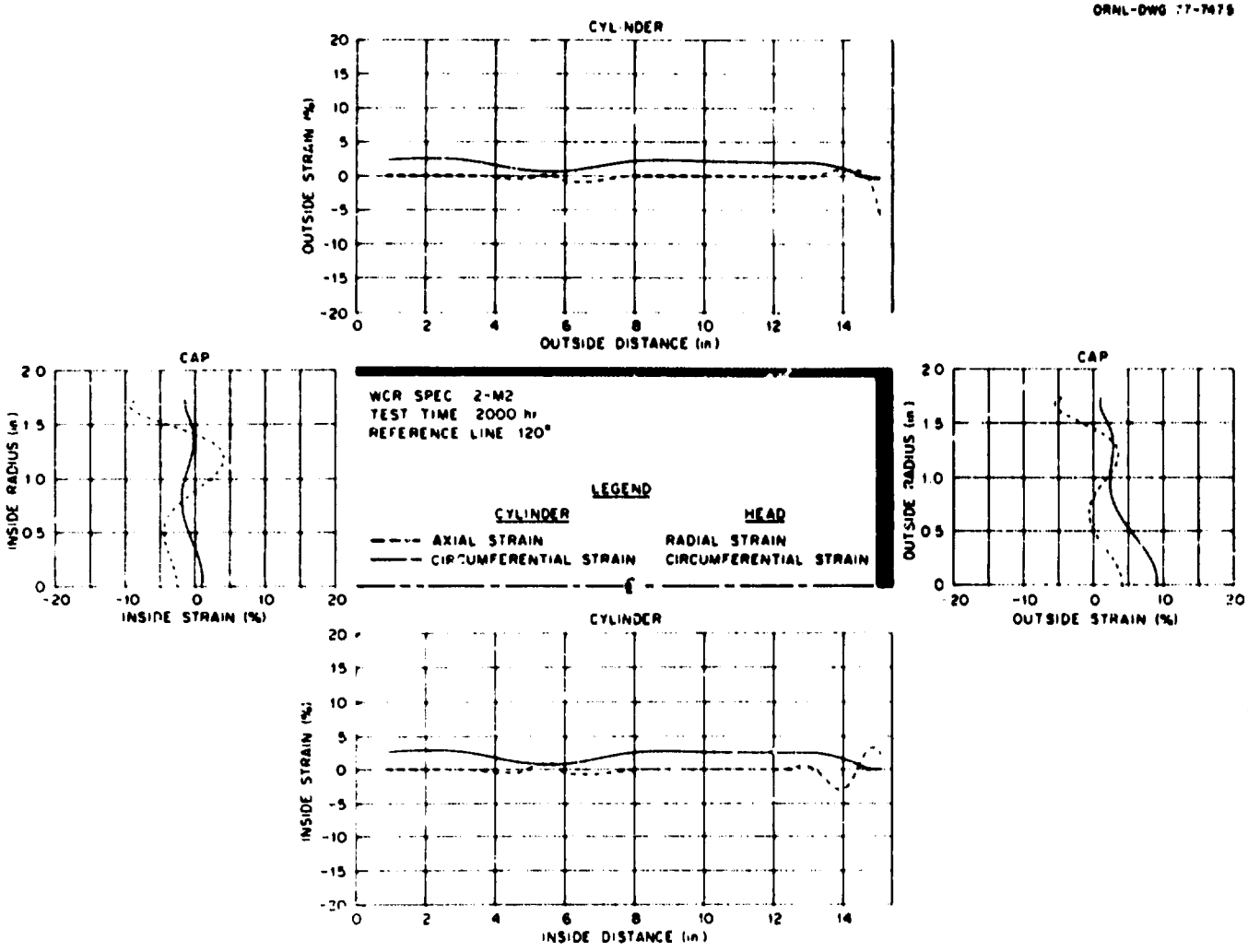

Fig. A9-c. Surface strain distribution for specimen 2-M2 along the axial reference plane, θ = 120°, at 2000 hr (1 in. = 2.54 cm).

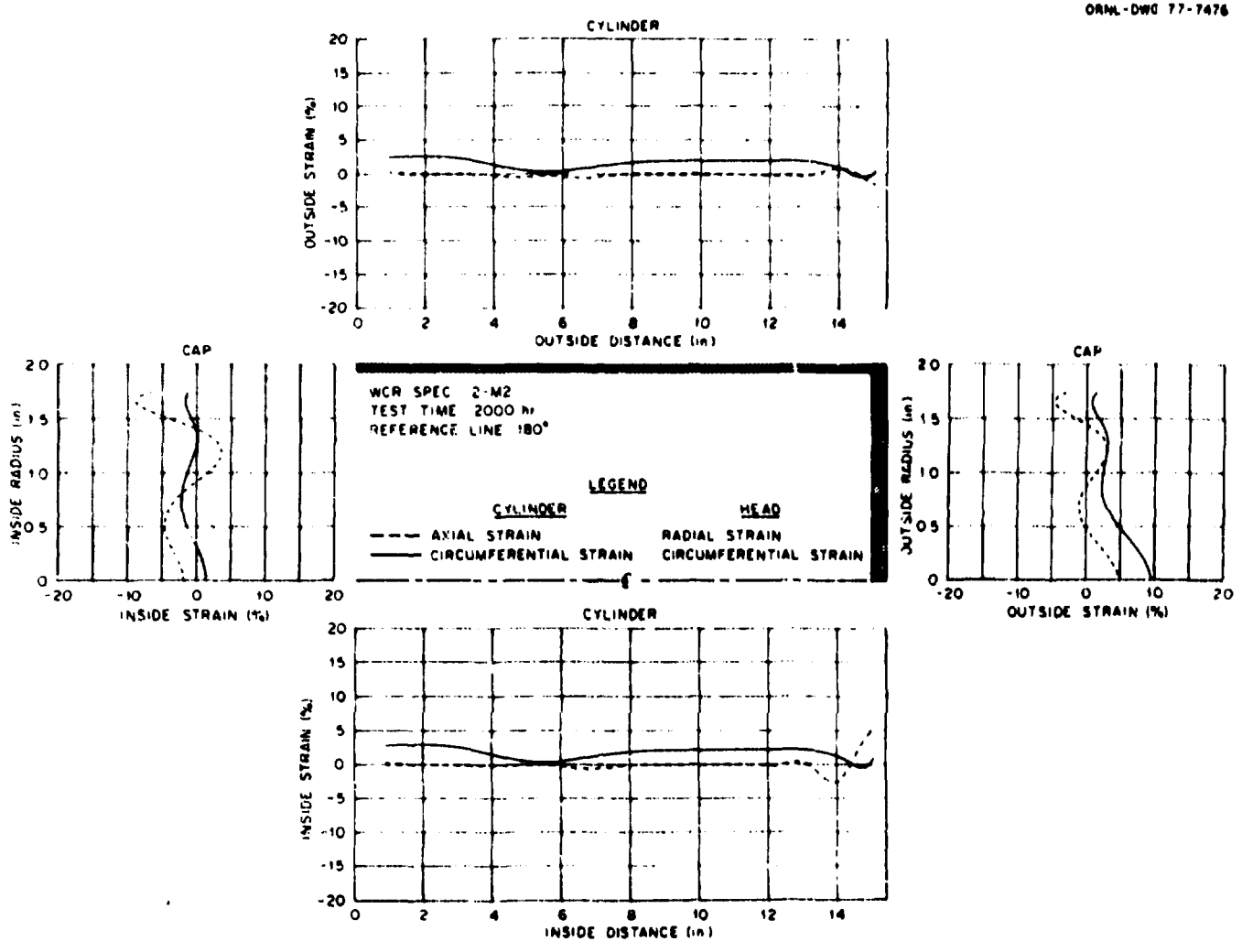

Fig. A9-d. Surface strain distribution for specimen 2-M2 along the axial reference plane, θ = 180°, at 2000 hr (1 in. = 2.54 cm).

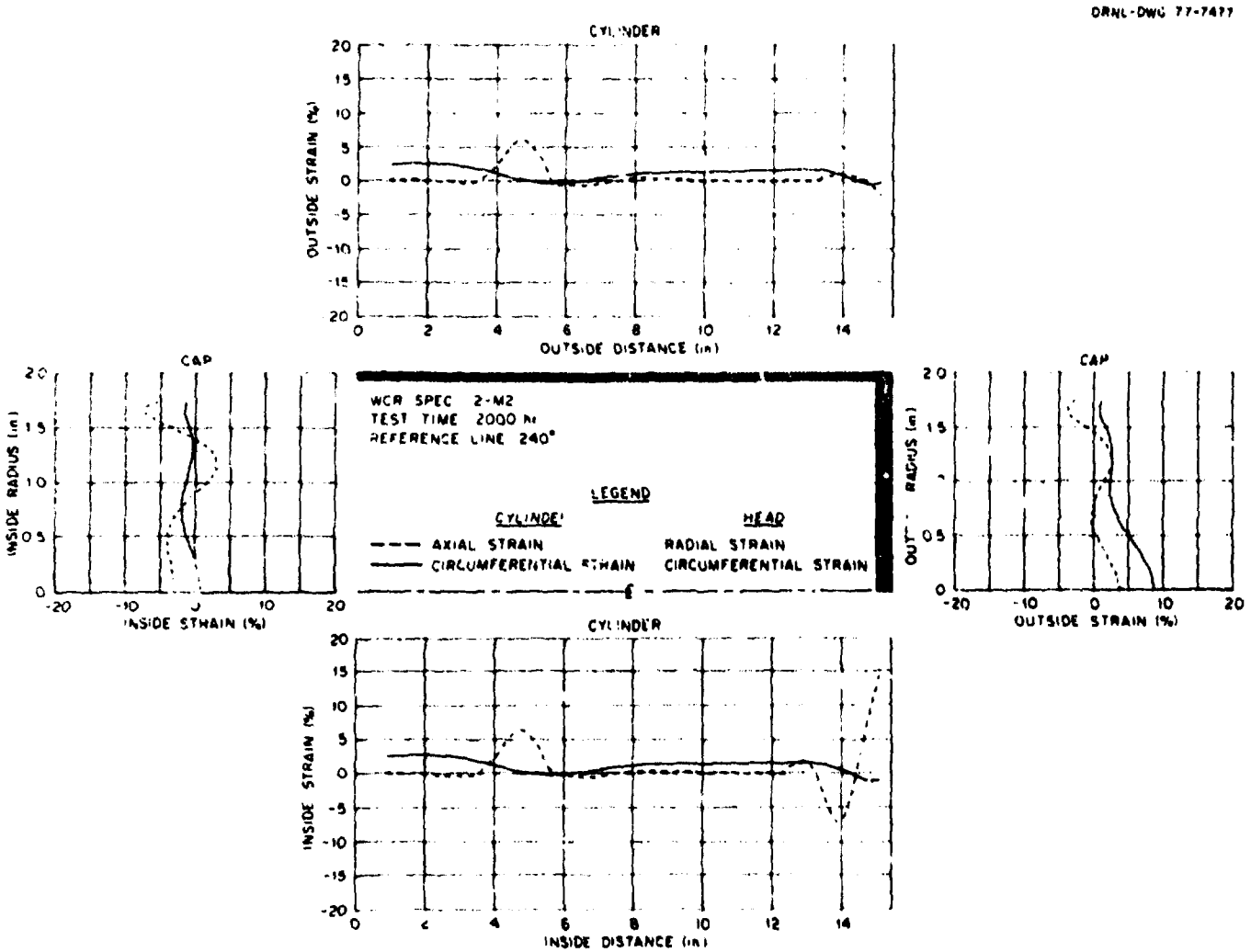

Fig. A9-e. Surface strain distribution for specimen 2-M2 along the axial reference plane, $\theta = 240^{\circ}$, at 2000 hr (1 in. = 2.54 cm).

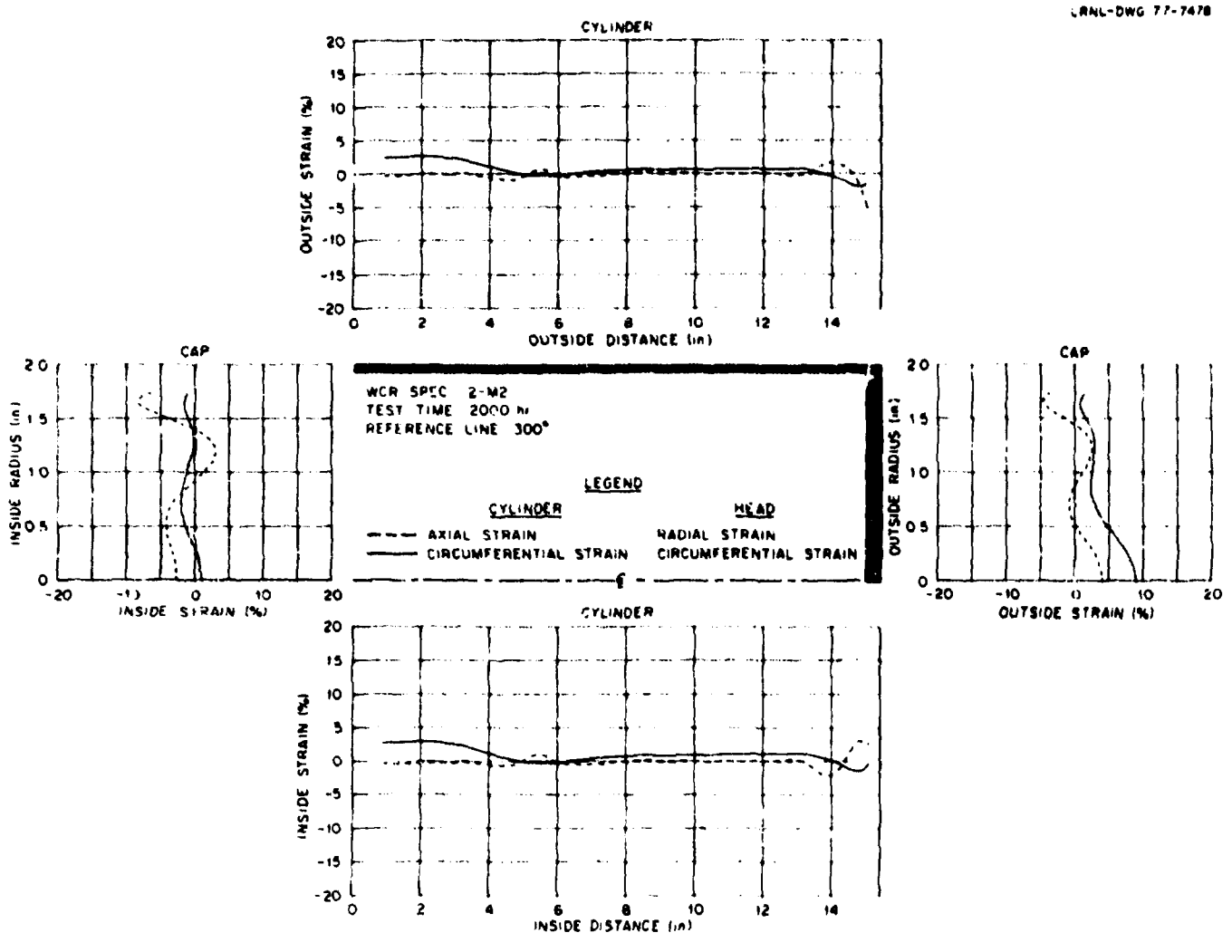

Fig. A9-f. Surface strain distribution for specimen 2-M2 along the axial reference plane, θ = 300°, at 2000 hr (1 in. = 2.54 cm).

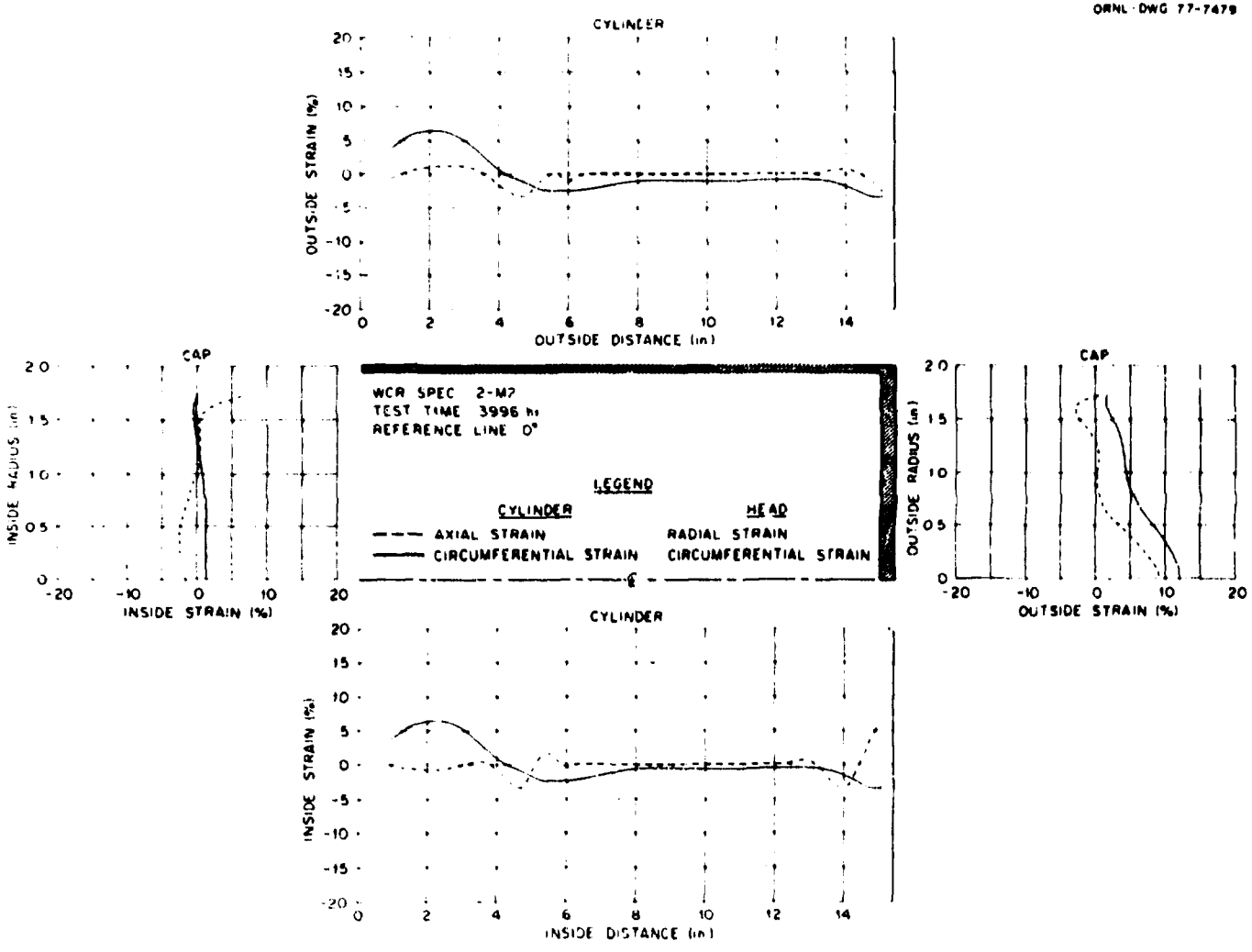

Fig. A10-a. Surface strain distribution for specimen 2-M2 along the axial reference plane, $\theta = 0°$, at 3996 hr (1 in. = 2.54 cm).

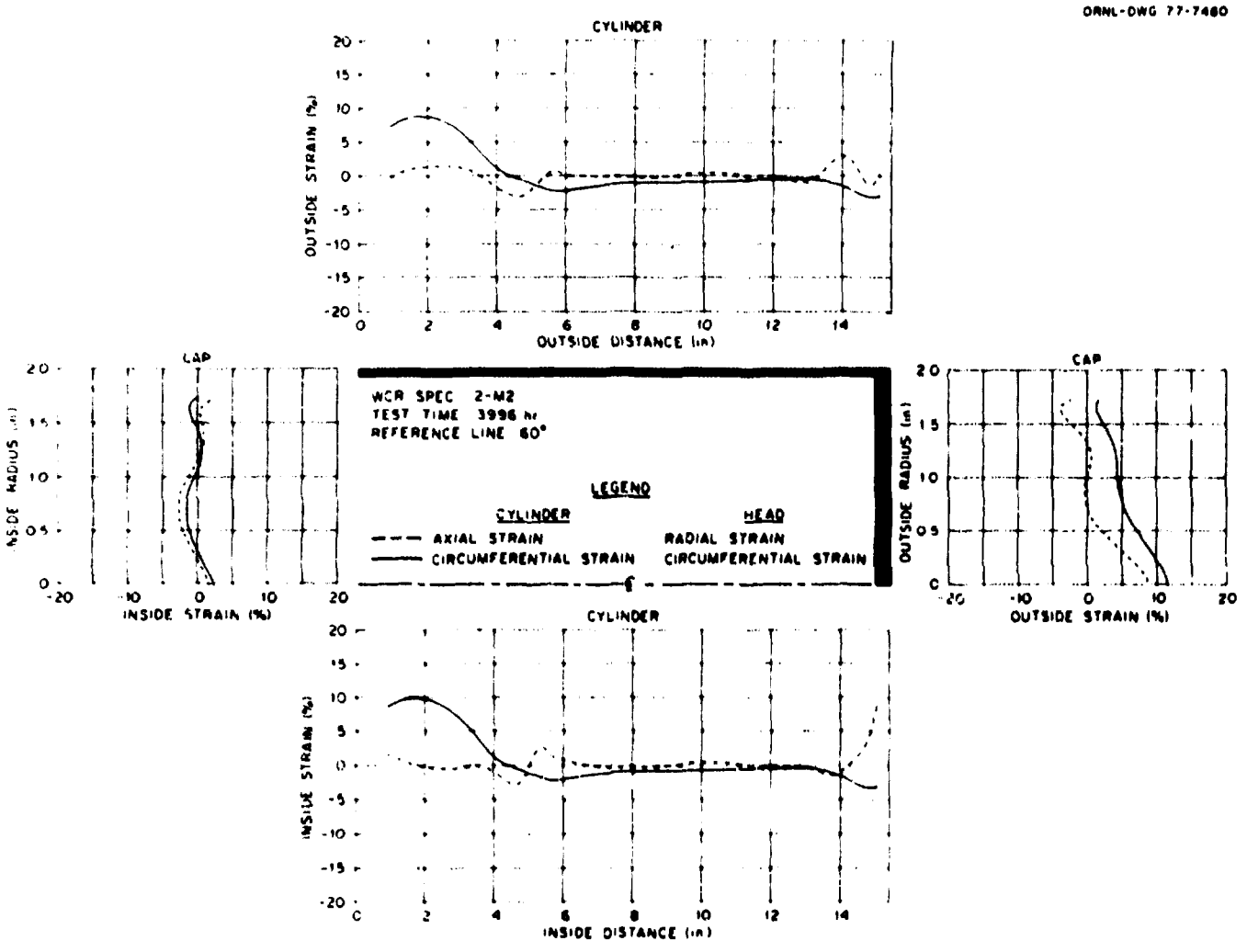

Fig. A10-b. Surface strain distribution for specimen 2-M2 along the axial reference plane, $\theta = 60°$, at 3996 hr (1 in. = 2.54 cm).

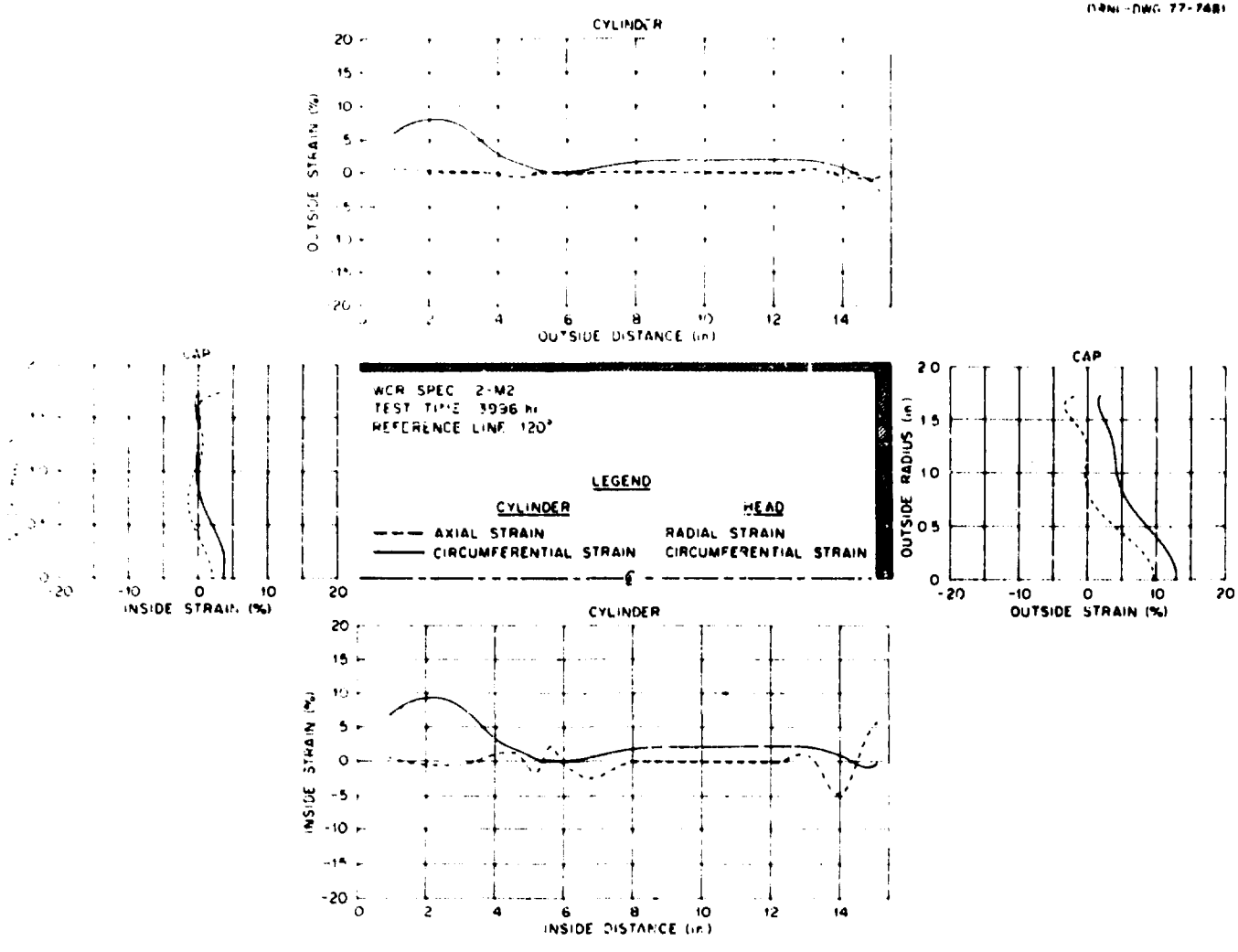

Fig. A10-c. Surface strain distribution for specimen 2-M2 along the axial reference plane, $G = 120°$, at 3996 hr (1 in. = 2.54 cm).

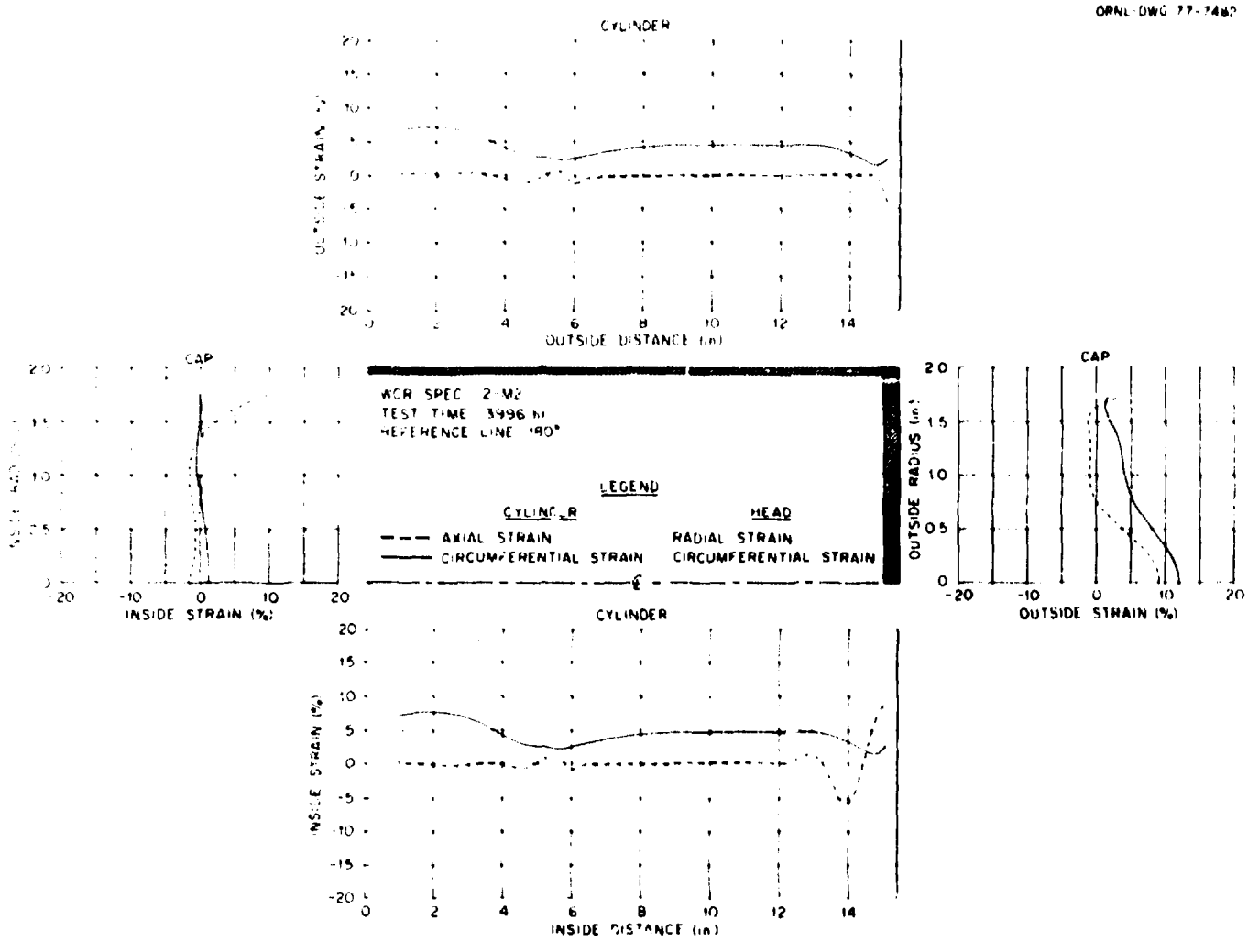

Fig. A10-d. Surface strain distribution for specimen 2-M2 along the axial reference plane, $\theta = 180^{\circ}$, at 3996 hr (1 in. = 2.54 cm).

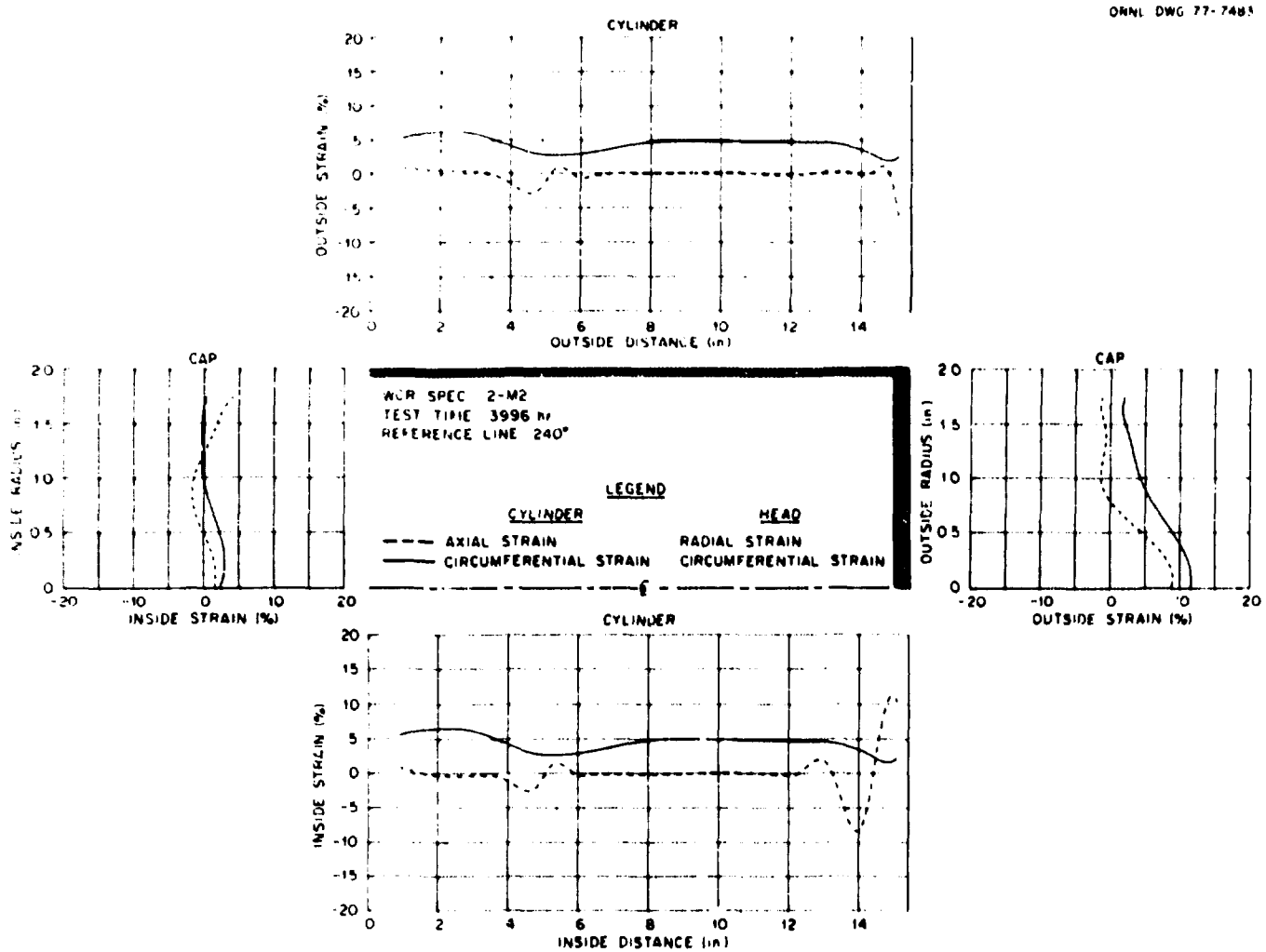

Fig. A10-e. Surface strain distribution for specimen 2-M2 along the axial reference plane, θ = 240°, at 3996 hr (1 in. = 2.54 cm).

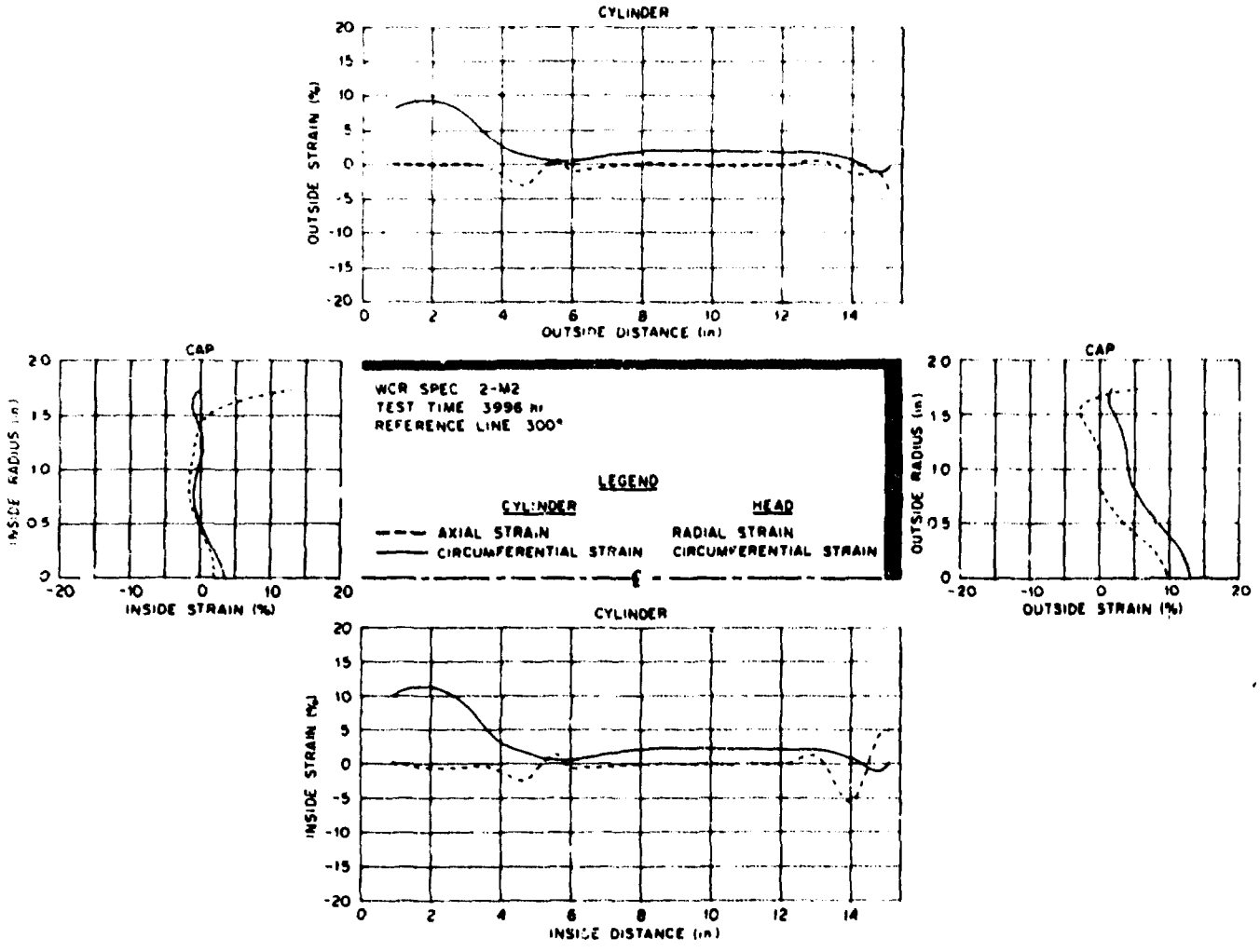

Fig. A10-f. Surface strain distribution for specimen 2-M2 along the axial reference plane, $\theta = 300^{\circ}$, at 3996 hr (1 in. = 2.54 cm).

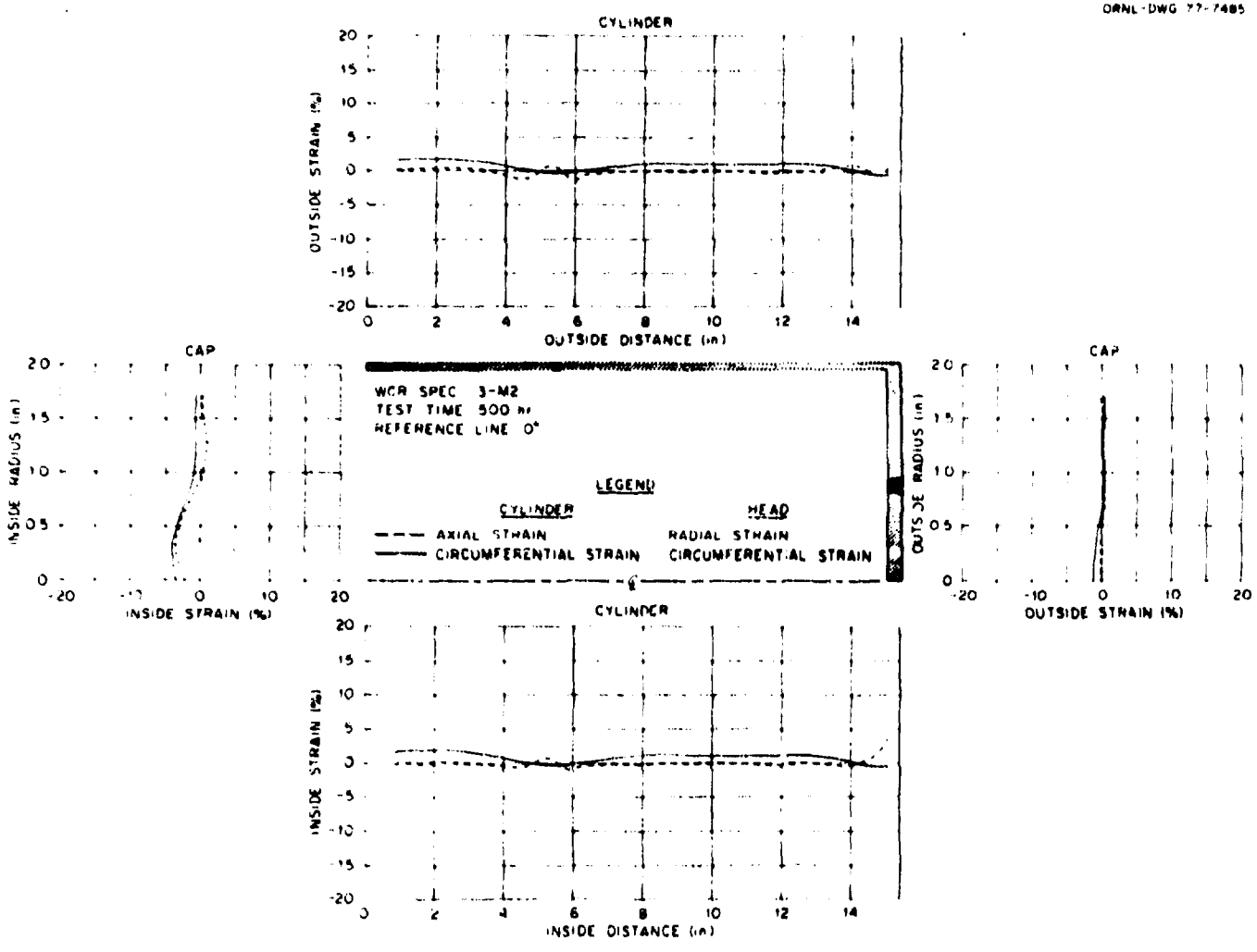

Fig. A11-a. Surface strain distribution for specimen 3-M2 along the axial reference plane, $\theta = 0°$, at 500 hr (1 in. = 2.54 cm).

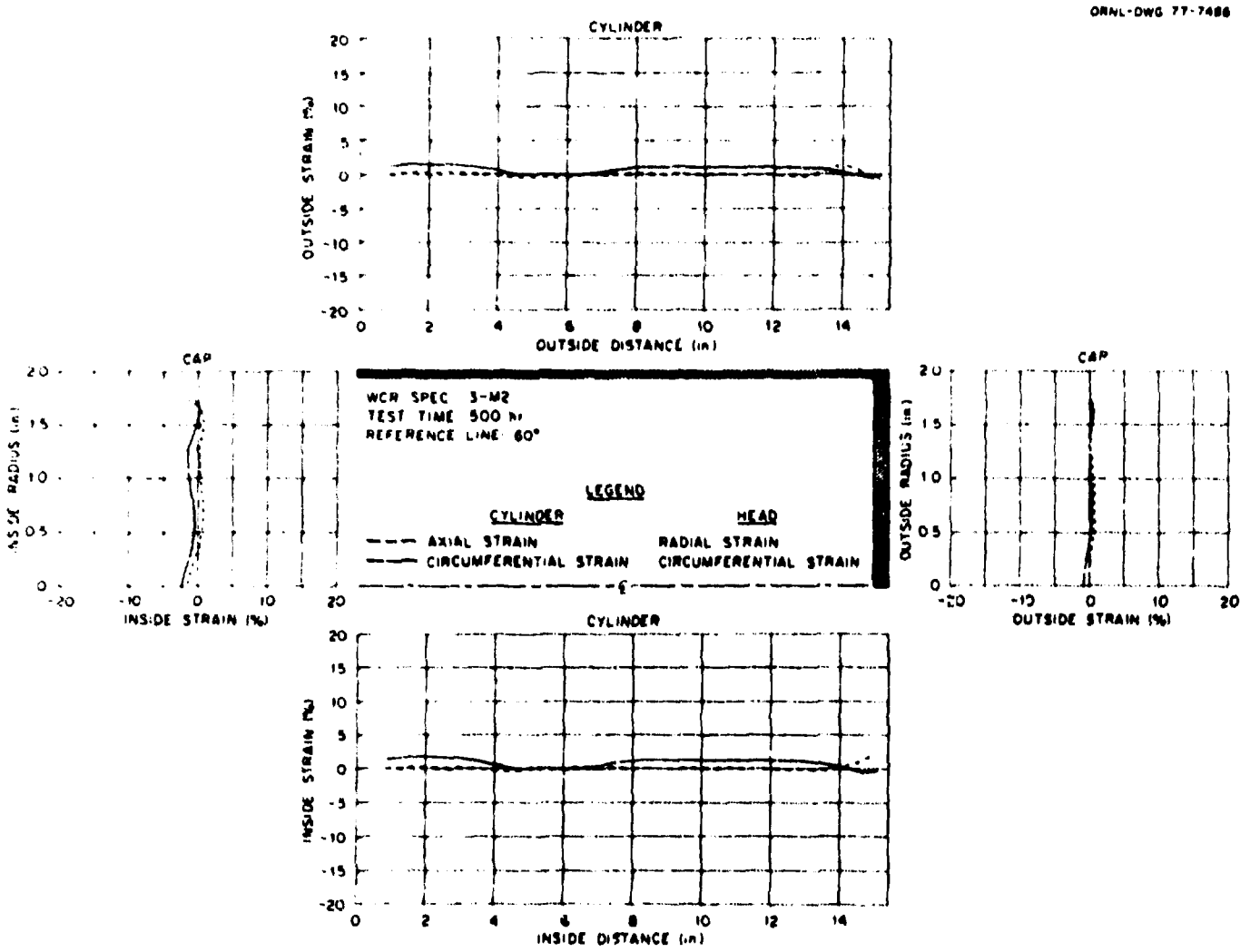

Fig. A11-b. Surface strain distribution for specimen 3-M2 along the axial reference plane, $\theta = 60^{\circ}$, at 500 hr (1 in. = 2.54 cm).

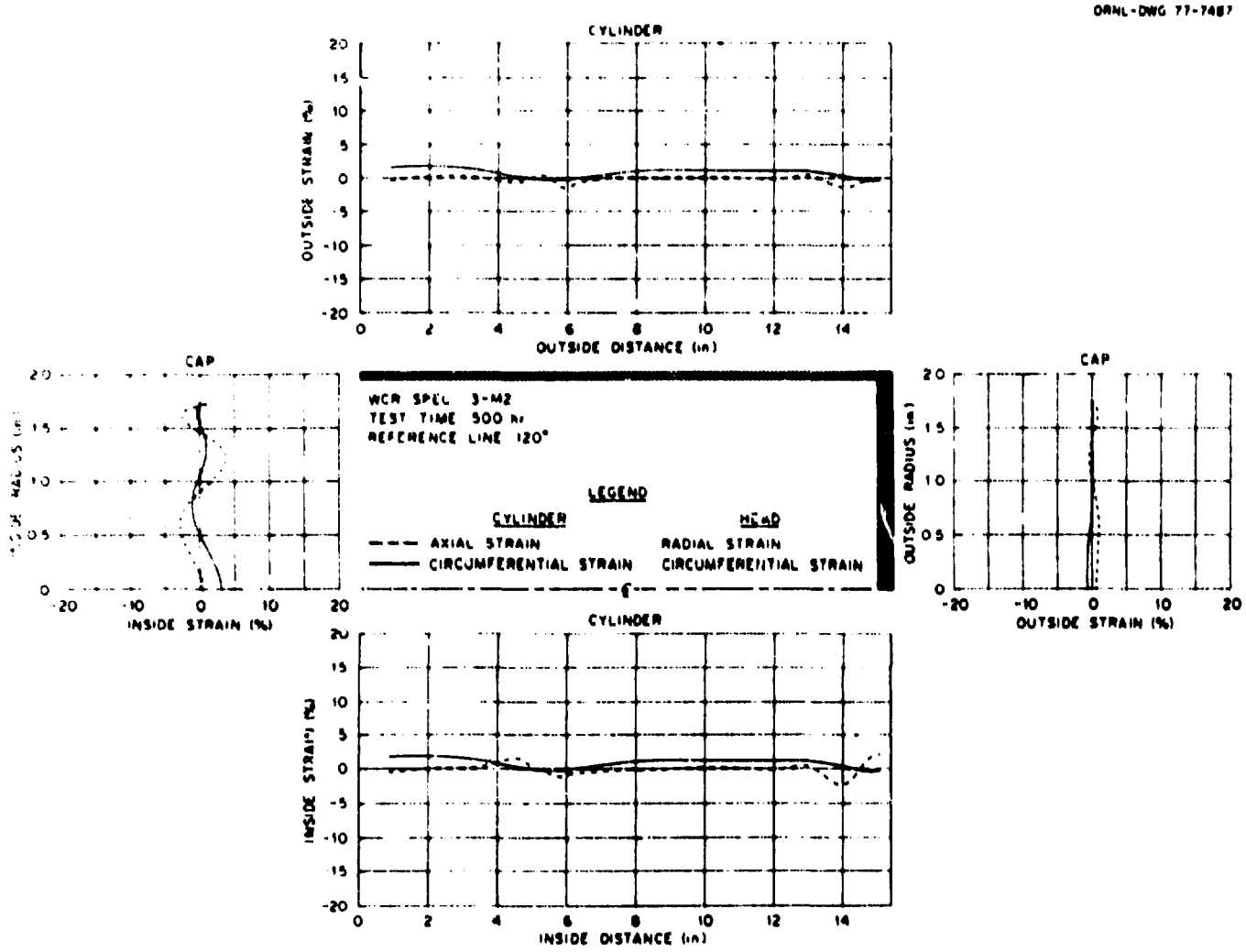

Fig. A11-c. Surface strain distribution for specimen 3-M2 along the axial reference plane, $\theta = 120^{\circ}$, at 500 hr (1 in. = 2.54 cm).

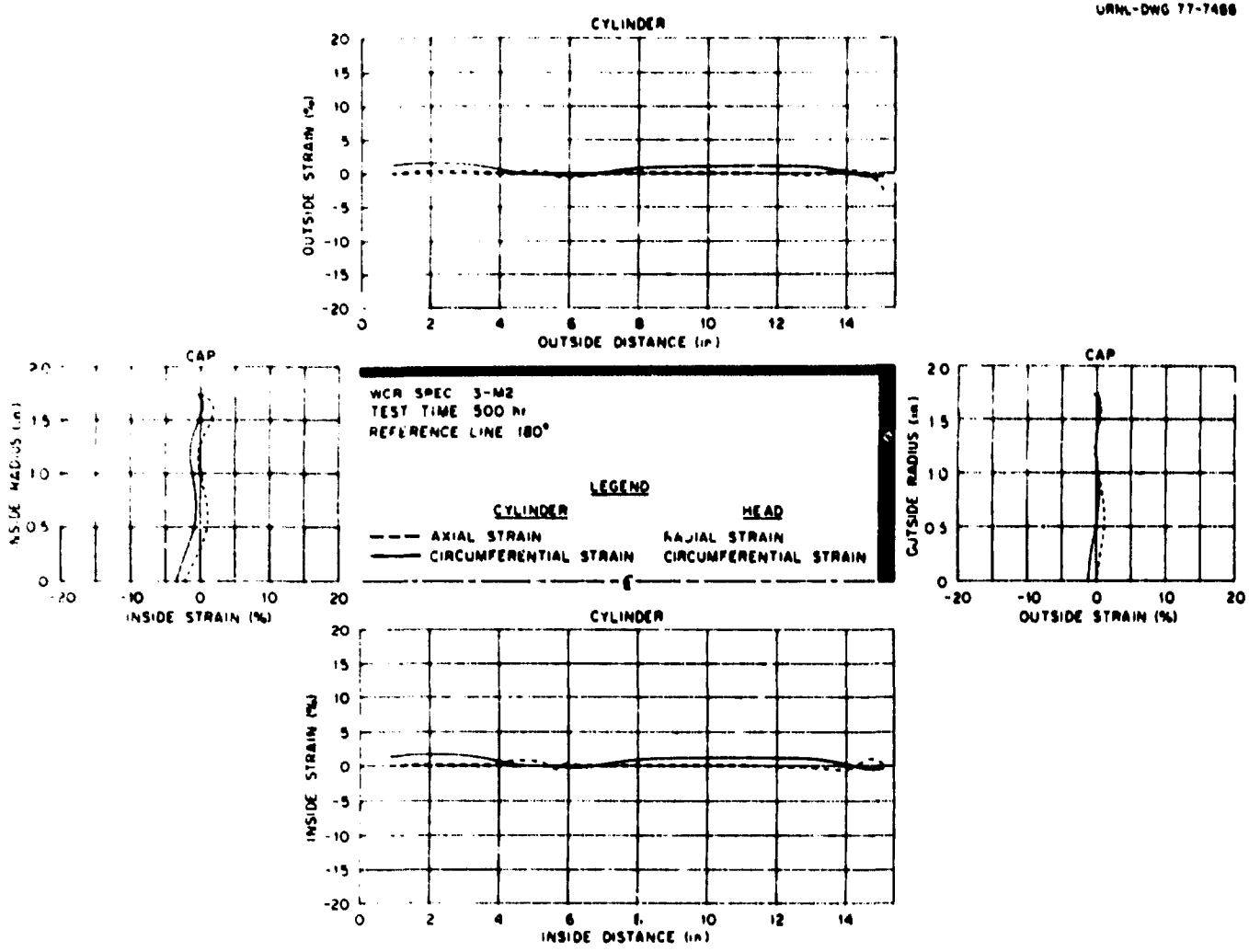

Fig. All-d. Surface strain distribution for specimen 3-M2 along the axial reference plane, θ = 180°, at 500 hr (1 in. = 2.54 cm).

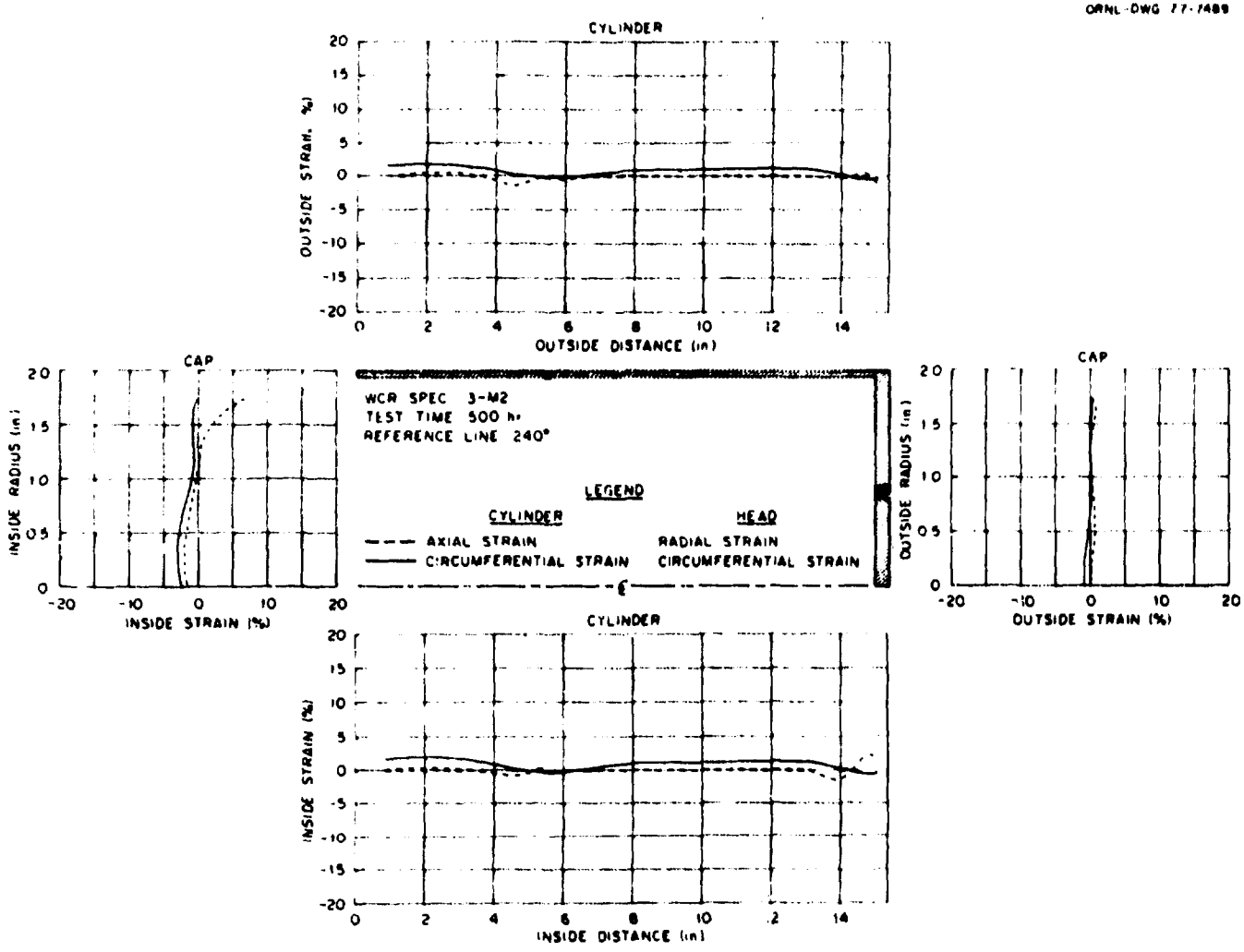

Fig. All-e. Surface strain distribution for specimen 3-M2 along the axial reference plane, $\theta = 240°$, at 500 hr (1 in. = 2.54 cm).

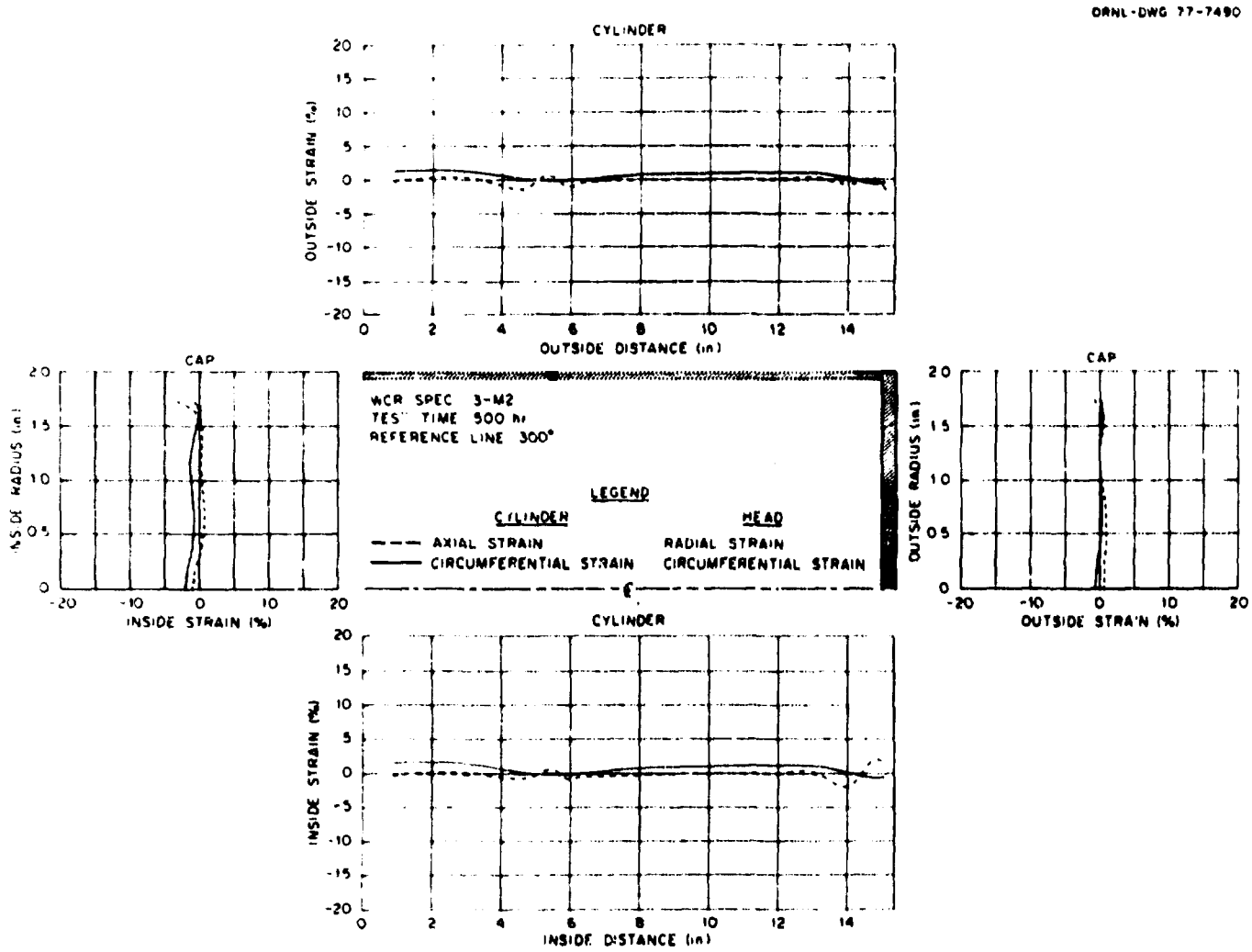

Fig. A11-f. Surface strain distribution for specimen 3-M2 along the axial reference plane, $\theta = 300°$, at 500 hr (1 in. = 2.54 cm).

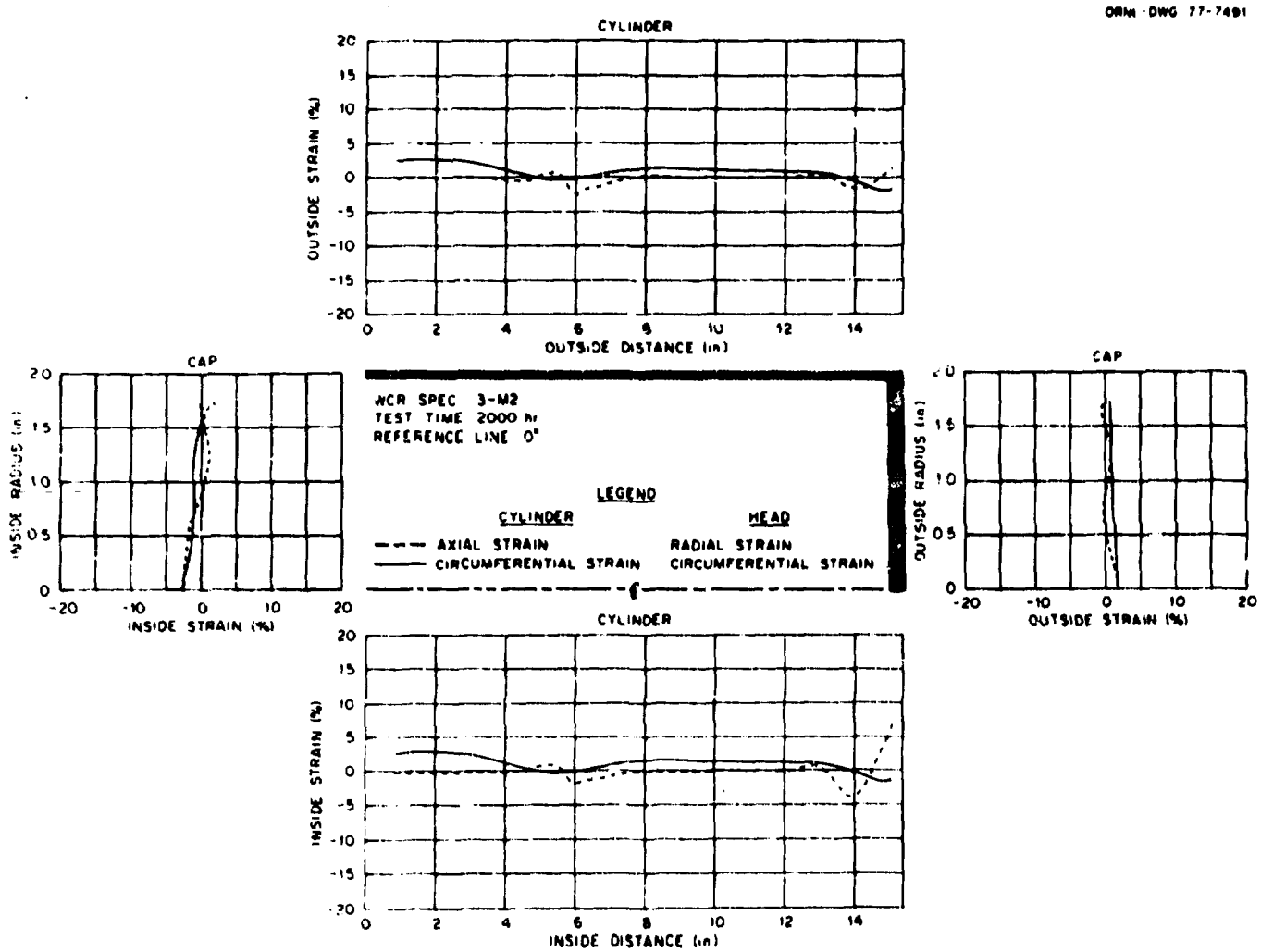

Fig. A12-a. Surface strain distribution for specimen 3-M2 along the axial reference plane, $\theta = 0°$, at 2000 hr (1 in. = 2.54 cm).

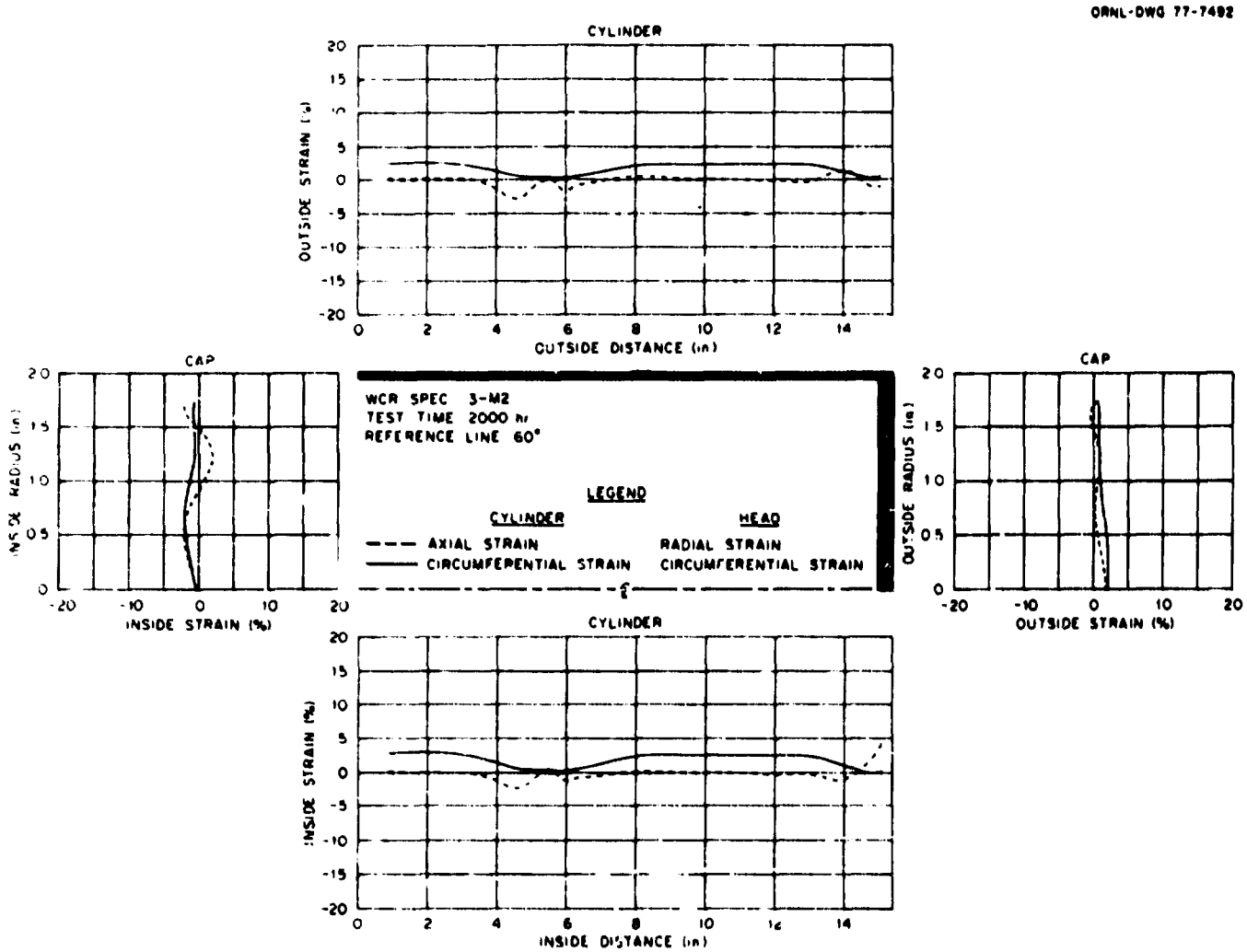

Fig. A12-b. Surface strain distribution for specimen 3-M2 along the axial reference plane, $\theta = 60°$, at 2000 hr (1 in. = 2.54 cm).

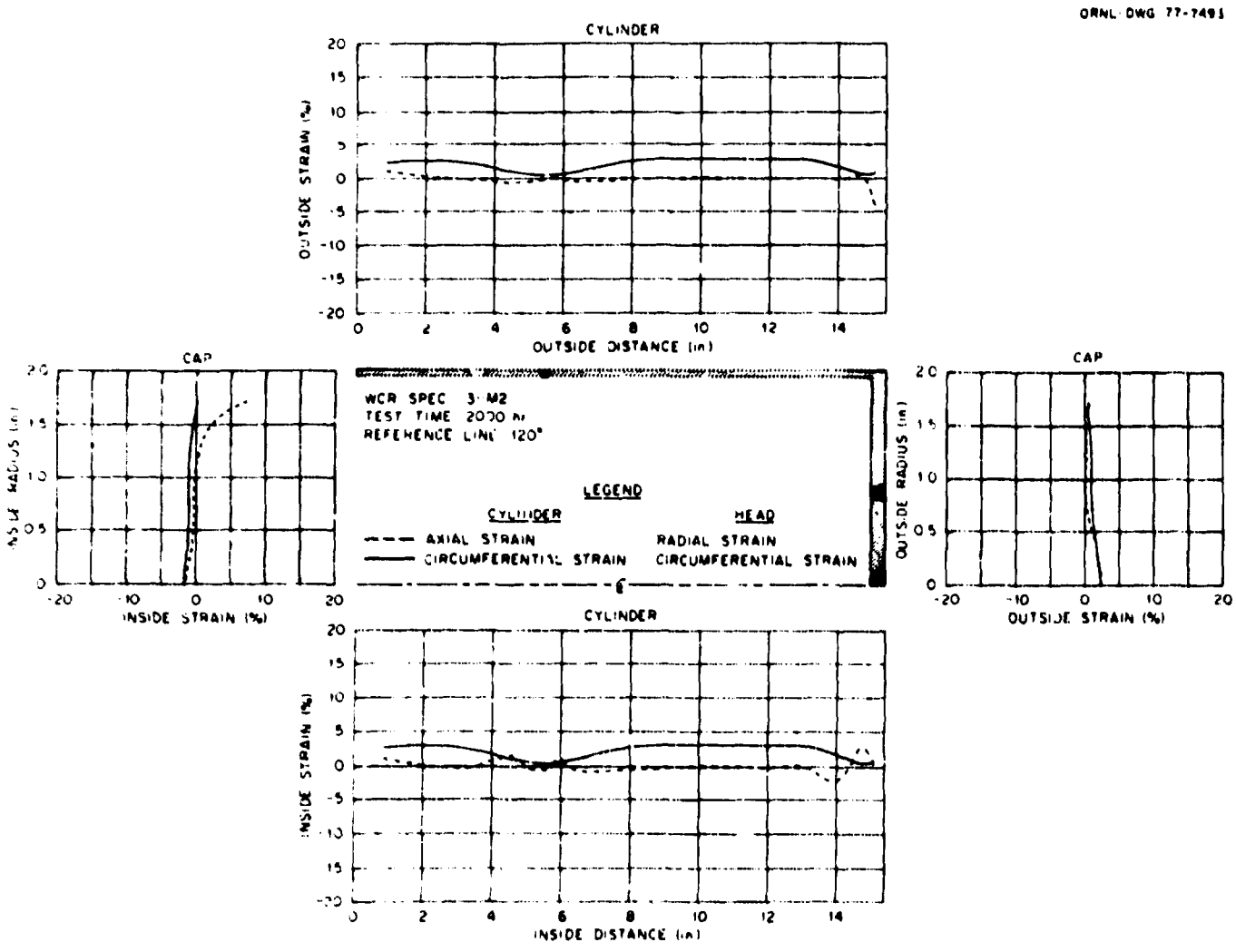

Fig. A12-c. Surface strain distribution for specimen 3-M2 along the axial reference plane, $\theta = 120°$, at 2000 hr (1 in. = 2.54 cm).

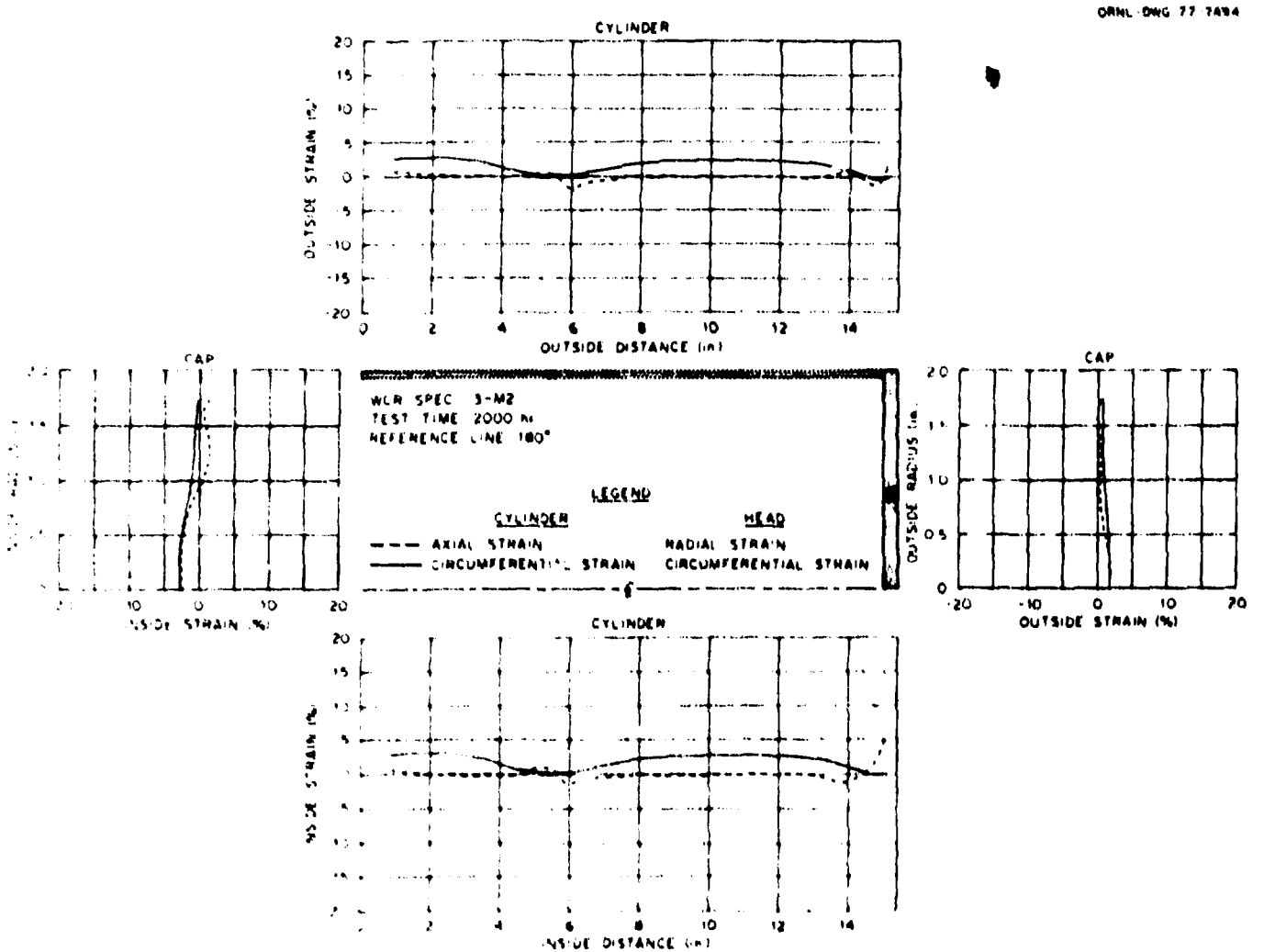

Fig. A12-d. Surface strain distribution for specimen 3-M2 along the reference plane, $\theta = 180°$, at 2000 hr (1 in. = 2.54 cm).

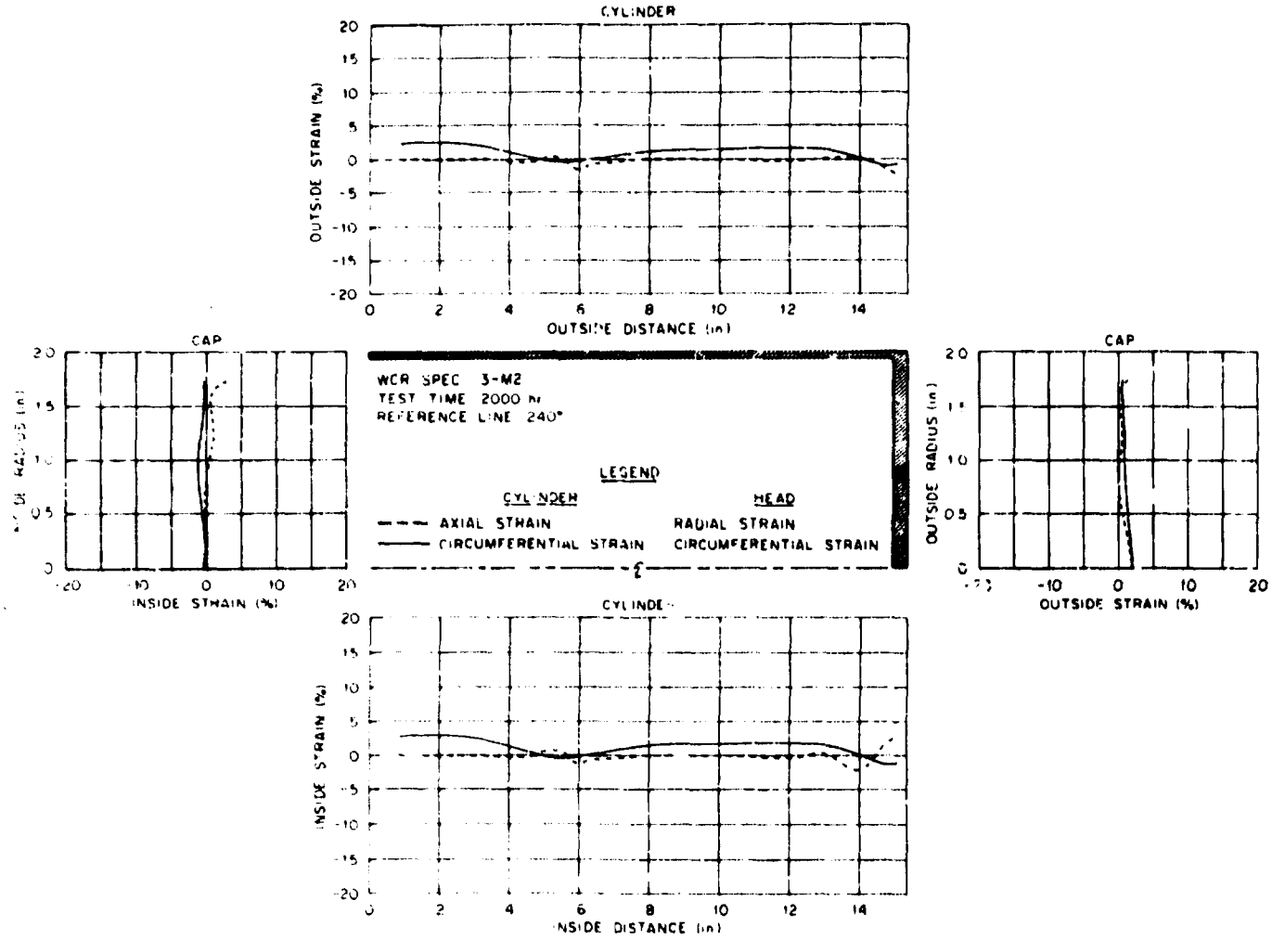

Fig. A12-e. Surface strain distribution for specimen 3-M2 along the axial reference plane, θ = 240°, at 2000 hr (1 in. = 2.54 cm).

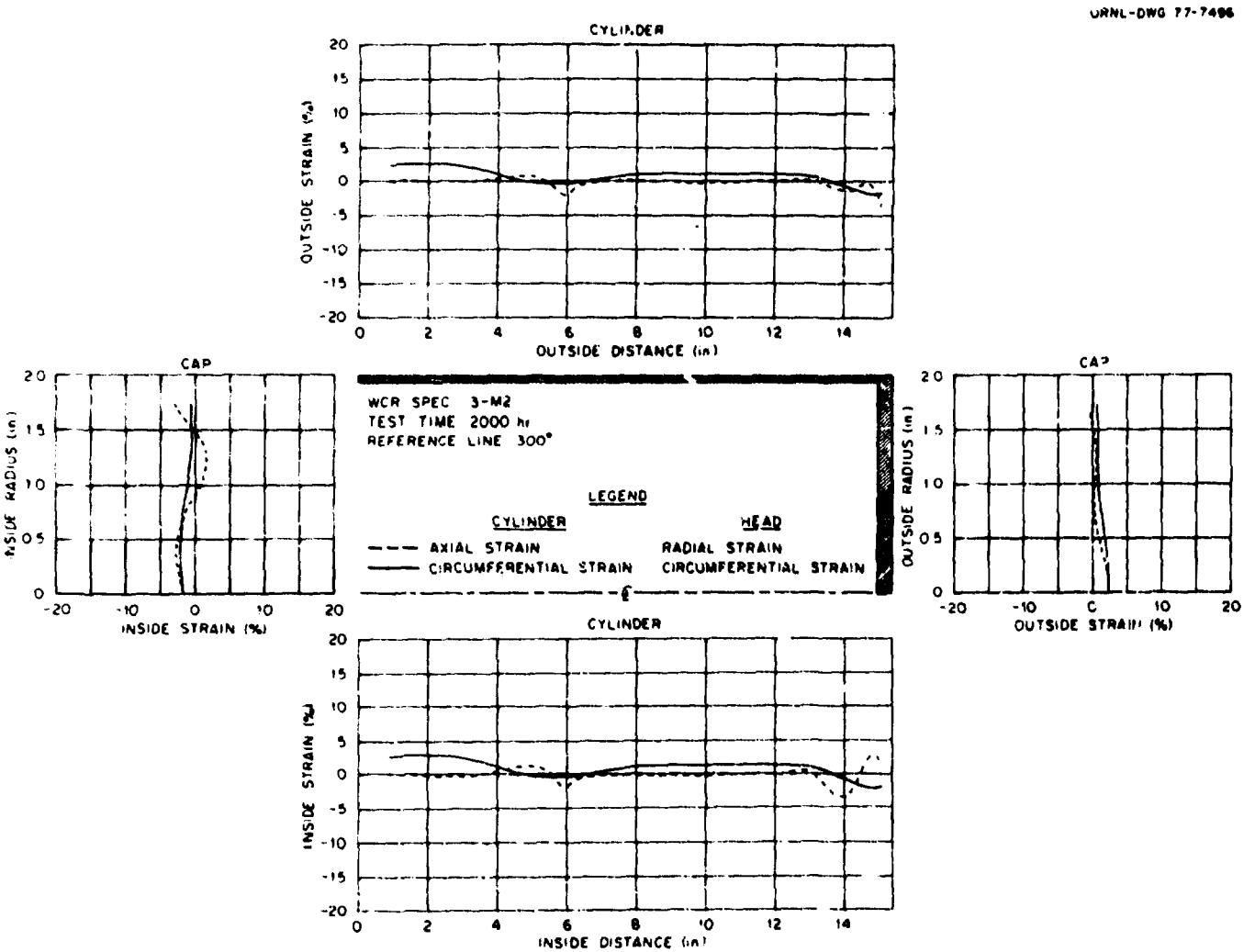

Fig. A12-f. Surface strain distribution for specimen 3-M2 along the axial reference plane, θ = 300°, at 2000 hr (1 in. = 2.54 cm).

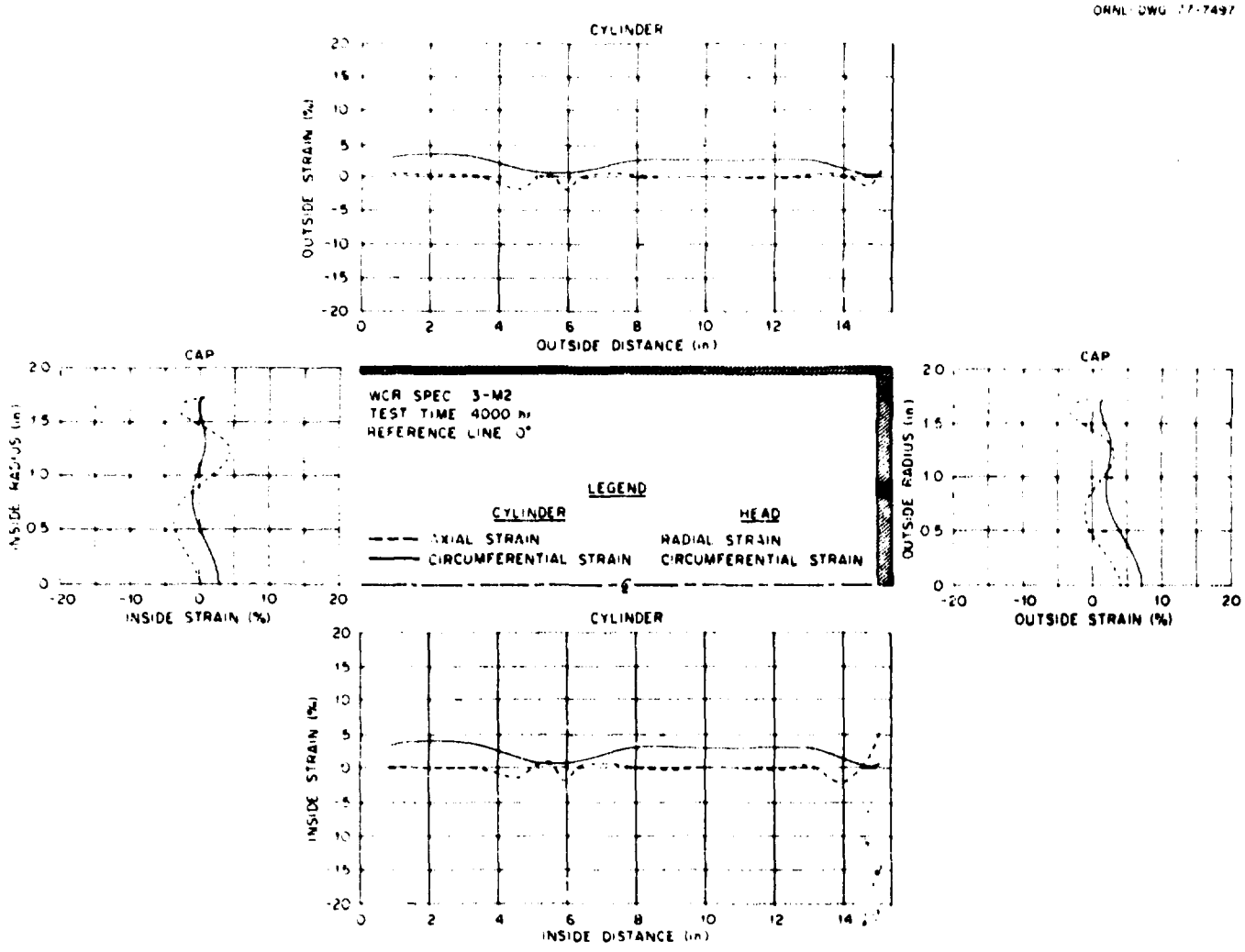

Fig. A13-a. Surface strain distribution for specimen 3-M2 along the axial reference plane, $\theta = 0°$, at 4000 hr (1 in. = 2.54 cm).

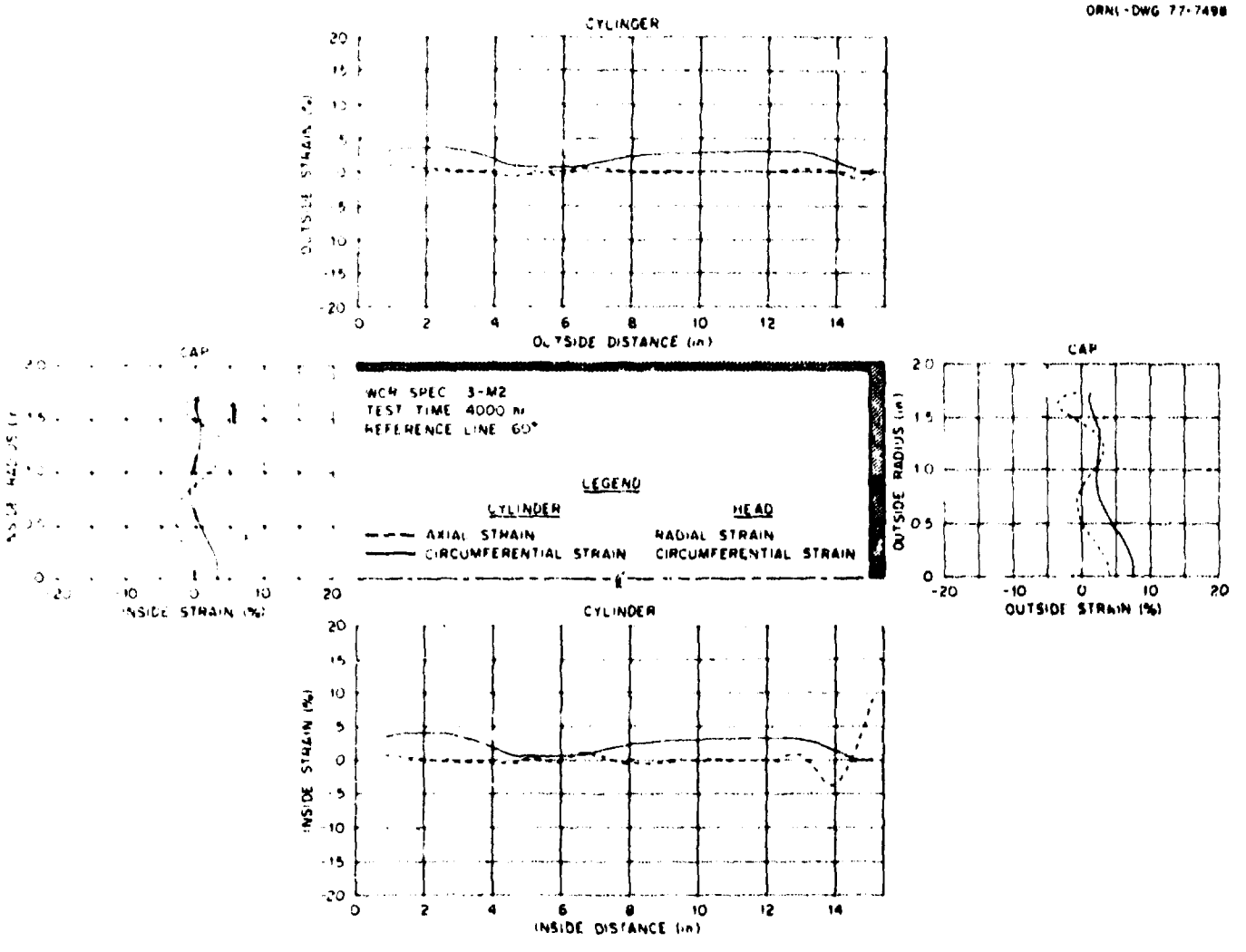

Fig. A13-b. Surface strain distribution for specimen 3-M2 along the axial reference plane, $\theta = 60^{\circ}$, at 4000 hr (1 in. = 2.54 cm).

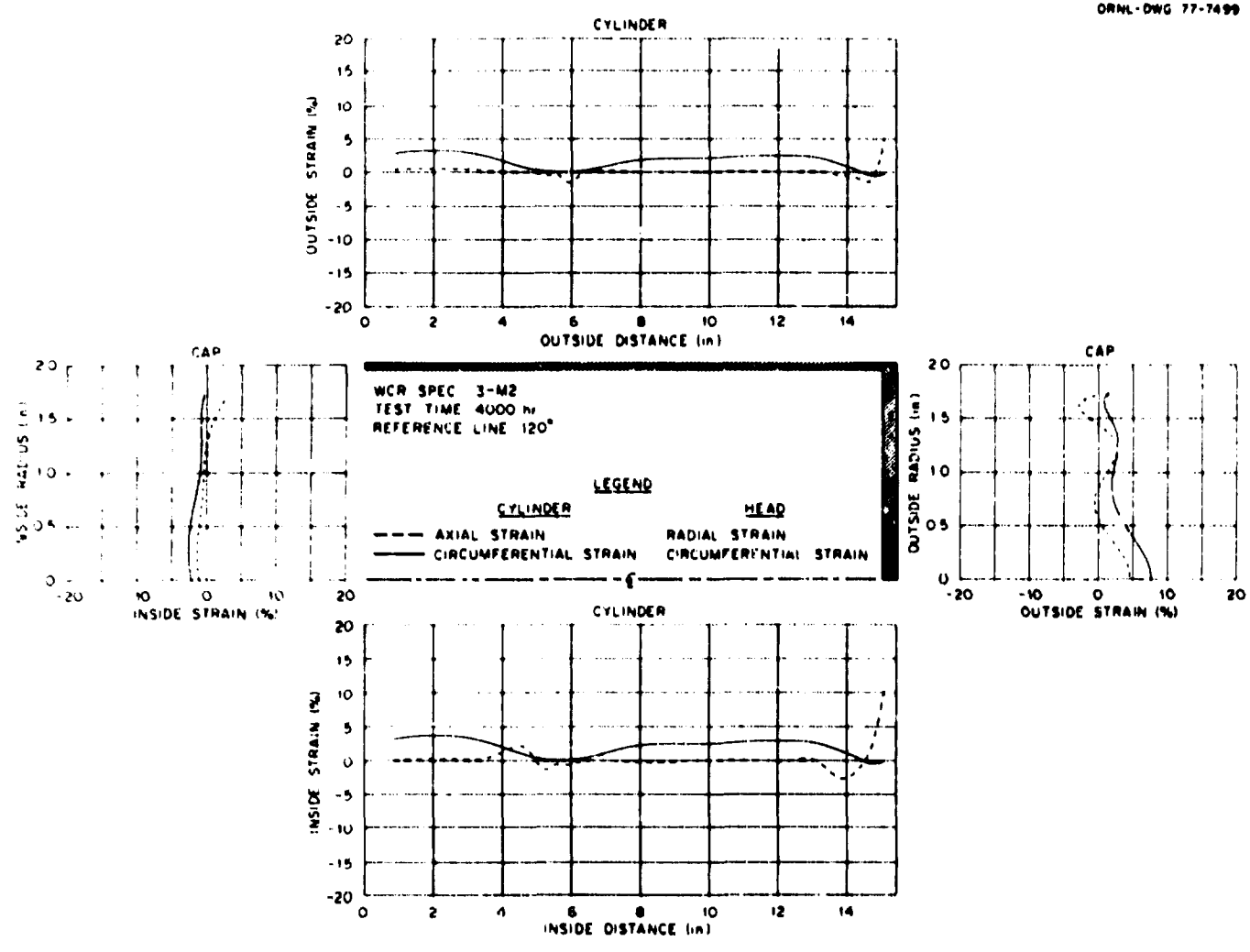

Fig. A13-c. Surface strain distribution for specimen 3-M2 along the axial reference plane, θ = 120°, at 4000 hr (1 in. = 2.54 cm).

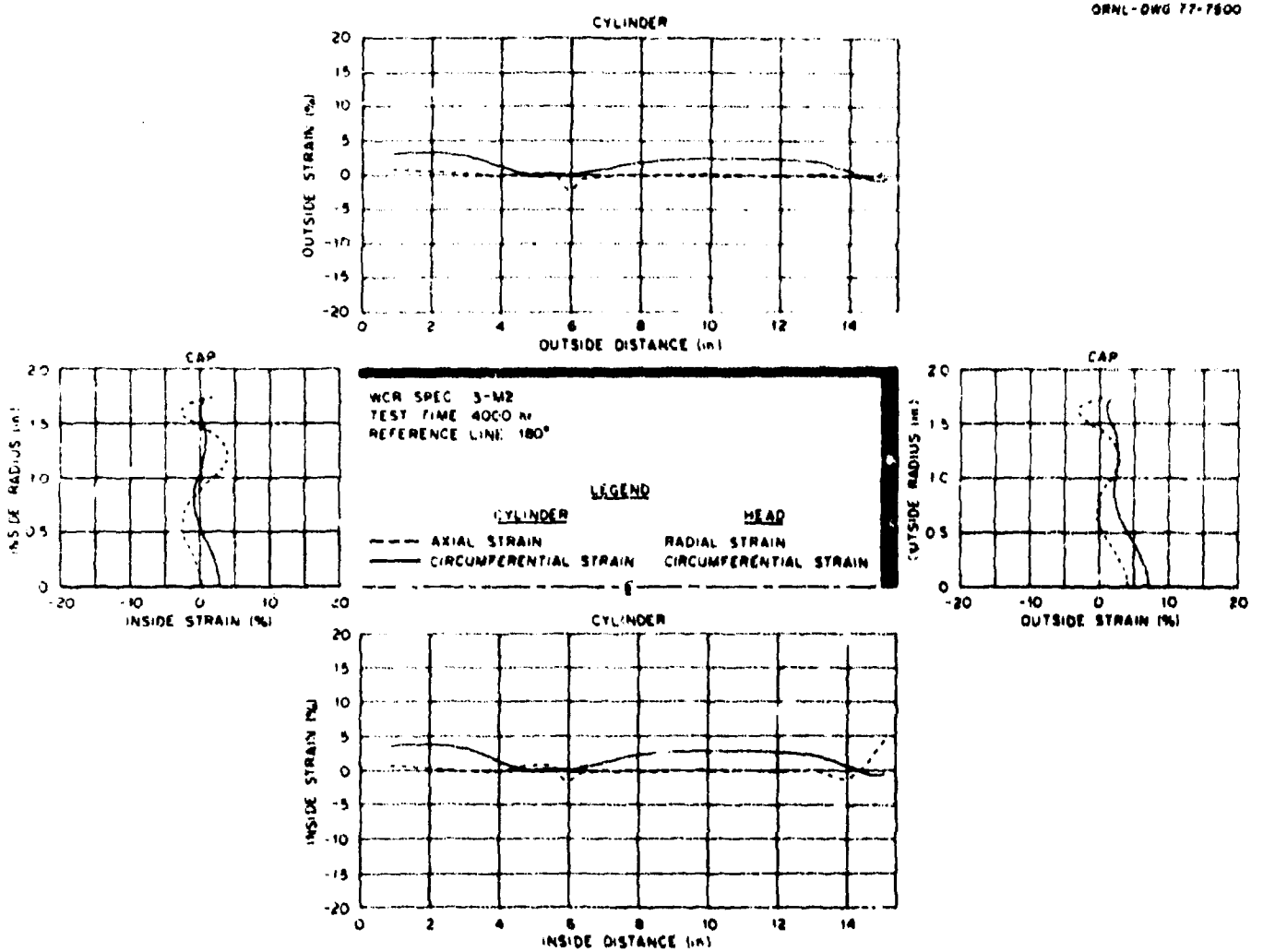

Fig. A13-d. Surface strain distribution for specimen 3-M2 along the axial reference plane, $\theta = 180°$, at 4000 hr (1 in. = 2.54 cm).

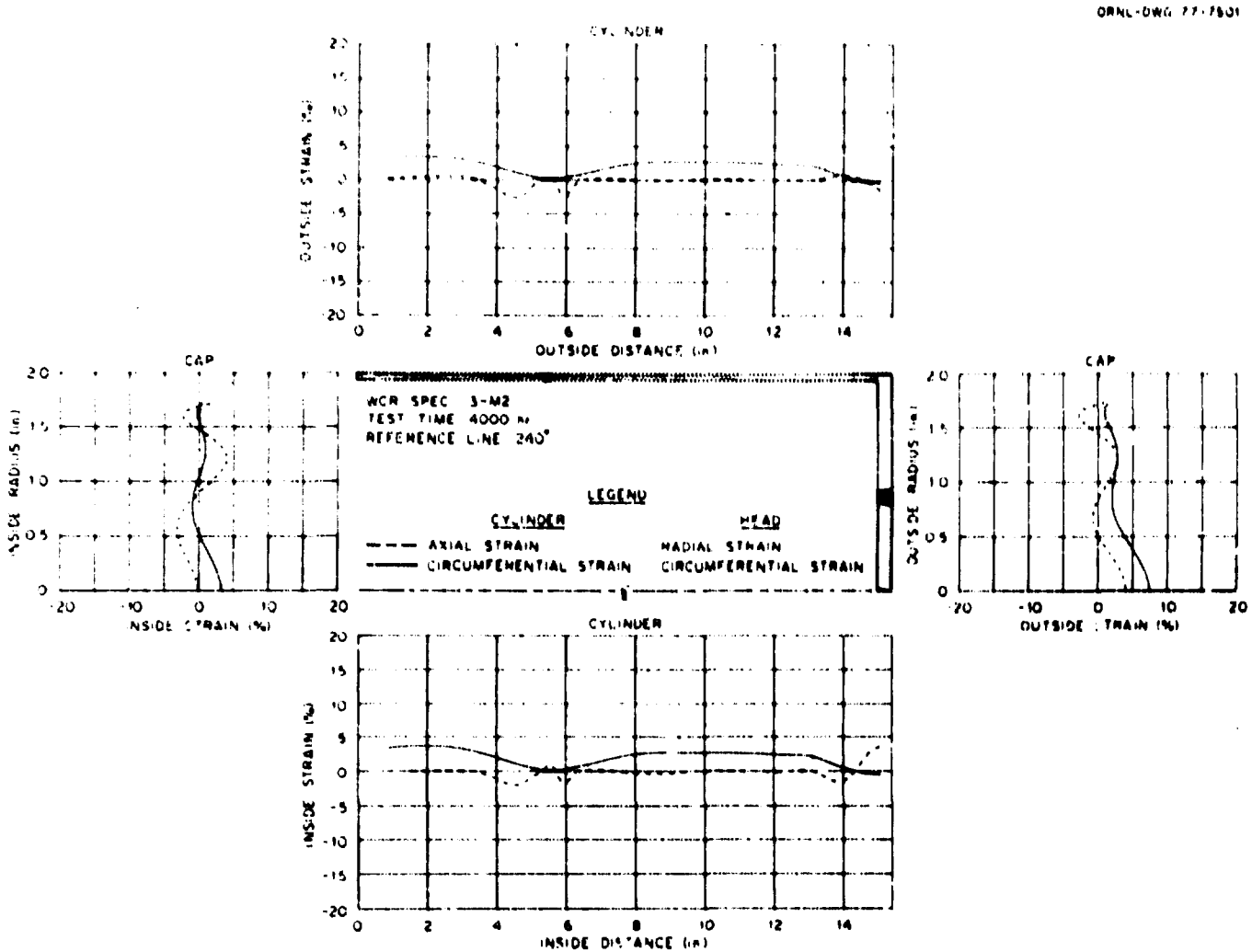

Fig. A13-e. Surface strain distribution for specimen 3-M2 along the axial reference plane, θ = 240°, at 4000 hr (1 in. = 2.54 cm).

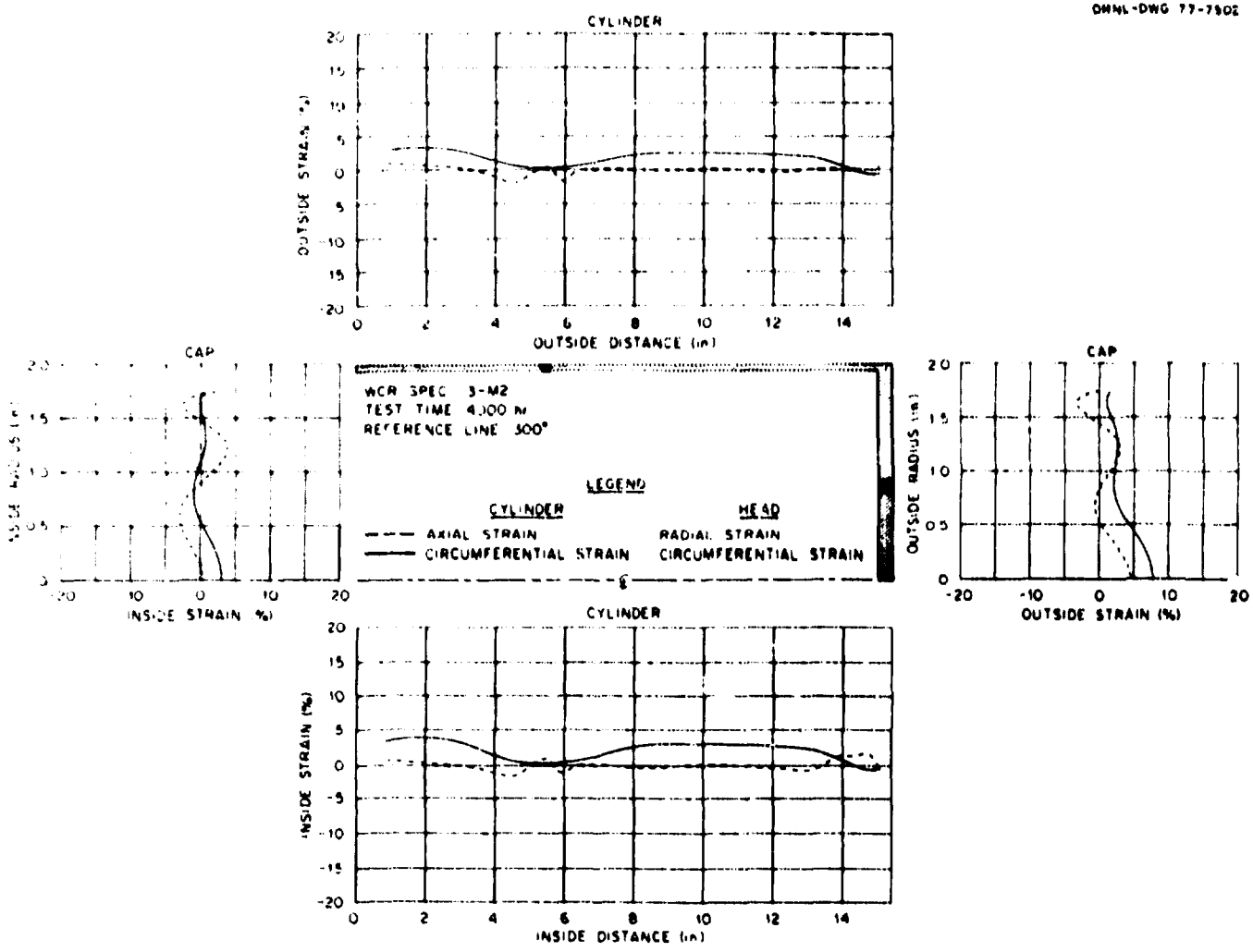

Fig. A13-f. Surface strain distribution for specimen 3-M2 along the axial reference plane, θ = 300°, at 4000 hr (1 in. = 2.54 cm).

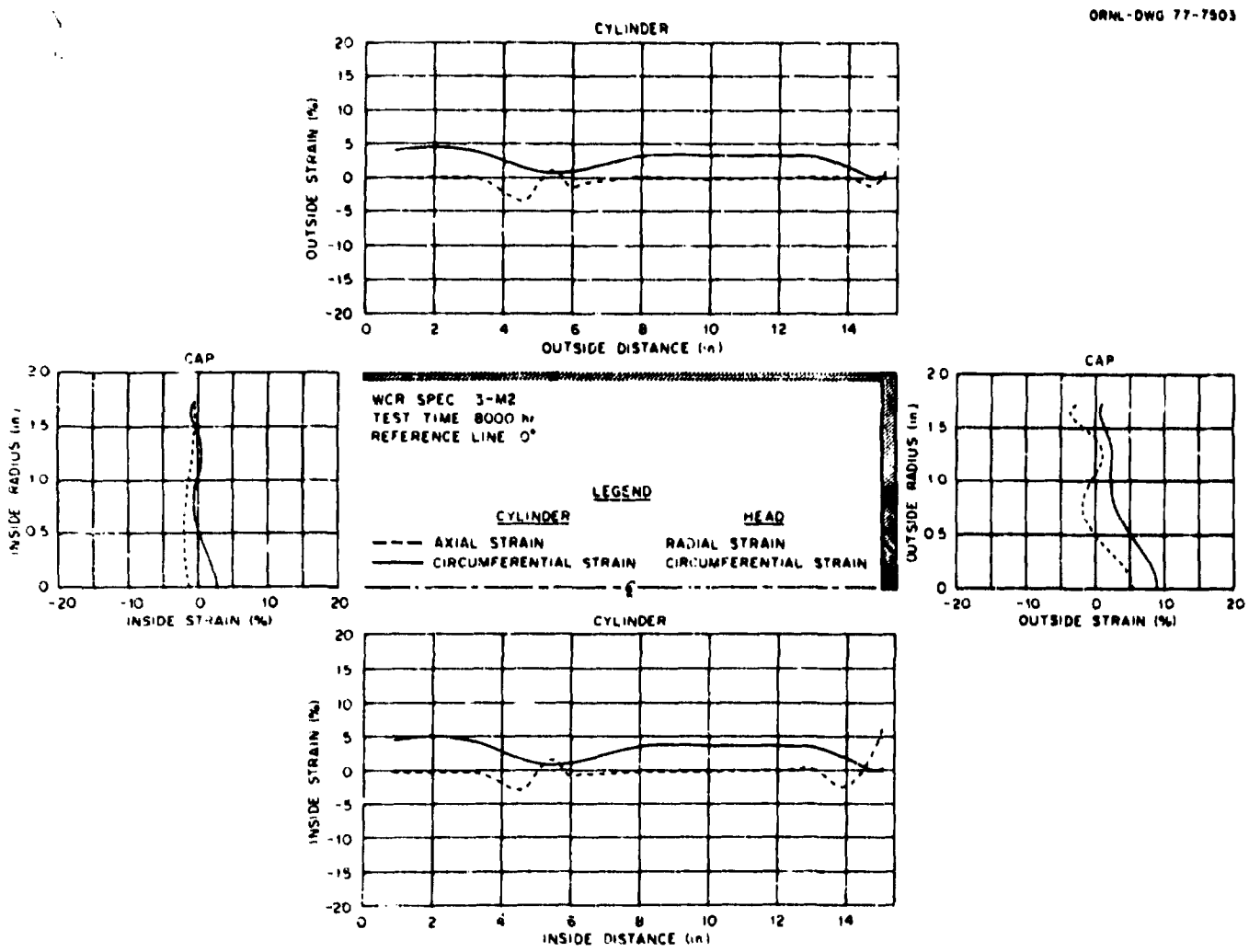

Fig. A14-a. Surface strain distribution for specimen 3-M2 along the axial reference plane, $\theta = 0°$, at 8000 hr (1 in. = 2.54 cm).

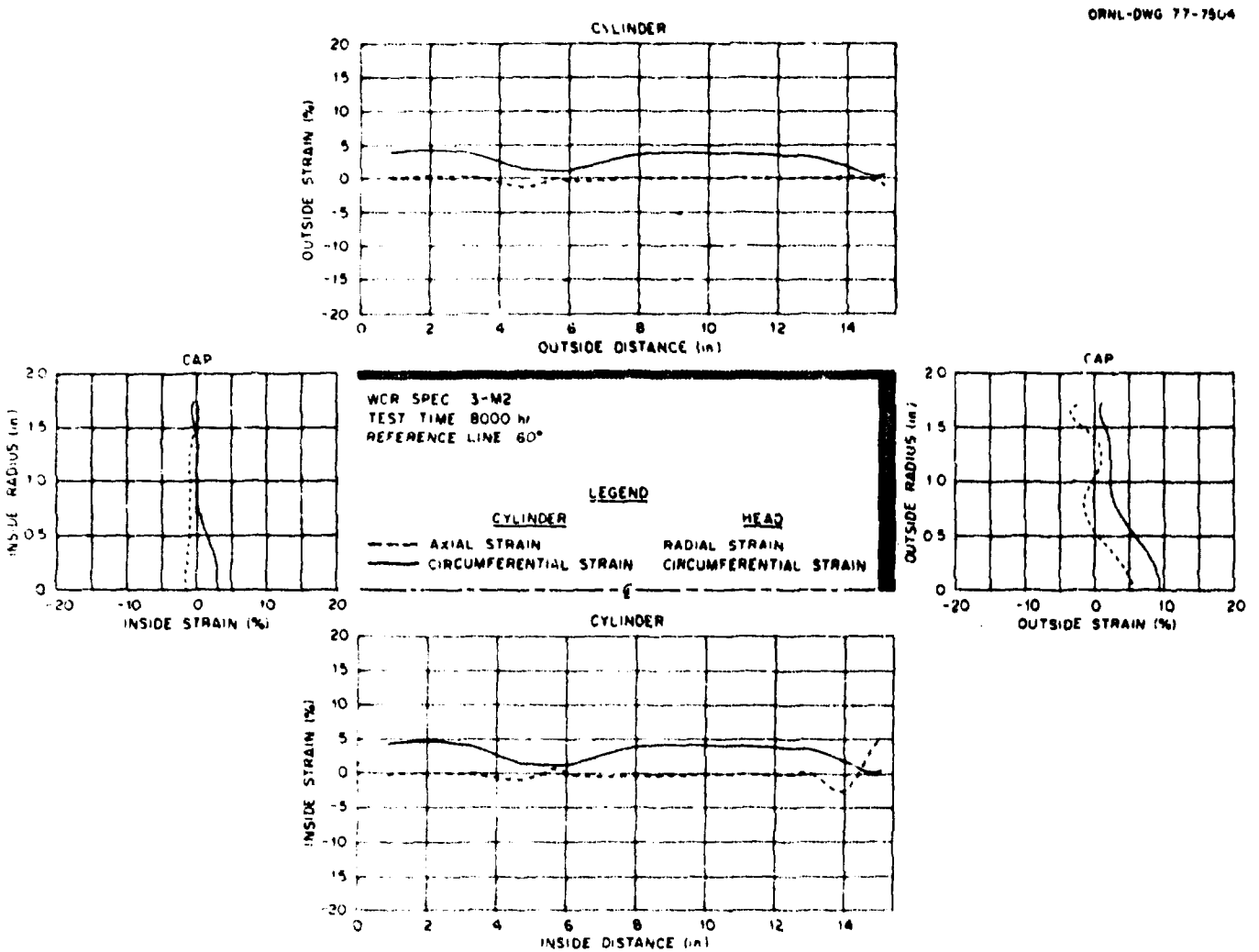

Fig. A14-b. Surface strain distribution for specimen 3-M2 along the axial reference plane, $\theta = 60°$, at 8000 hr (1 in. = 2.54 cm).

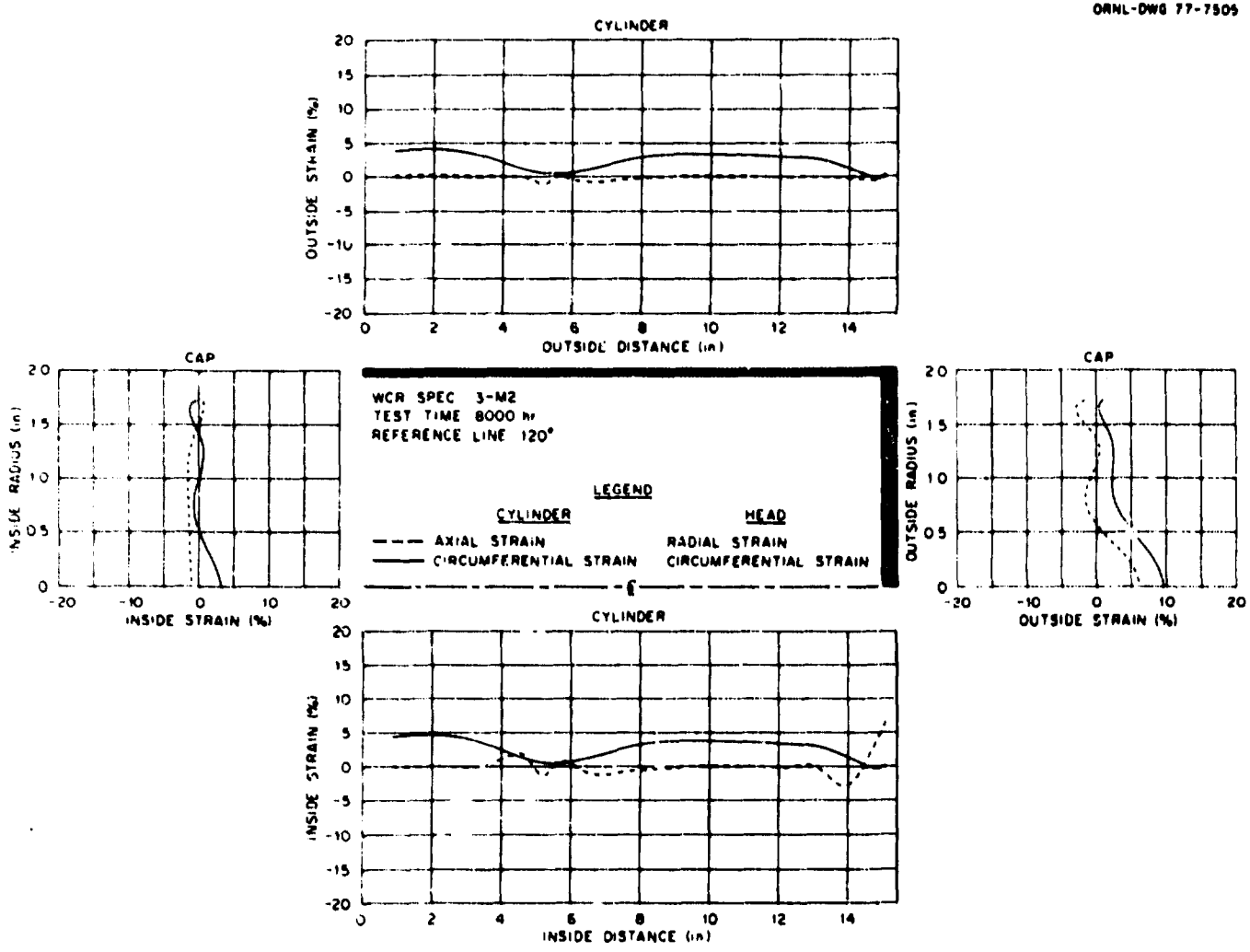

Fig. A14-c. Surface strain distribution for specimen 3-M2 along the axial reference plane, θ = 120°, at 8000 hr (1 in. = 2.54 cm).

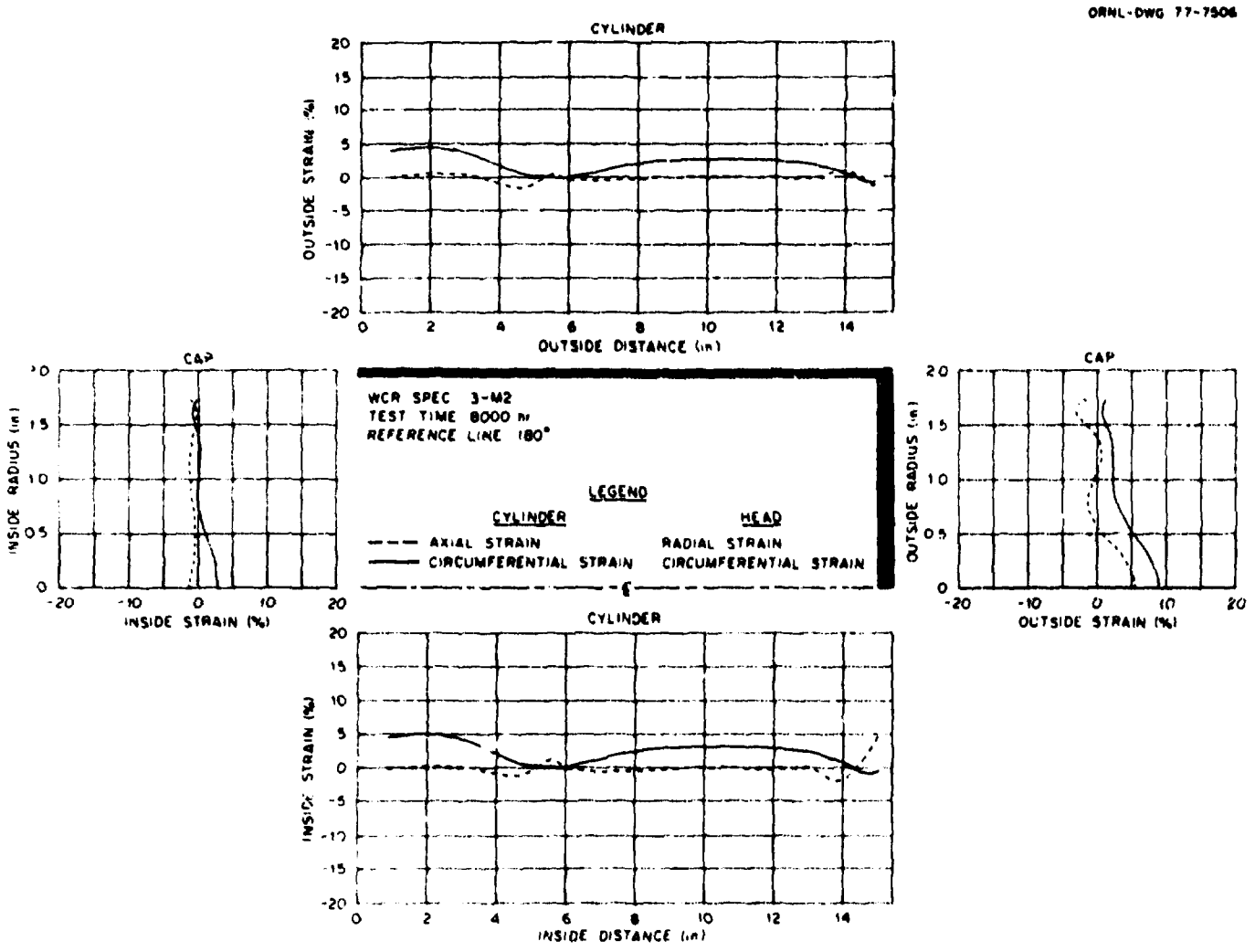

Fig. A14-d. Surface strain distribution for specimen 3-M2 along the axial reference plane, $\theta = 180°$, at 8000 hr (1 in. = 2.54 cm).

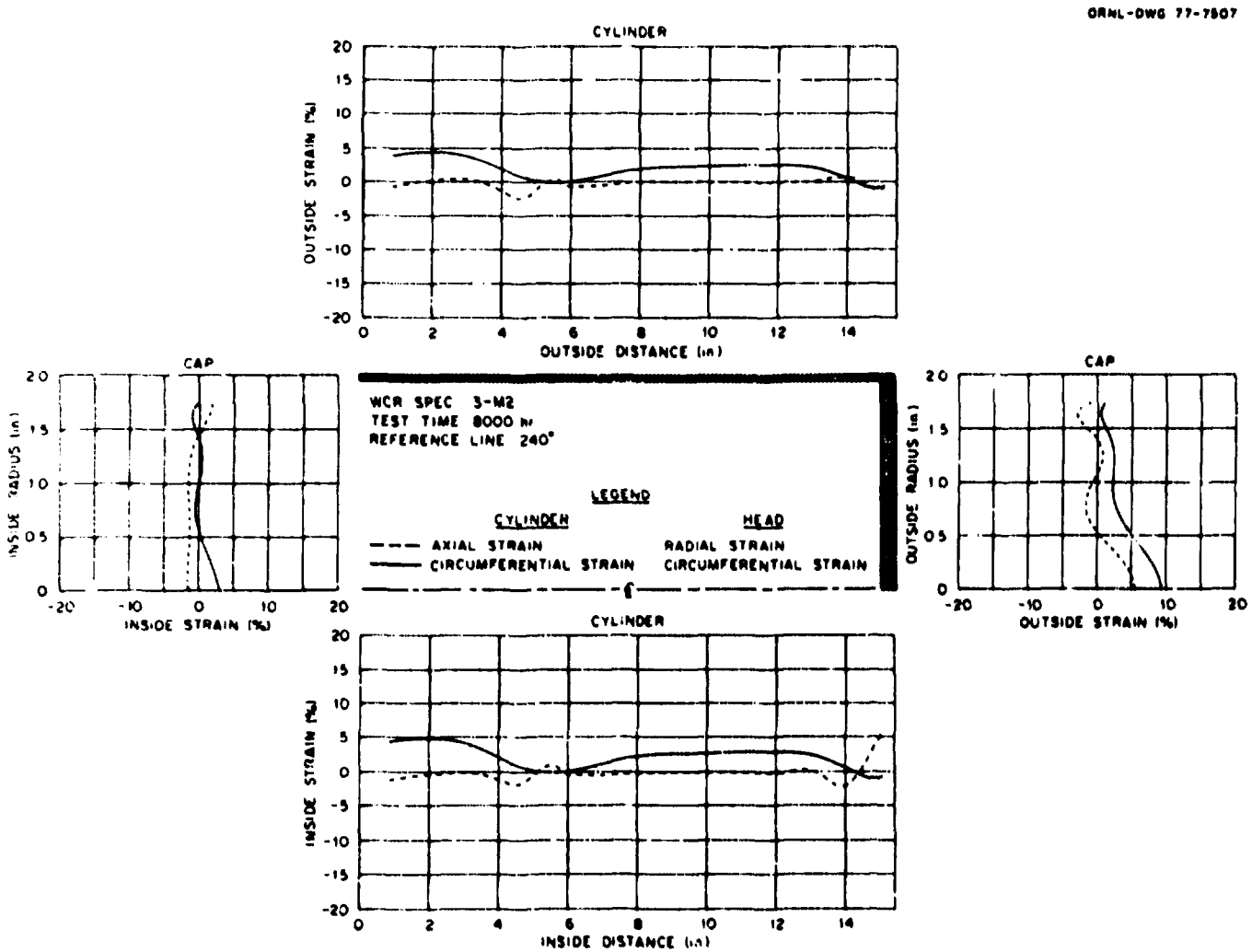

Fig. A14-e. Surface strain distribution for specimen 3-M2 along the axial reference plane, $\theta = 248^{\circ}$, at 8000 hr (1 in. = 2.54 cm).

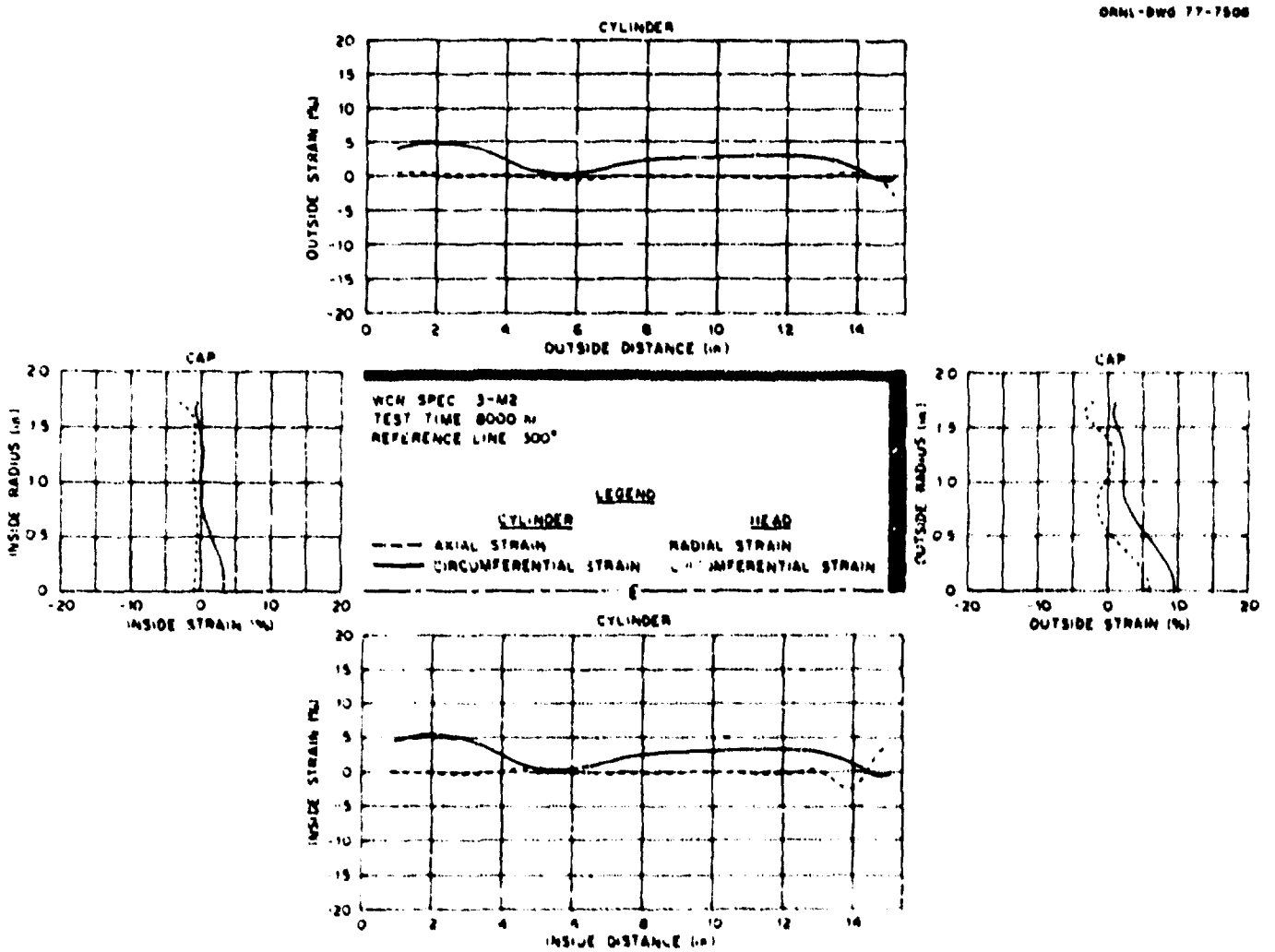

Fig. A14-f. Surface strain distribution for specimen 3-M2 along the axial reference plane, $\theta = 300^{\circ}$, at 8000 hr (1 in. = 2.54 cm).

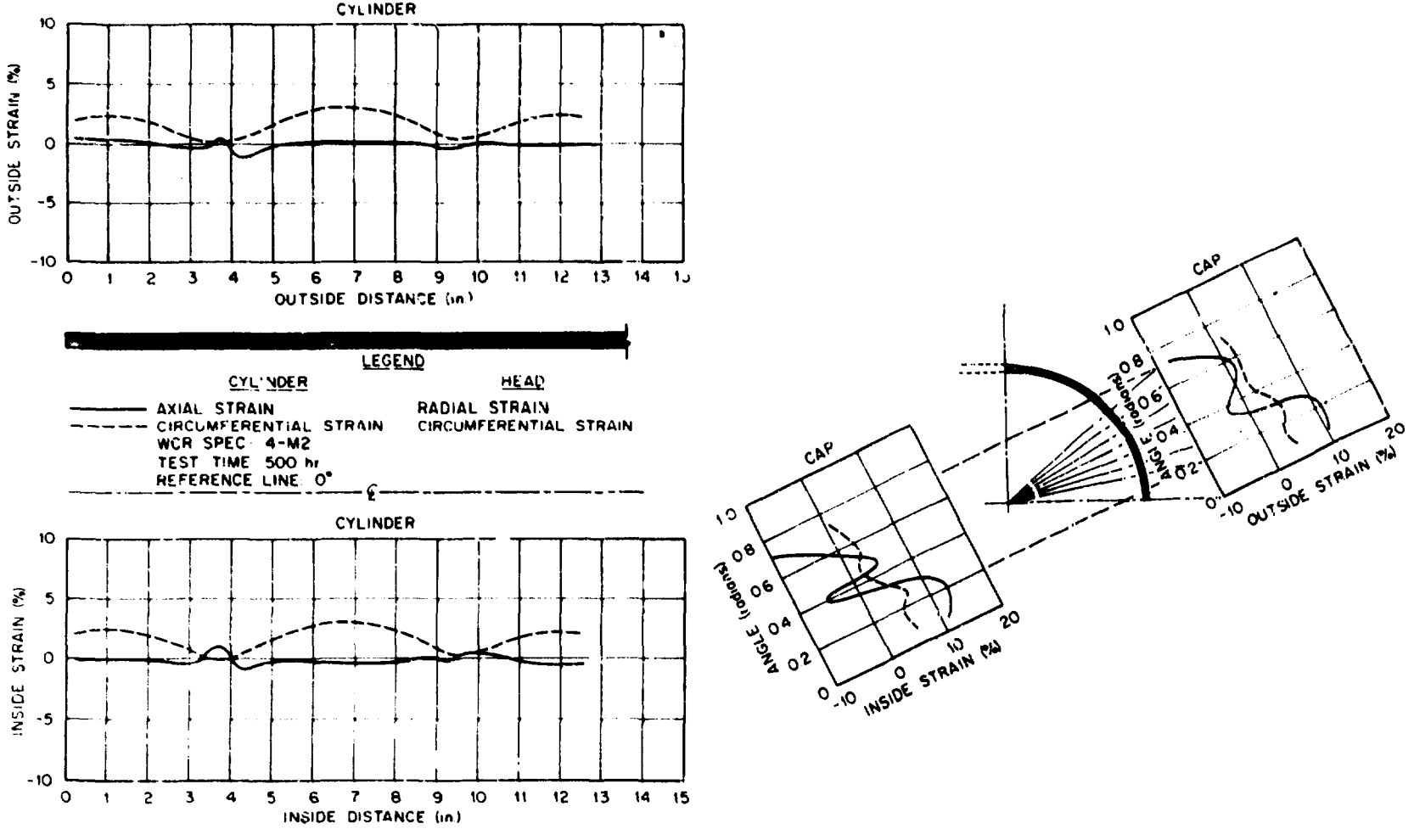

Fig. 5-a. Surface strain distribution for specimen 4-M2 along the axial reference plane, $\theta = 0°$, at 500 hr (1 in. = 2.54 cm).

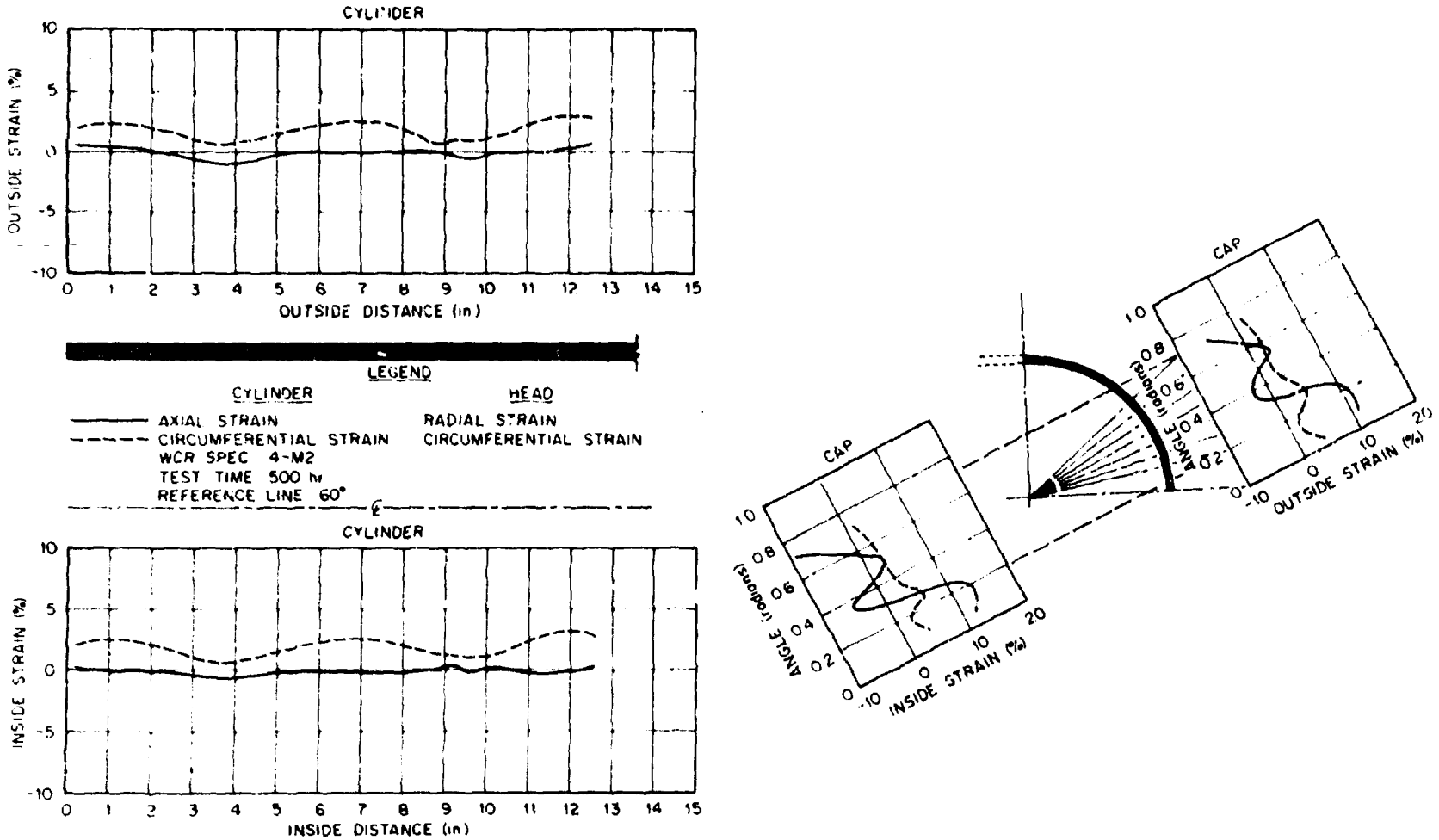

Fig. A15-b. Surface strain distribution for specimen 4-M2 along the axial reference plane, $\theta = 60^{\circ}$, at 500 hr (1 in. = 2.54 cm).

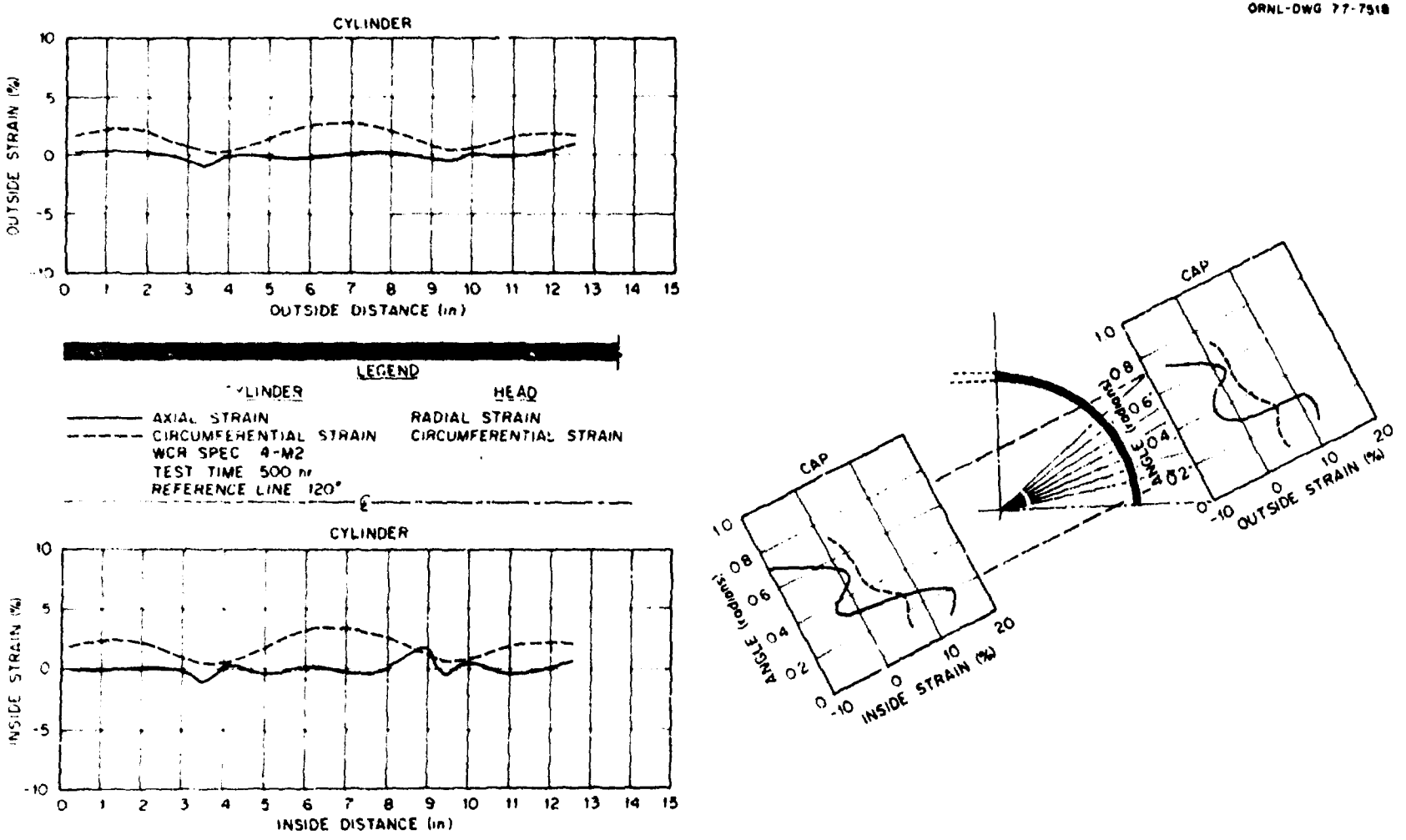

Fig. A15-c. Surface strain distribution for specimen 4-M2 along the axial reference plane, $\theta = 120°$, at 500 hr (1 in. = 2.54 cm).

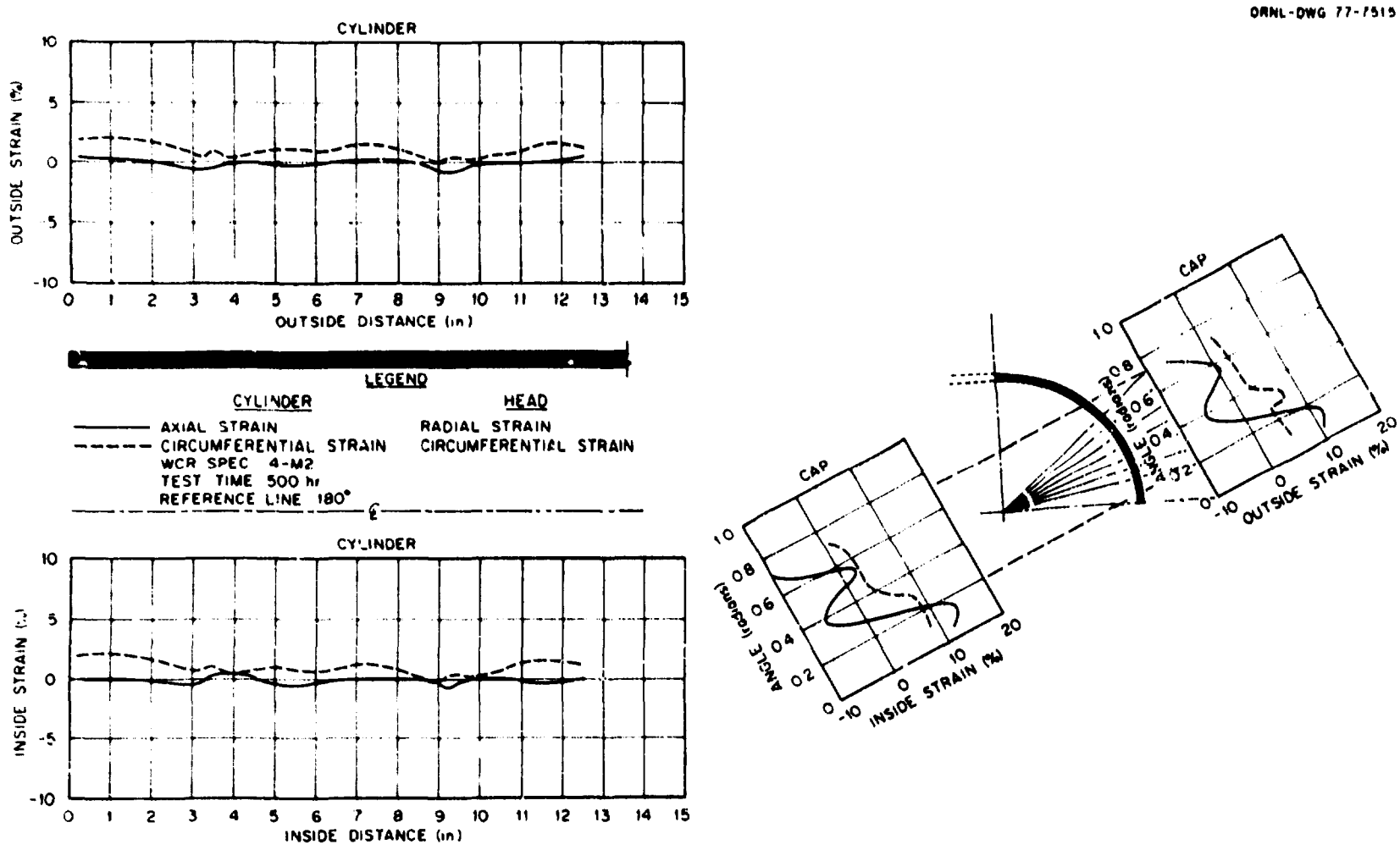

Fig. A15-d. Surface strain distribution for specimen 4-M2 along the axial reference plane, $\theta = 180°$, at 500 hr (1 in. = 2.54 cm).

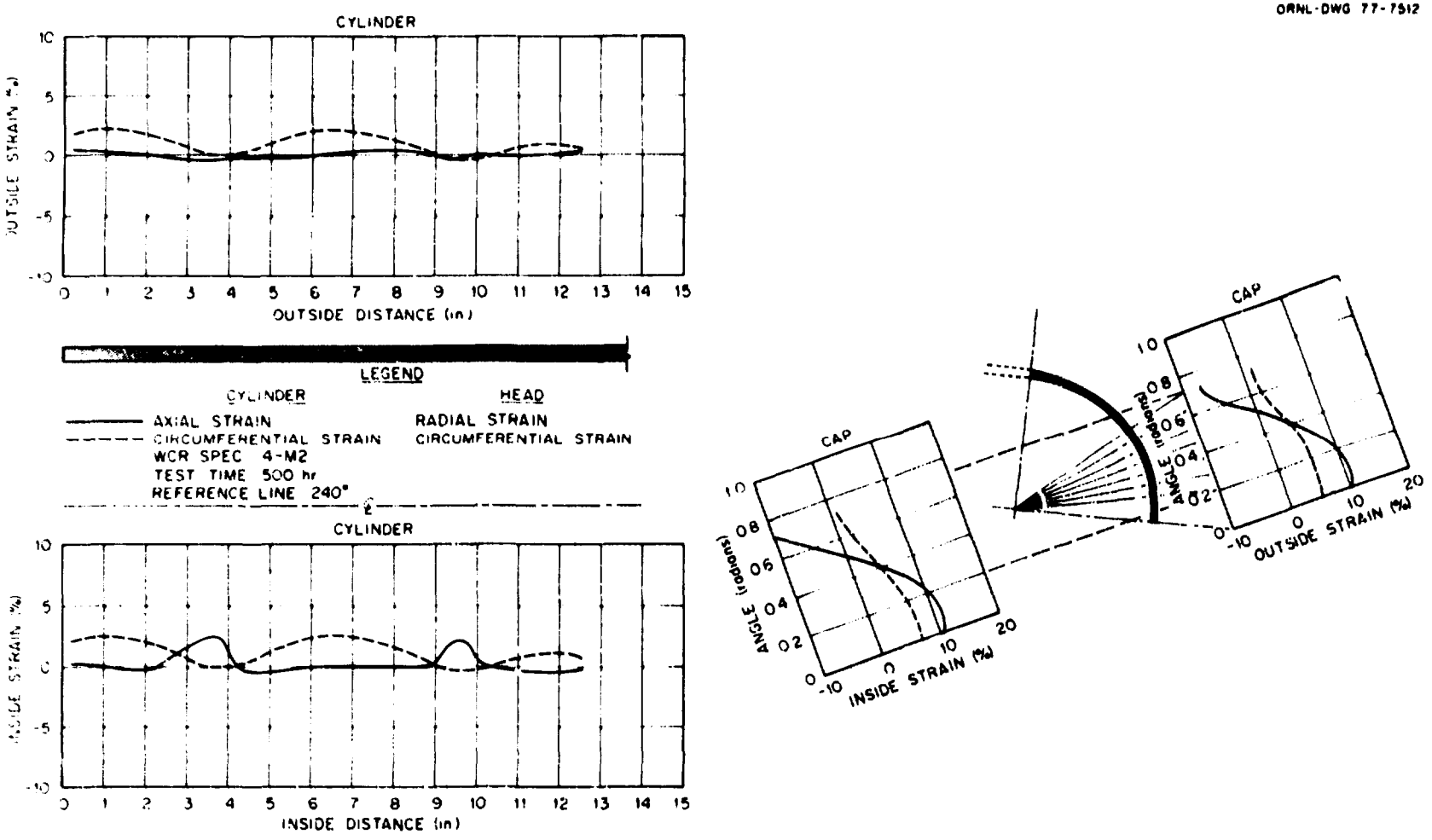

Fig. A15-e. Surface strain distribution for specimen 4-M2 along the axial reference plane, $\theta = 240°$, at 500 hr (1 in. = 2.54 cm).

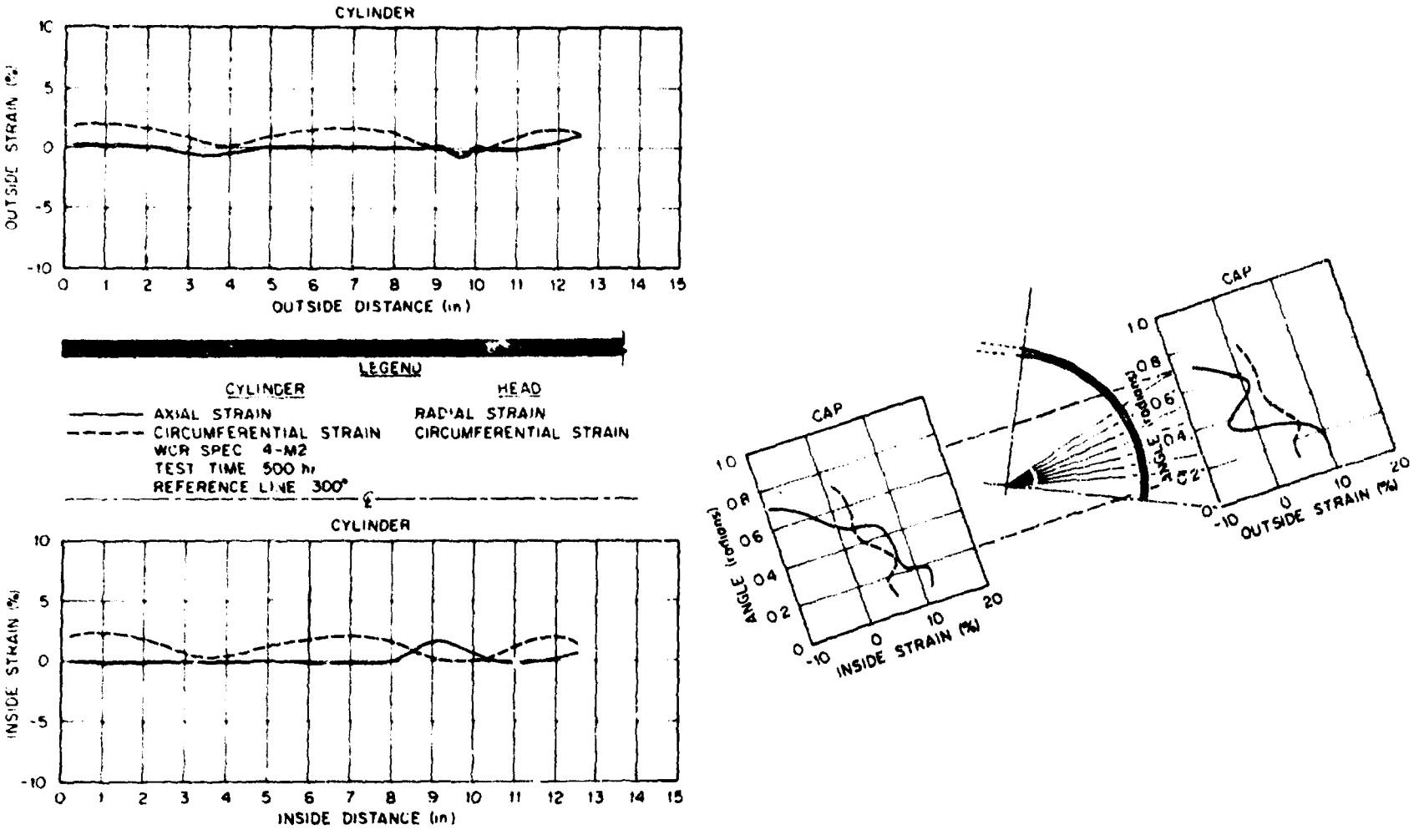

Fig. A15-f. Surface strain distribution for specimen 4-M2 along the axial reference plane, $\theta = 300^{\circ}$, at 500 hr (1 in. = 2.54 cm).

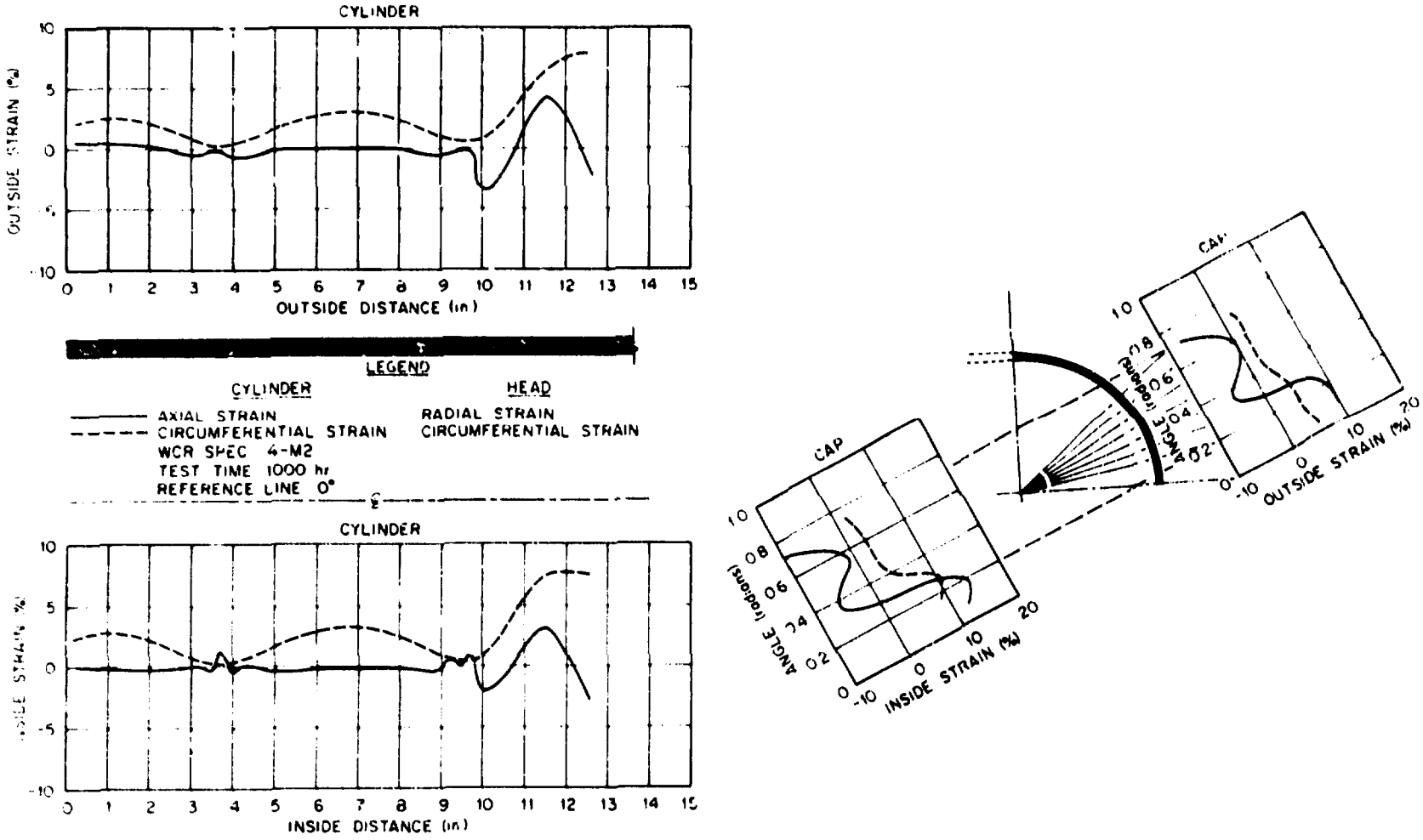

Fig. A16-a. Surface strain distribution for specimen 4-M2 along the axial reference plane, $\theta = 0^{\circ}$, at 1000 hr (1 in. = 2.54 cm).

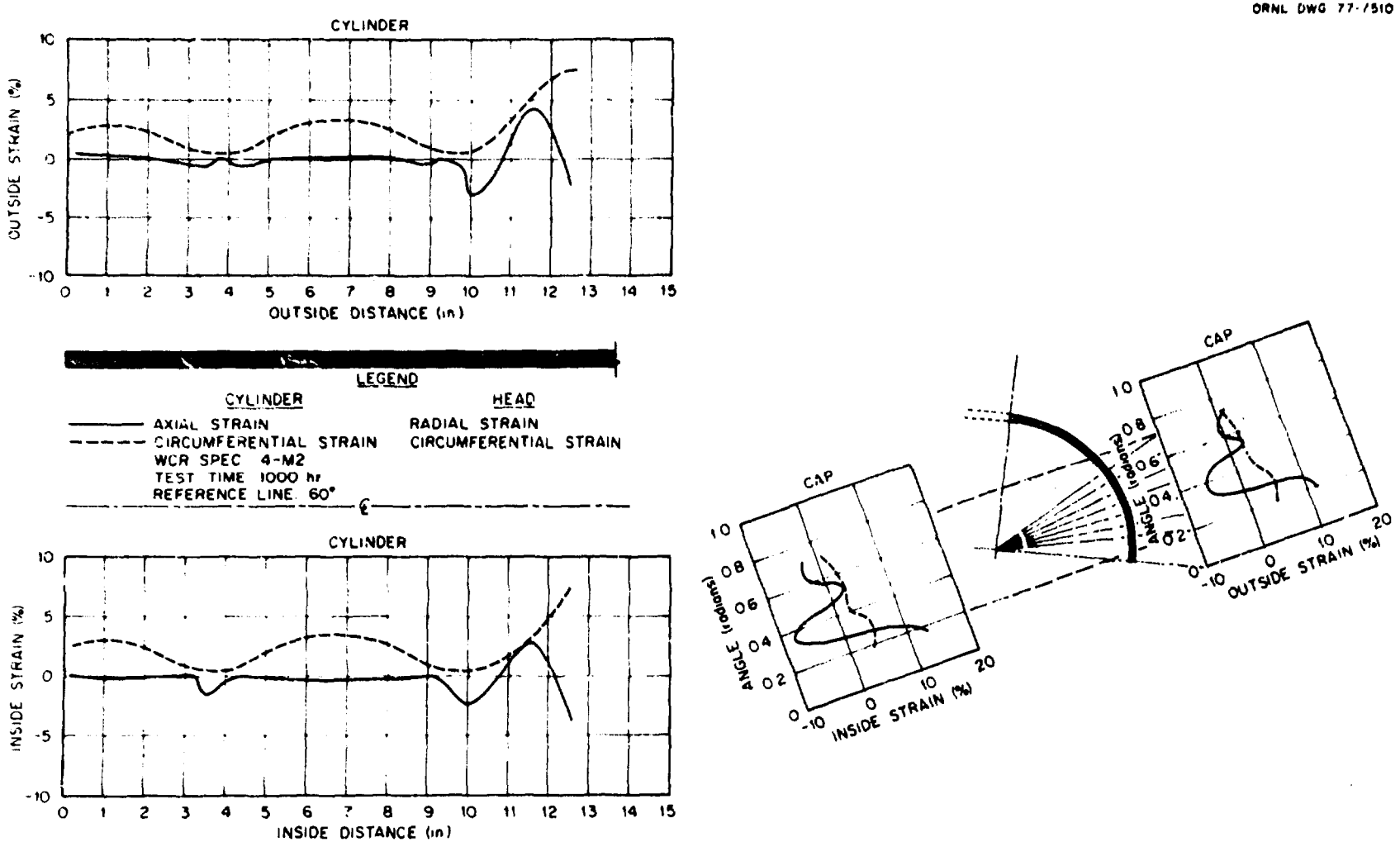

Fig. A16-b. Surface strain distribution for specimen 4-M2 along the axial reference plane, $\theta = 60°$, at 1000 hr (1 in. = 2.54 cm).

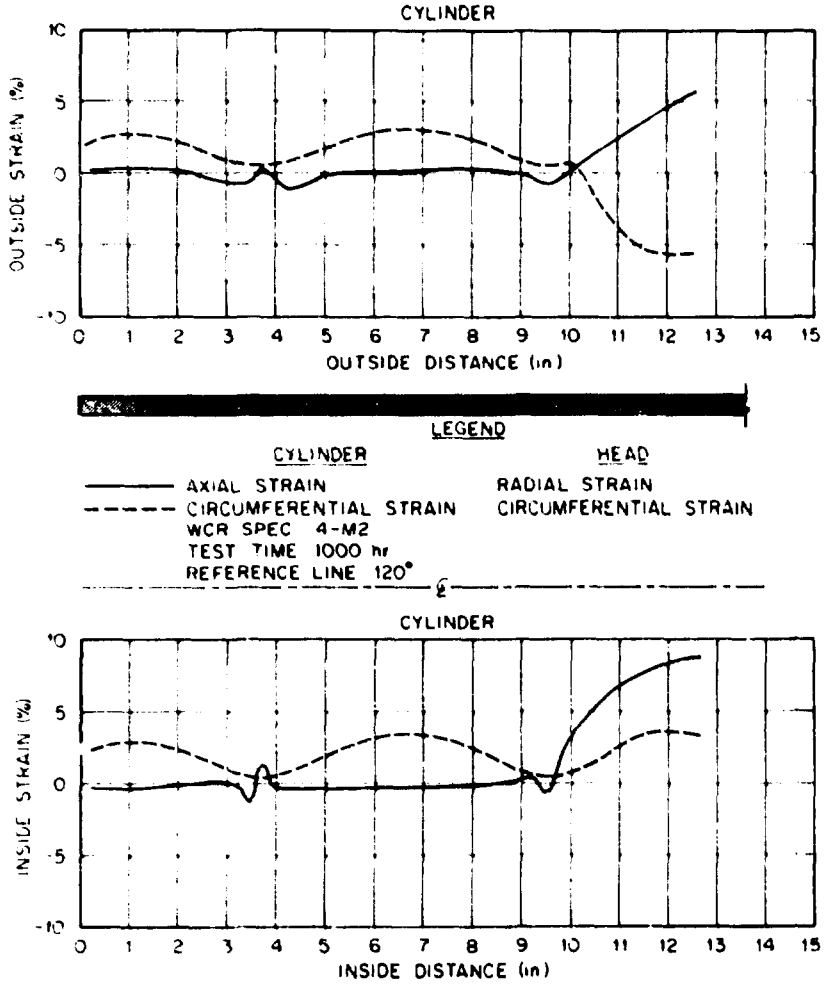

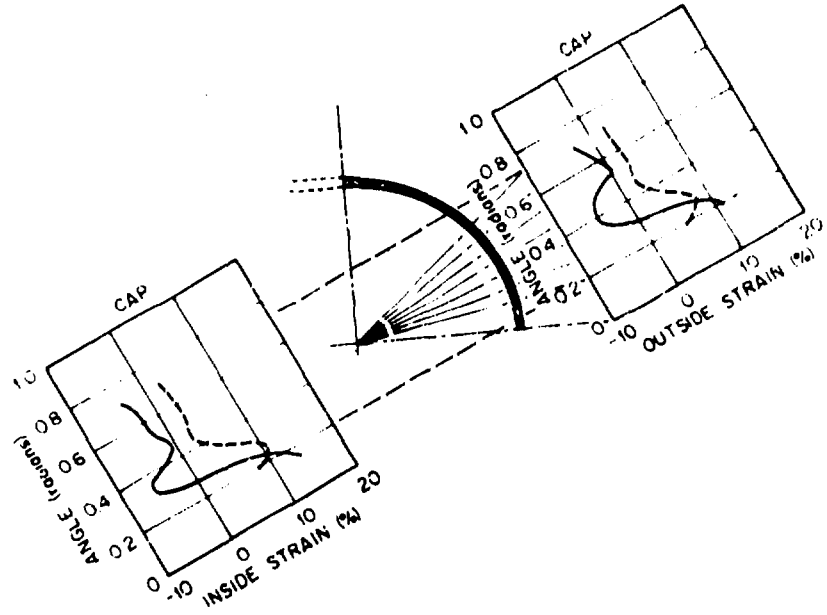

Fig. A16-c. Surface strain distribution for specimen 4-M2 along the axial reference plane, θ = 120°, at 1000 hr (1 in. = 2.54 cm).

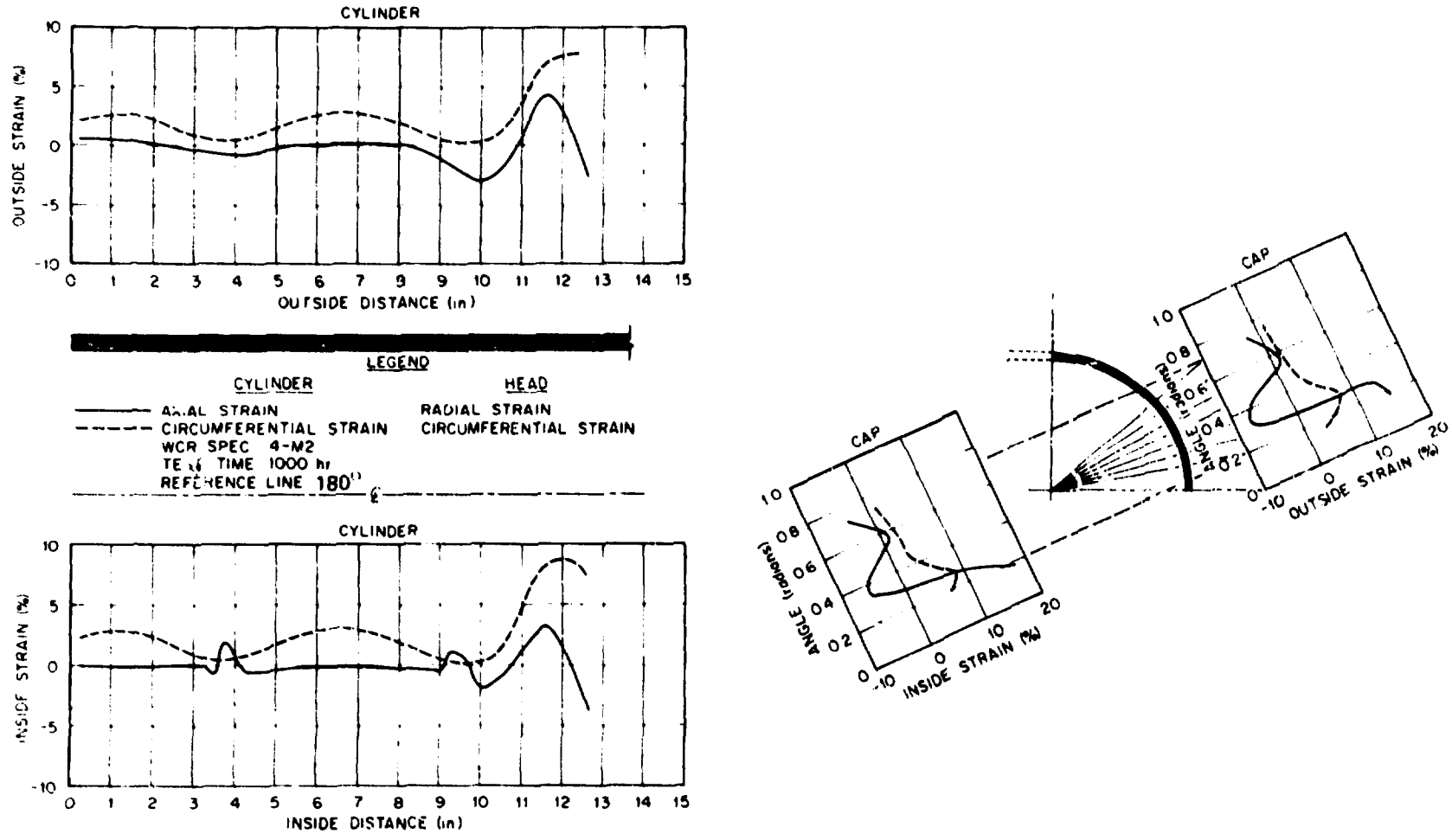

Fig. A16-d. Surface strain distribution for specimen 4-M2 along the axial reference plane, $\theta = 180^{\circ}$, at 1000 hr (1 in. = 2.54 cm).

ORNL-DWG 77-7516

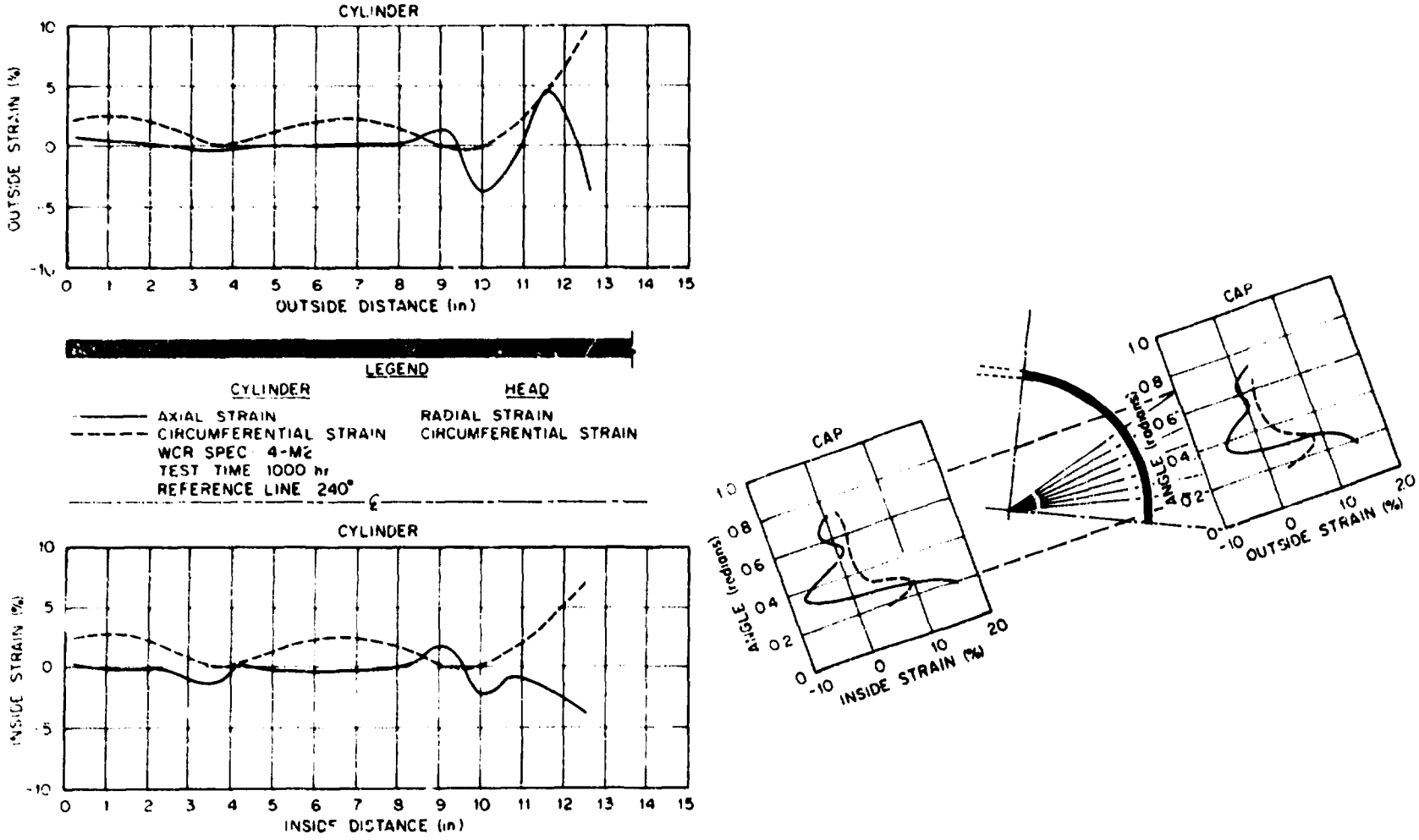

Fig. A16-e. Surface strain distribution for specimen 4-M2 along the axial reference plane, θ = 240°, at 1000 hr (1 in. = 2.54 cm).

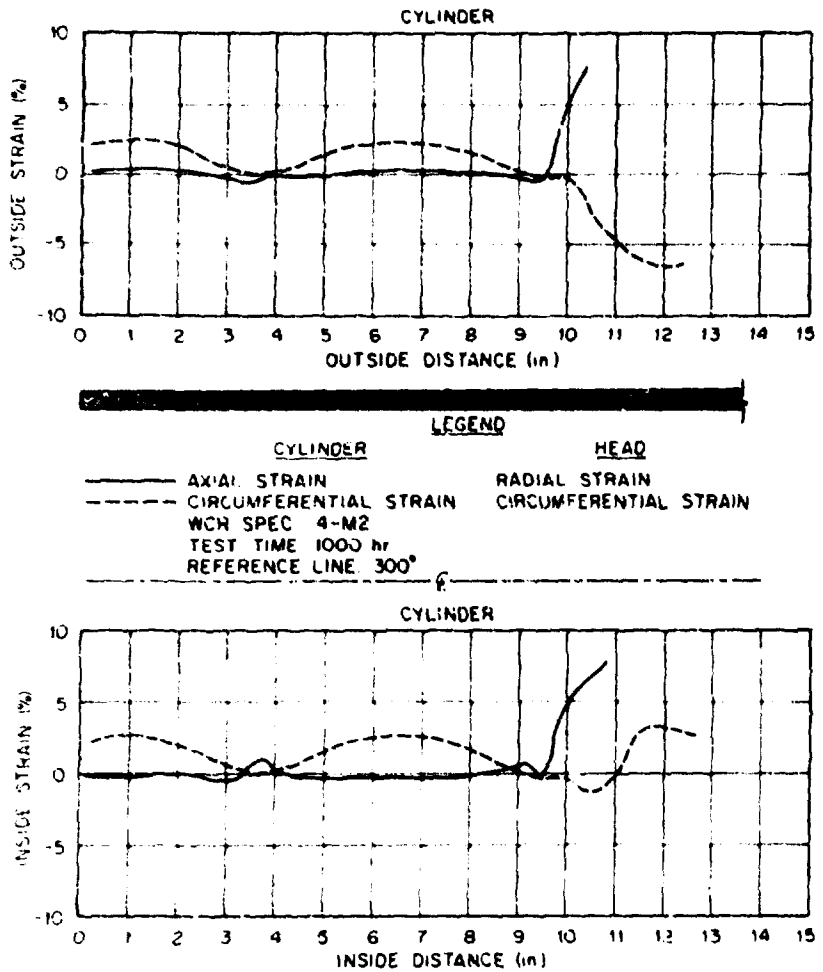

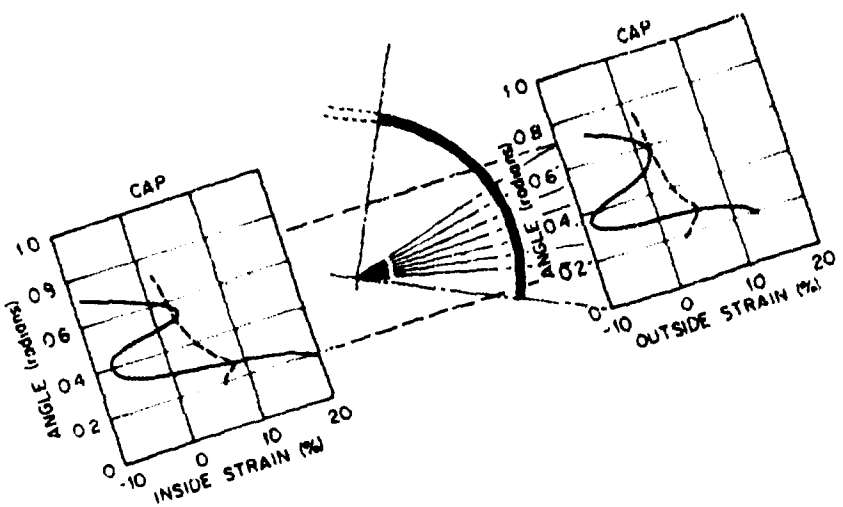

Fig. A16-f. Surface strain distribution for specimen 4-M2 along the axial reference plane, $\theta = 300^{\circ}$, at 1000 hr (1 in. = 2.54 cm).